MODELING AND VALIDATION FOR OPTIMIZATION OF ELECTROWINNING PERFORMANCE

by

Joshua Michael Werner

A dissertation submitted to the faculty of
The University of Utah
in partial fulfillment of the requirements for the degree of

Doctor of Philosophy

Department of Metallurgical Engineering

The University of Utah

August 2017

The University of Utah Graduate School

STATEMENT OF DISSERTATION APPROVAL

The dissertation of **Joshua Michael Werner**
has been approved by the following supervisory committee members:

Michael Free,	Chair(s)	**June 6, 2017** Date Approved
Darryl Butt,	Member	**June 6, 2017** Date Approved
York R. Smith,	Member	**June 6, 2017** Date Approved
Michael Simpson,	Member	**June 6, 2017** Date Approved
James Sutherland,	Member	**June 6, 2017** Date Approved

by **Manoranjan Misra**, Chair/Dean of
the Department/College/School of **Metallurgical Engineering**
and by **David B. Kieda**, Dean of The Graduate School.

ABSTRACT

Industrial electrowinning systems are by nature complex, and it can be challenging to evaluate the effects of parametric variation experimentally in production environments. Finite element simulations provide an alternative to physical experimentation. However, simulation of these systems are resource intensive and require coupled multiphysics interactions to accurately model. Despite these challenges, simulation can provide a cost effective means for improvement and optimization. To make it easier to improve operational efficiency and reducing electrowinning costs a model was developed using COMSOL Multiphysics finite element analysis (FEA) software. This work reviews the literature published on the subject providing context to the potential advances in approach. The proposed modeling strategy is presented, beginning with the Nernst–Planck equation describing the migration, convection and diffusion of ionic constituents in an electrolyte. This was coupled with a two-phase computational fluid dynamics (CFD) model to accurately describe mass transport in the system. This coupled approach will allow for accurate deposit morphology modeling. Further, roughness, operational cost and various stochastic methods will be incorporated to describe shorting and cost impact. The objective of this work is to provide a validated, more advanced model to determine the effects of operational parameters on electrowinning performance to facilitate optimization.

This work is dedicated to my loving wife and children, without their support this work would not have not have been possible.

CONTENTS

CHAPTERS

LIST OF FIGURES

LIST OF TABLES

NOTATION AND SYMBOLS

Chapter 1

β	current efficiency fraction
m_{dep}	deposited mass
z	number of electrons
F	Faraday's constant
I	current
i_{dep}	deposition current density
i_{total}	current density
t	time
A_w	atomic weight

Chapter 2

κ	conductivity
∇	Gradient
Φ	potential
k_{Ag^+}	silver mass transport coefficient
i_{L,Ag^+}	silver limiting current density
F	Faraday's constant
C_{Ag^+}	concentration of silver
C_i	concentration of species i
$k_{\text{Cu}^{2}+}$	copper mass transport coefficient
$D_{\text{Cu}^{2}+}$	copper diffusion coefficient

Chapter 3

a_j	activity of species j
a_k	ionic radius
A_w	atomic weight
a_z	related to the ionic radius and is specific to the ionic species
C_{Cu}	concentration of copper
$C_{\text{H}_2\text{SO}_4}$	concentration of sulfuric acid
∇c_i	concentration gradient
$C_{O,B}$	bulk oxidant concentration of the oxidized species
$C_{O,S}$	surface concentration of the oxidized species
$C_{R,B}$	bulk concentration of the reduced species

$C_{R,S}$	surface concentration reduced species
$D_{0,\mathrm{Cu}^{2+}}$	diffusion of copper
D_i	diffusivity of species of species i
F	Faraday constant
$\mathbf{F}$	volume force
$\mathbf{g}$	gravity vector
I	ionic strength of the solution
$\mathbf{I}$	identity matrix
$i_{electrolyte}$	current density in the electrolyte
i_{loc}	local current density at the interface (also called the charge transfer current density)
i_s	current density in the electrode
i_0	equilibrium exchange current density
k	denotes an index
m_j	concentration of species j
m^0	reference concentration
Mw_{Cu}	molecular weight of copper
N	total number of ionic species in the acqueous solution
N_i	flux density of species i
n	number of participating electrons
p	pressure
Q_k	general current source term
R	ideal gas constant
T	temperature
thk_{loc}	local thickness
t	time
u_i	mobility of species i
$\mathbf{u}_l$	velocity vector
z	charge of species
z_i	charge of species i
α_a	anodic symmetry factor
α_c	cathodic symmetry factor, z is the number of electrons transferred in the rate limiting step (typically 1)
γ_j	activity coefficient
ϵ	permittivity of the vacuum
ϵ_r	dielectric constant
ϵ_0	electrical charge of one electron
η	electrode over potential
μ	dynamic viscosity
ν	velocity vector
ρ	density
ρ_l	density

σ_s	conductivity of the electrode
ϕ_l	phase volume fraction
$\nabla\Phi_l$	electric field
$\nabla\Phi_s$	electric field

Chapter 4

A	area of diffusion
A_i	appropriate electrode
a_j	is the activity of species j and is unit-less
A_c and A_a	areas of the cathode and anode respectively
C	concentration of species i
∇c_i	concentration gradient
$C_{i,bulk}$	concentration of *i*th species in bulk
$C_{\mathrm{bulk,Fe^{2+}}}$	is the bulk Fe^{2+} concentration
$C_{\mathrm{bulk,Fe^{3+}}}$	bulk Fe^{3+} concentration
$C_{\mathrm{Fe\ Total}}$	total iron concentration
$C_{in,\mathrm{Fe^{2+}}}$	inlet concentration of Fe^{2+}
$C_{in,\mathrm{Fe^{3+}}}$	inlet concentration of Fe^{3+}
$C_{O,B}$	bulk oxidant concentration of the oxidized species
$C_{O,S}$	surface concentration of the oxidized species
$C_{R,B}$	bulk concentration of the reduced species
$C_{R,S}$	surface concentration reduced species
$D_{eff,main}$	effective diffusion coefficient
D_i	diffusion coefficient of *i* species
$D_{\mathrm{Fe^{2+}}}$	diffusion coefficients of ferrous ions
$D_{\mathrm{Fe^{3+}}}$	diffusion coefficients of ferric ions
$D_{inf,Alt}$	infinite diffusion of species
$D_{inf,main}$	infinite diffusion of species
$\mathbf{F}$	volume force
$\mathbf{g}$	gravity vector
$\mathbf{I}$	identity matrix
I	current density
I_{limit}	limiting current density
i_{loc}	Local current density at the interface (also called the charge transfer current density)
i_0	Equilibrium exchange current density
m_j	concentration of species j
M_t	amount of Cu^{2+}

m^0	reference concentration
Mw_{Cu}	Attomic weight of Cu
N_i	species flux of *i*th species
$N_{\mathrm{Fe}^{2+}}$	molar flux of Fe^{2+}
$N_{\mathrm{Fe}^{3+}}$	molar flux of Fe^{3+}
p	pressure
t	time
μ_T	Turbulent factor
u_i	mobility
$\mathbf{u}_i$	represents the velocity vector of the specified component
$\mathbf{u}_l$	velocity vector
$\dot{V}$	volumetric flow rate
Vol	tank volume
z_i	charge
α_a	Anodic symmetry factor
α_c	Cathodic symmetry factor, z is the number of electrons transferred in the rate limiting step
γ_j	activity coefficient
δ	diffusion boundary layer thickness
δ_c and δ_a	boundary layer thicknesses of the cathode and anode respectively
δ_i	boundary layer thickness of the *i*th species reacting a the the electrode
μ	dynamic viscosity
μ_l	dynamic viscosity of the liquid
ν	velocity vector
ρ_l	density
$\nabla\Phi_l$	gradient of the electric field
ϕ_l	phase volume fraction

Chapter 5

a	first-time leap
$(i_{local-ave}$	average local current vector
n	simulation number
r	exponent base
Vel_{loc}	local deposit velocity
$\mathrm{Vel}_{\mathrm{local-ave}}$	deposit growth velocity
X_{loc}	total deposit thickness
X_{loc_i}	local deposit position of the *i*th simulation period
ξ_i	time duration of the *i*th simulation period
τ_i	deposit or real time duration of the *i*th simulation period

Chapter 6

$A_{\text{cathode full scale}}$	area full scale cathode
$A_{\text{cathode test scale}}$	area test scale cathode
$A_{\text{sample coupon}}$	area coupon
b	roughness function intercept
$C_{\text{electrode,Cu}^{2+}}$	bulk and electrode surface concentration of copper
$C_{\text{bulk,Cu}^{2+}}$	bulk concentration of copper
F	Faraday constant
$F_{x,\text{full scale}}$	full scale probability
$F_{x,\text{test scale}}$	test scale probability
I	current density
I_{limit}	limiting current density
$i_{limit,Cu^{2+}}$	limiting current density of copper
m	roughness function slope
N_{sample}	number of the sample sorted from smallest to largest
$N_{\text{Total samples}}$	total number of features
$N_{Cu^{2+}}$	molar flux of copper
$T_{\text{full scale}}$	full scale ratio
$T_{\text{test scale}}$	test scale ratio
z	charge of species
β	Weibull parameter
α	Weibull parameter

Chapter 7

$C_{\text{electrode,Cu}^{2+}}$	bulk and electrode surface concentration of copper
$C_{\text{bulk,Cu}^{2+}}$	bulk concentration of copper
$k_{\text{Cu}^{2+}}$	mass transfer coefficient of copper
$N_{\text{Cu}^{2+}}$	molar flux of copper

ACKNOWLEDGEMENTS

It is not possible to conclude a work such as this with out the help and assistance of many others. I would like to acknowledge first and foremost my wife Katie and my children, Wyatt, Eleanore, Elijah, Samantha, Bianca and Duncan whose help, support and sacrifices in this endeavor have allowed me the opportunity to complete this work. My parents have also offered encouragement and inspiration for me to attempt such an arduous task. I would also like to acknowledge my friend and mentor Dr. Michael Free who took a chance on me, bringing me back to school. He has become a great mentor and friend. To Zongliang who has assisted me significantly in the modeling aspects of this work, without which I could not have accomplished in the time alloted, and JaeHun for experimental work which was invaluable. A particular debt of gratitude is owed to the SME Foundation for the PhD. fellowship. Without this award it would not have been possible to complete my PhD. I gratefully acknowledge Amira for their sponsorship of this work through grant P705C. Alas, there are too many to mention, but with a grateful heart I acknowledge my own weaknesses and frailties and the need I have of my many friends and helpers over the years. Thank you.

CHAPTER 1

INTRODUCTION

1.1 Overview

Electrowinning is the electrochemical process of depositing metal from dissolved metal ions without replacement of metal ions via anodic dissolution. This is an important method [1] for a variety of primary and secondary metals processing scenarios. Of primary operational importance is the topography of cathodic deposits. Irregularities in the form of surface perturbations (roughness, nodule formation), geometric irregularities (misaligned, bent or tilted cathodes) are often the driving factors in short circuiting, which influences current efficiency and the frequency of the harvest cycle, thereby impacting operational costs.

Industrial electrowinning systems are by nature complex. Figure 1.1 is provided to show these complexites and the multiphysics nature of electrowinning systems. This schematic representation of a single anode cathode pair shows the major influences of the system. Copper is deposited at the anode via cathodic reactions. Oxygen is generated at the anode due to the counter reaction of water splitting. The evolution of oxygen bubbles contributes significantly to the agitation of the solution via buoyancy and slip-drag forces of bubble movement. Accurate modeling of solution density changes due to the copper depletion at the cathode is critical to the simulation. Diffusion, migration and bulk species transport combine to describe the movement and concentration of species of interest.

1.2 Economic Considerations

For economic reasons, it is critical to prolong the electrodeposition time before short-circuiting, which is caused by the abnormal growth of copper deposit as dendrites or nodules. Nodules, which are rough hemispheres, can be formed as protruding structures on the cathode. The current densities on dendrites or nodules are generally much higher than those on relatively flat deposits. As a result, these protruding structures can

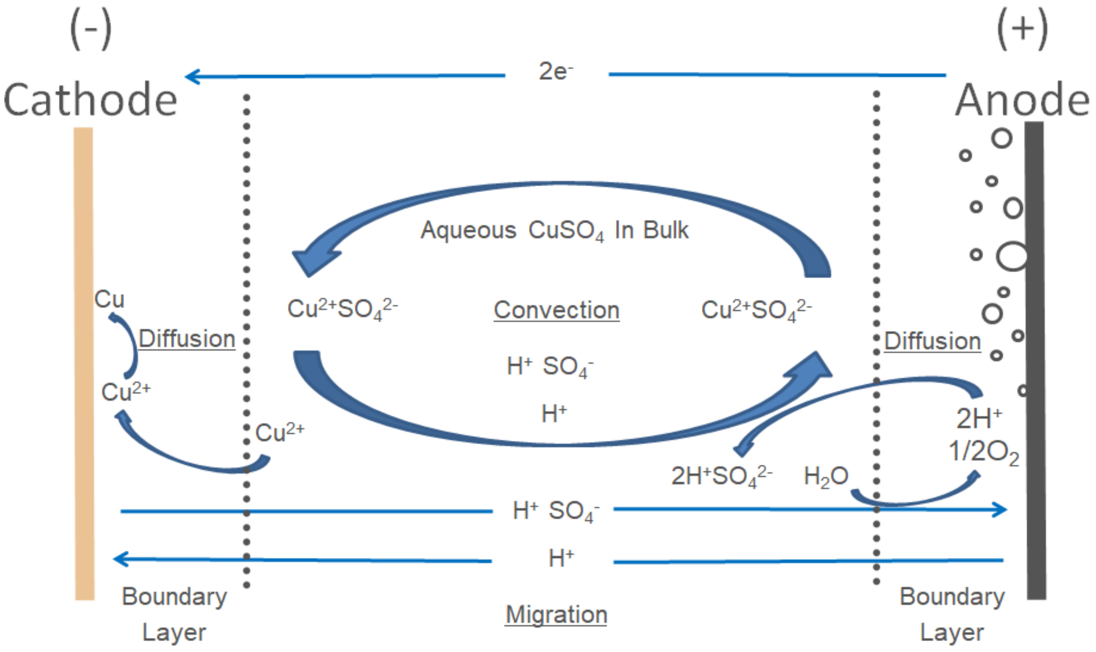

Figure 1.1: Schematic representation of a copper electrowinning cell. Note stoichiometry is unbalanced for illustrative purposes due to neglecting of complexation.

experience accelerated growth. To reduce the formation of and growth of nodules, electrolyte additives are used in many tank houses. Nevertheless, the formation and growth of dendrites or nodules often occurs when additives are used. In addition to dendrite and nodule formation, there can be significant differences in deposit thickness that are location specific due to local conditions on an electrode. The combination of nodule formation and non-uniform growth can lead to premature short-circuiting. Therefore, accurate prediction of cathode deposit topography in copper electrowinning is important to the prediction of short-circuiting. The local growth of the cathode deposit directly determines the operating time before short-circuiting.

Figure 1.2 was developed to illustrate the methodology for predicting electrowinning cell performance and costs. The summation of these costs will cover the majority of the operational expenses and performance criteria found in most electrowinning operations.

- **Current Efficiency.** Current efficiency often provides the most direct effect on cost and performance. Current efficiency is the amount of current that goes to the formation of electrowon metal. It is given by the expression (1.1):

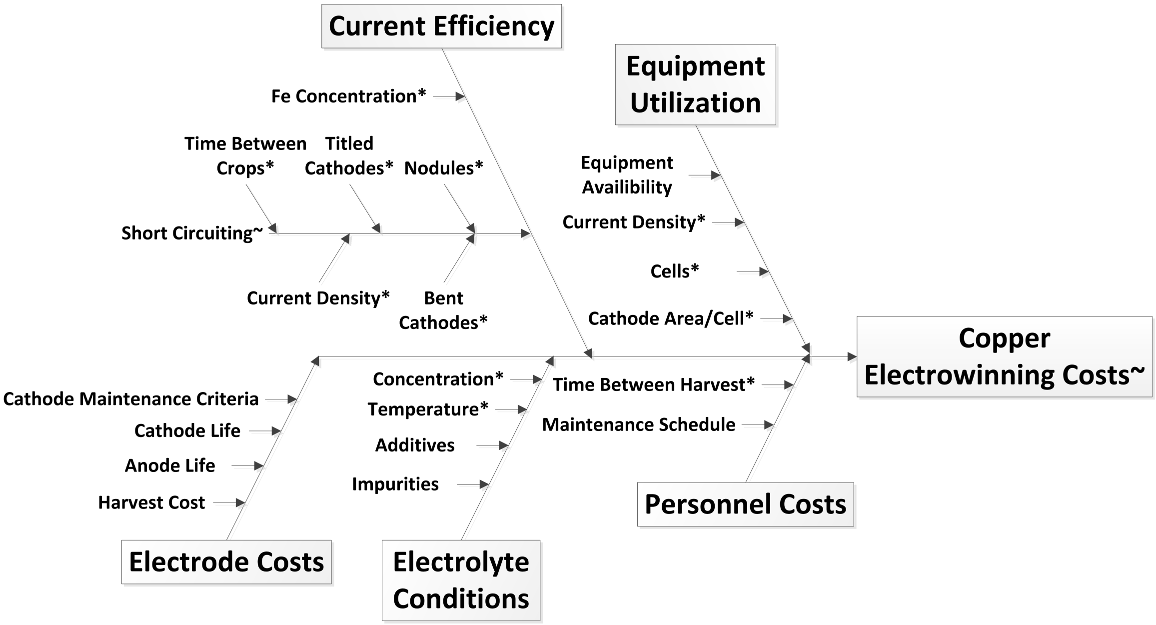

Figure 1.2: Model inputs and outputs for copper electrowinning cost determination. * indicates modeled inputs, ˜ indicates modeled outputs.

$$\beta = \frac{i_{\mathrm{dep}}}{i_{\mathrm{total}}} \tag{1.1}$$

where i_{dep} and i_{total} are the deposition and total current density respectively. Further current efficiency may be measured practically by the expression (1.2) [2] where total current I is compared to the deposited mass.

$$\beta = \frac{m_{\mathrm{dep}} z F}{I t A_w} \tag{1.2}$$

where β is the current efficiency fraction, m_{dep} is the deposited mass, z is the number of electrons in the reaction, F is Faraday's constant, I is current, t is time and A_w is atomic weight.

The key factors in current efficiency can further be subdivided into electrochemical and geometric parts. The electrochemical parts are primarily influenced by the presence of iron. The $\mathrm{Fe}^{3+} + \mathrm{e}^{-} \leftrightarrow \mathrm{Fe}^{2+}$ half-cell reaction in the cell robs current from the cathode. Likewise, short-circuiting achieves the same effect by allowing an alternate current path outside useful deposition. Short-circuits are caused by a number of factors, but they are primarily related to deposit geometry and quality.

- **Equipment Utilization.** The costs incurred in this group are concerned with the specific production capacity of the equipment.

- **Electrode Costs.** These costs are included to capture the ongoing cost of replacement and maintenance of the electrodes and harvest of the metal.

- **Electrolyte Conditions.** Operationally these factors are often associated with deposit quality. These costs include reagents, cost of heating and the effects on the deposit of these parameters.

- **Personnel Costs.** Lastly included are personnel costs associated with operations. These are directly influenced by the harvest cycle times and by the overall equipment maintenance.

1.3 Scope of Work

The objective of this work is to develop a model of sufficient accuracy and usability as an improvement and optimization tool for electrowinning tank houses. To achieve this objective a number of modeling techniques are utilized (primarily finite element analysis) to explore the various interactions of input and output parameters. In so doing a framework will be constructed to allow economic impact to be determined for various operating conditions (see Figure 1.2). The focus of this work will be to utilize finite element analysis to estimate the local deposit thickness in a electrowinning cell utilizing a multiphysics approach, which includes ion transport via the Nernst–Plank equation and fluid dynamics via Euler–Euler two phase flow. Also, validation methodologies will be discussed utilizing prior work, experimentation and instrumentation.

This work will not include any attempts to determine any microscale phenomena such as nucleation or the effect of parameters on deposit grain structure. Rather, this work will evaluate the macroeffects such as deposit topography and stochastic mechanisms such as shorting.

In summary, the objectives of this work are to (see Figure 1.3):

1. Develop an combined electrochemical model/multiphase fluid model which predicts local current density.

2. Enhance model depth to consider species found in the electrolyte and local current efficiency.
3. Perform a numeric study into the heterogeneous equilibrium speciation reactions and iron electrode kinetics.
4. Develop a model to evaluate fluid structure interactions with the deposit.
5. Develop a roughness model to use with the deposit model to predict short circuiting.
6. Translate learnings from small scale to full size configurations and compare to literature.
7. Develop a model for short circuit effects on current efficiency.
8. Develop cost parameters model to allow prediction of operating costs.
9. Perform experimentation and develop instrumentation to validate the modeling.

This work is intended to assist industrial partners to reduce the time and costs associated with improving operational efficiency. By achieving these objectives novel and valuable contributions will be made to the field to advance understanding and provide a valuable tool.

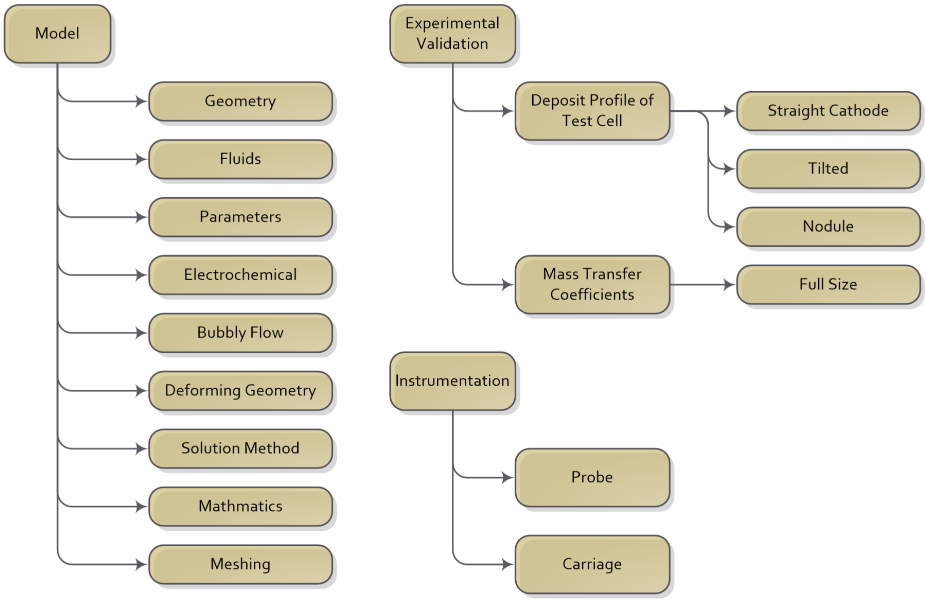

Figure 1.3: Methodological approach.

CHAPTER 2

LITERATURE SEARCH

Critical to the outcome of any research work is the determination of what has been accomplished in the field. As such a literature review was conducted to evaluate the field and identify any needs which have not been addressed. Time and effort were preserved in the utilization of prior work. The search was conducted to satisfy two questions. What had been modeled and what can we learn from it? The second is what parameters are needed for our model? The following are the findings from the search.

2.1 Prior Modeling

To understand the mechanics of the model and to provide a context for its developments a review of select literature is provided. The literature sources focus primarily on different models that attempt to predict electrowinning behavior. Several models are included which are not electrowinning because they provide interesting or critical insights which are valuable for consideration. In terms of modeling there were several critical elements that were searched for and addressed. These are:

- What fluid dynamic equations were utilized? Were bubbles considered?
- What transport equations were utilized?
- Were electrode kinetics considered? If so how?
- What was the objective of the model?
- How was the model validated?

Some of the early work in modeling these systems by Ziegler et al. [3][4][5], used RANS κ–l type Euler–Euler fluid flow modeling as the basis of their simulation. Turbulent diffusivity is used to simulate the movement of bubbles. This work provides comparisons to the tracer work in references [6] and [7] and includes calculations of changes in electrolyte conductivity due to bubbles. The boundary conditions of the model are given in the associated thesis. Comparisons to the work of Ettel are described in [4].

Kisdnasamy et al. [8] studied the affect of adhering gas bubbles on electrode surfaces on electrolyte conductivity. They reproduced this by utilizing Styrofoam balls to electrodes and comparing the results to Maxwell's and Bruggeman's equations. Their experimental data was compared to each, showing general agreement with the overall trend. They presented an expression to better fit the results.

Nguyen et al. [9] present an electrowinning model considering time dependent diffusion and migration between parallel plates. The copper chloride system is modeled. They use the Nernst–Planck equation in a dimensionless form utilizing finite difference techniques. This work does not appear to model natural convection, but rather, forced convection due to inlet and outlet flows as an electrochemical reactor. Of interest is the inclusion of anode and cathode kinetic parameters. They found that the aspect ratio of the separation distance to the length of the electrodes (0.5>aspect ratio) was the determining factor if it was necessary to include the migration term.

Smyrl et al. [10] investigate the influence of electrode kinetics on edges. In this paper, it is on a rotating disc electrode. They conclude the primary current (ohmic) distribution is acceptable everywhere but the edge where kinetics become important. This of interest in the general discussion of when and how electrode kinetics should be used over primary current simplifications. They handle mathematically the differences between the two and show the stabilizing influence of the electrode kinetics to prevent singularities or infinite current conditions.

Bark et al. [11] examined the problem in greater depth including transport via the Nernst–Planck equation and the addition of anodic and cathodic reaction kinetics as part of their model. In their work, they chose to algebraically formulate their model rather than use finite element techniques. However, this is of limited application due to the evaluation of electrorefining rather than electrowinning, which didn't include effects from bubbles.

Marshall et al. [12] attempt a modeling electrochemical deposition. They use a simplified Navier–Stokes equation. They begin by examining a 1D problem before moving to a 2D. They include concentration distributions, electrostatic potentials and fluid velocities.

Diffusion, migration and convection were considered. This paper was interesting in that it simulated dendrite growth on a projecting filament and was included in the literature search for contrast.

Dahlkild [13] provides additional insights by utilizing a two-phase equation of a Navier-Stokes type of model that accounts for gas fraction and gas diffusion. This model considers gas evolution. The modeling of transport is interesting with the transference associated with species flux in a binary electrolyte and Bulter–Volmer electrode kinetics. Boundary layers were modeled with derived mathematical expressions. This model appears to correlate well with the experimental data of Hine and Murakami [14].

Progressing further, Sokolichin and Eigenberger [15] provide a review of the Euler–Euler framework for the treatment of the Navier–Stokes equation for two phase flow treated under a single momentum conservation equation. This paper is quite useful as a fundamental basis for the fluid flow approximations of the Euler–Euler model.

Philippe [16] in modeling a hydrolysis cell pursues a different approach using the current density as a function of Ohm's Law with the current density vector being:

$$I = -\kappa \nabla \Phi \tag{2.1}$$

where I is current, κ is conductivity and Φ is potential. The effect of gas interactions with conductivity is included using the Bruggman relation [16]. The fluid flow equations used are of a Lagrangian nature with a force coupling term added to the base Navier–Stokes equation to produce the effect of bubbles.

Wuthrich et al. [17] consider the effect of bubbles on the voltage characteristics of the cell. They study a system in high current ranges where the gas formation begins to inhibit hydrolysis reactions. Wuthrich's work presents a quantitative model of the gas effects on the limiting current.

Free et al. [18] discuss electrowinning modeling and performance in this work. They focus on specific power consumption of deposition and current efficiency. Experimentation was performed via rotating disc electrode. Parasitic reactions were also considered with a model compared to experimental data.

Although the work of Cifuentes et al. [19] does not contain a traditional electrowinning design it is of interest due to the cathodic model. Their work considers speciation utilizing copper cathode reactions and ferric-ferrous anodic reaction. Thus no O_2 is generated at the anode. Debye–Hückel models are used to calculate activities and typical mass balance based on equilibrium relationships are utilized. It is somewhat unclear how $HCuSO^{+}_{4(aq)}$ is considered as it has an assigned diffusion coefficient, but doesn't appear in the speciation tables.

The work of Volgin et al. [20] presents significant illumination into the nature of the effects of speciation. Although not applied to electrowinning, the work is useful due to the study of the cathodic processes. The premise of the work is to solve for the effects of the natural buoyancy force due to electrolyte density change from the local copper concentration. This establishes fluid flow which is solved dimensionlessly with migration, diffusion and convection to determine the limiting current density. Useful diffusion, density and viscosity expressions are provided and the model is solved via variable simplification and normalization. Volgin includes terms for the heterogeneous chemical reactions of species in the mass transport equations. Close examination reveals that speciation is treated as occurring instantaneously fast with the transport equations providing transport limitations. The activities and species are calculated locally. Reaction kinetics for thermodynamic species equilibrium are not explicitly defined. Rather it is implied through the equations that the reactions are instantaneously fast due to equilibration. Therefore, kinetics is by inference based solely on mass transport.

The results are of great interest. There were several combinations of speciation attempted, but the two of significance were domain dependent equilibrium speciation and the assumption of full dissociation.

The results of this work show the similarity between full dissociation and equilibrium speciation. This is in agreement with what Newman has presented [21], that is that at high concentrations of supporting electrolyte full dissociation or speciation becomes less important and that the effect of speciation on the limiting current due to migration decreases with increasing supporting electrolyte.

Aldas et al. [22] studied a hydrolysis cell utilizing two phase flow and diffusion modifications due to gas fraction as a means of modifying conductivity with the Bruggman relation. Also incorporated were resistivity measurements to test the validity of the model. The Butler–Volmer equation is also modified via the gas fraction to influence the electrode kinetics. This is significant in that the Nernst–Planck equations are used for transport modeling; two-phase flow of Euler–Euler type and electrode kinetics are combined in one model.

Ribeiro et al. [23] present a model based on convection and diffusion and a form of electrode kinetics. The resulting effect of forced convection on the boundary layer and concentration profile is studied.

Pohjoranta et al. [24] present a paper on a model of an adjustable cell on which are located the working and counter electrodes. The purpose was to measure and model the ohmic resistance of the solution. Nernst–Planck equations are utilized for transport. A semianalytical version of the Butler–Volmer equation is also utilized. The utilization of a Lambert W–function to couple the ohmic electrolyte resistance to the electrokinetic response of the electrodes is also used, thus modeling the system as a secondary current distribution. The model results show reasonable correlation with the experimental data and it appears as though the assumptions utilized throughout are valid.

Volgin et al. [25] appear to expand on the work presented in [20] by extending the model to additional systems considered. These are KI, $AgNO_3$, $K_4Fe(CN)_6$ and $CuSO_4$.

Kawai et al. [26] modeled electrorefining based on transport flow with conductance and a simple speciation method. Kawai presents results for the time dependence of the cathodic concentration profile.

Leahy et al. [27] provides an excellent comparison of an electrowinning model to previous work. Convection and diffusion are modeled, but the effects of gas conductivity on the electrolyte are not considered.

Free's [28] work is included for reference with regard to discussion of leaching and electrowinning modeling.

Kim et al. [29] present a simplistic Navier-Stokes model of forced convection between two plates. Both electrorefining and electrowinning are considered. The Tafel approximation is utilized for electrode kinetics at the working electrode.

Hemmati et al. [30] studied multielectrode electrorefining using a RANS (Reynolds averaged Navier–Stokes) k–ω turbulent mode. The cathodic transport is simplistic based on the current density, but it considers multiple cathode-anode pairs. They used a Schmidt number, diffusion, and turbulence terms for transport. Their model is driven simply by

Faradaic consumption at the cathode.

Leahy et al. [31] in an expansion of his previous paper utilizes a RANS–SST (Shear Stress Transport) for time averaged turbulent flow. The cathodic transport is handled based on the current density and transference number and Faraday expressions are used for anodic and cathodic generation. Attention is paid to the transient nature of the fluid flow.

Shukla et al. [32], [33] provide basis for the current study proceeding the current work under the same sponsorship. A copper sulfate electrowinning system is studied via design of experiments to determine a model for roughness. Failure analysis statistics are utilized to predict time to short. A COMSOL model is presented. The model utilizes Navier–Stokes transport and a volume force is utilized to simulate buoyancy forces from the anodic gas evolution. This work is particularly important to the present study in the determination of the current density relationship to deposit roughness. This work is discussed extensively in Chapter 6.

The work of Robinson et al. [34], [35] is included for the insights into deposit modeling. It is rather unique in the thickness and geometries considered in the work. Further, simplifications were attempted to reduce the results from the modeling in to an expression which would describe the deposit thickness.

The work of Zeng et al. [36], [37] is included for reference. This work focuses on modeling electrorefining and is primarily concerned with describing the transport of anode slimes to the cathode. It is included due to the similarities of modeling an electrorefining cell with Navier–Stokes and Nernst–Planck equations. Also, included in reference [37] were electrolyte parameters developed as part of this work.

Najminoori et al. [38] use a model that is very similar to that of Hemmati et al. [30] with RANS Euler–Euler k-ω as the CFD (computational fluid dynamic) component and the same type of transport equation. Gas is produced at the anode according to the Faraday expression. This work is significant because it contains more than one electrode set.

Hreiz et al. [39] provide a review of what they term ”Vertical Plane Electrode Reactors with Gas Electrogeneration” or VPERGEs. This article focuses on the varying cell and fluid flow configurations surveyed. The literature with regard to bubble formation, properties and measurement techniques are covered. Models surveyed include a table listing the type of transport, turbulence and electrochemical coupling.

Hreiz et al. [40] then present their own model after reviewing the literature in [39] with a Euler–Lagrange model validated with PIV (Particle image velocimetry). The cell was a double electrode gas generation type. Gas fractions and cell velocities were studied and captured. Additional modifications to the injection point were needed to reproduce key features. The numerical results were in general agreement with the experimentation. The use of the Euler-Lagrange method was to capture numerically the bubble dispersion without having to account for added volume forces.

Litrico et al. [41] included coupled mass transport and deposition models. This occurred in a channel with parallel electrodes.

2.1.1 Summary of Prior Modeling

As referenced in the prior literature there has been a wide array of modeling presented. These models may be broken down into sub sections of what they include and approach. To better present these finding the following Tables 2.1-2.3 are presented for clarity. References were selected for their pertinence in providing context to evaluate areas which have not been address in the literature.

From these tables, it can be seen that the state of the art model would consider the following:

- Two phase flow considering bubbles and effects on volume forces
- Nernst–Planck equations to couple mass transport including resistive effects from bubbles
- Butler–Volmer electrode kinetics coupled with surface concentrations
- Localized current density
- Transient effects
- Experimental validation

For this model turbulence will not be considered, with the flows being in the range of 10,000 Reynolds number for the test cell utilized. This is discussed further in subsequent chapters.

Table 2.1: Summary of pertinent models: CFD type.

Name	Year	System	CFD Model
Ziegler [3],[4],[5]	1986	Cu EW	Euler-Euler with bubble turbulence k-l
Bark [11]	1995	Cu ER	Navier-Stokes No gas
Dahlkild [13]	2001	Single Vertical Electrode–Electrolysis H20	Navier-Stokes type accounting for gas fraction and gas diffusion
Philippe [16]	2005	EW	Navier–Stokes with momentum exchange
Volgin [20]	2008	Cu ED	See Paper
Aldas [22]	2008	Electrolysis H20	Naiver–Stokes based 2 phase tracking with Friction interaction
Kawai [26]	2010	Cu ED	Navier–Stokes no gas
Leahy [27]	2010	Cu EW	Navier–Stokes with bouyancy forces
Shukla [32]	2013	Cu EW	Navier–Stokes with buoyancy forces
Robinson [34]	2014	Cu ER	Navier–Stokes with density considerations
Hemmati [30]	2010	Cu ER	RANS $k-\omega$ turbulent model
Leahy [31]	2014	Cu EW	Rans (SST) Naiver–Stokes based 2 phase tracking
Najminoori [38]	2015	Cu EW	Euler–Euler RANS $k-\omega$
This Work	2017	Cu EW	Euler–Euler

Note: (EW is for Electrowinning, ER is for Electroreffining, and ED is for Electrodeposition)

Table 2.2: Summary of pertinent models continued: electrochemical considerations.

Name	Speciation	Transport Model	Electrode Kinetics	Gas Electrolyte Effects
Ziegler	No	Unknown	Unknown	Unknown
Bark	No	Nernst–Planck transferance diffusivity	Bulter-Volmer	None
Dahlkild	No	Nernst–Planck type (see paper)	Bulter-Volmer modified with gas fraction	Conductivity by Bruggman equation
Philippe	No	Conductivity only	Bulter–Volmer	Conductivity by Bruggman equation
Volgin	Yes	Nernst–Planck type (see paper)	Limiting current	Not considered
Aldas	No	Nernst–Planck	Bulter–Volmer modified with gas fraction	Conductivity and diffusivity modified by Bruggman equation
Kawai	Yes	Transference	Bulter–Volmer	None
Leahy	No	Transference and convection–diffusion	Faraday	None
Shukla	No	Nernst–Planck	Buttler–Volmer	None
Robinson	No	Nernst–Planck	Buttler–Volmer	None
Hemmati	No	Turbulence, diffusion Schmidt number	Faraday	None
Leahy	No	Turbulence, diffusion Schmidt number	Faraday	None
Najminoori	No	Turbulence, diffusion Schmidt number	Faraday	None
This Work	Yes	Nernst–Planck	Bulter–Volmer	Diffusivity modified by Maxwell equation

Table 2.3: Summary of pertinent models continued: validation and objective.

Name	Verification	Objective
Ziegler	Velocity Mapping-Comparison to other work	Current Distribution, bubble velocity and movement
Bark	None	Study Natural Convection
Dahlkild	None – Comparison to other work	Bubble electrolyte interaction
Mandin	None – Comparison to other work	Bubble electrolyte interaction
Volgin	None	Determine limiting current and concentration gradients
Aldas	Solution resistivity measurement and video feed experimentation	Verification of void fraction and model
Kawai	Experimentation	Current distribution transients
Leahy	Comparison to experimentation	Gas fraction and velocities
Shukla	Model results utilized as validation	Roughness-short circuiting
Robinson	Deposit thickness comparison to model	Simplified deposit thickness expression
Hemmati	None (need to varify)	Cell performance
Leahy	None	Flow dynamics with mixing and transport
Najminoori	In plant Measurements	3d hydro dynamic flow dynamics
This Work	Plating and deposit measurement	See following

2.2 Tracer Techniques to Determine Mass Transport

While the purpose of modeling is utilizing mathematics to determine the response of a system, utilizing tracer species for co-deposition allows determination of mass transfer properties and hence fluid properties by evaluation of deposit composition.

The work of Ettel et al. [6] stands in a preeminent place as an early attempt to understand the fluid-electrochemical interactions in copper electrowinning. The approach was to use low concentrations of a more noble species, in this case silver, to be able to calculate the mass transfer coefficient of the depositing species. The mass transport coefficient is given by the following relationship [6]:

$$k_{\mathrm{Ag}^+} = \frac{i_{L,\mathrm{Ag}^+}}{FC_{\mathrm{Ag}^+}} \tag{2.2}$$

The mass transfer coefficient k_{Ag^+} is determined to be a ratio of the limiting current density and the concentration. Because the mass transport of both the tracer species and the main depositing species are related the following relationships are developed by Ettel [6] correlating the two.

$$k_{\mathrm{Cu}^{2+}} = k_{Ag^+} \left(\frac{D_{\mathrm{Cu}^{2+}}}{k_{Ag^+}} \right)^{\frac{3}{4}} \tag{2.3}$$

$$k_{\mathrm{Cu}^{2+}} = k_{\mathrm{Ag}^+} \left(\frac{D_{\mathrm{Cu}^{2+}}}{k_{\mathrm{Ag}^+}} \right)^{\frac{2}{3}} \tag{2.4}$$

where k_{Ag^+} is the silver mass transport coefficient , i_{L,Ag^+} is the silver limiting current density, F is the Faraday's constant, C_{Ag^+} is the concentration of silver, $k_{\mathrm{Cu}^{2+}}$ is the copper mass transport coefficient and $D_{\mathrm{Cu}^{2+}}$ is the copper diffusion coefficient.

With equation (2.3) for laminar natural convection conditions and equation (2.4) for laminar flow. The apparent difference between these two equations is type of laminar flow. The k_{Ag^+} is determined by assay of the copper deposit. Thus by assaying the deposit for copper, the mass transport coefficient may be determined and the in-situ hydrodynamic conditions ascertained.

Additional work with regard to both natural and forced agitation was presented by Gendron et al. [7] which added Ni and Cu under different parameters (see Figure 2.1). The silver mass transport coefficient determined from Ettel's [6] and Gendron's [7] work is presented in Figure 2.1.

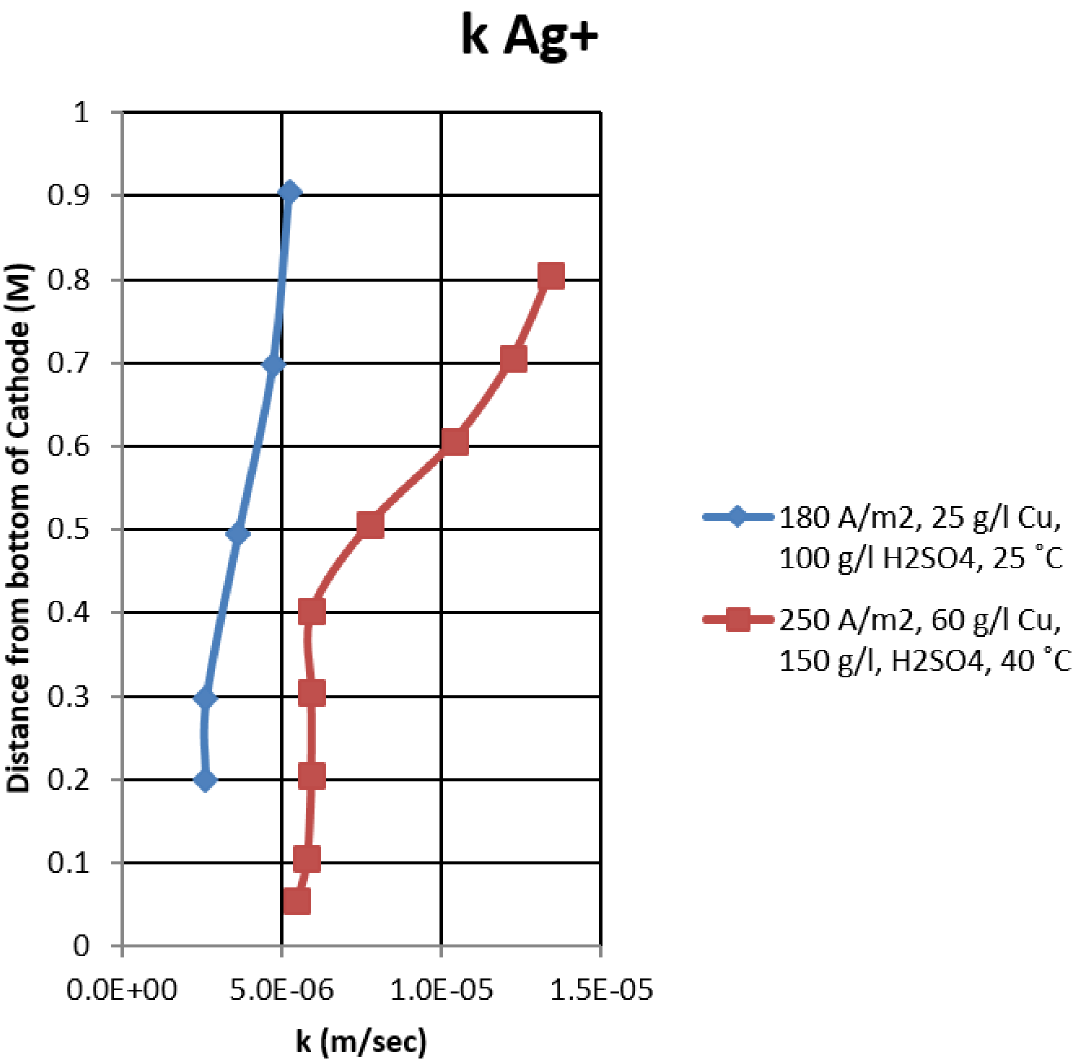

Figure 2.1: Vertical distribution of k_{Ag^+} in conventional copper electrowinning cell. Adapted from [6] and [7].

O'Keefe et al. [42] summarize and explore the utilization of tracer techniques. Copper and zinc electrowinning were studied utilizing co-deposited tracer techniques and results were provided. Further insights are provided by O'Keefe et al. [43] which included an expression for the diffusion layer thickness based on the mass transfer and diffusion coefficients.

2.3 Electrolyte Properties

In order to successfully model electrolyte systems a number of physical properties are needed. These include density, viscosity, diffusion coefficients, speciation etc. The following were investigated in the research to provide context and meaning.

2.3.1 Density, Viscosity and Conductance

Price et al. [44] present an important work for industrial electrolyte solutions. Over the ranges typical for electrowinning and electroefining they provide data and equations for density, viscosity and conductance. Data and equations found in this work were heavily drawn upon and are discussed in greater detail in sections 3.2.2.1 and 3.2.2.2.

Laliberte et al. [45] provide a very interesting methodology based on literature review to handle all manner of multicomponent inorganic ionc solutions, including $CuSO_4$ and sulfuric acid systems of interest. It is based on an Excel spread sheet implementation and is quite useful.

As a logical next step Laliberte et al. [46] extend the model to viscosity. The Excel model is updated to include both viscosity and density. The power of this work is the simplicity of the model which fits a wide range of electrolyte combinations.

Zafarani et al. [47] provide a viscosity calculation framework for the prediction of viscosity for mixed electrolytes from a more theoretical perspective. Although interesting, the complexity of the method versus the benefits is not warranted for inclusion in this work.

Agnew [48] builds upon the work of Laliberte [45], [46] but rewrites the equation to include an Arrhenius term for additional insight. The new equations are simply a restatement of the prior work of Laliberte [45] and [46].

2.3.2 Diffusion Coefficients

Tham [49] investigated the effect of salts on nonelectrolytes and that work is included here for the discussion of a type of diffusion theory. This provides context into multicomponent diffusion theory of which this system exhibits.

Miller et al. [50] provides a survey of important $CuSO_4$ properties such as mutual diffusion coefficients, conductance, osmotic coefficients and ionic transport coefficients. The main drawback is that it is not in the presence of sulfuric acid and as such the interactions are not captured in this paper. For mutual diffusion coefficients, the equations of Pitzer are utilized. Several other species are included for reference to $CuSO_4$.

Madsen [51] investigated the diffusion coefficient of ferric ions with chronopotentiometry. Madsen provides temperature and supporting sulfate electrolyte concentration effects on the ferric diffusion coefficient. This work shows the relative independence of the type of sulfate on the diffusion coefficient. The drawback in this work is the apparent underestimation of the diffusion coefficient, both in terms of standard published values for infinite dilution and in view of the work of Moats [52].

Bernard et al. [53] provide insights into self-diffusion using mean spherical approximation. This work attempts to address the breakdown of the Debye–Hückel equation in concentrated electrolyte solutions. In the present work, this type of theory was not needed due to the empirical diffusion coefficient fits of the data from Moats [52], [54] and the use of the Stokes–Einstein relationship for simple diffusion representation of other electrolyte species.

Further Bernard et al. [55] extended a mean spherical approximation method to predict conductance.

Anderko et al. [56] explored self-diffusion in multicomponent electrolyte systems. This work provides insight into the literature on multicomponent diffusion theory. Their objective was to model self-diffusion. Concentration dependence and ionic radius are considered amongst others. They achieve good fits to the data. This paper appears fundamental for at least two reasons. The first is the literature review and the second is the enhancement of existing theory to provide a model. Although the concepts were not utilized in this study, it does however represent a logical step for more robust determination of diffusion coefficients.

Moats et al. [54] studies the effective diffusion of copper in industrial electrolytes utilizing linear sweep voltammetry with a rotating disk electrode. Although data are provided, an expression is not. Section 3.2.3.2 provides the derivation of the diffusion coefficient.

Moats et al. [52] provide a practical investigation in to the diffusion of ferric ion diffusion in electrowinning solutions. Section 4.2.7 covers in depth the derivation of a diffusion coefficient from the data presented in this paper. Chronoammperometry was utilized to determine the diffusion of ferric ions. The effects of temperature, copper, sulfuric acid, chlorine ion, manganese and cobalt concentrations were determined. Chlorine, manganese and cobalt were found to not influence the results. This work also included the affect on current efficiency in an electrowinning system.

2.3.3 Speciation

Stirp et al. [57] provide an equilibrium speciation model of ferric and ferrous sulfate systems at low pH based on a Davies activity model. The limitation of this model is that it does not consider pH of less than 1 with 1-4 the studied range. The comment that the model is limited by the activity coefficient at low pH is significant.

Casas et al. [58] explore equilibrium speciation of sulfuric acid-copper systems utilizing Pitzer and Davies activity models as appropriate. Their work also includes possible hydroxide combinations. At lower acid concentrations the models proved accurate, but experimental data were not readily available for accurate high acid conditions. However, $HCuSO_{4(aq)}^{+}$ is not included as one of the species. Of note is that this work showed that the amount of $CuSO_{4(aq)}$ in equilibrium is less than 5% at acid concentrations of greater than 2 molar.

Wang et al. [59] provide a more fundamental model of activity using a Pitzer–Debye–Hückel type. This work accounted for the Gibbs energy of the long range electrostatic interactions, short range ion to ion interactions and a middle range interaction of ionic types that are not included in the long-range interactions. It combines "an expression for the excess Gibbs energy with chemical equilibrium relations that arise from ion association, complex formation, hydrolysis, etc." This work is cited for the sulfuric acid speciation results and as an example of the complexity that has been attempted in the field.

Wang et al. [60] provide modeling insights utilizing the activity using a Pitzer–Debye–

Hückel type. Calculations and experimental data are provided.

Volgin et al. [20] provide a equilibrium framework of homogenous chemical reactions as part of their model development, which will be covered in a later section. $HCuSO_{4(aq)}^{+}$ is not considered in their work.

Yue et al. [61] provide a good survey of the potential reactions. The temperature range is also extended to 150 °C.

2.3.4 Activities

The concentrated electrolytes found in electrowinning solutions require special consideration. Traditional activity models are suitable for dilute concentrations and are not accurate for concentrated electrolytes. Accurate activities are crucial for the determination of equilibrium concentrations of species and equilibrium potentials.

The work of Samson et al. [62], [63] was selected for use due to its simplicity and ease of use. They further modified the Davies equation to produce a more accurate expression than that of Pitzer. Examination of the fit and data lead to the selection of this model for extensive use. Implementation and collection of the needed parameters for use can be found in section 3.2.3.1.

Anderko et al. [64] provide an excellent summary of various attempts to calculate activity coefficients in electrolyte solutions. Their work also includes discussion of thermodynamic models, interaction forces and diffusion coefficients.

2.3.5 Dielectric Coefficients

Hasted et al. [65] in this oft cited work develop a model for the dielectric constant of ionic solutions. The work is theoretical in nature with comparison to data.

Rao et al. [66] investigate the dielectric constants of electrolytes over various ranges. This is included for reference because these parameters are needed to satisfy the activity coefficient calculation found in the work of Samson et al. [63], [62]

Wang [67] further develops a model for the dielectric constant in mixed-solvent electrolytes with comparison to data provided.

In view of the findings of these papers it was determined that it could be possible to derive a simpler expression. This can be found in section 3.2.3.1, equation (3.8).

2.4 Electrode Kinetics

The next item investigated was the reaction kinetics on various electrodes.

2.4.1 Copper

Copper has been studied for a number of years and the work of Mattsson and Brokris [68] with regard to copper reduction kinetics was reviewed and refined by Newman [21]. The results of these works are discussed further in section 3.2.4.5.

Wagner et al. [69] include additional work with regard to studying the copper deposition mechanism with alternating current voltammetry. Also included in the study were the effects of ferrous species on this reaction. This was the only reference found exploring the mixed reactions on the copper cathode. This work discusses the influence of iron with regard to its effect on charge transfer.

2.4.2 Oxygen on Lead

The generation of oxygen at the anode is an important part of the eletrowinning system and accounts for much of the energy costs. The following literature was surveyed to determine applicable reaction kinetics.

Bose et al. [70] study the oxygen generation on lead with varying acid concentrations utilizing rotating disk electrodes. They also calculated diffusion coefficients for oxygen with varying sulfuric acid concentrations.

Laitinen et al. [71] provided much needed background into oxygen evolution on lead anodes. This paper also considers the growth of PbO layers and the associated reaction rates. In particular, the paper covers temperature dependency. This relationship is utilized in the present work and is discussed further in section 3.2.4.6.

Codaro et al. [72] studied the formation of PbO_2 in sulfuric acid systems and the associated oxygen generation kinetics. They explore the current response with a type of expanded equation related to the system studied. The fit of data to equations is good and includes oxygen evolution kinetics at high overpotentials.

Pavlov et al. [73] performed a study much the same as Laitinen et al. but develop the theory of the reaction mechanism in a substantive manner. Tafel and Arrhenius curves are well presented and discussion of the activation energies and hydrated anodic layer is interesting.

2.4.3 Iron

The literature did not seem to contain many references to the kinetics of iron in sulfate systems with regard to electrowinning. Those references that were found specifically focused on the anodic reaction.

Petrocelli et al. [74] study the over-voltage in several systems ferrous/ferric sulfate was investigated on bright platinum electrodes with exchange and charge transfer coefficients given.

The next few references appear to be part of a larger study to understand and develop electrowinning with alternate anode reactions utilizing the oxidation of Fe^{2+} rather than oxygen.

Cifuentes et al. [75] studied the kinetics of the electrolytic Fe^{2+}/Fe^{3+} oxidation on various anode materials. These include platinum, platinum/titanium, iridium oxide/titanium, ruthinium oxide/titanium and graphite. They were attempting to understand the effect of various parameters such as acid concentration, temperature etc. on the reaction kinetics of iron. They found that sulfuric acid played only a small role in the kinetics. They found that Pt resulted in the fastest kinetics with Pb being the slowest and the others performing about the same.

Cifuentes et al. [76] continued their work reporting on a small test cell utilizing the anode reaction of Fe^{2+}/Fe^{3+}. They call the system: reactive electrodialysis (RED). Speciation is considered for the anolyte and the catholyte.

Cifuentes et al. [77] further study both the anodic and cathodic kinetics with regard to temperature dependence in the RED cell.

Cifuentes et al. [19] discussed modeling the RED cell as covered previously in section 2.1.

This concludes the section of work specifically to the RED cell.

Sandoval et al. [78] present on work done at Freeport–McMoRan at the pilot scale with regard to the same type of electrowinning system as described by Cifuentes [75] - [77], [19]. In this case iron was reduced by the utilization of sulfur dioxide to allow for reuse. In this test, there was no membrane and as such the current efficiency was lowered to 85%.

Tjandrawan et al. [79] use a rotating disc electrode to study the electrochemical oxidation of Fe^{2+} on lead alloys. They find that the reaction is mass transport limited.

Wagner et al. [69] were covered in section 2.4 which discussed the role of iron in modification of copper reaction kinetics.

2.5 Current Efficiency Due to Iron

The primary driver of base current efficiency in copper electrowinning cells is the concentration of iron in the electrolyte. Because of the cost impact to copper production it is important to review what has been published as a basis for further development.

Moats [52] presents work to determine the effective diffusivity of Fe^{2+} in synthetic electrowinning solutions via chronoamperometry. The data in the paper for effective diffusivity of Fe^{2+} are discussed extensively in section 4.2.7. This work utilizes a expression from Ettel [6] to compare the diffusion of iron to that of copper to determine the mass transfer coefficients knowing the boundary layer thickness. What is not shown in this work is just as important as what is. Utilizing this data and methodology the current efficiency of the cell may be determined. This methodology is covered extensively in Chapter 4.

Khouraibchia and Moats [80] performed a set of experiments to determine a response surface expression for current efficiency. They also provided an expression of energy consumption. Both of these expressions consider copper, iron and current density. Notably what is missing is the temperature effect.

The work of Yue et al. [61] has been covered previously in section 2.3.3 and is mentioned again here for the presentation of the redox potential of iron in view of speciation.

2.6 Deposition Studies

In review of the literature work could not be located which discussed the topography of copper electrowinning deposits. As such, the search was extended to examine what is typical in the field of electrochemistry. It was found that most literature examined small scale deposits on the order of less than 1 mm. Large fluid structure interactions with the deposit were not found. The following are provided as a survey of some of the literature surveyed:

- Zhang et al. [81]

- Nelissen et al. [82]
- Giannopoulou et al. [83]
- Heng et al. [84]
- Pinto et al. [85]
- Patil et al. [86]
- Litrico et al. [41]
- Johnson et al. [87]

2.7 Residence Time Studies

Another aspect of accurate study of the deposition of copper in electrowinning systems is the concentration at which the copper is deposited. In tank houses a single cell may have many cathodes and several thousand amps of current. Cells are typically fed with solution at a given flow rate and drained via outlets with an overflow weir. In such a system the question is: What is the bulk concentration of copper in the cell and does it vary between the inlet and outlet? The simplest assumption is that a cell behaves like a well stirred reactor, with the bulk concentration being equal to the outlet. However, literature was searched to determine the validity of this assumption.

Rawling et al. [88] performed tracer stimulus response studies to determine the residence time characteristics of a copper electrowinning tank. The experiment was conducted on an industrial cell running at 228 (A/m^2) with 49 cathodes. The data are analyzed with a model consisting of 96 batch mixers in parallel. The comment is made, however, that the results are almost the same as a continuously stirred batch reactor. This means that data show that treatment of the tank as perfectly mixed with a bulk concentration is not an unreasonable assumption.

Kimmerle et al. [89] and Leroy et al. [90] present a two-part study in the concentration profiles in electrowinning circuits. The data are not particularly relevant as the cell was a small bench scale type and the electrolyte path cascaded from one electrode set to the next preventing mixing. Thus the fluid flow in this study cannot be counted as representative of an industrial tank.

Zinc electrowinning, presented in the work of Scott et al. [91], was included for its discussion of ramifications of residence time in their modeling of zinc electrowinning systems.

Aminian et al. [92] consider residence times in SX-EW circuits including electrowinning on the pilot scale. The electrowinning cell contained 6 cathodes. They find that generally the tank can be modeled as a perfect mixer. Short circuiting of the flow was found to be on the order of 1%. This is in agreement with Rawling [88].

These findings that a tank may be represented by a perfectly mixed reactor are significant in simplifying the treatment of the bulk concentration.

2.8 Current Distribution via Circuit Networks

Another important aspect to consider in electrowinning circuits is the electrical distribution system and the interaction with the electrochemical portions of the process. Bus bar connections to electrodes are critical and this important topic is discussed in the literature. For the purposes of this review only those papers which consider both the electrochemical response and the circuit analysis were included.

Laitinen presents two different publications [93], [94] to present work dealing with developing a model of an electrolysis cell group. This work considered both electrowinning and electrorefinning. The objective of this work was to develop a finite element model of a cell group.

Time effects were considered as changes in electrode thickness which did have an effect on the separation distance and hence electrolyte resistance. The effect of deposits with time are linear as deposit thickness changes with average dimensional changes. Local deposit topography and roughness are not considered. Because of the objective of this model in electrical conduction, contact resistance, heat transfer and electrical resistance as a function of temperature were included. The models for polarization, which were gathered from laboratory measurements, are not concentration or temperature dependent, but only voltage dependent and very simplistic and it doesn't appear that variations with concentration were included. Heat transfer was also considered owing to the modeled temperature dependence of resistance. Contact resistance was modeled from an empirical expression.

The focus of the model was to provide design decision feedback for electrical connections and conductor sizing. Hydrodynamic considerations are not incorporated. This work focuses on a 3D model with 2D shells (zero thickness) for cathodes.

Also included in the model were provisions for stochastic variation of critical parameters. Specifically, stochastic methods were presented for bus bar contact resistance, electrode separation spacing and short circuiting. For shorting calculations the number of shorts were fixed and the location in the cell group was randomly distributed (cathode electrode position and tank and electrode pair). The short was modeled as bus bar contact current of 1600 A. In this study the models were run under two conditions, no shorting and arbitrary shorting. Shorting was assumed to be the predominant driver of current efficiency. The reported values for current efficiency were 90.4% as modeled versus about 95% in industrially measured systems. What is beneficial about this work is that temperature and geometric conductivity effects are modeled. However, this is balanced by several omissions, namely:

- Fe concentration and its effects on current efficiency.
- Copper concentration variations across the tank from inlet to outlet.
- Numbers of shorts were not assumed to be a function of time.
- Shorting was constant with no transient considerations of individual short properties with time.

Contact failures were modeled, single short circuits were modeled and electrode positioning were modeled.

As this work is a study in FEM to provide CAE (computer aided engineering) the model provides a feedback response for optimization of the bus bar system. Laitinen presented a methodology to perform multiobjective optimizations and proceeded to explore the optimization space. The methodology approaches the design space sequentially rather than as a whole to reduce computational expense.

Blackett et al. [95] provides an interesting addition by modeling the electrochemical response via diodes in the circuit. They also consider misalignment of electrodes and short circuiting and poor contacts in the model.

2.9 Noduling-Roughness

The literature did not contain many specific references to noduling or roughness with regard to electrowinning. The notable exception is the work of Shukla et al. [32], [33]. This was discussed previously in section 2.1 and Chapter 6. There appear to be a few references with regard to electrorefining which are not included in this report. For general reference with regard to deposit quality and effect of additives and transport the following references are included:

- Lafront et al. [96]
- Free et al. [97]
- Rodchanarowan et al. [98]

2.10 Research Needs

As demonstrated from this brief review, there has been a significant body of work with regard to the simulation of electrowinning. However, it is also notable that there exist significant gaps in the historic modeling. Fundamentally, the prior work has focused either on simplified fluid modeling or on simplifying electrochemical models. Also, deposition modeling based on the effects of fluid flow in electrowinning has not been covered extensively in the literature. These needs will be addressed by combining computation fluid dynamics with multispecies transport factoring complexation, gas and electrode kinetic effects. To our knowledge no one model has treated these in a unified approach with transient deposition to probe the fluid structure interactions in copper electrowinning systems. As identified in section 1.3 the proposed scope of work represents the items of research and model development needed to address these gaps.

CHAPTER 3

DEVELOPMENT OF A MODEL AND ASSOCIATED VALIDATION METHODS FOR DETERMINING LOCAL ELECTROWINNING ELECTRODE CURRENT DENSITY

3.1 Introduction

As covered in sections 2.1 and 2.1.1 there is ample opportunity for advancing the modeling of electrowinning systems. As such the focus of this chapter will cover the development of the foundation of a 2D electrowinning Finite Element Model to study localized current distributions along the cathode. It will also present the experimental validation methods needed to produce results to compare to the model.

3.1.1 Review

The literature has been review and discussed previously in sections 2.1 and 2.1.1. However, of particular insight for the development of models in this chapters were: [3], [4], [11], [13], [15], [16], [20], [22], [26], [27], [30], [31] and [38].

The works of Free [2] and Newman [21] were also heavily drawn from for inspiration and clarification of electrochemical principles.

3.2 Methods

The methods utilized in this study fall under two broad categories. The first is the theory and creation of a finite element electrowinning model. The second is the strategy used to validated the model. The research was primarily conducted using COMSOL Multiphysics 5.2a.

3.2.1 Geometry

A test cell was designed and fabricated to produce copper deposits for model validation. The test cell is shown in Figure 3.1.

Figure 3.2 shows the general layout of the cathode and anode pair with shielding and key dimensions. The model was simplified to a 2D geometry because of planer electrodes. It is assumed that the centerline of the cell as represented by section AA in Figure 3.2 represents a plane of symmetry and as such the 2D infinite width holds true. The geometric representation in COMSOL is shown in Figure 3.3.

3.2.2 Fluids

Critical to the validity of the model are determining suitable expressions for critical parameters such as density and viscosity.

3.2.2.1 Density

The equation used for density was a modified form of an equation provided by Price et al. [44] and it is shown as equation (3.1).

$$\rho = 1018.56 + 2.38 Mw_{\mathrm{Cu}} C_{\mathrm{Cu}} + 0.54 C_{\mathrm{H_2SO_4}} - 0.59T \tag{3.1}$$

where, ρ is in kg/m^3, C_{Cu} is in mol/m^3, $C_{\mathrm{H_2SO_4}}$ is in kg/m^3, Mw_{Cu} is in kg/mol, T is in °C. The fit of the data to the expression is shown in Figure 3.4.

This equation is applied across the electrolyte domain, and varies with the concentration of Cu^{2+}.

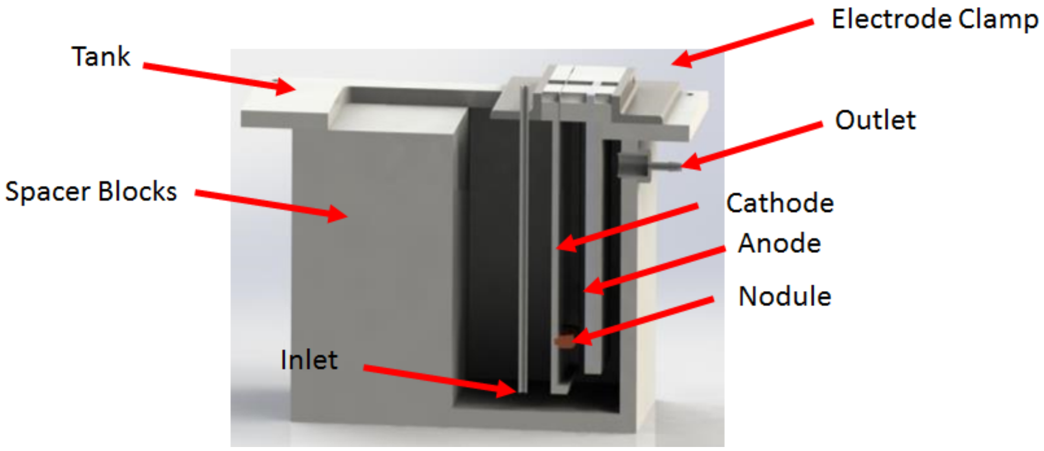

Figure 3.1: Rendering of test cell showing major components of electrowinning test cell.

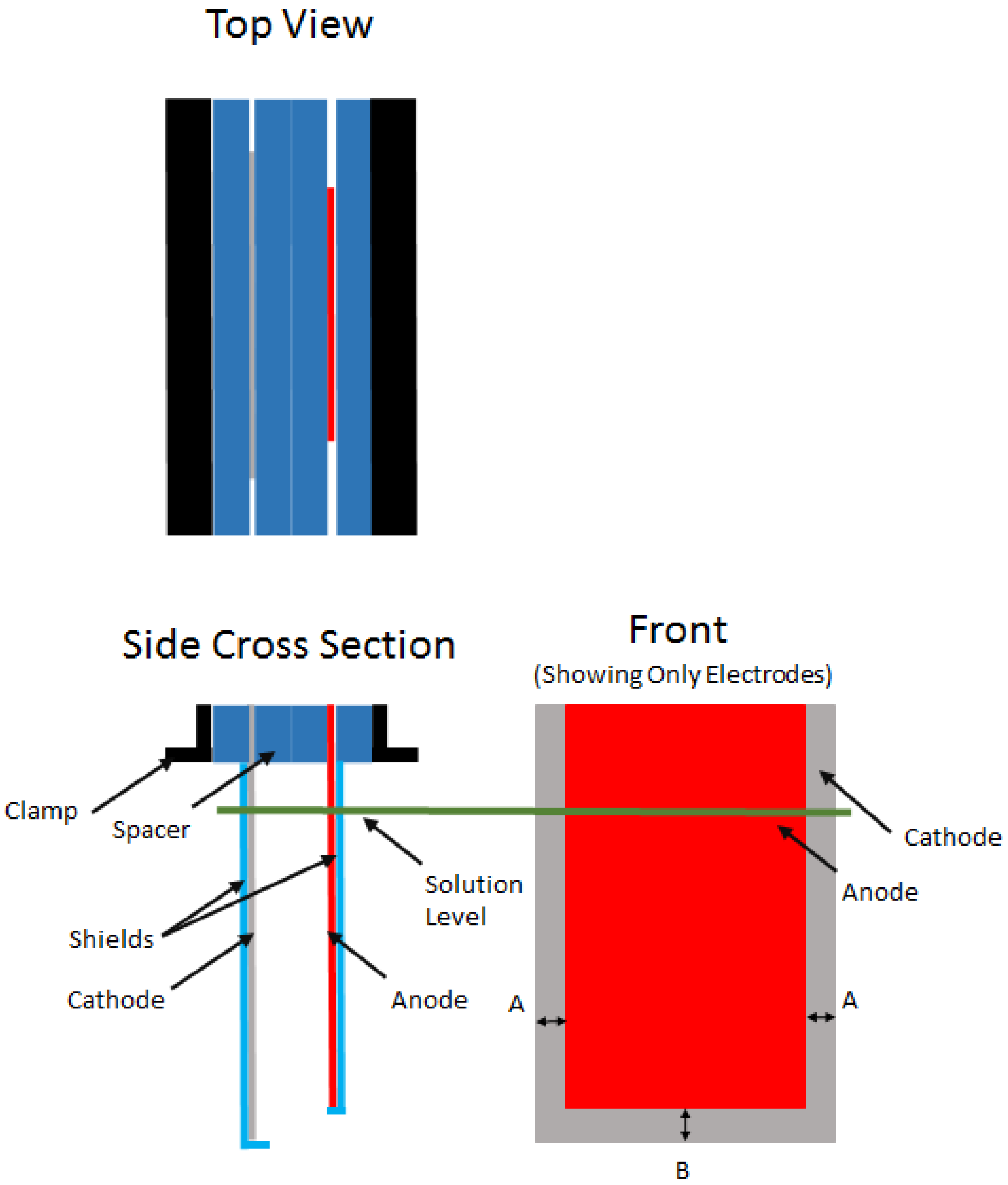

Figure 3.2: Typical cathode and anode arrangements. The cathode as placed in solution measures approximately 0.170 m tall by 0.140 m wide. The anode is approximately 0.155 m tall by 0.102 m wide. Dimension A in is 18.5 mm and dimension B is 16 mm. The cathodic recess and shield edge thickness are all 1/4 inch. The electrolyte level is 0.170 m above the bottom of the cathode.

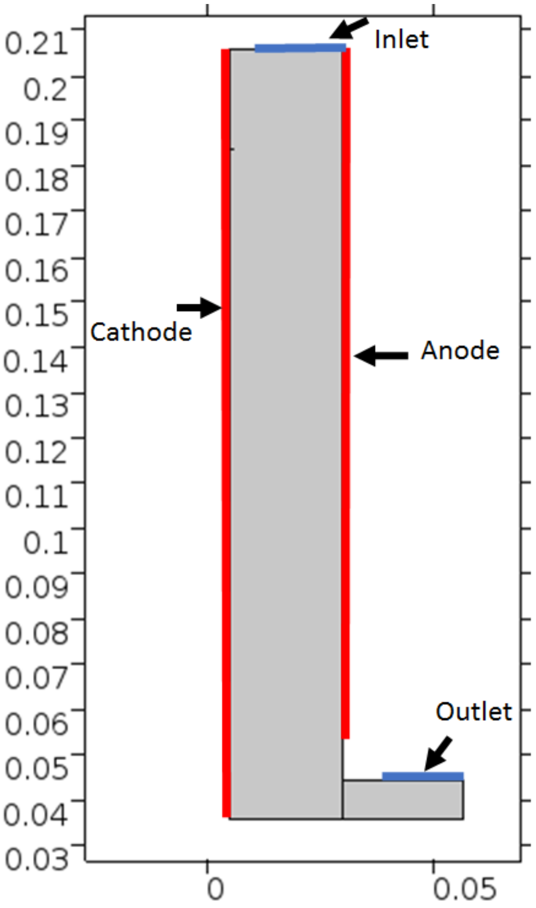

Figure 3.3: Geometry as represented in COMSOL multiphysics. Units in m.

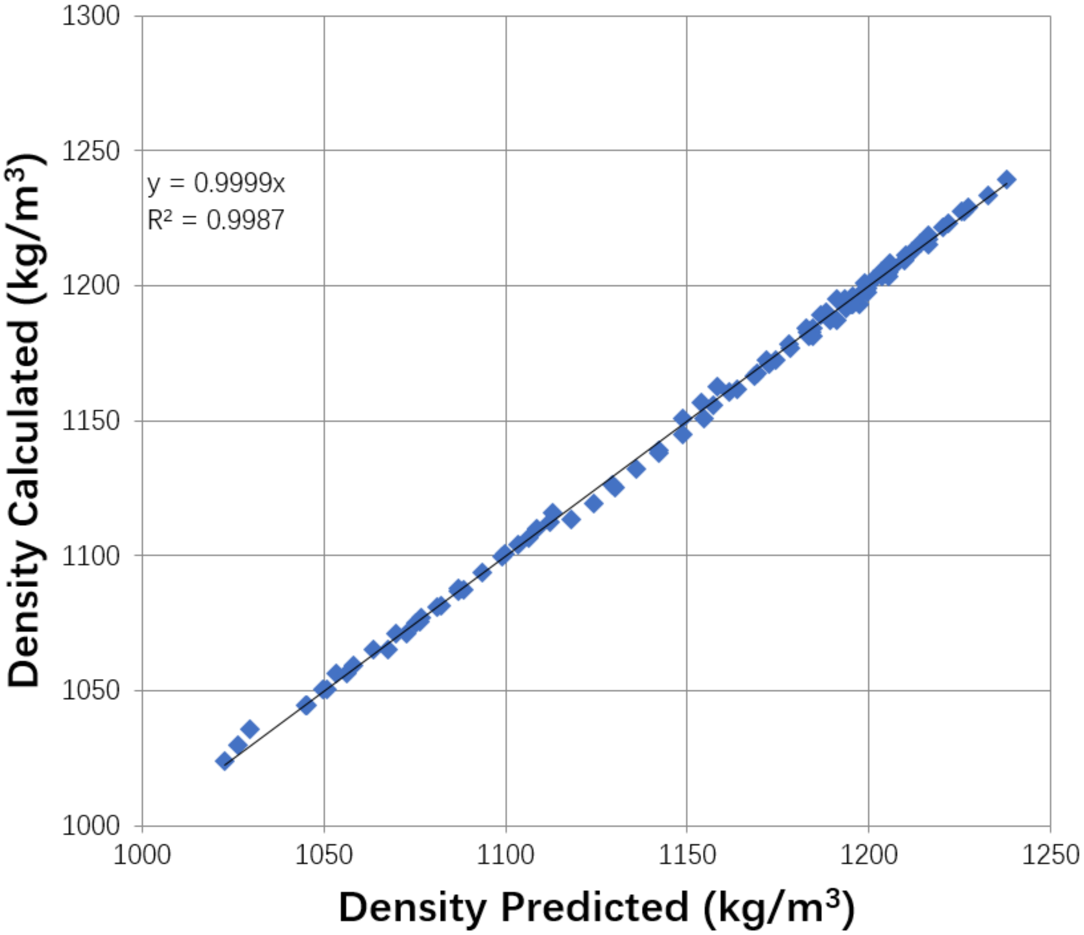

Figure 3.4: Density model fit. Equation modified from that presented in reference [44]

3.2.2.2 Viscosity

The equation for dynamic viscosity was determined by linearizing the temperature term and performing linear regression from data obtained from Price et al. [44].

$$\begin{aligned} \mu = \frac{1}{1000}(&-1989.46 + 0.010353 Mw_{\mathrm{Cu}} C_{\mathrm{Cu}^{2+}} \\ &+0.0014685 C_{\mathrm{H_2SO_4}} + 1983.72 e^{\left(\frac{1}{T}\right)} \end{aligned} \tag{3.2}$$

where μ is the dynamic viscosity in $Pa \cdot s$, C_{Cu} is the localized cupric ion concentration in mol/m^3, Mw_{Cu} is in kg/mol, and $C_{\mathrm{H_2SO_4}}$ is the initial H_2SO_4 concentration in kg/m^3.The fit of experimental to model is shown in Figure 3.5. This equation is also applied across the electrolyte domain, varying with the concentration of Cu^{2+}.

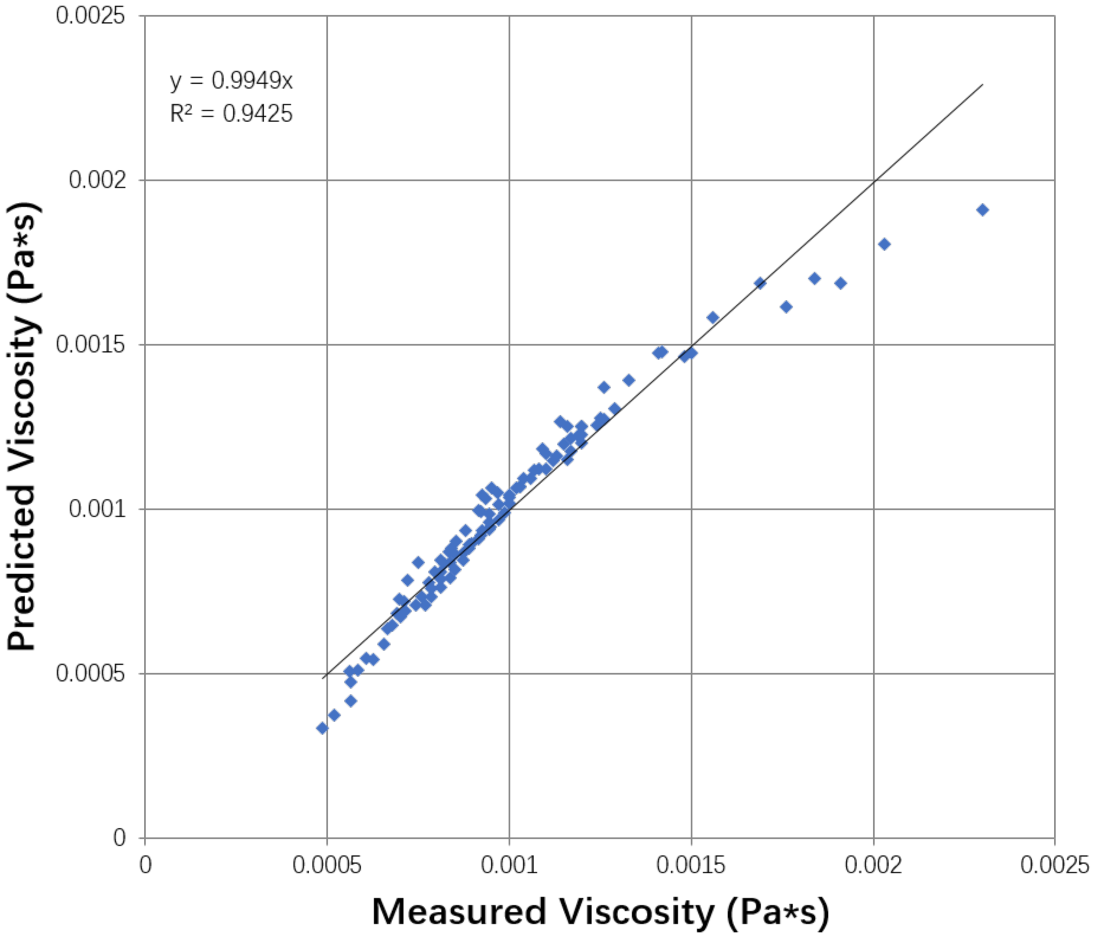

Figure 3.5: Viscosity model fit. Equation empirically fit from data presented in reference [44]

3.2.3 Parameters

In addition to fluid parameters, physical phenomena such as species activity and diffusion must be considered. In concentrated electrolytes more complicated activity calculation methods must be used [2].

3.2.3.1 Activity Model

Activities are given by the following expression (3.3):

$$a_j = \gamma_j \frac{m_j}{m^0} \tag{3.3}$$

where, a_j is the activity of species j and is unit-less, γ_j is the activity coefficient, m_j is the concentration of species j, $m^0$is the reference concentration.

Only the species involved in the reaction affect the potential. However, all species in an ionic solution affect the ”thermodynamic concentration” known also as activity. This modification occurs through the use of the activity coefficient.

Most fundamental formulas for the determination of activity coefficients have been determined for dilute electrolytes. Increasing discrepancies arise for more concentrated solutions (I>0.1) like those found in electrowinning cells. Literature was reviewed for a suitable high concentration expression. The work of Samson further modified the Davies equation to produce a more accurate expression than that of Pitzer. The following is the equation from Sampson et al. [62], [63].

$$\ln \gamma_i = -\frac{A z_i^2 \sqrt{I}}{1 + a_k B \sqrt{I}} + \frac{(0.2 - 4.17 \times 10^{-5} I) A z_i^2 I}{\sqrt{1000}} \tag{3.4}$$

where I is the ionic strength of the solution, which is calculated using equation (3.5):

$$I = 0.5 \sum_{i=1}^{N} z_i^2 C_i \tag{3.5}$$

z_i is the charge of a given ionic species and N is the total number of ionic species in the acqueous solution. In equation (3.4), A and B are temperature-dependent parameters, given by equations (3.6) and (3.7):

$$A = \frac{\sqrt{2} F^2 e_0}{8\pi (\epsilon R T)^{3/2}} \tag{3.6}$$

$$B = \sqrt{\frac{2F^2}{\epsilon R T}} \tag{3.7}$$

where F is the Faraday constant, ϵ_0 is the electrical charge of one electron and $\epsilon = \epsilon_r \epsilon_0$ is the permittivity of the vacuum, R is the ideal gas constant and T is the temperature.

Finally, the parameter a_k in equation (3.4) is related to the ionic radius and is specific to the ionic species.The results of the Pitzer and extended Davies models are compared as shown in Figure 3.6.

The model requires both the ionic radius and the dielectric constant. In order to supply the dielectric constant, an expression was derived from the data supplied in reference [63]. The premise was that the dielectric constant is a function of ionic strength and ionic radius.

$$\epsilon_r = 127.9614 + 0.01378I + 5.6111 \times 10^{10} a_k + 2.5422\,|z| \tag{3.8}$$

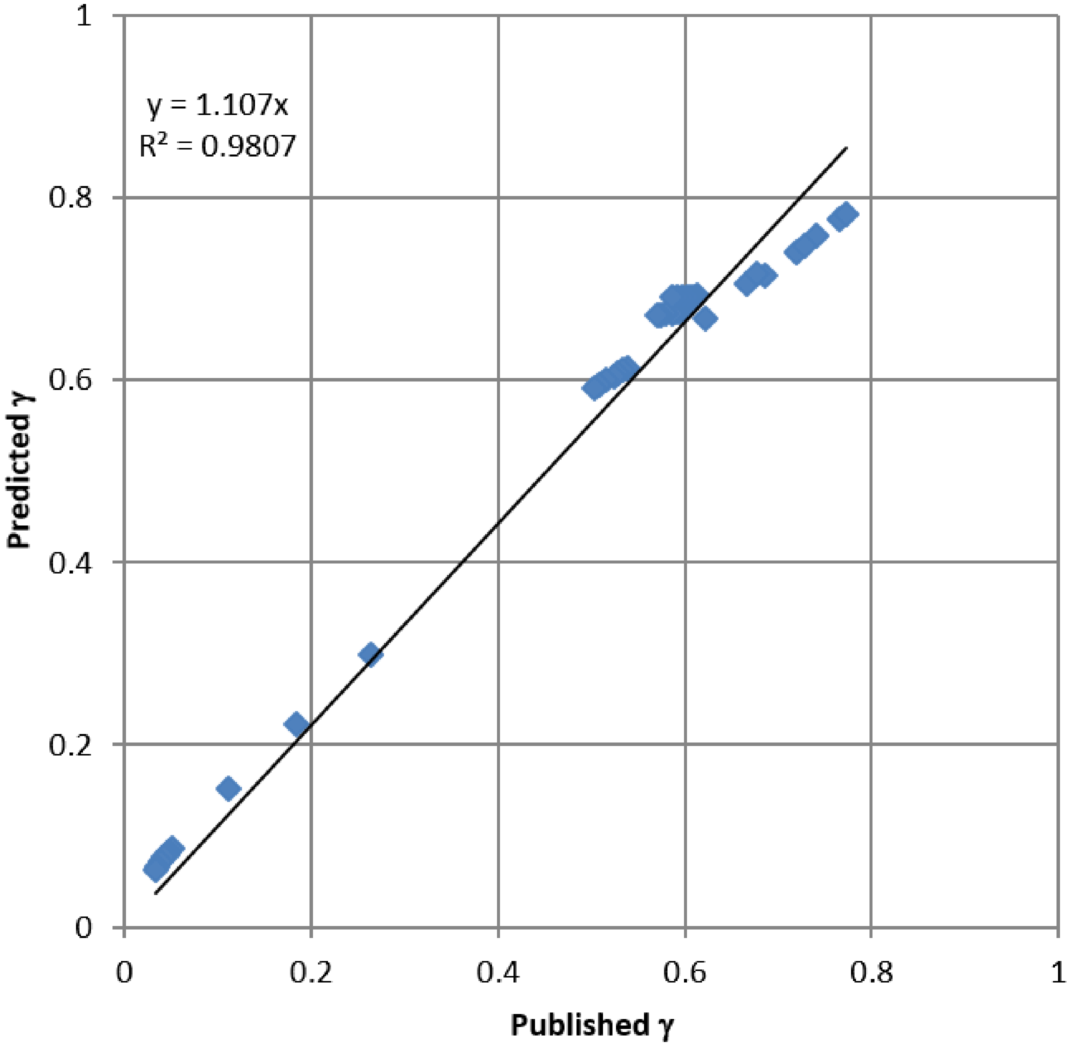

Figure 3.6: Predicted versus published activity coefficient utilizing equations (3.4-3.8) and the data found in reference [63].

where, ϵ_r is dielectric constant (unitless); I is ionic strength, mol/m^3; a_k is ionic radius in m; z is charge of species. To verify this equation the results were compared to the data provided in reference [63] as shown in Figure 3.7. Use of the empirical fit dielectric equation showed reasonable agreement with the data provided.

3.2.3.2 Diffusion Coefficients

Diffusion Coefficients for copper were calculated using the work of Moats et al. [54]. The work of Moats et al. was reviewed and regression was utilized to develop the following expression:

$$\begin{aligned}\log D_{0,\mathrm{Cu}^{2+}} &= -0.676 - 0.481 log(C_{i,\mathrm{H_2SO_4}} Mw_{\mathrm{H_2SO_4}}) \\ &-0.156 log(C_{i,\mathrm{Cu}} Mw_{\mathrm{Cu}}) + 0.9885\left(\frac{-8340.61}{8.314T}\right)\end{aligned} \tag{3.9}$$

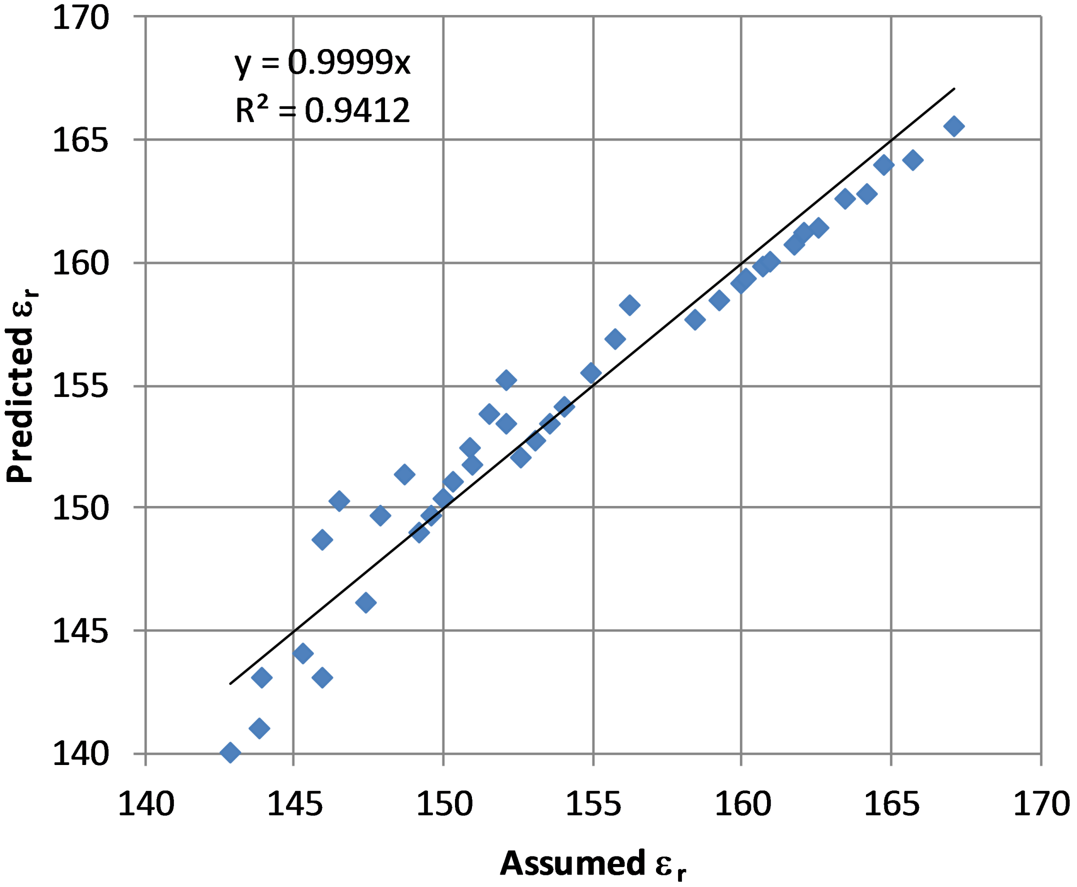

Figure 3.7: Fit of the predicted vs. assumed dielectric constant e_r. Data and equations from [62], [63].

where $D_{0,\mathrm{Cu}^{2+}}$ is in cm^2/s, $C_{i,\mathrm{H_2SO_4}}$ and $C_{i,\mathrm{Cu}}$ are the initial concentrations in mol/m^3, $Mw_{\mathrm{H_2SO_4}}$ and Mw_{Cu} are in kg/mol, T is temperature in K. This equation has the following range: $C_{i,\mathrm{Cu}}$=35-60 (g/L), $C_{i,\mathrm{H_2SO_4}}$=160-250 (g/L), T=40-65 °C. This expression demonstrates a reasonable fit of the data.

The diffusion coefficient in this model is set as a constant over the electrolyte domain for $D_{0,\mathrm{Cu}^{2+}}$. This assumption was made from the data being generated from a rotating disk electrode via the Levich equation. As such, the diffusion coefficient takes into account the overall effect of the boundary layer concentration and other effects. The diffusion coefficient is utilized by the model in the same way.

For $\mathrm{SO_4^{2-}}$ the diffusion coefficient was calculated by solving for the ionic radius using the Stokes-Einstein relation with a initial value of 1.065×10^{-9} cm^2/s in 25 °C water. This was then modified via viscosity for electrolyte for use in the model.

3.2.4 Electrochemical Model

3.2.4.1 Governing Equations

To model the electrodeposition process in this study, the Tertiary Nernst-Planck interface was utilized to solve for the electrolyte potential (Φ_l), the current density distribution (i_l), and the concentrations of various species (C_i) [99]. A set of governing equations was used and solved [21], [99]. In electrolyte, the governing equation for mass transfer in solution is the Nernst-Plank equation:

$$N_i = -z_i u_i F C_i \nabla \Phi_l - D_i \nabla C_i + C_i \nu \tag{3.10}$$

where N_i, z_i, u_i, C_i, D_i are the flux density, charge, mobility, concentration, and diffusivity of species i, F is Faraday's constant, $\nabla \Phi_l$ is an electric field, ∇C_i is a concentration gradient, and ν is the velocity vector.

Because there are no homogeneous reactions in the electrolyte, the material balance is governed by the equation:

$$\frac{\partial C_i}{\partial t} + \nabla \cdot \mathbf{N_i} = 0 \tag{3.11}$$

In the electrolyte, the current density is governed by:

$$i_{electrolyte} = -F^2 \nabla \Phi_l \sum z_i^2 u_i C_i - F \sum z_i D_i \nabla C_i + F \nu \sum z_i C_i \tag{3.12}$$

where $i_{electrolyte}$ is the current density in the electrolyte, and other variables are defined previously. Due to the electroneutrality of the electrolytic solution, the last term on the right is zero ($\sum z_i C_i = 0$). Therefore,

$$i_{electrolyte} = -F^2 \nabla \Phi_l \sum z_i^2 u_i C_i - F \sum z_i D_i \nabla C_i \tag{3.13}$$

On the electrodes, the current density is governed by Ohms Law:

$$i_s = -\sigma_s \nabla \Phi_s \tag{3.14}$$

where i_s is the current density at the electrode, σ_s is the conductivity of the electrode and $\nabla \Phi_s$ is an electric field. With conservation of current in the electrolyte and electrodes, we have:

$$\nabla \cdot i_k = Q_k \tag{3.15}$$

where k denotes an index that is l for the electrolyte and s for the electrode, and Q_k is a general current source term and was zero in this model [100]. Therefore, eq. (3.15) becomes:

$$\nabla \cdot i_k = 0 \tag{3.16}$$

At the electrode-electrolyte-interface, the overpotential η is defined as:

$$\eta = \Phi_s - \Phi_l \tag{3.17}$$

where Φ_s is the electric potential of the electrode, Φ_l is the potential of the electrolyte adjacent to the electrode.

The current density in the electrolyte adjacent to the electrode has the following relationship with the local current density term in a modified form of the Butler-Volmer equation (3.18)[100]:

$$i_{loc} = i_o \left[\frac{C_{R,S}}{C_{R,B}} exp\left(\frac{\alpha_a z F}{RT} \eta \right) - \frac{C_{O,S}}{C_{O,B}} exp\left(\frac{\alpha_c z F}{RT} \eta \right) \right] \tag{3.18}$$

where i_{loc} is the local current density at the interface (also called the charge transfer current density), i_0 is equilibrium exchange current density, $C_{R,S}$ is the surface concentration reduced species, $C_{R,B}$ is the bulk concentration of the reduced species, $C_{O,S}$ is the surface concentration of the oxidized species, $C_{O,B}$ is the bulk oxidant concentration of the oxidized species, α_a is the anodic symmetry factor, α_c is the cathodic symmetry factor, z is the number of electrons transferred in the rate limiting step (typically 1), F is the Faraday constant, R is the gas constant, T is the absolute temperature, and η is the overpotential.

The current density in the electrolyte adjacent to the electrode has the following relationship with the local current density term in the Butler-Volmer equation [100]:

$$i \cdot \mathbf{n} = i_{loc} \tag{3.19}$$

where i is the current density in the electrolyte at the interface, $\mathbf{n}$ is the unit normal vector to the electrode surface, and i_{loc} is the local current density. See subsequent sections for additional details for cathode and anode kinetics.

3.2.4.2 Electrolyte Species Considered

A review of the literature show that the Copper Sulfate Acid system is complex and dissociates into a number of species. For simplicity the species considered in this work are Cu^{2+}, H^+ and HSO_4^-. The excess sulfate from the copper dissociation is assumed to become bisulfate. The concentrations of each of these species are set initially with no generation due to heterogeneous chemical reactions between species.

3.2.4.3 Equilibrium Potential

In order to determine cell voltages the equilibrium potential of both the anodic and cathodic reactions needed to be calculated. The equilibrium potential or E is given by the Nernst Equation (3.20):

$$E = E^0 - \frac{2.303RT}{nF} \log\left(\frac{a_{\text{products}}}{a_{\text{reactants}}}\right) \tag{3.20}$$

This equation uses the standard thermodynamic potential along with the product and reactant activities to determine the equilibrium potential for a half-cell reaction.

3.2.4.4 Effects of Bubbles

The effect of diffusion is modified by the presence of oxygen bubbles formed at the anode. For this work the approach is to make diffusion modification a function of gas fraction in the electrolyte. Table 3.1 shows several equations for this purpose. These were adapted from the work of Hammoudi et al. [101] which originally represented conductivity as a function of gas fraction. The selection of any of these equations at gas fractions <0.1 is rather arbitrary as there is little variation.

In this work the Maxwell equation form Table 3.1 was utilized. This allows variation of both diffusivity and migration. Hence, the changes in electrolyte conductivity and its effects can be considered as a function of dispersed gas bubbles in the electrolyte.

Migration was modeled by relating mobility to diffusion using the Nernst-Einstein relation:

$$u = \frac{zFD}{RT} \tag{3.21}$$

3.2.4.5 Cathode Kinetics

For simplification in this paper it is assumed that copper is deposited on the cathode according to the following chemical reaction (3.22):

$$\mathrm{Cu}^{2+}_{(\mathrm{aq})} + 2\mathrm{e}^- = \mathrm{Cu} \tag{3.22}$$

However, for kinetics it is understood that the reaction above proceeds in two steps which are:

$$\mathrm{Cu}^{2+}_{(\mathrm{aq})} + 1\mathrm{e}^- = \mathrm{Cu}^{1+}_{(\mathrm{aq})} \qquad Slow \tag{3.23}$$

$$\mathrm{Cu}^{1+}_{(\mathrm{aq})} + 1\mathrm{e}^- = \mathrm{Cu} \qquad Fast \tag{3.24}$$

Accordingly, Newman [21] in reviewing Mattsson and Brokris [68] proposes (3.25):

$$i_{expr} = i_0(C_r e^{(\frac{\alpha_a F\eta}{RT})} - C_0 e^{(\frac{\alpha_c F\eta}{RT})}) \tag{3.25}$$

where, C_r is metallic copper and equal to 1, $C_o = C_{\mathrm{Cu}^{2+}/\mathrm{Cu}^{2+}_{\mathrm{Bulk}}}$, α_a is the anodic charge transfer coefficient, α_c is the cathodic charge transfer coefficient, i_o is the exchange current

Table 3.1: Diffusion modification based on gas fraction [101].

Relative Diffusion	Author
$D = D_0\frac{1-\varepsilon}{1+\varepsilon}$	Rayleigh
$D = D_0\frac{1-\varepsilon}{1+0.5\varepsilon}$	Maxwell
$D = D_0\frac{8(1-\varepsilon)(2+\varepsilon)}{(4+\varepsilon)(4-\varepsilon)}$	Tobias
$D = D_0(1-\varepsilon)^{1.5}$	Bruggeman
$D = D_0(1-1.5\varepsilon+0.5\varepsilon^2)$	Prager

density. η is the over voltage calculated by the difference between the equilibrium potential and the electrode potential.

In reviewing this work in light of Newman's equation for the copper reaction [21] it was determined that appropriate cathodic and anodic charge transfer coefficients are 0.545 and 1.455, respectively. For the exchange current density the following equation (3.26) was used [68]:

$$i_{of} = i_{oi}(\frac{a_{\mathrm{Cu}f}}{a_{\mathrm{Cu}i}})^{1-\frac{\beta}{2}} \tag{3.26}$$

where, i_{of} is the exchange current density at the desired concentration, i_{oi} is the exchange current density at the reference concentration, $a_{\mathrm{Cu}f}$ is the final activity, $a_{\mathrm{Cu}i}$ is the reference activity at i_{oi}, β is the symmetry factor. From the works cited above i_{oi} is set at 1 mol/l was 100 A/m^2.

From the literature cited the copper reaction is based on Cu^{2+}. However, thermodynamics indicate that CuHSO_4^+ is the dominant copper species. It is assumed that in the boundary layer the CuHSO_4^+ dissociates into copper ions and bisulfate ions. Therefore, for simplicity, the cathodic flux reaction is likely to proceed according to equation (3.27).

$$\mathrm{CuHSO}_4^+ + 2\mathrm{e}^- \rightarrow \mathrm{Cu}^0 + \mathrm{HSO}_4^- \tag{3.27}$$

This is important because it reduces the migration current carried bu copper species due to the change in charge from Cu^{2+}.

3.2.4.6 Anode Kinetics

For the anodic reaction the work of Laitinen [71] was referenced. This work represents experimental determination of i_o at different temperatures on a Pb-PbO$_2$ electrode. Figure 3.8 shows the effect of temperature on i_o. The data from Figure 3.8 were used to develop equation (3.28). It is important to note that logarithmic expressions were attempted, but were not as accurate as this expression.

$$i_0 = 7 \times 10^{-9} T - 2 \times 10^{-6} \tag{3.28}$$

where, i_0 is the exchange current density in A/m^2, T is temperature in K.

The anodic reaction is assumed to be:

$$\mathrm{H_2O} \rightarrow \mathrm{H}^+ + 2\mathrm{e}^- + \mathrm{O}_{2(\mathrm{g})} \tag{3.29}$$

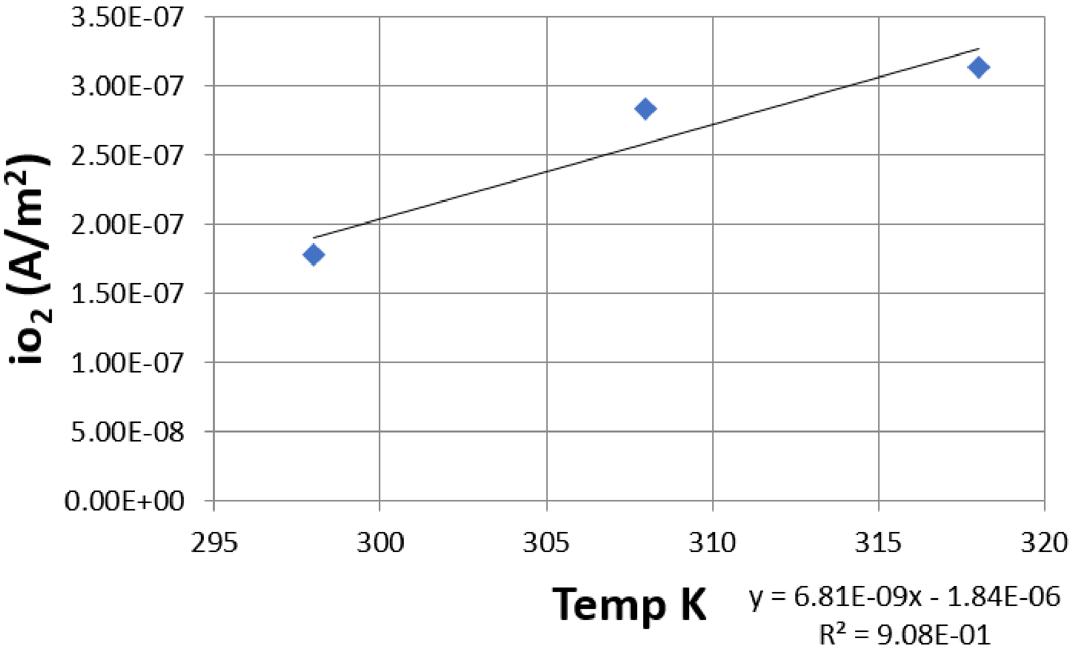

Figure 3.8: Anodic exchange current density versus temperature.

3.2.4.7 Boundary Conditions

Boundary conditions are typical with insulation on all boundaries except the cathode and anode. Species flux occurs at the inlet, outlet, cathode and anode. See Figure 3.3 for reference. No slip conditions are used throughout for domain boundaries.

3.2.5 Bubbly Flow

The form of the bubbly flow (BF) equations used assumes that the fluid is noncompressible and utilizes the following additional assumptions [102]:

- The gas phase density is insignificant compared to the liquid phase density
- The motion between the phases is determined by a balance of viscous and pressure forces
- Both phases are in the same pressure field
- Low gas concentration is low
- Turbulence is not modeled

The resulting equation (3.30) from COMSOL is [103]:

$$\phi_l \rho_l \frac{\partial \mathbf{u}_l}{\partial t} + \phi_l \rho_l \left(\mathbf{u}_l \cdot \nabla\right) \mathbf{u}_l = \nabla \cdot \left[-p2\mathbf{I} + \phi_l \rho_l \left(\nabla \mathbf{u}_l + \left(\nabla \mathbf{u}_l\right)^T\right)\right] + \phi_l \rho_l \mathbf{g} + \mathbf{F} \tag{3.30}$$

The continuity equation (3.31) simplified via the low gas concentration assumption ($\phi_g < 0.01$) is:

$$\phi_l \nabla \cdot \mathbf{u}_l = 0 \tag{3.31}$$

The gas phase velocity (3.32) is given by:

$$\mathbf{u}_g = \mathbf{u}_l + \mathbf{u}_{slip} \tag{3.32}$$

where $\mathbf{u}_i$ represents the velocity vector of the specified component. $\mathbf{u}_l$ is the velocity vector (SI unit: (m/s)

p is the pressure (SI unit: Pa)

ϕ_l is the phase volume fraction (SI unit: m^3/m^3)

ρ_l is the density (SI unit: kg/m^3)

$\mathbf{g}$ is the gravity vector (SI unit: m/s^2)

$\mathbf{F}$ is any additional volume force (SI unit: N/m^3)

μ_l is the dynamic viscosity of the liquid (SI unit: Pas)

μ_T is any additional volume force (SI unit: N/m^3)

$\mathbf{I}$ is the identity matrix

The density of the gaseous phase is derived from the ideal gas law for oxygen. The slip model is of the pressure-drag balance type and the drag coefficient is from the Hadamard-Rybczynski model for small spherical bubbles.

3.3 Experimental Validation

3.3.1 Experimentation

3.3.1.1 Current Density Determination From Deposition

As mentioned in section 3.2.1 a test cell was created to produce deposits for model validation. Several different geometries were used to provide a range of comparisons. Figure 3.9 shows three different electrode configurations used for validation. These were selected as a representation of typical geometric occurrences in tank houses. Direct comparison of effective current density is obtained by numerical integration of the obtained deposit. The

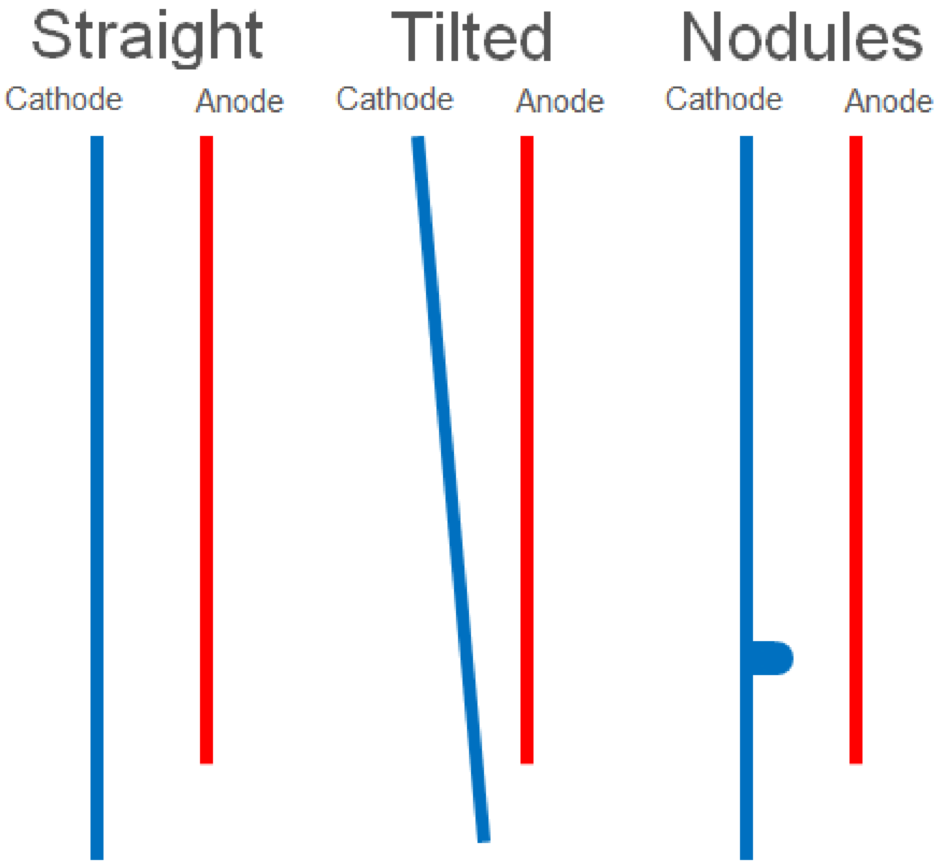

Figure 3.9: Electrode geometries used for validation.

comparison of current densities between the deposit and that of the model was a key to the evaluation. Thickness is converted to current density via the expression (3.33).

$$i_{loc} = \frac{thk_{loc} n F \rho}{t A_w} \tag{3.33}$$

where i_{loc} is the local current density, thk_{loc} is the local thickness, n is the number of participating electrons, F is Faraday's constant, ρ is density, t is time, A_w is atomic weight. Further, by numerically integrating via expression (3.34) the average current density is obtained.

$$\text{Average Current Density} = \sum \frac{\Delta\text{Cathode Length} * i_{loc}}{\text{Cathode Length}} \tag{3.34}$$

The geometric parameters of the test cell and model are covered in Tables 3.2-3.4. The cathode height corresponds to the length of the cathode in the electrolyte. The shield recess is the set back distance from the edge of the cathode shield to the cathode surface. The shield thickness is the width of the shielding around the cathode. Anode to cathode gap

Table 3.2: Straight cathode model geometric parameters.

Parameter	Dimension (m)
Cathode height	0.170
Shield recess	0.0064
Shield thickness	0.0063
Anode to cathode gap	0.02467
Anode length	0.155
Cathode shield to tank	0.0297

Table 3.3: Titled cathode model geometric parameters.

Parameter	Dimension (m)
Cathode height	0.170
Shield recess	0.0064
Shield height	0.0063
Anode to cathode gap	0.02467
Anode length	0.155
Cathode shield to tank	0.0297
Bend angle	6.2773 (deg)

Table 3.4: Nodule cathode model geometric parameters.

Parameter	Dimension (m)
Cathode height	0.170
Shield recess	0.0064
Shield height	0.0063
Anode to cathode gap	0.02467
Anode length	0.155
Cathode shield to tank	0.0297
Nodule diameter	0.009525
Nodule length	0.0127
Nodule position	0.033

is the distance between the anode and cathode. For the tilted cathode geometry the anode to cathode gap in Table 3.4 is the largest gap between the anode and cathode at the top of the cell. The bend angle is the angle that the cathode was bent. Anode length is the length of the anode in the electrolyte. Cathode shield to tank is the distance from the bottom of the tank to the lower part of the cathode shield. In the model this distance is omitted and the bottom of the cathode is modeled as the bottom of the tank. For the nodule cathode described in Table 3.4 the additional dimensions of nodule diameter, nodule length and position (from the bottom of the cathode to the centerline of the nodule) are included.

In order to capture the deposit thickness two different 3D scanners were utilized. For the straight and tilted cathode the NextEngine 3D scanner was utilized with a resolution of 0.127 mm. However, due to the nature of taking multiple scans and merging them into a composite, the spacial resolution is expected to be less. The other scanner utilized was Artec Spider 3D Scanner. This is a hand held unit that features better accuracy with a point accuracy to 0.05 mm. However, in practice due to the nature of surface roughness the filtering algorithm removed some of the feature roughness. Comparison between the roughness in the experimental current density figures in section 3.4 show what appears to be roughness differences from the straight and tilted cathode results to the nodule cathode. These differences are due to the difference in 3D scanner capture and filtering.

The 3D data were imported to MeshLab allowing the raw mesh to be cleaned and simplified. This is an important step as Solidworks has a limit of 90,000 faces for an .stl file import. In addition the mesh was translated and rotated to achieve proper axis alignment. In Solidworks a perpendicular plane was created and the intersection with the mesh generated the 2D profile that the current density was calculated from.

3.3.1.2 Experimental Setup

As shown in Figures 3.1, 3.2 and 3.3, the electrodes incorporated shielding and were arranged to represent the configuration shown in Figure 3.9 to evaluate the effects of straight, tilted cathodes and nodules on current local current efficiency.

To achieve cost effective replenishment of the copper in solution a system was developed. As shown in Figure 3.10 the cell resides in a bath held under isothermal conditions. The cell volume with spacers is 4.6 L and the level is maintained by an overflow port.

The temperature of electrolyte is maintained at 40 °C by an isothermally controlled (68 °C) water bath around the cell. The temperature difference is due to the insulative nature of the tank and the incoming temperature and flow rate of the electrolyte. Figure 3.11 shows the test cell setup in the water bath.

Electrolyte is pumped from the holding barrel to the cell (see Figure 3.10). The overflow is collected in the copper dissolution vessel, which is filled with copper turnings. The dissolution vessel is a shallow vessel tilted at a slight angle to allow gravity based feeding of the electrolyte. The electrolyte from the electrowinning cell flows into the bottom of the upper end of the dissolution vessel to allow flow through the turnings. The turnings are kept damp with the electrolyte to facilitate oxidation and dissolution of the copper turnings. In addition a recirculation loop in the leaching system was added to further increase the concentration of copper should it be required. This recirculation is fed via drip lines on top of the copper to further increase the solution exposure to the copper which is dampened by electrolyte.

Copper concentration is checked once per day using open circuit potential measurements with a multimeter. The open circuit potential measurements were calibrated by utilizing solutions of know concentration to determine a calibration curve. Additional copper dissolution is performed as needed. The copper utilized was copper turnings 99+% pure from Flinn Scientific model C0089. The copper enriched solution is collected in the receiving barrel before being filtered. The solution is then returned after filtration to the holding tank where the process is repeated. The volume of solution is 50L which requires the solution to be recycled once per day. Power was supplied by a BK precision 1761 DC power supply. The cathodes were 316 stainless with lead anodes being supplied by a project sponsor.

The experiment was run according to parameters in Tables 3.5 and 3.6.

Due to the transient nature of the models the steady state concentration of copper was calculated at 36.7 g/L from the data found in Tables 3.5 and 3.6. This constituted the bulk electrolyte concentration of copper for the models.

Guar (SIGMA G4129-250g) is added via NE 4000 (New Era pump systems) series syringe infusion pump using the following methodology. The deposit rate is calculated according to the current efficiency and Faradays law.

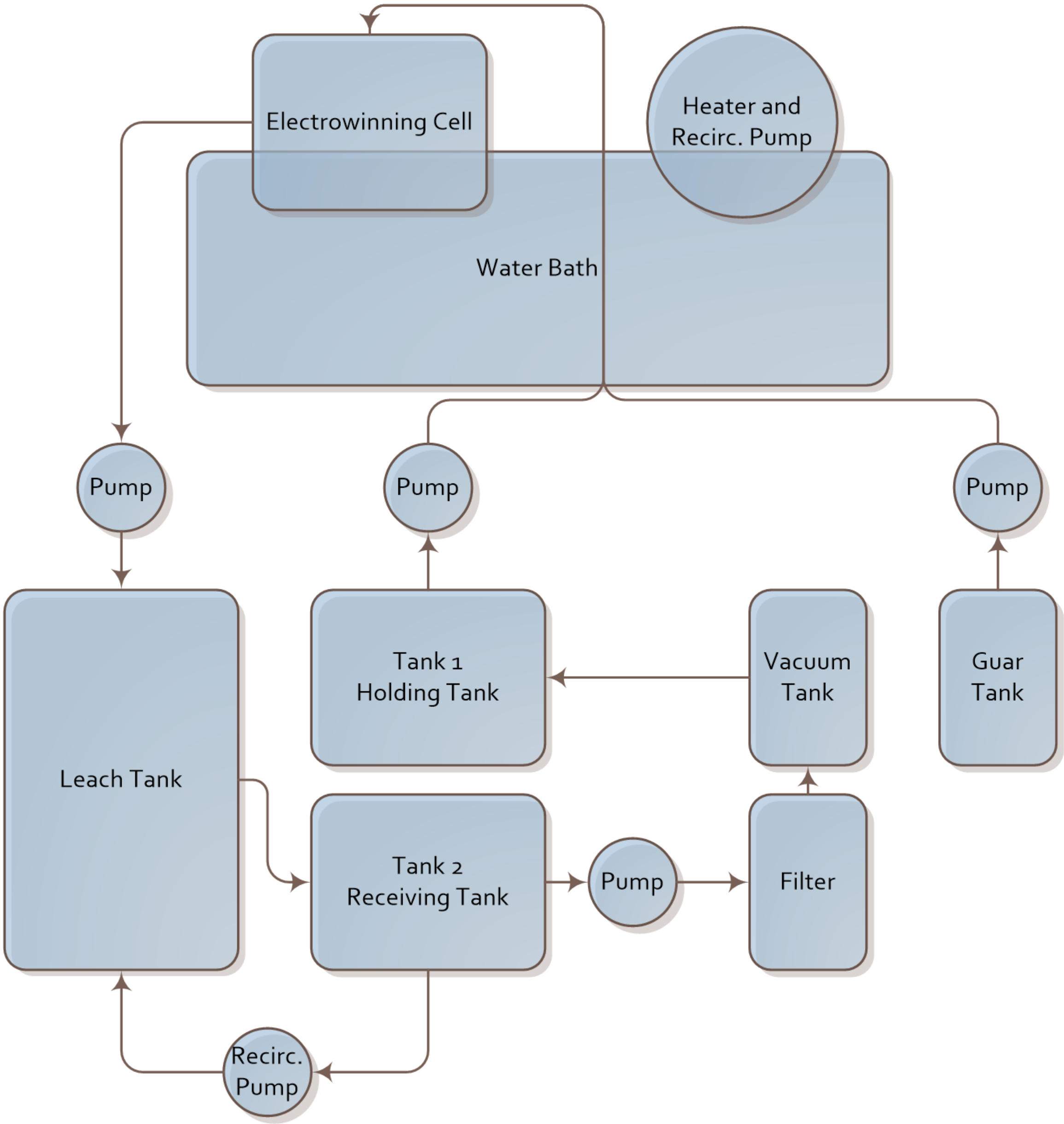

Figure 3.10: Copper replenishment leaching setup.

Figure 3.11: Electrowinning test cell setup.

Table 3.5: Electrolyte parameters.

Elements	Concentration (g/l)	Chemical Composition	Typical Purity
Copper	40	$CuSO_4 \cdot 5H_2O$	99+%
Sulfuric acid	180	H_2SO_4	95+%
Cobalt	0.1	$CoSO_4 \cdot 7H_2O$	98+%
Iron	2	$FeSO_4 \cdot 7H_2O$	99+%
Chloride	0.002	HCL	38%

Table 3.6: Cell parameters.

Cathode Area	0.02376m^2
Anode Area	0.01583m^2
Cell Volume	4.6 L
Temperature	40 °
Amperage	5.14A
Current density	324.7A/m^2
Typical Guar concentration	0.0174g guar/(l·hr)
Inlet flow rate	29.5mL/min
Distance between anode and cathode	see Tables 3.2-3.4

$$\frac{\text{Mass}}{\text{time}} = \frac{IA_w}{nF}\beta = (\text{g Cu /sec}) \tag{3.35}$$

β is current efficiency. The current efficiency was assumed to be 95% based on experimental data. This allowed the calculation of the guar concentration in the following equation:

$$\begin{aligned}(\text{g guar/lguar solutoin}) = (\text{deposit rate})\frac{\text{g Cu}}{\text{sec}}x(\text{guar rate})\frac{\text{gguar}}{1,000\text{kg Cu}}\\ x\frac{1\text{kgCu}}{1,000\text{g Cu}}x\frac{1\text{day}}{1\text{L guar solution}}x\frac{86,400\text{sec}}{1\text{day}}\end{aligned} \tag{3.36}$$

Equation (3.36) allowed the injection concentration of guar to be determined based on the needed addition rate shown in Table 3.6.

3.4 Results and Discussion

All tests with the exception of the straight cathode were run to a period of short circuiting with the anode. Table 3.7 shows the run times of the experiments. All data presented are from the centerline of the cathode as the model was performed using 2D and symmetry assumptions. Current density (2D) was derived from the 3D experiment by measuring the thickness of the centerline deposit of the cathode and determining the average current density from the Faraday equation. This was necessary because the cathode had a larger area than the anode. The edge effects on the electrode sides are not considered in the 2D model whereas the bottom edge is.

3.4.1 Experimental Results

The primary results of experimentation were to produce deposits on stainless steel cathodes to calculate the local depositing current density. The methods to convert de-

Table 3.7: Run time.

Experiment	Effective Current Density (A/m^2)	Run Time(Days)
Straight	277	9.9
Tilted	277.7	8.6*
Nodule	176.2	5.96**

*Ran until shorting

**Ran until shorting. However, 3 nodules were on cathode and the largest shorted. See Figure 3.33.

posit thickness into depositing current density were discussed previously in section 3.3.1.1 equation 3.33. The experimentally determined current densities for each of the various cathode geometries may be found in Figures 3.12, 3.13, 3.14. Unless otherwise noted all results presented are determined from the model results.

3.4.2 Straight Cathode Results

The electrowinning model was run as a transient study. Figure 3.15 shows the model calculated copper concentration as a function of time and was included to show the validity of the chosen simulation time ranges. Specifically Figure 3.15 shows the development of the cathodic concentration at three different points along the cathode and apparent steady state after about 60s. Another interesting aspect of this figure shows the varying concentration of copper along the cathode and the different times required to fully develop the boundary layer. The fastest forming boundary layer occurred at the top of the cathode, with the longest developing below this. The reasons for this will be discussed further in subsequent figures showing the hydrodynamic factors involved in creating these results. The most significant aspect of Figure 3.15 is the display of the transient concentration change of the copper at the cathode. In order to compare the results of the model to those determined experimentally it was important to compare comparable cell conditions. Because a transient model was used the simulation had to be run to a point of steady state before valid comparisons could be made. Thus, the model simulation consisted of two main portions. The first was, running the simulation from time zero to the time required to reach steady state. The second was to run the model for an additional period of time to time average the parameters of interest. This is important to the study as results consist of

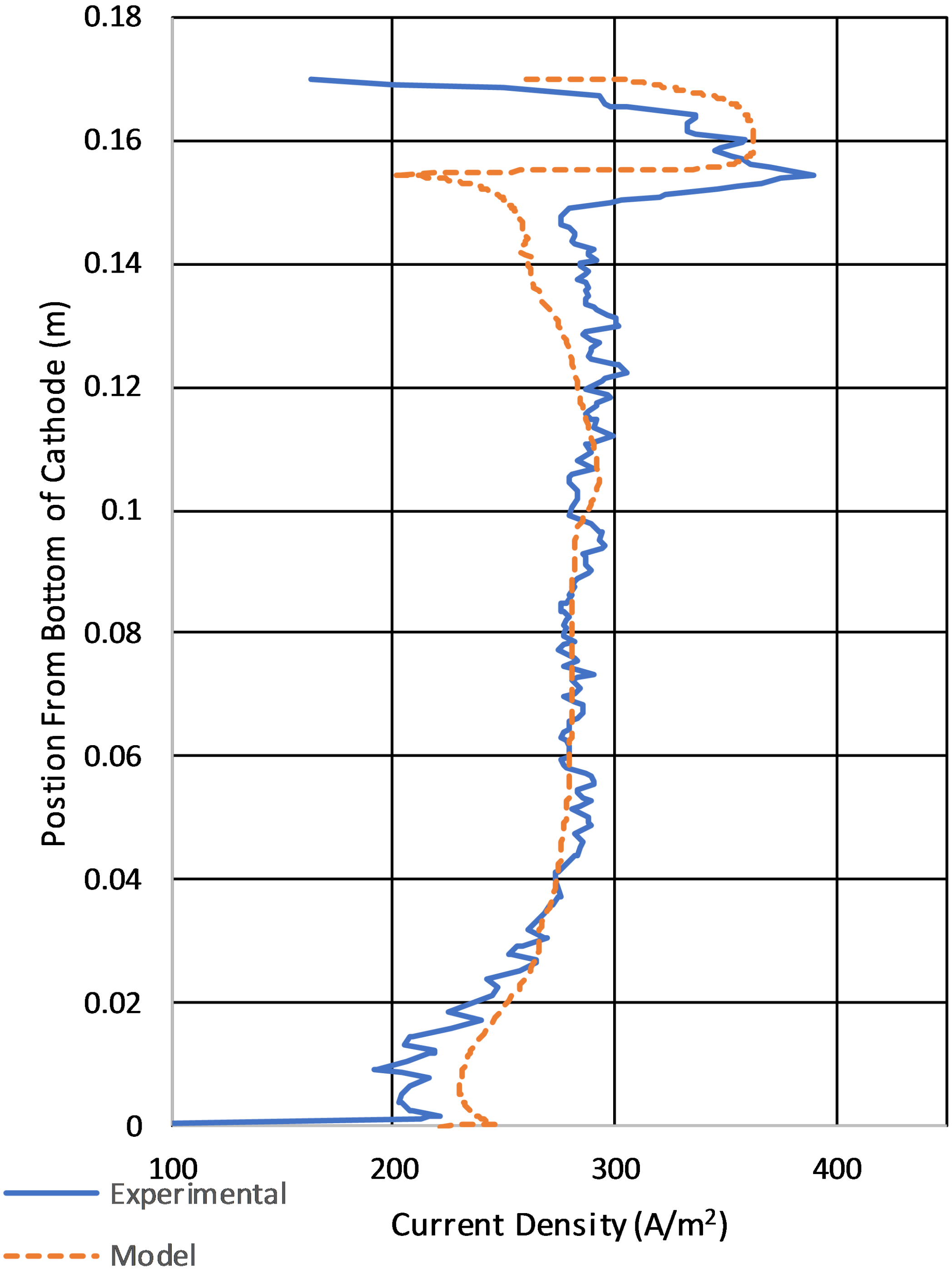

Figure 3.12: Average current density (60-90s) comparison model to experiment for straight cathode. See Tables 3.5, 3.6 and 3.7 for model parameters.

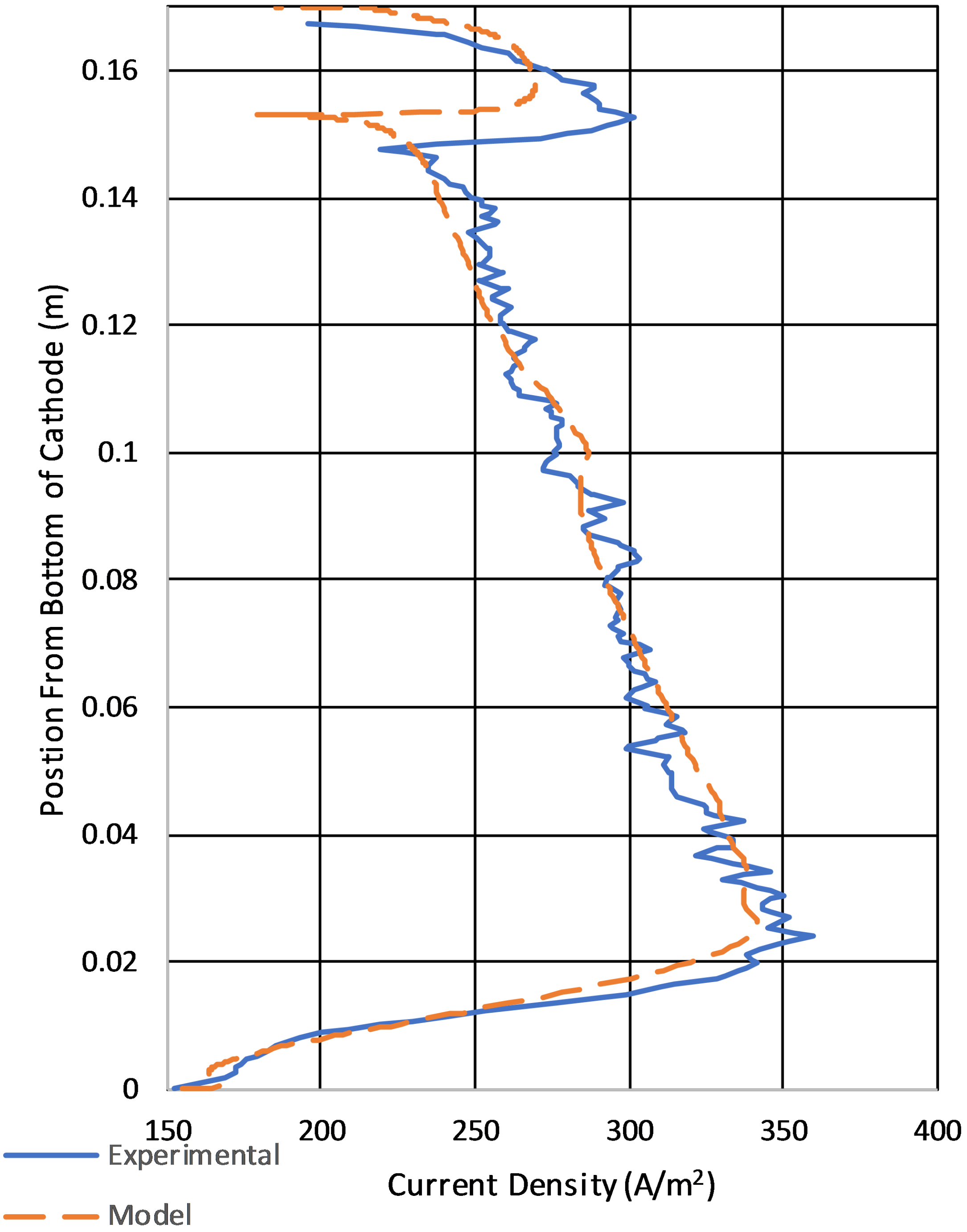

Figure 3.13: Average current density comparison (60-90s) model to experiment for tilted cathode. See Tables 3.5, 3.6 and 3.7 for model parameters.

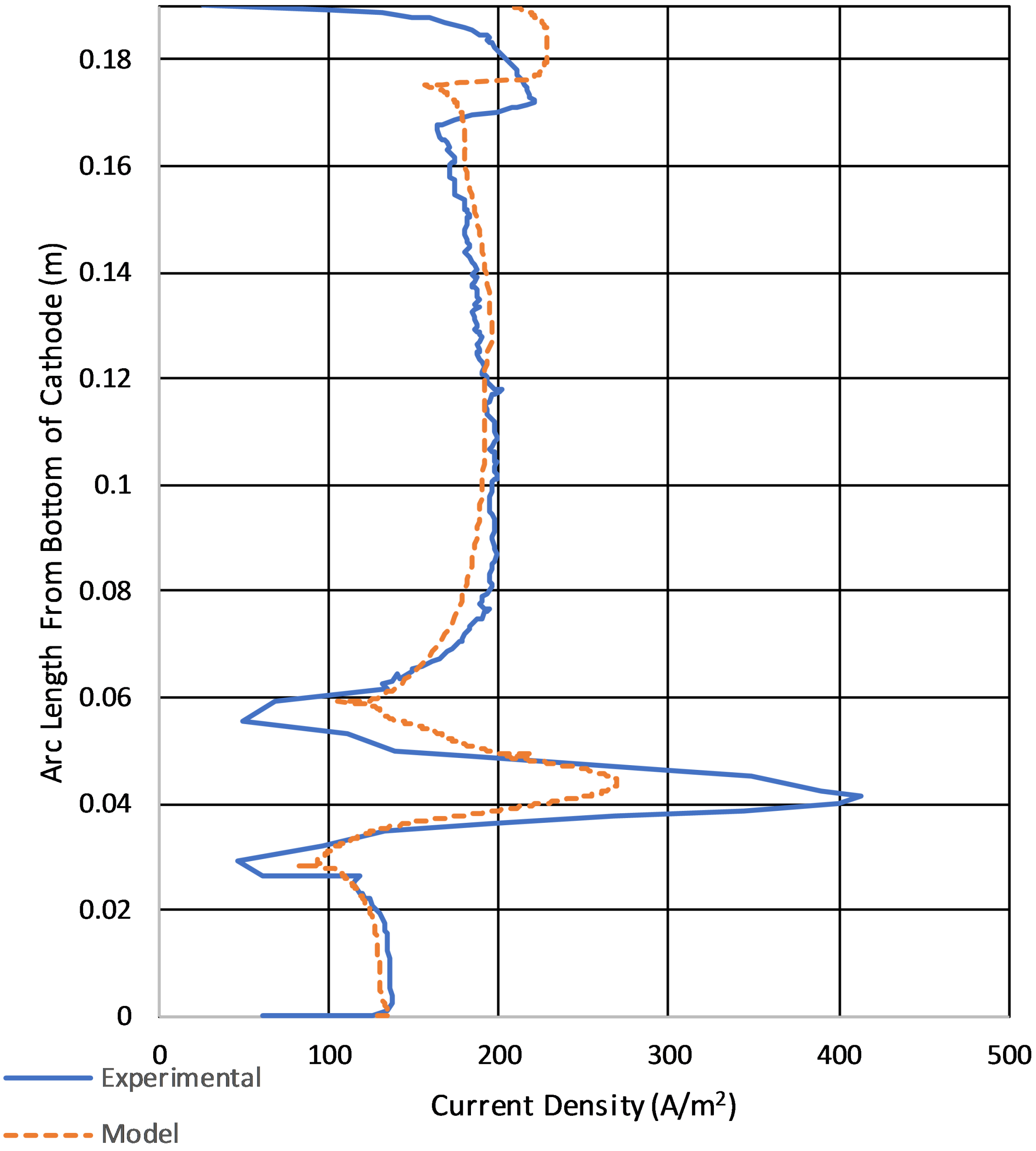

Figure 3.14: Average local current density comparison model averaged (60-90s) to experiment for nodule cathode. See Tables 3.5, 3.6 and 3.7 for model parameters.

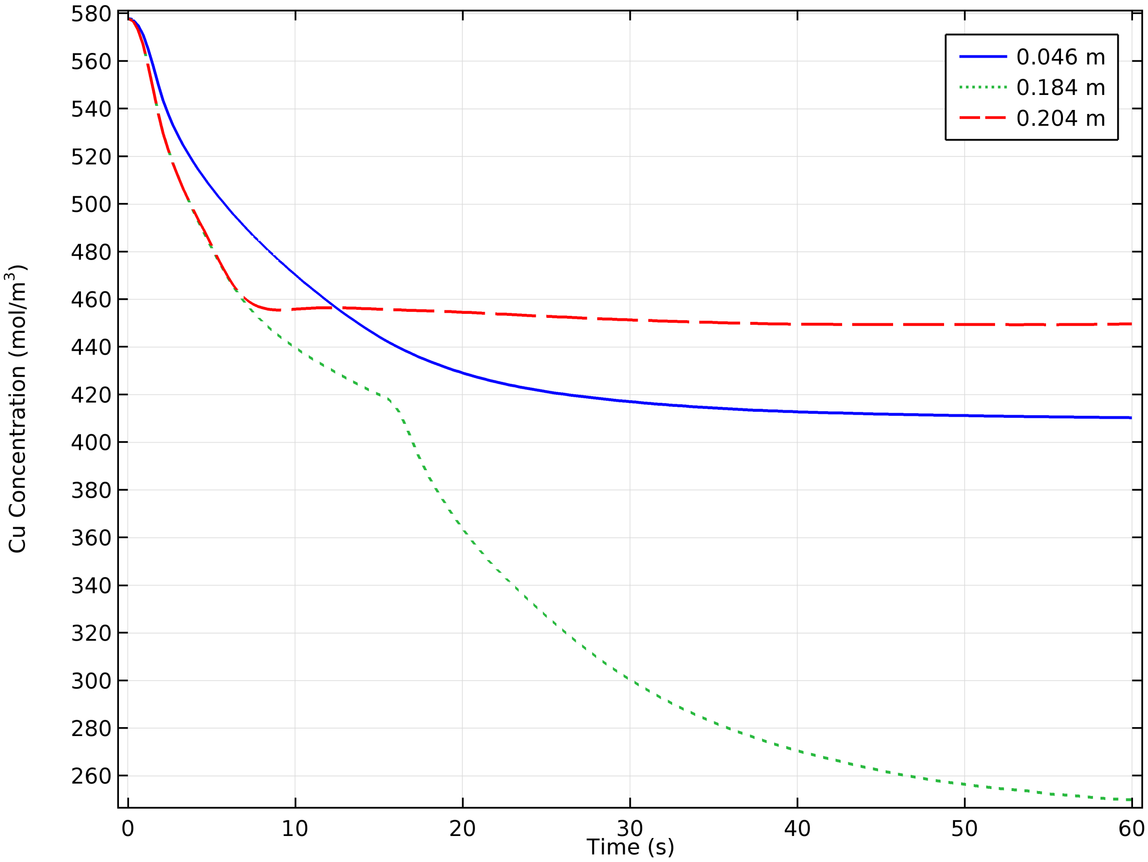

Figure 3.15: Modeled cathode copper concentration (0-60s) at various points along the cathode. Dimensions given in the legend correspond to y axis positions along the cathode (distance from bottom of cell) as shown in Figure 3.3. See Tables 3.5, 3.6 and 3.7 for model parameters.

running the simulation to steady state (as shown by Figure 3.15) then averaging the results in a following time period (60-90s). Many of the subsequent figures will show the time averaged results of a 30s period following arrival at steady state.

Figure 3.16 shows the boundary layer concentration gradient at a specific point on the cathode. This figure was included to provide insights into the nature of the cathodic boundary layer. The model requires a suitable balance of accuracy from finer mesh and practical run time to solution. These competing factors of a finer mesh requiring a longer run time and a coarse mesh producing faster, but less accurate results were fundamental to developing a practical electrowinning model. To address this trade-off the mesh was refined predominantly at the cathode boundary layers where the accuracy was needed to understand the transport phenomena in the electrolyte. Figure 3.16 shows the mesh resolution in the boundary layer. Observations of this plot show 5 nodes in the boundary

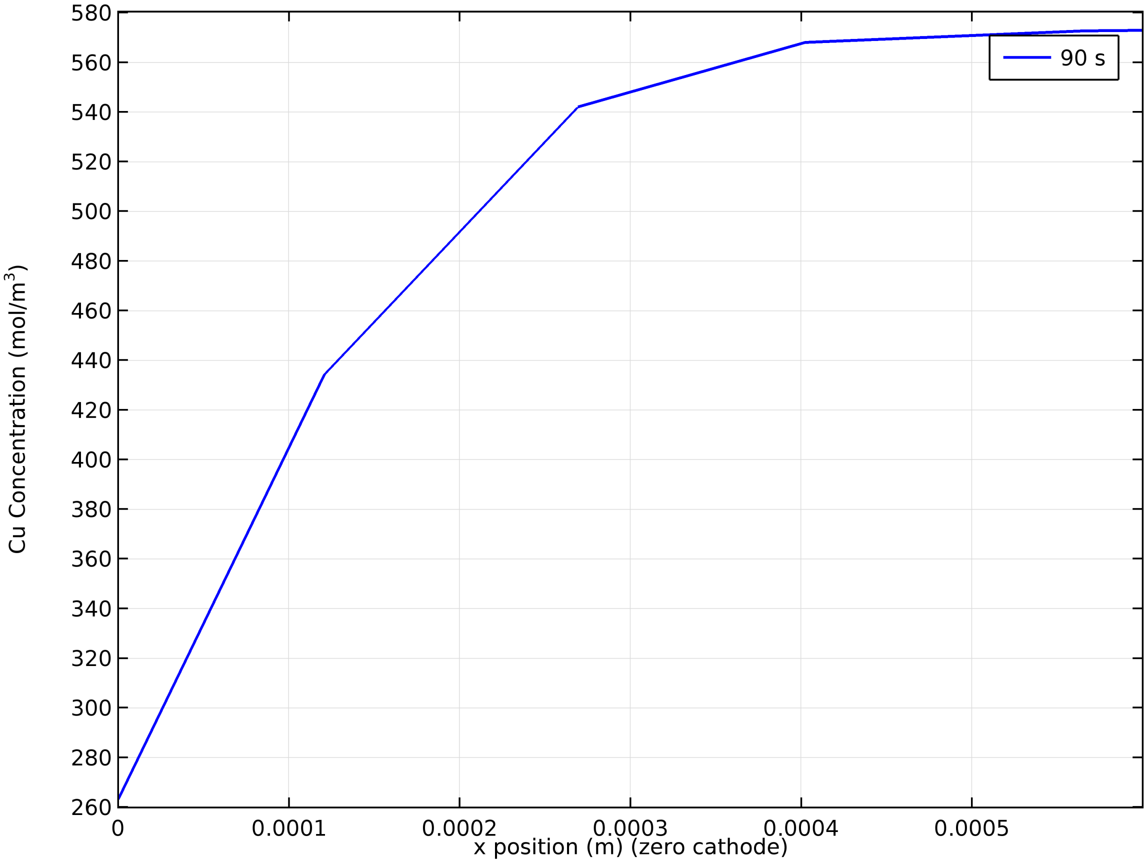

Figure 3.16: Modeled boundary layer at y position 0.15 m from bottom of tank (see Figure 3.3 for postion in cell) and 90s. See Tables 3.5, 3.6 and 3.7 for model parameters.

layer which is about 500 microns thick. The first node point is at the surface of the cathode. Subsequent node points are shown at the intersection of the linear line segments. The concentration of copper is a linear interpolation between the solution at the node points. This is the cause of the linear portions of the concentration curve. Refinement of the mesh in this area would produce a more continuous curve, but with a higher computational price. Figure 3.16 shows the balance attempted in resolving the copper concentration in the boundary layer. In general the mesh was refined in areas of high gradients (such as the boundary layer). Thus, in areas like the bulk electrolyte and at the anode where resolution of the mass transport was not needed the mesh was less refined.

Figure 3.12 is the most significant figure type of the results section. It compares the average modeled current density at the cathode from 60-90s to the current density determined from deposit thickness. It also highlights the effect of the limiting of the electrode kinetics through overpotential. In general it appears that the measured current density and the model data are in general agreement. The largest apparent difference between the model calculated current density and that calculated from the deposit thickness is the apparent roughness. The current density variation shown in Figure 3.12 in the experimental data is due to two factors. The first is from the actual deposit roughness as shown in Figure 3.33. The second is due to the resolution of the 3D scanner used to measure the surface and discretize the measurements into a surface mesh for measurements. In the model apparent roughness in the results is likely due to numerical aberrations form the selected mesh size. Another important aspect to note in the apparent roughness difference of the data is the difference in the data types. The the copper deposit measured to determine the current density experimentally had time to fully develop roughness through the course of days. The model calculated current density was determined over 30s and without the benefit of mesh resolution and deposit/boundary layer feedback which did not produce the same roughness in the data. Observations of Figure 3.12 also show differences in the magnitude of the current density showing lower current densities in the area of the observed ridge and notch a the top of the cathode and overestimating at the bottom. The position of the feature at the top of the cathode shows reasonable positional agreement between the experimental and modeled results.

Figure 3.17 shows the copper concentration calculated from the model at the cathode

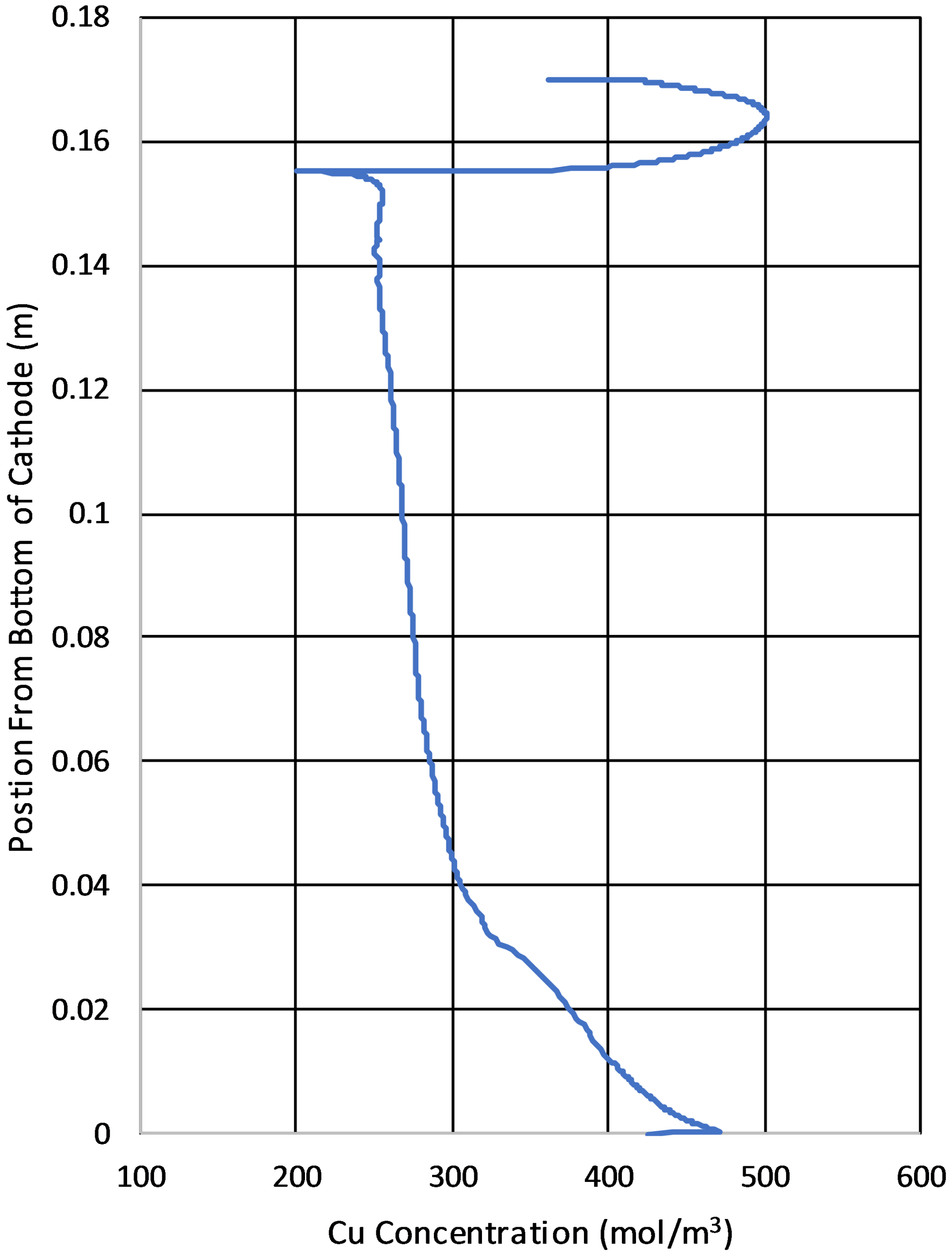

Figure 3.17: Modeled straight cathode copper concentration calculated from the model along the cathode (90s). See Tables 3.5, 3.6 and 3.7 for model parameters.

surface at 90s. A key finding of the model is the higher copper concentration at the top of the cathode due to an increase in local mass transport. This along with the results in Figure 3.12 provide insights into the formation of a copper ridge at the top of the cathode. The results in Figure 3.17 are similar to those discussed in Figure 3.12. This is because copper concentration and current density are related by the Butler–Volmer expression. Note that in Figure 3.17 the results are presented without time averaging.

The extent of migration transporting the electroactive species of significant interest in eletrochemistry. Figure 3.18 shows the split between diffusive and migration fluxes as a ratio of the total flux. It this instance migration accounts for about 1/4 of the total flux. The model calculated results shown in Figure 3.18 are interesting in that across the length of the cathode the mode of transport as measured at the surface of the cathode varies by approximately 10%. As shown in Figure 3.18 the top of the cathode shows increased transport due to migration. This is explained by the higher copper concentration at the cathode in this region as shown in Figure 3.17. Thus with a higher concentration the concentration gradient is less owing to lower diffusion and increasing migration. The difference between migration and diffusion and the effect on transport will be covered further in Chapter 4 where additional species composing the electrolyte will be considered.

Figure 3.19 is similar to Figure 3.17 showing copper concentration but with the difference of presenting data in the cell rather than the cathode. In particular, Figure 3.19 shows concentration differences due to the transport form the electrolyte flow.

Figure 3.20 shows the electrolyte velocity showing the vortex formed at the top of the cell. This Figure shows the cause of the results in Figures 3.12 and 3.17. The results in Figure 3.20 are significant in showing the formation of a single stable vortex at the top of the cathode. This is due to the height of the cathode chosen. If the cathode was taller the vortex would become unstable and separate. This is the reason that the notch phenomenon is not observed in full size electrowinning cells. This result can be contrasted in with those of full size cells in Chapter 7.

Figure 3.21 shows the gas fraction in the cell. The results show little carryover of the gas back down the cell, with the majority exiting the electrolyte at the top. The maximum gas fraction is listed at 0.007 and occurs in only a limited portion along the anode, with the majority of the cell below the 0.01 threshold for mentioned for the low gas assumption

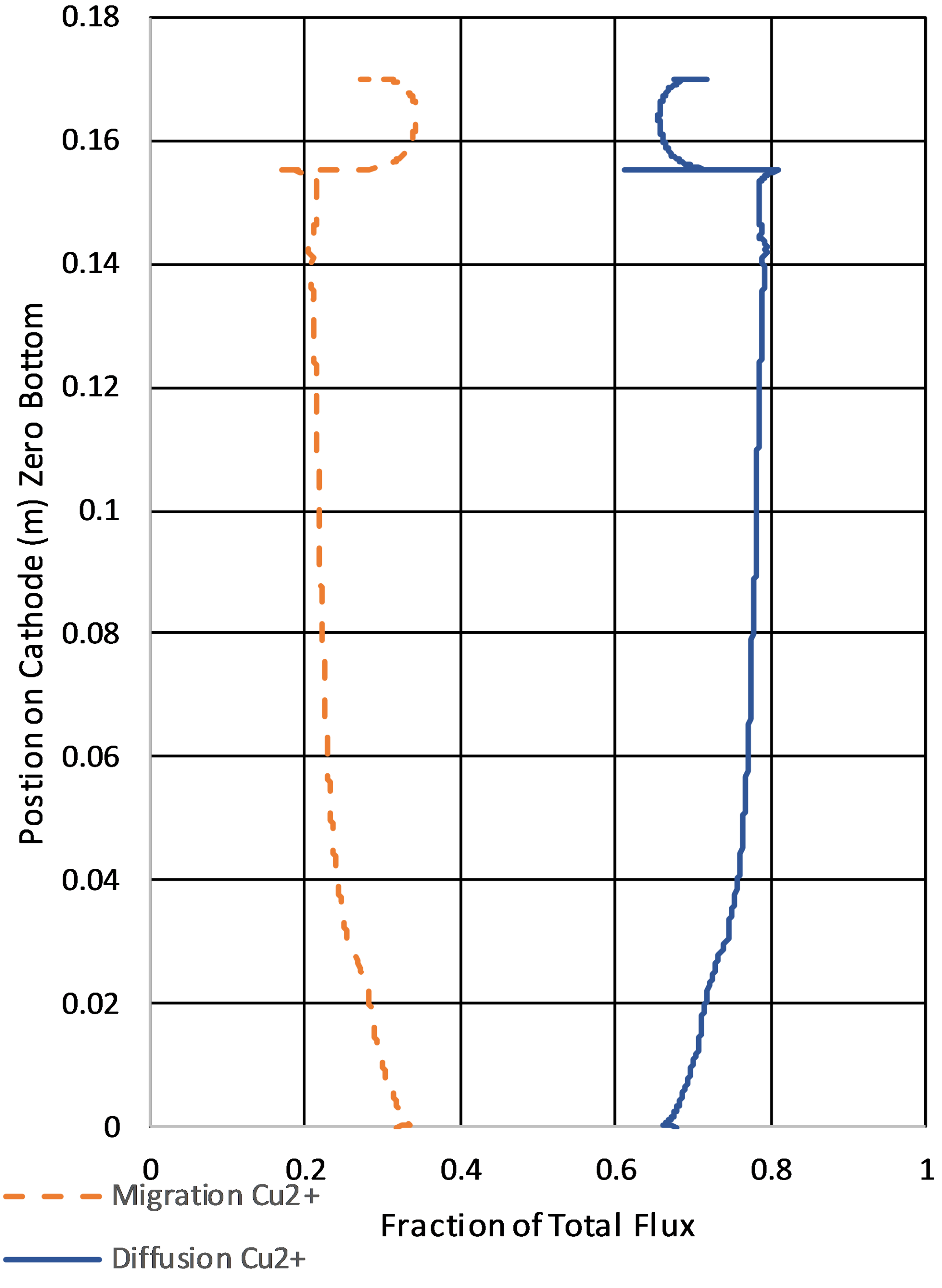

Figure 3.18: Modeled straight cathode flux type ratio calculated by the model along the cathode at 90s of simulation. See Tables 3.5, 3.6 and 3.7 for model parameters.

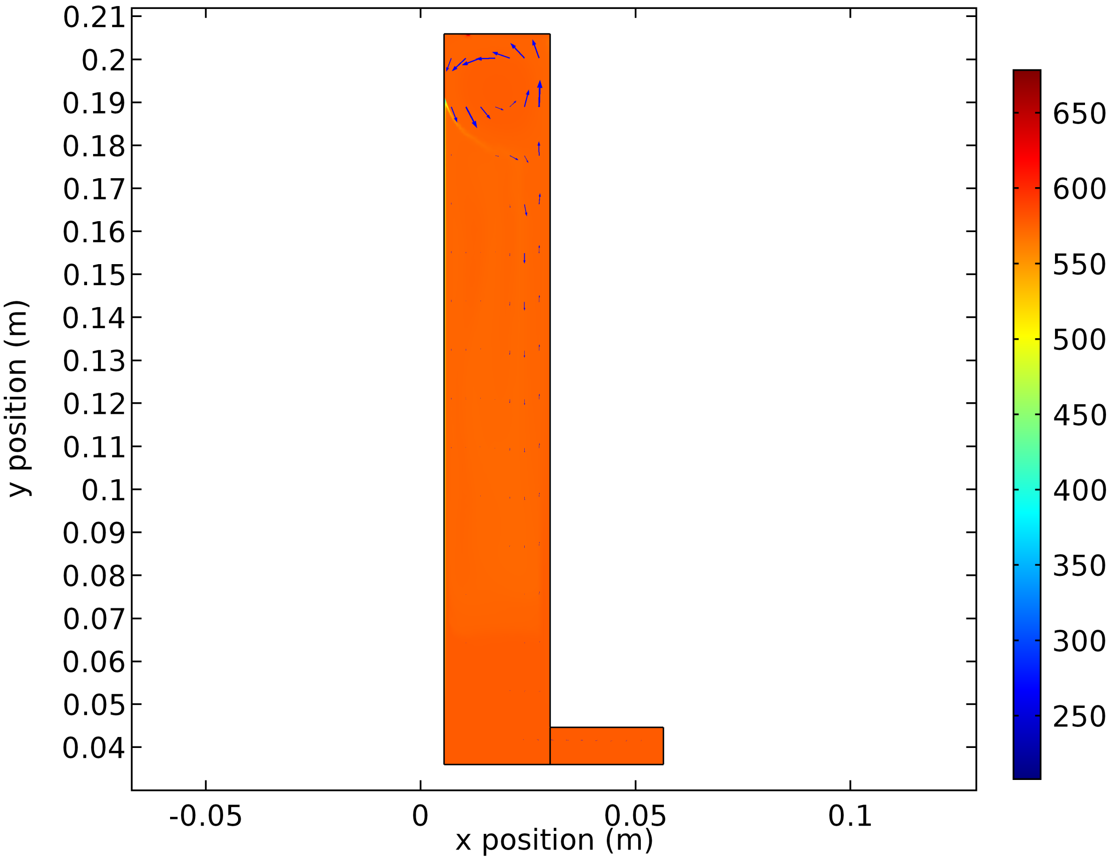

Figure 3.19: Modeled straight cathode cell copper concentration (mol/m^3) with arrows as velocity vectors (90s). See Tables 3.5, 3.6 and 3.7 for model parameters.

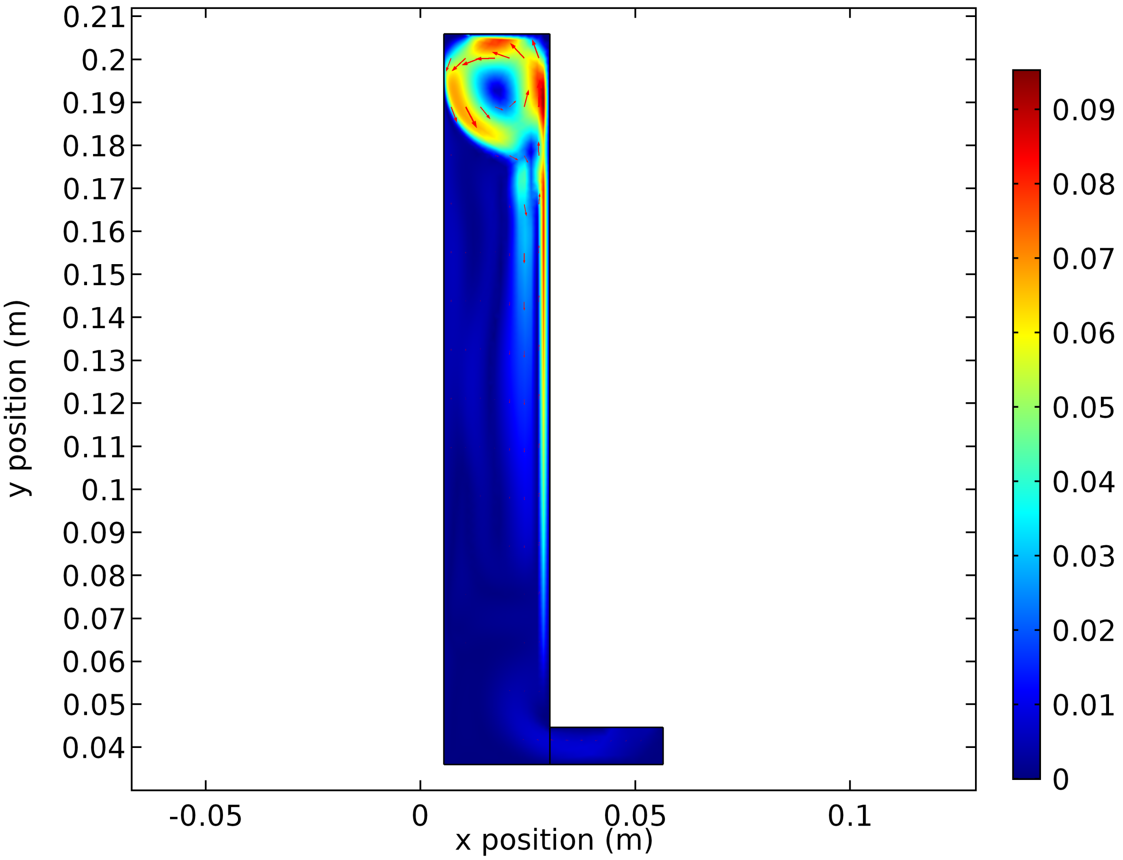

Figure 3.20: Modeled straight cathode cell electrolyte velocity (m/s) with arrows as velocity vectors (90s). See Tables 3.5, 3.6 and 3.7 for model parameters.

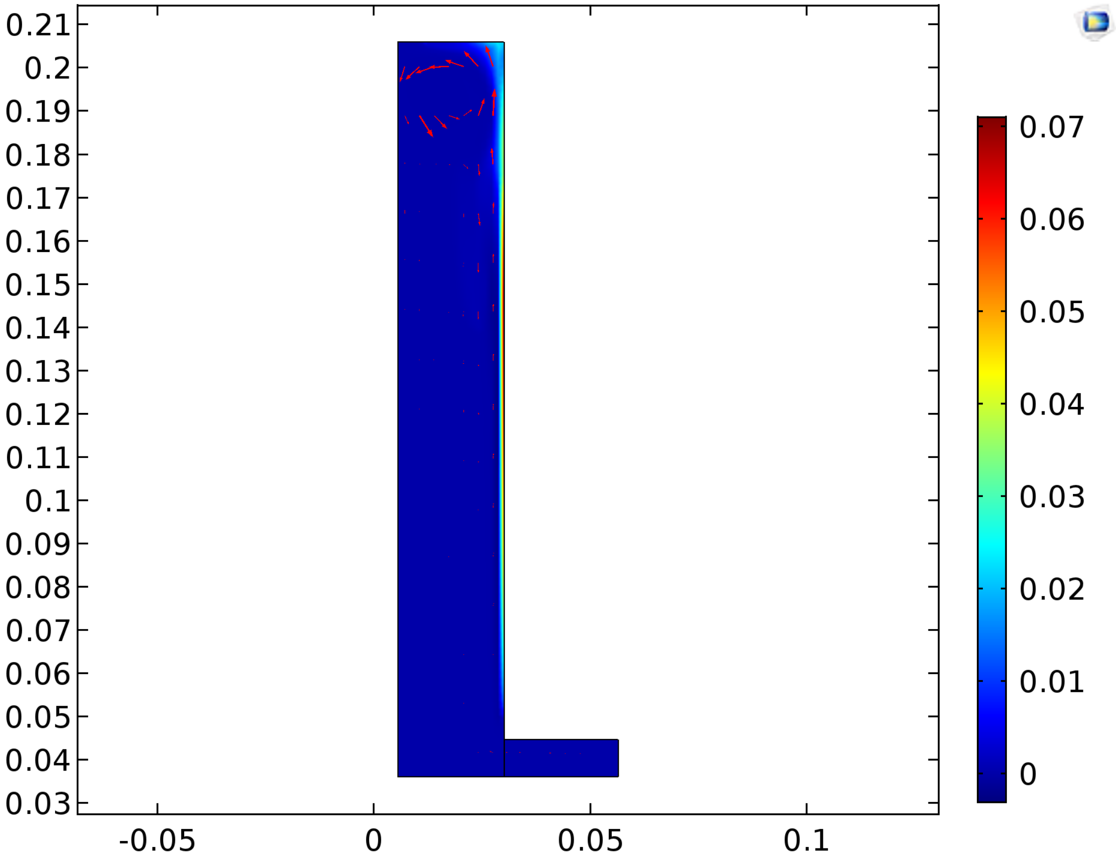

Figure 3.21: Modeled straight cathode cell gas fraction (vol gas/vol electrolyte) with arrows as velocity vectors (90s). See Tables 3.5, 3.6 and 3.7 for model parameters.

for the bubbly flow governing equations. This assumption was made in light of the higher local gas fraction due to the limited portion of the electrolyte having a higher gas fraction and the vindication of the results. It appears sufficient to maintain the low gas fraction simplification in light of adding additional computational expense.

The mass transport coefficient is provided in Figure 3.22 calculated according to equation:

$$k = \frac{Flux_{Cu^{2+}}}{C_{Cu^{2+},bulk} - C_{Cu^{2+},electrode}} \tag{3.37}$$

Figure 3.22 shows the variation of the mass transport along the cathode and includes the contributions from both migration and diffusion. From this plot it is apparent why there is enhanced deposition at the top of the cell with roughly 5x increase in mass transport at highest compared to the lowest transport areas. In the instance of electrowinning in the presented test cell the local transport variations are significant as shown by Figure 3.22 and should not be ignored.

3.4.3 Titled Cathode Results

The tilted cathode shows many of the same features as the straight cathode with primary difference being the current density distribution from the spacial alignment. Because of this the discussion in this section will focus primarily on the differences between the straight and tilted cathode.

Figure 3.13 shows the current density comparison from the experimental to the model. It is helpful to contrast this to Figure 3.12 for the straight plate geometry. In comparison, the tilted cathode shoes a less pronounced ridge at the top of the cathode because of the lower local current density. The highest current density on the tilted cathode is located at the point closest to the anode at about 0.02 m from the bottom of the cathode. This is because of the lower potential drop in the electrolyte from the decreased distance to the anode. The current density is lowered somewhat by the electrode kinetics. The increase in current density showing a maximum at 0.025 is due to the proximity of the cathode to the bottom of the anode. This increase is explained by the lower electrolyte resistance caused by the decrease in distance. From Ohm's law the lower resistance will increase the current flow to this area. However, electrode kinetics cannot be discounted with current density also determined by local overpotential which has concentration dependence.

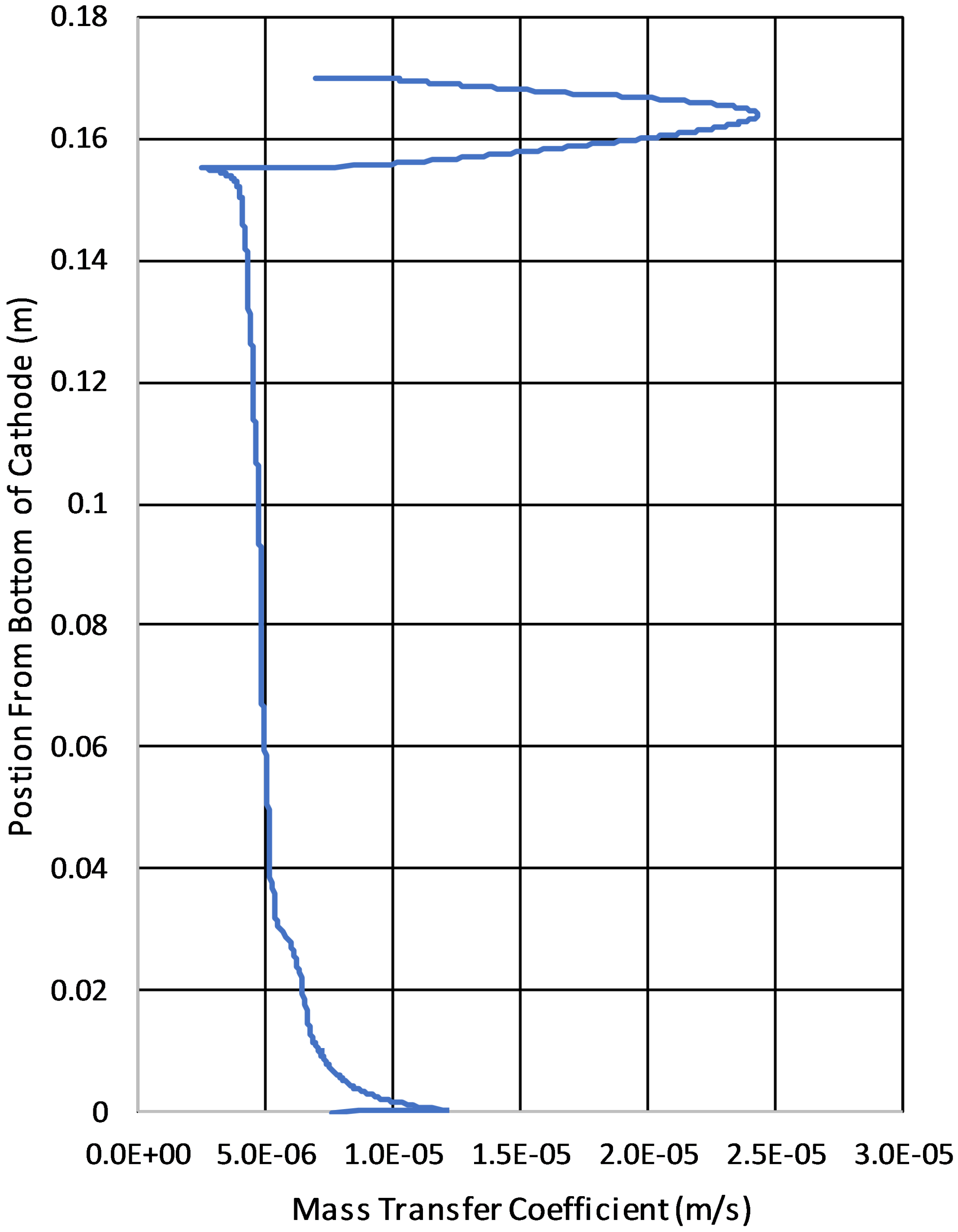

Figure 3.22: Modeled straight cathode average mass transfer coefficient along the cathode surface (60-90s). See Tables 3.5, 3.6 and 3.7 for model parameters.

Figure 3.23 shows the copper concentration along the cathode for the tilted geometry. If varies significantly from Figure 3.17 showing the straight cathode in that the location of the titled cathode closest to the anode show lower copper concentration. This is because of the increased current density from the proximity to the anode. The results showing the lower concentration at the point of minimum anode to cathode separation distance is significant in terms of the moderating impact of overpotential and electrode kinetics due to concentration. As the concentration decreases the overpotential will need to increase negating some of the lower electrolyte resistance at the point of closest proximity.

In conjunction with Figure 3.23, Figure 3.24 shows copper concentration across the electrolyte domain. The apparent difference between the results in Figure 3.24 versus those of the straight cathode in Figure 3.19 are not great. The maximum velocities in each are approximately equal and the tilt in the lower part of the cell does not significantly vary the vortex at the top of the cell.

Figure 3.25 shows much the same velocity profile as does Figure 3.20. The geometry does not seem to affect the vortex at the top of the cell owing to similar dimensions at the top where recirculation occurs. The difference in ridge current density is due not to the mass transport, but rather to the current density distribution from proximity to the anode with associate drop in electrolyte resistance.

Figure 3.26 shows the gas fraction in the cell. Again, there is not much difference between the straight and titled geometries that is of significance

3.4.4 Nodule Cathode Results

Out of all of the current density profiles the most difficult to obtain is the cathode nodule. A brief description of the process is warranted because of the difference in data presentation and collection methods. The process begins by obtaining a 3D surface scan of the deposit as shown in Figure 3.27. Figure 3.27 shows the nodule cathode scan with the base that it was scanned upon. The base is oriented to the x,y,z axes via translation and rotation. Thus the thickness of the cathode may be subtracted out. These data are then imported in to a CAD program (Solidworks) where a cut plane is utilized to obtain a 2D profile along the centerline of the cathode.

The cathodic nodule data are best presented in terms of perimeter or arc length along

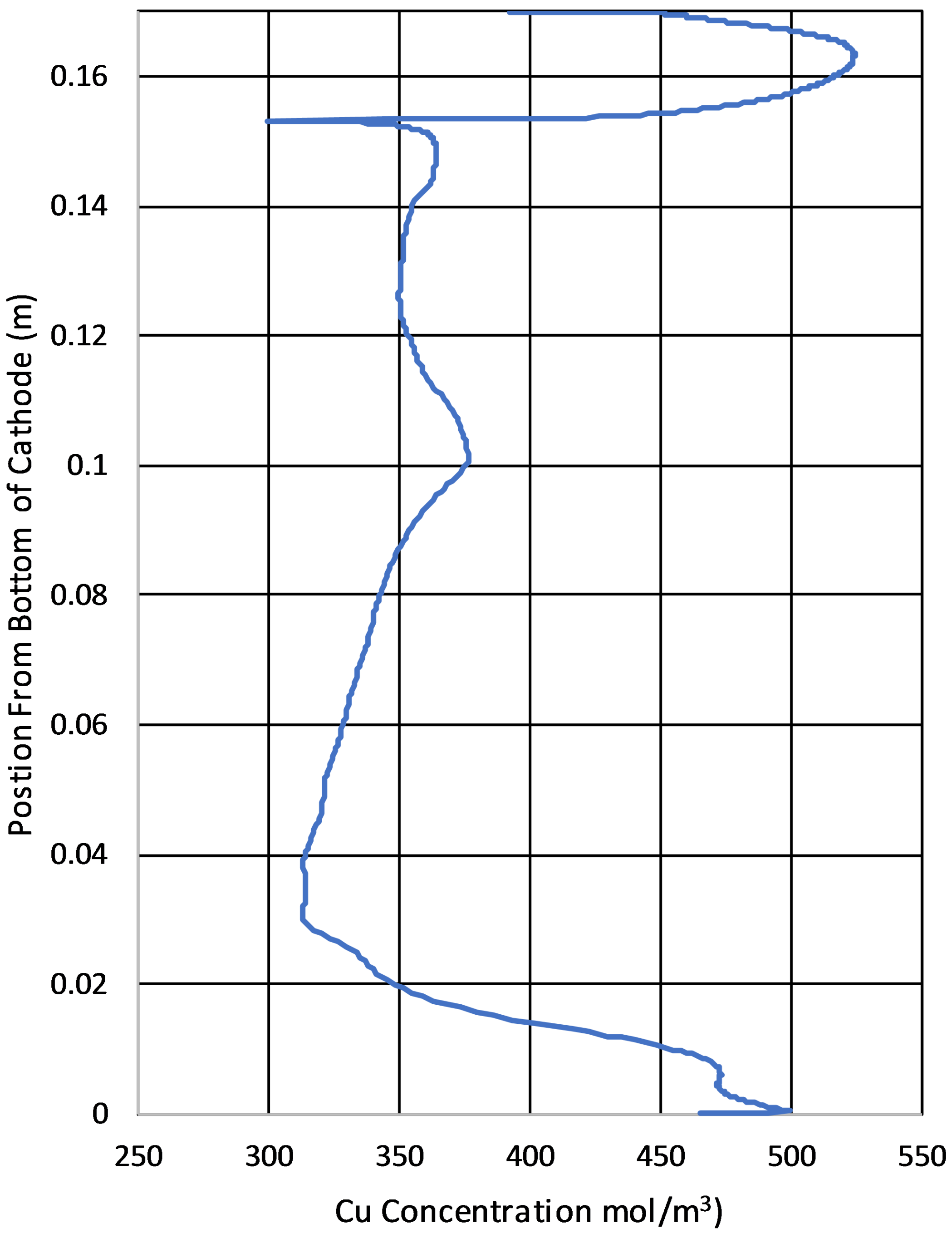

Figure 3.23: Modeled tilted cathode copper concentration along the cathode. See Tables 3.5, 3.6 and 3.7 for model parameters.

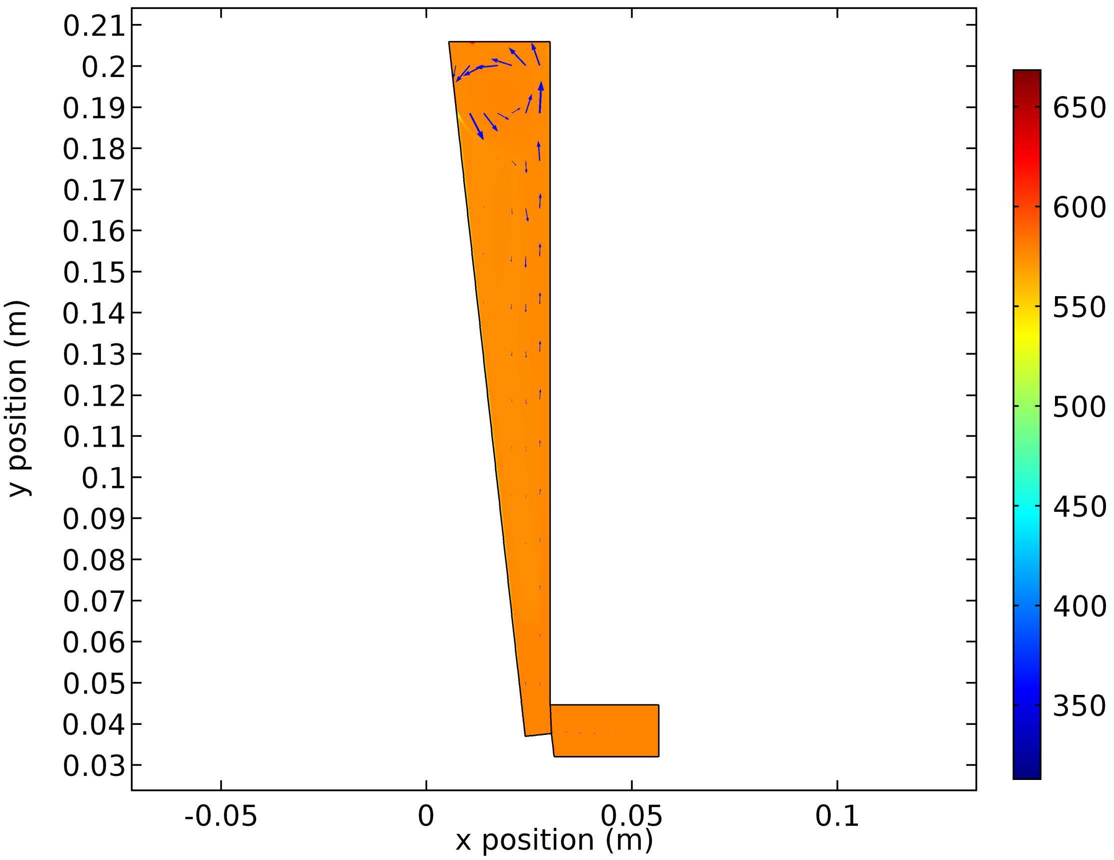

Figure 3.24: Tilted cathode cell copper concentration (mol/m^3) with arrows as velocity vectors (90s). See Tables 3.5, 3.6 and 3.7 for model parameters.

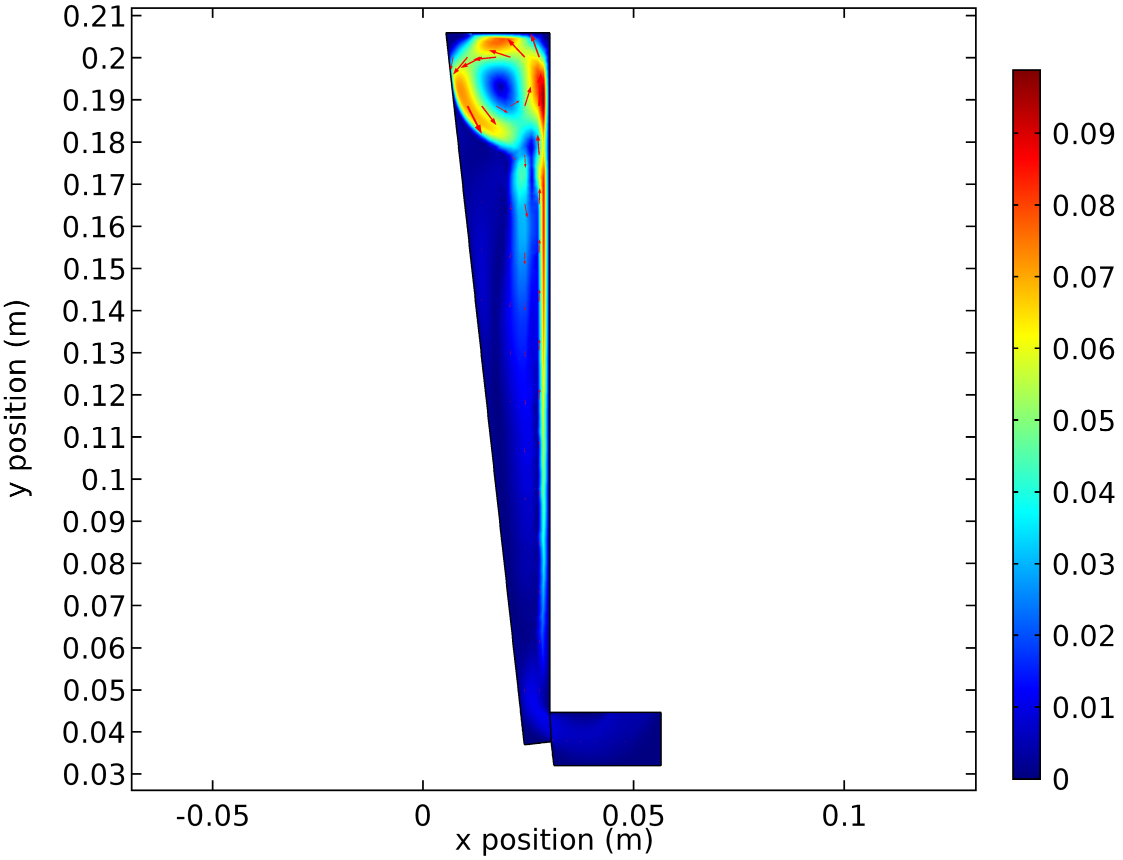

Figure 3.25: Tilted cathode cell electrolyte velocity with arrows as velocity vectors (90s). See Tables 3.5, 3.6 and 3.7 for model parameters.

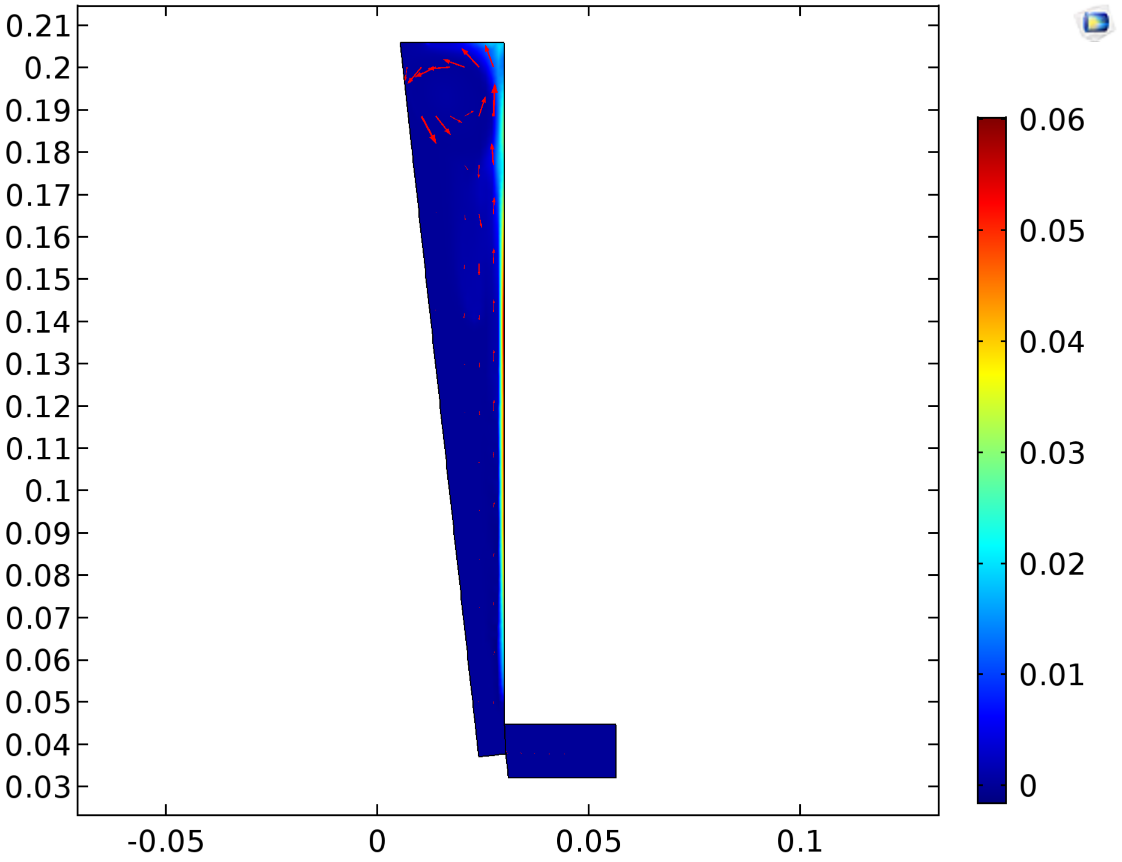

Figure 3.26: Tilted cathode cell gas fraction (vol gas/vol electrolyte) with arrows as velocity vectors (90s). See Tables 3.5, 3.6 and 3.7 for model parameters.

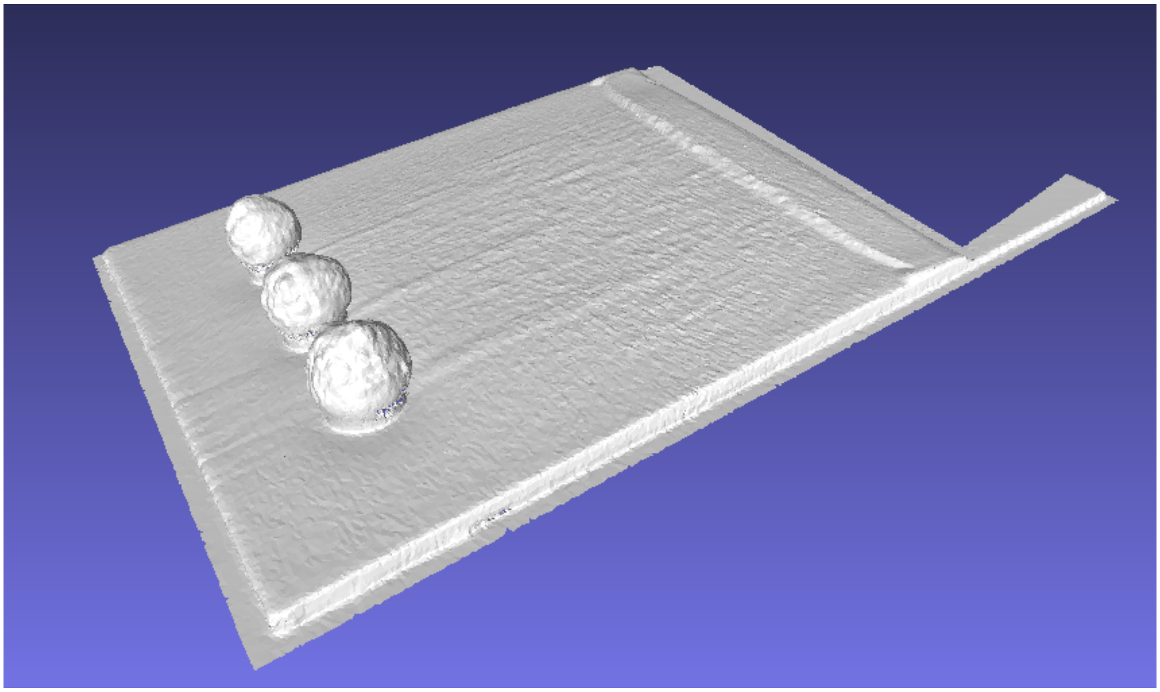

Figure 3.27: 3D scan showing nodules and base plane for geometric reference.

the cathode which allows presentation of the data in standard xy graphical form. The second discussion point is how the deposit profile was determined. Figure 3.28 shows the cross-section diagram of the nodule with electrodeposit. As with all of the presented data the cathodes were processed with a 3D scanner. Care was taken to scan the underside of the nodule deposit due to overhang. A centerline plane was used to determine the intersection profile for export for the calculation of current density. In the case of the nodule the deposit was superimposed over the original geometry as shown in Figure 3.28. A point was determined at the base of the nodule of theoretical ”zero current”. This is a simplification based on the normal vector of deposit growth. The lines on each side of this point indicate where current is fully dependent on deposit thickness. A series of measurement lines normal to the original surface were drawn to determine deposit thickness. Thus, deposit thickness and associated arc length were determined. This allows direct comparison of measured data to the model output.

Figure 3.14 shows the comparison of current density from experimental to modeled. The model shows good agreement with the experimental, except at the nodule. The troughs at the nodule base are underestimated by the model. This may be due to the method of

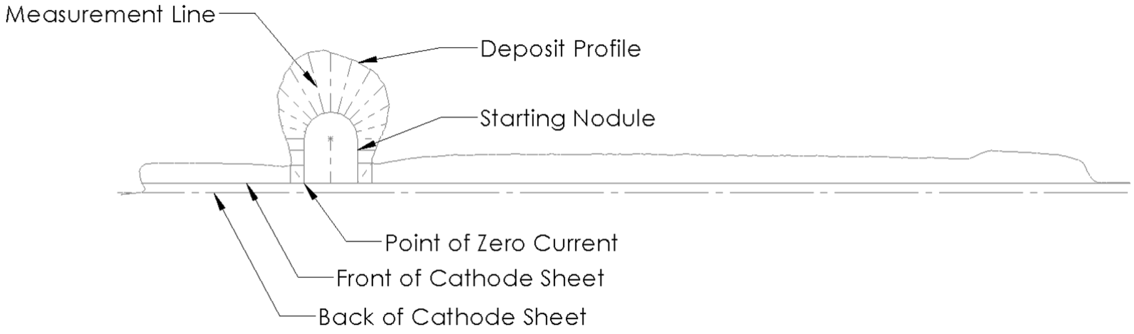

Figure 3.28: Cross section of nodule showing measurement lines for reference.

determining the current efficiency from the deposit thickness. The model did not have to contend with changing boundary geometry. Also, the maximum current density is under represented by approximately 130 A/m^2. This may be due to the additional nodules shown in Figure 3.27. These were included to test different shapes and in the instance of this model the geometry for the middle nodule was utilized. However, this should have been compensated by the determination of the average current density from the deposit thickness. Because numerical integration was used to determine the nodule deposit thickness, the center average between adjacent data points was used. That is why in Figure 3.14 the current does not reach zero at the nodule base.

Figure 3.29 shows the copper concentration at the modeled cathode surface. The variation is quite pronounced particularly along the nodule where the mass transport varies widely. It is important to consider that the 2D representation considers this feature as infinitely wide and the flow around the nodule sides is not considered.

Figure 3.30 shows the copper concentration in the cell. Note the concentrations due to the flow effects from the nodule and the resulting boundary layer. Of all the three geometries presented the nodule cathode shows the most variation along the cathode. In Figure 3.30 and Figure 3.29 the coupled electrolyte resistance decreased due to anode proximity and fluid flow contributions lead to the variation in the copper concentration.

Figure 3.31 shows the electrolyte velocity which explains the mass transport effects in the cell. Compared to the straight cathode in Figure 3.20 the nodule cathode in Figure 3.31 shows a slight decrease in maximum fluid velocity, but largely remains the same as the straight cathode. This difference is the result of the lower modeled current density as

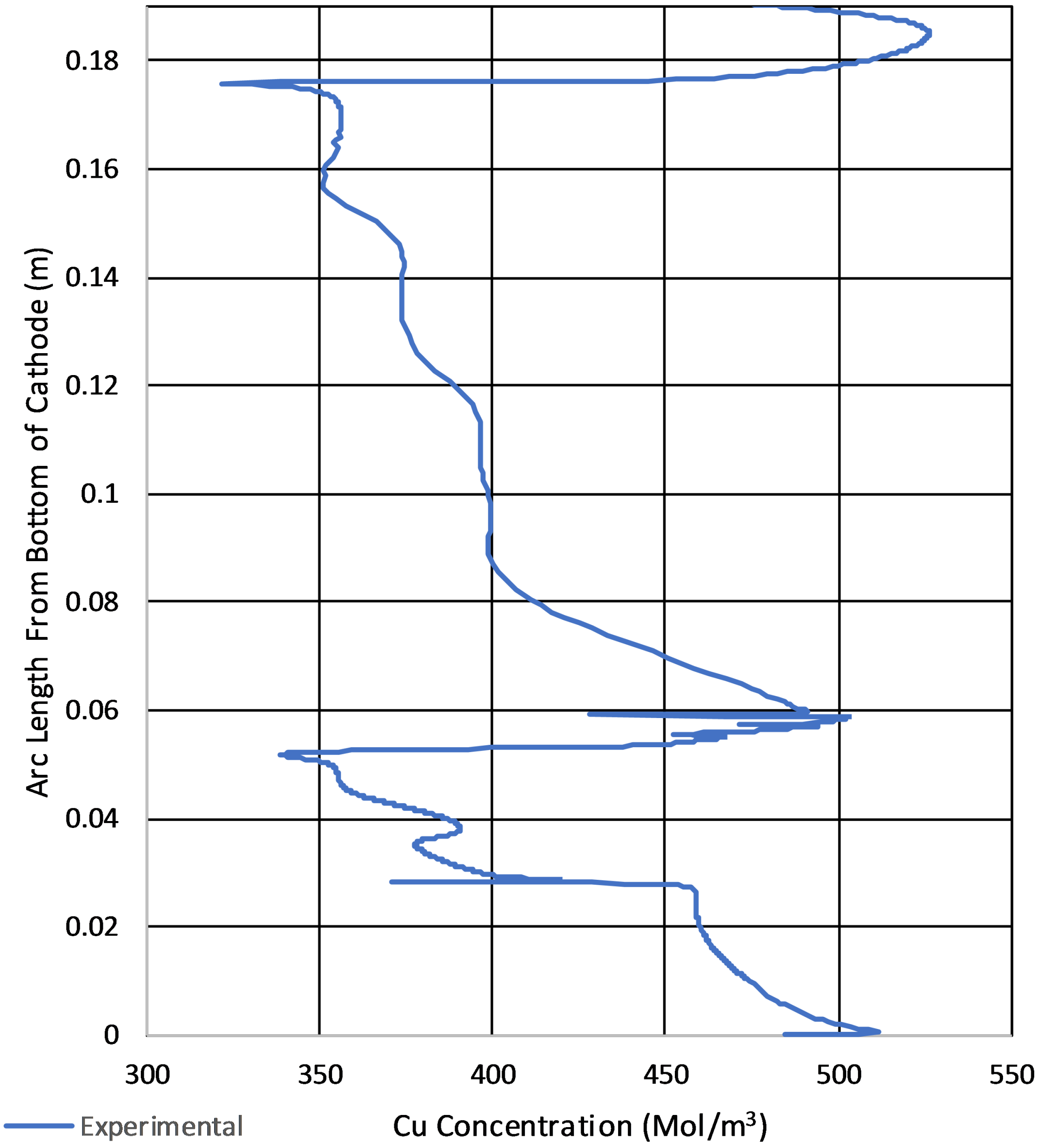

Figure 3.29: Model results of nodule cathode test copper concentration along the cathode. See Tables 3.5, 3.6 and 3.7 for model parameters.

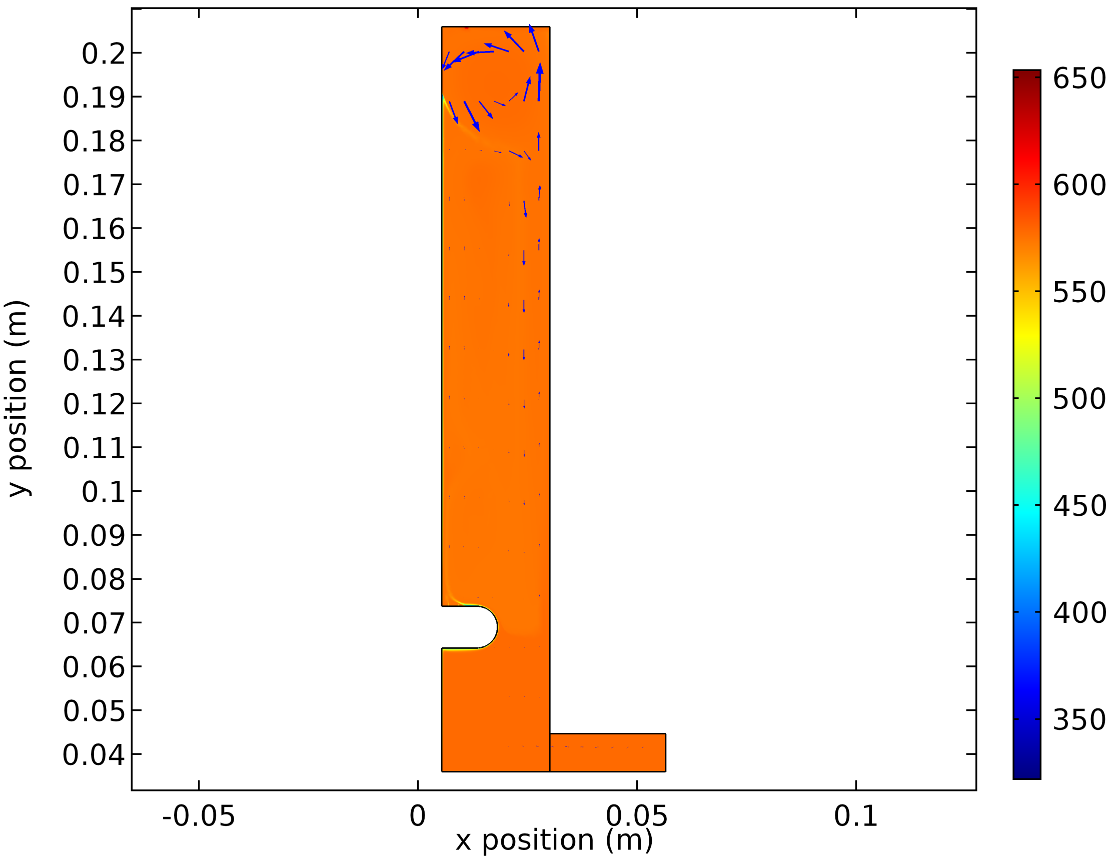

Figure 3.30: Model results of nodule cathode cell copper concentration (mol/m^3) with arrows as velocity vectors (90s). See Tables 3.5, 3.6 and 3.7 for model parameters.

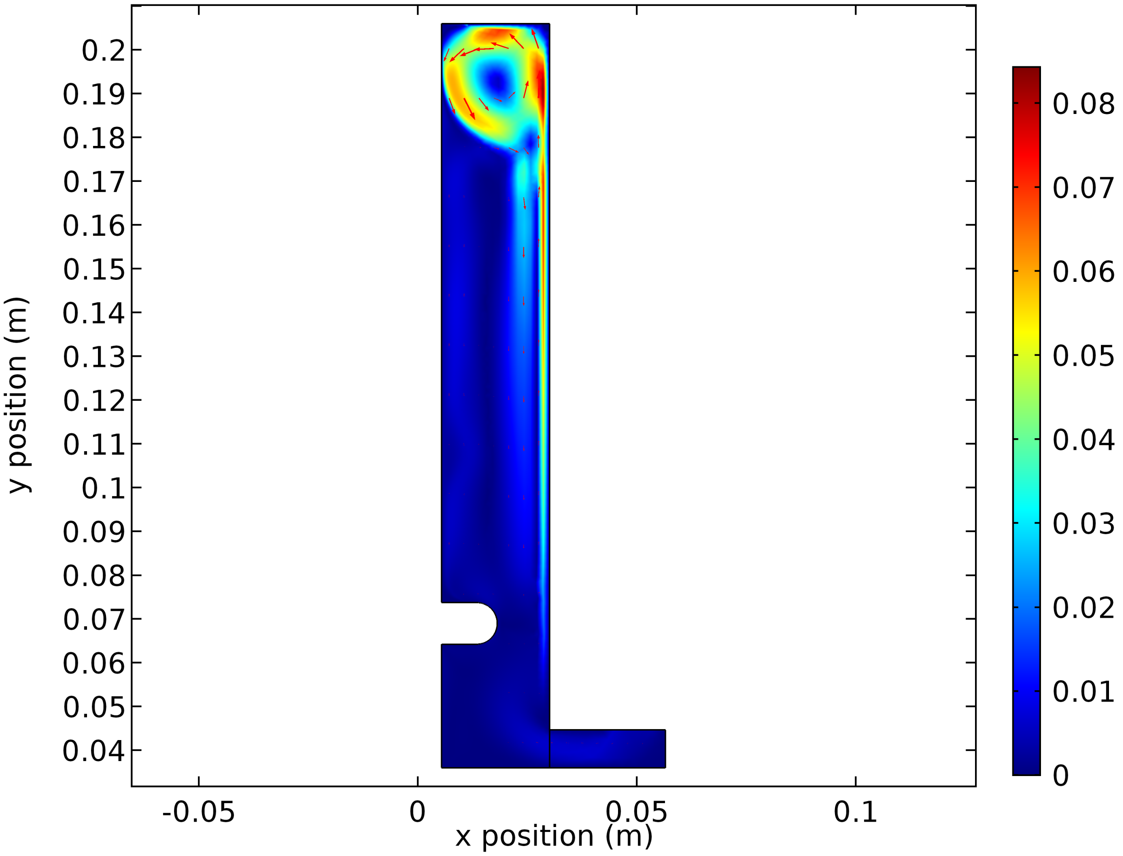

Figure 3.31: Model results of nodule cathode cell electrolyte velocity with arrows as velocity vectors (90s). See Tables 3.5, 3.6 and 3.7 for model parameters.

shown in Table 3.7.

Lastly, Figure 3.32 shows the local gas fraction in the cell. Of note is the lower gas fraction presented by this model. This can be explained by Table 3.7 with a lower current density being utilized.

3.4.5 Discussion of Flow Conditions

Figure 3.33 shows the results of completed experiments. The formation of a ridge near the top of the cathode is common among them.

To our knowledge this ridge has not previously been noted extensively or discussed in detail. Larger industrial cells do not have this ridge. Results shown in Figures 3.20, 3.25 and 3.31 show the fluid circulation vortex at the top of the cell. This affects the cathodic copper concentration shown in Figures 3.17, 3.29 and 3.23. Further, because of the decrease of copper along the cathode, the electrolyte becomes less dense and rises buoyantly. This

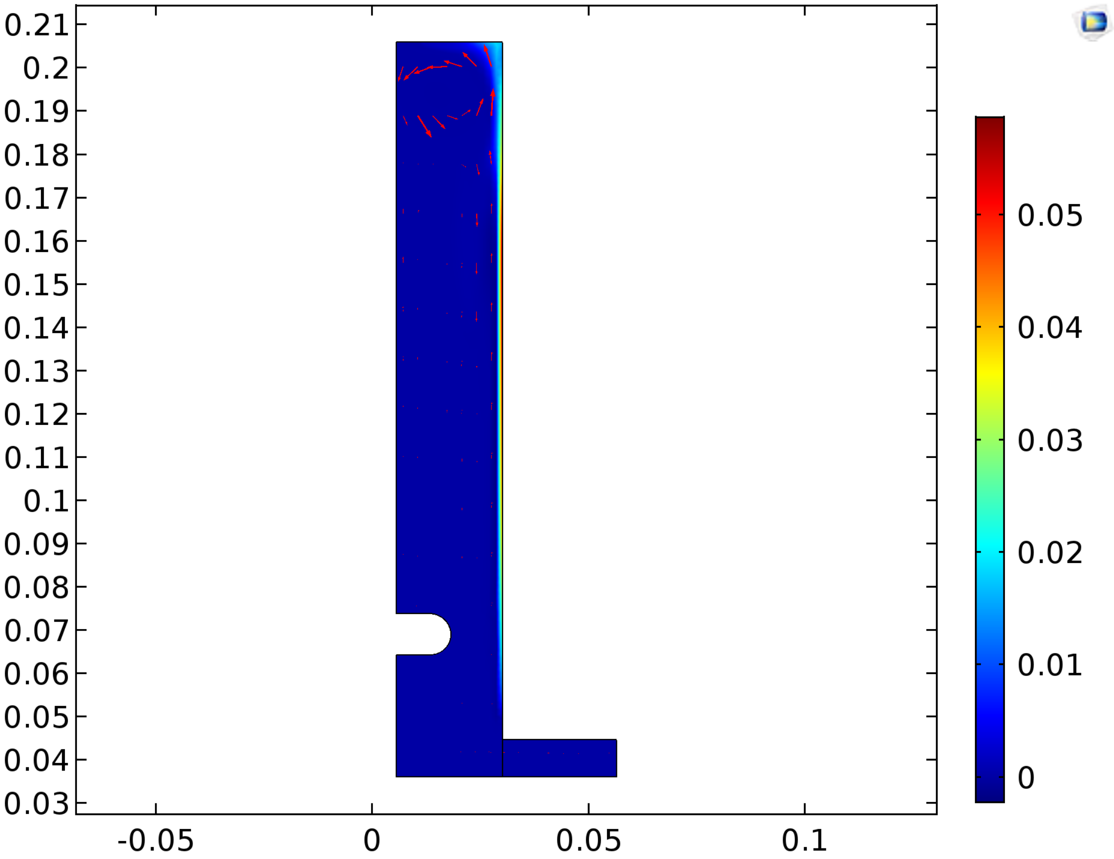

Figure 3.32: Model results of nodule cathode cell gas fraction with arrows as velocity vectors (90s). See Tables 3.5, 3.6 and 3.7 for model parameters.

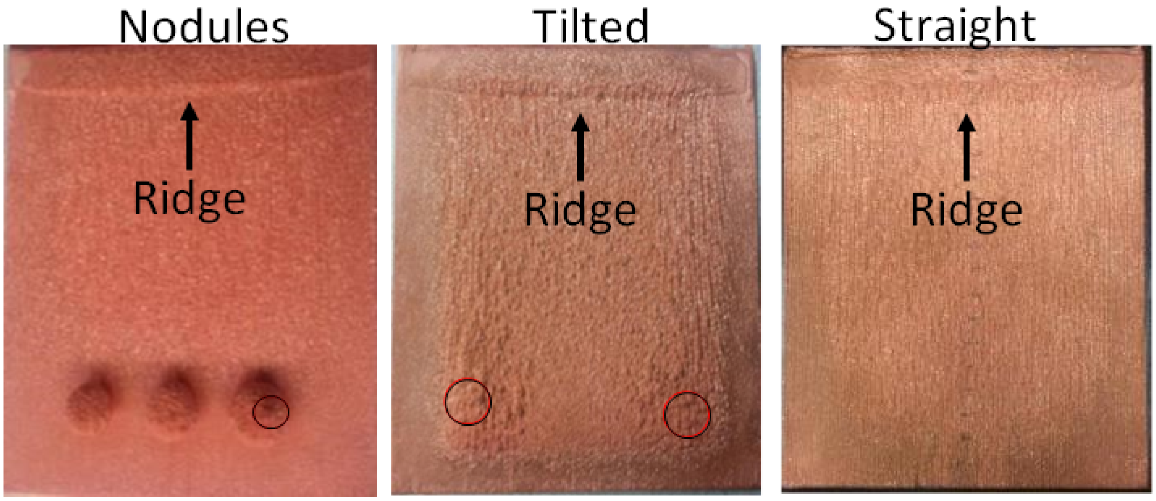

Figure 3.33: Experimental results showing a "Ridge" near the top of the cathode with circles indicating anodic contact.

upward flow of lower concentration electrolyte meets the vortex at the top. This is seen in the lower concentration "ribbon" shown at the top of the cell. The increased mass transport at the cathode top is due to flow. This further increases the local current density as shown in Figures 3.19, 3.24 and 3.30. These conditions create the ridge in the deposit near the top. This effect is shown in the cell velocity plots in Figures 3.20, 3.25 and 3.31. The selected height of the cell was serendipitous. Shorter cells would reduce the vortex and taller cells have multiple unstable and random voracities that eliminate the ridge. Thus, in our study the model and measured validation of the ridge formation provide confidence in the accuracy of the model.

In this model the calculated Reynolds number is above 10,000. This was shown in the model convergence in that the fluid flow is predominantly laminar with a slight wobble. This flow regime is problematic in terms of computing. As such the model was run to 60s which allowed for fully developed flow. The following 30 (60-90s) seconds were used to determine the average current density provided.

3.4.6 Concerns and Potential issues

In reviewing this work there are a number of potential issues that should be addressed.

The first utilizes three species for electrochemical modeling. Cu-Acid systems are known to have multiple species which are not represented. As the Nernst–Planck equations are solved these will have an effect on the system such as changing the resistivity, cell potential and limiting current density due to supporting electrolyte. It is intended that this will be investigated in future work with this paper serving as a preliminary investigation.

The second is with regard to the position of the inlet. Due to the 2D simplified geometry there is not sufficient mixing in the cell to draw electrolyte from the bottom of tank. So, by necessity electrolyte must flow between the electrodes. To address the short run times utilized in the model on bulk concentration, the steady-state cell copper concentration was determined and utilized. Due to the small inlet velocity, the modeled fluid velocity between the electrodes is not expected to be affected significantly.

The third point is that the model utilizes a 2D representation of 3D flow effects. Observed flow conditions show that the bubbles induce a flow that moves the electrolyte at the top of the cell both down and out to the sides. This increases the mixing and may be the reason for the vertical difference of the ridge on the top of the cell when compared to experimental data. This is also compounded by the use of an average current density rather than the total cell current. These two issues would be better understood by a 3D model which may be pursued in subsequent work.

In conjunction with the third point, the fourth point is the lack of determination of the effects of the fluid structure interactions on the deposit shape. Ideally the model would be recomputed to allow for topological influences on the fluid flow. This will be examined further. Lastly, there are some errors due to scanning resolution and needed mesh preparation for deposit measurements.

3.5 Summary

Overall the experimental results of the straight and tilted cathodes align well with the 3 species model presented. The nodule cathode experiment appeared to under predict the current density on the cathode. Euler–Eluer flow with the appropriate Nernst–Planck coupling for transport modeling appears to be well suited for this application. It is interesting the alignment is in general agreement with a substantial deposit thickness. However, additional work is needed to further investigate the effects of fluid structure interactions, speciation and current efficiency.

CHAPTER 4

REFINEMENT OF MODEL BY CONSIDERING SPECIATED ($CUSO_4$ - H_2SO_4) ELECTROLYTE

4.1 Introduction

As discussed in Chapter 1 a model was developed consisting of Cu^{2+}, H^+ and SO_4^{2-}. In view of the literature it is apparent that this simplistic representation does not adequately describe the equilibrium concentration of the bulk electrolyte. As such, this chapter will seek to refine the model by providing an equilibrium speciation framework. In addition, current efficiency will be included.

4.1.1 Current Efficiency and Current Density

Current efficiency in electrowinning is of paramount interest due to the impact it has on the copper production costs. It is defined as a ratio of total versus parasitic current (reactions that are unwanted) [2]:

$$\beta = \frac{i_{\text{total}} - i_{\text{parasitic}}}{i_{\text{total}}} \tag{4.1}$$

Or as a current to deposited mass equation (1.2)[2].

If current lost due to mechanical or deposit short circuiting is omitted in copper electrowinning the primary factor influencing current efficiency is iron concentration. Moats and Khouraibchia [52] present a study examining the effects of Fe^{3+} as well as common impurities of chloride, manganese and cobalt on current efficiency. They found that Fe was the most significant factor. The other contaminates did not show appreciable impact on current efficiency. Copper, sulfate and acid concentration all had effects due to interactions with mass transport properties. These findings are important to allow all other species to be excluded and retain confidence in the accuracy of the results.

4.1.2 Speciation of Copper-Iron-Sulfuric Acid Electrolyte System

Copper electrowinning systems are by nature complex. This complexity comes from the nature of the equilibrium chemical reactions possible in the electrolyte. To begin this study let us consider copper sulfate. This salt speciates according to the following reactions (4.2), (4.3):

$$\mathrm{CuSO}_{4(aq)} \leftrightarrow \mathrm{Cu}^{2+} + \mathrm{SO}_4^{2-} \tag{4.2}$$

$$\mathrm{CuHSO}^{+}_{4\mathrm{(aq)}} \leftrightarrow \mathrm{H}^{+} + \mathrm{CuSO}_{4(aq)} \tag{4.3}$$

Further, similar reactions exist for sulfuric acid according the following (4.4), (4.5):

$$\mathrm{H_2SO_4} \leftrightarrow \mathrm{H}^{+} + \mathrm{HSO}_4^{-} \tag{4.4}$$

$$\mathrm{HSO}_4^{-} \leftrightarrow \mathrm{H}^{+} + \mathrm{SO}_4^{2-} \tag{4.5}$$

The literature contains several works relating to this system both from a speciaition and modeling perspective.

The literature search outlined in section 2.3.3 provides background into works elucidating speciation. Specifically, these are: [19], [20], [58], [59].

4.1.3 Effects of Speciation

The effects of speciation in the copper-iron-acid system are not insignificant. The subtle interplay between these species in electrochemical systems is best described by the Nernst-Plank Equation [21].

$$N_i = -z_i u_i F c_i \nabla \Phi_l - D_i \nabla c_i + c_i v \tag{4.6}$$

where N_i, z_i, u_i, c_i, D_i are the flux density, charge, mobility, concentration, and diffusivity of species i, F is Faraday's constant, $\nabla \Phi_l$ is an electric field, ∇c_i is a concentration gradient, and v is the velocity vector.

Because of the relationships that this equation represents the nondepositing species can have a significant impact on the depositing species. One such interaction is the lowering of the limiting current density with the addition of a supporting electrolyte. Thus electrical current may be carried in the electrolyte by other species based on the following equations where i is the current density in the electrolyte (with the electroneutrality assumption), and the other variables are defined previously:

$$i_{electrolyte} = -F^2 \nabla \Phi_l \sum z_i^2 u_i c_i - F \sum z_i D_i \nabla c_i \tag{4.7}$$

The interplay between the various species and the reacting ones is subtle and complex. Newman [21] devotes an entire chapter (19) to the discussion of the effect of migration on limiting current densities. Of note is that while the supporting electrolyte increases the conductivity of the solution, the available reactant species at the cathode may decrease due to enhanced migration of nonreacting species, thus lowering the limiting current density. This is thoroughly discussed with copper sulfate-sulfuric acid systems in reference [21]. With the addition of a supporting electrolyte Newman conclusively shows that the migration effect is greatly diminished. Conversely, this work also shows that due to the abundance of sulfuric acid, the dissociation and concentration of bisulfate is significant and must be considered.

The question is then raised, what is the impact of the copper speciation on electrowinning current density and efficiency?

4.1.4 Modeling Speciated Electrowinning Systems

The pertinent models developed in the literature were provided previously. Suffice it to mention that Cifuentes et al. [19] and Volgin et al. [20] are of particular interest and were covered in section 2.1.

The results of this work show the similarity between full dissociation and equilibrium speciation. This is in agreement with what Newman has presented [21], that is that at high concentrations of supporting electrolyte full dissociation or speciation becomes less important and that the effect of speciation on the limiting current due to migration decreases with increasing supporting electrolyte.

4.1.5 Model Objectives

In light of the information presented previously this work seeks to determine local and average current efficiency utilizing a Euler–Euler bubbly flow CFD (computational fluid dynamic) model coupled with Nernst–Plank transport equations with speciated sulfuric acid. Copper species will be treated as a single component due to use of an “effective” diffusion and lack of impact due to migration with an abundance of supporting electrolyte. Iron will not be included as a component in the electrolyte, but is included in the current efficiency equation. COMSOL Multiphysics 5.2 will be used to model this system.

4.2 Methods

4.2.1 Experimental Conditions

4.2.1.1 Geometry

The layout of the test cell was discussed previously in section 3.2.1, Figures 3.1, 3.2, 3.3.

4.2.1.2 Current Density Determination From Deposition

As mentioned previously several test cell geometries were used to provide a range of deposits for model validation. See section 3.3.1.1 Figure 3.9.

4.2.1.3 Experimental Setup

As shown previously in Figures 3.1, 3.2, 3.3, the electrodes incorporated shielding and were arranged to represent the configuration shown in Figure 3.9 to evaluate the effects of straight cathodes, tilted cathodes and nodules on local current efficiency. The experimental setup was covered previously in section 3.3.1.2.

4.2.2 Determination of Ferric/Ferrous Ratio

The determination of Fe^{3+} / Fe^{2+} is not trivial. There are several species available for iron complexation. Also, Fe^{3+} in the system can act as an oxidizer. It is important to mention that most Fe^{3+} is complexed as $FeSO_4^+$. Under the condition of constant iron (neglecting migration effects due to the abundance of supporting electrolyte) Fick's first law of diffusion will govern the species flux the electrode according to equation (4.8), [2].

$$\frac{dN_i}{dt} = -D_i A \left(\frac{C_{\text{bulk}} - C_{\text{electrode}}}{\delta} \right) \tag{4.8}$$

where N_i is the species flux of i species, t is time D_i is the diffusion coefficient of i species, A is the area of diffusion, C is the concentration of species i and δ is the diffusion boundary layer thickness. This equation assumes a linear concentration profile.

Assuming that the boundary layers and areas of the electrodes are the same and that at steady-state the rate of ferric generation will equal the rate of ferrous generation the equations of flux may be set equal to each other. Considering that these reactions occur at their limiting current density allows further simplification to $C_{electrode} = 0$. An additional equation (4.9) provides the concentration relationship.

$$C_{\text{Fe Total}} = C_{\text{bulk,Fe}^{3+}} + C_{\text{bulk,Fe}^{2+}} \tag{4.9}$$

Solving equations (4.8) and (4.9) yields:

$$C_{\text{bulk,Fe}^{3+}} = \frac{D_{\text{Fe}^{2+}} * C_{\text{Fe Total}}}{D_{\text{Fe}^{3+}} + D_{\text{Fe}^{2+}}} \tag{4.10}$$

where $C_{\text{Fe Total}}$ is the total iron concentration, $C_{\text{bulk,Fe}^{3+}}$ is the bulk Fe^{3+} concentration, $C_{\text{bulk,Fe}^{2+}}$ is the bulk Fe^{2+} concentration.

This relationship although useful is not often indicative of reality. To address this the second derivation assumes mass balance where not only the reaction rate is considered, but the effects of the inlet and outlet. The following derivation assumes that:

- The cell is well stirred.
- The current density is constant.
- The current efficiency is constant.
- Fe^{3+} and Fe^{2+} have the same boundary layer thickness.
- The reactions occur at limiting current density so the electrode surface concentration is zero.

To begin the steady-state mass balance of Fe^{2+} equates to:

$$\left.\frac{dN_{\text{Fe}^{2+}}}{dt}\right|_{\text{cathode}} + C_{\text{in,Fe}^{2+}}\dot{V} - C_{\text{bulk,Fe}^{2+}}\dot{V} - \left.\frac{dN_{\text{Fe}^{2+}}}{dt}\right|_{\text{anode}} = 0 \tag{4.11}$$

The steady-state mass balance of Fe^{3+} equates to:

$$\left.\frac{dN_{\text{Fe}^{3+}}}{dt}\right|_{\text{anode}} + C_{\text{in,Fe}^{3+}}\dot{V} - C_{\text{bulk,Fe}^{3+}}\dot{V} - \left.\frac{dN_{\text{Fe}^{3+}}}{dt}\right|_{\text{cathode}} = 0 \tag{4.12}$$

Further at the electrodes:

$$\left.\frac{dN_{\text{Fe}^{3+}}}{dt}\right|_{\text{anode}} = \left.\frac{dN_{\text{Fe}^{2+}}}{dt}\right|_{\text{anode}} \tag{4.13}$$

and

$$\left.\frac{dN_{\text{Fe}^{2+}}}{dt}\right|_{\text{cathode}} = \left.\frac{dN_{\text{Fe}^{3+}}}{dt}\right|_{\text{cathode}} \tag{4.14}$$

Substitution is also available with the following expression:

$$\frac{dN_i}{dt} = D_i \frac{A_i C_{i,\text{bulk}}}{\delta_i} \tag{4.15}$$

And defining intermediate variable of:

$$\alpha = D_{\text{Fe}^{3+}} \frac{A_c}{\delta_c} \tag{4.16}$$

$$\beta = D_{\text{Fe}^{2+}} \frac{A_a}{\delta_a} \tag{4.17}$$

Combining equations (4.16) and (4.17) with (4.11) and (4.12) produces:

$$C_{\text{bulk,Fe}^{2+}} = \frac{2C_{\text{in,Fe}^{3+}} + 2C_{\text{in,Fe}^{2+}} + \dot{V} C_{\text{in,Fe}^{2+}}}{\alpha + \beta + \dot{V}} \tag{4.18}$$

$$\begin{aligned} C_{\text{bulk,Fe}^{3+}} = & \frac{(\beta + \dot{V}) C_{\text{in,Fe}^{3+}}}{\alpha + \beta + \dot{V}} + \frac{(\beta + \dot{V}) C_{\text{in,Fe}^{2+}}}{\alpha + \beta + \dot{V}} + \\ & \frac{\dot{V}(\beta + \dot{V}) C_{\text{in,Fe}^{2+}}}{\alpha(\alpha + \beta + \dot{V})} - \frac{\dot{V} C_{\text{in,Fe}^{2+}}}{\alpha} \end{aligned} \tag{4.19}$$

where $N_{\text{Fe}^{2+}}$ is the molar flux of Fe^{2+}, $N_{\text{Fe}^{3+}}$ is the molar flux of Fe^{3+}, $\dot{V}$ is the volumetric flow rate, $C_{\text{in,Fe}^{3+}}$ is inlet concentration of Fe^{3+}, $C_{\text{in,Fe}^{2+}}$ is inlet concentration of Fe^{2+}, N_i is the molar flux of ith species, A_i is area of appropriate electrode, δ_i is the boundary layer thickness of the ith species reacting athe the electrode, $C_{i,bulk}$ is concentration of ith species in bulk, $D_{\text{Fe}^{3+}}$ and $D_{\text{Fe}^{2+}}$ are diffusion coefficients of ferric and ferrous ions, respectively, A_c and A_a are the areas of the cathode and anode, respectively, δ_c and δ_a are the boundary layer thicknesses of the cathode and anode, respectively.

4.2.3 Determination of Copper Concentration at Steady State

It is not feasible, due to the fluid flow, to completely run the simulation continuously for the entire deposition duration. Correspondingly the following mass balance equation was derived to determine the average bulk concentration of copper ions:

$$\frac{dM_t}{dt} = \frac{-M_t}{\text{Vol}} \dot{V} - \frac{dM_{\text{electrode}}}{dt} + C_{\text{Cu}^{2+},\text{in}} \dot{V} \tag{4.20}$$

where M_t is the amount of Cu^{2+}, $\frac{dM_{\text{electrode}}}{dt}$ is the constant flux of Cu^{2+} and is constant determined from Faraday's law, $\dot{V}$ is volume flow rate, and Vol is the tank volume. Solving this differential equation yields:

$$M_t = Ce^{\left(-\frac{\dot{V}}{\text{Vol}} t\right)} - \left(\frac{\frac{dQ_{\text{electrode}}}{dt} + C_{\text{Cu}^{2+},\text{in}} \dot{V}}{\frac{\dot{V}}{\text{Vol}}} \right) \tag{4.21}$$

where C is a constant determined from the initial conditions and $\frac{dQ_{electrode}}{dt}$ is the electrode-posited flux of Cu^{2+}. Solving this equation with values from Tables 3.5 and 3.6 yields the results shown in Figure 4.1.

4.2.4 Activity and Specitation Calculation

Methods for the determination and utilization of activities were given previously in section 3.2.3.1.

4.2.5 Discussion of Approach Settings and Species Considered

The species considered are shown in Table 4.1. The ionic radius was back calculated from the Stokes–Einstein relation (4.22) with the viscosity of water at 25 °C.

$$D_i = \frac{kT}{6\pi r_i \mu} \tag{4.22}$$

where D_i is the diffusion coefficient of ith species, k is the Boltzmann's constant, T is the temperature in K, r_i is the ionic radius, μ is viscosity.

A critical question for multicomponent systems is what diffusion coefficients should be used? Shown in Table 4.1 are diffusion coefficients for species as found in reference

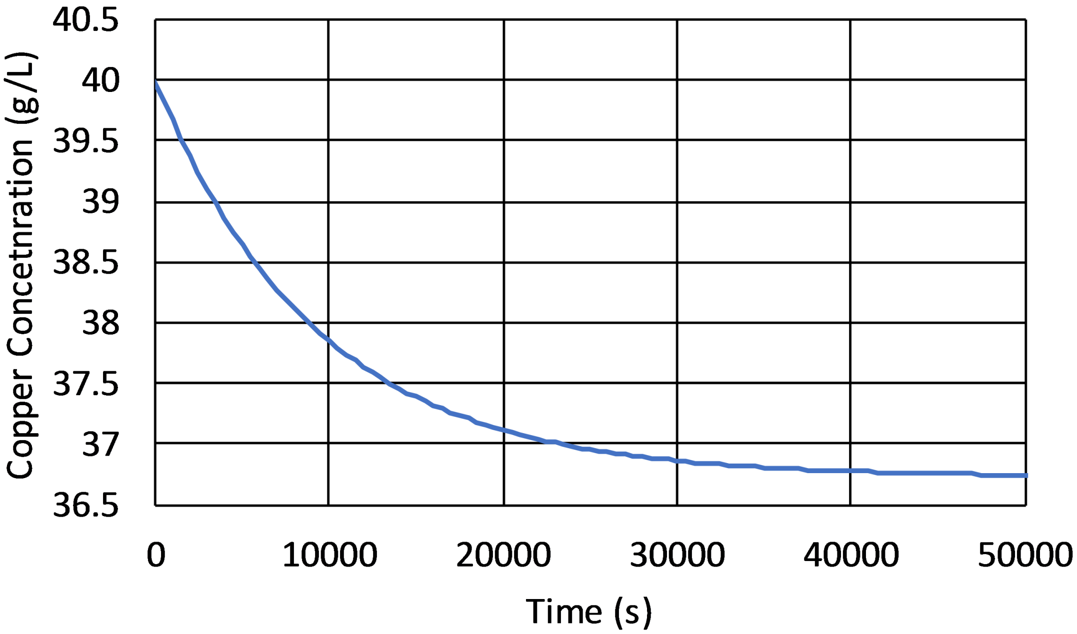

Figure 4.1: Bulk steady state copper concentration as a function of time.

Table 4.1: Species of consideration [21].

Elements	Dilute Diffusion Coefficient 25° C (m^2/s)	Ionic Radius (m)
Cu^{2+}	0.72 X10^{-9}	3.41 X10^{-10}
$HCuSO_4^+$	0.72 X10^{-9}	3.41 X10^{-10}
Fe^{2+}	0.72 X10^{-9}	3.41 X10^{-10}
$FeSO_4^+$	0.61 X10^{-9}	4.02 X10^{-10}
H^+	9.312 X10^{-9}	2.64 X10^{-11}
SO_4^{2-}	1.07 X10^{-9}	2.31 X10^{-10}
HSO_4^-	1.33 X10^{-9}	1.85 X10^{-10}

*Indicates special calculation of diffusion coefficient.

[21] for infinite dilution. Liberties have been taken in the case of $HCuSO_4^+$ and $FeSO_4^+$ to list a diffusion coefficient where none was specifically provided. This decision was based on the most common equilibrium species. Effective diffusion coefficients for both copper and iron were derived from data in studies by Moats et al. [52] and [54]. For simplicity the effective diffusion coefficient is considered for the target species (Cu^{2+}, $FeSO_4^+$). Other species ($HCuSO_4^+$, Fe^{2+}) diffusion coefficients are modified by the ratio of the main species to the other species diffusion coefficients at infinite dilution according to equation (4.23).

$$D_{\text{eff,other}} = \left(\frac{D_{\text{inf,other}}}{D_{\text{inf,target}}}\right) D_{eff,target} \tag{4.23}$$

where $D_{\text{eff,main}}$ is the effective diffusion coefficient of $HCuSO_4{}^+$ and $FeSO_4{}^+$ and $D_{\text{inf,Alt}}$ and $D_{\text{inf,main}}$ are the infinite diffusion of species listed in Table 4.1.

4.2.6 Effective Diffusion of Copper

The diffusion coefficient of copper utilized was discussed previously in section 3.2.3.2.

4.2.7 Effective Diffusion of Iron

Fe^{3+} was also determined from the data from Moats [52]. Statistical analysis was preformed to determine an expression for ferric ion diffusion. Each component was analyzed individually for its effects as shown in Figures 4.2-4.5.

From Figures 4.2-4.5 it can be seen that in the ranges presented the relationship of ferric concentration and ferric ion diffusion are linear. This allowed confidence in utilizing a

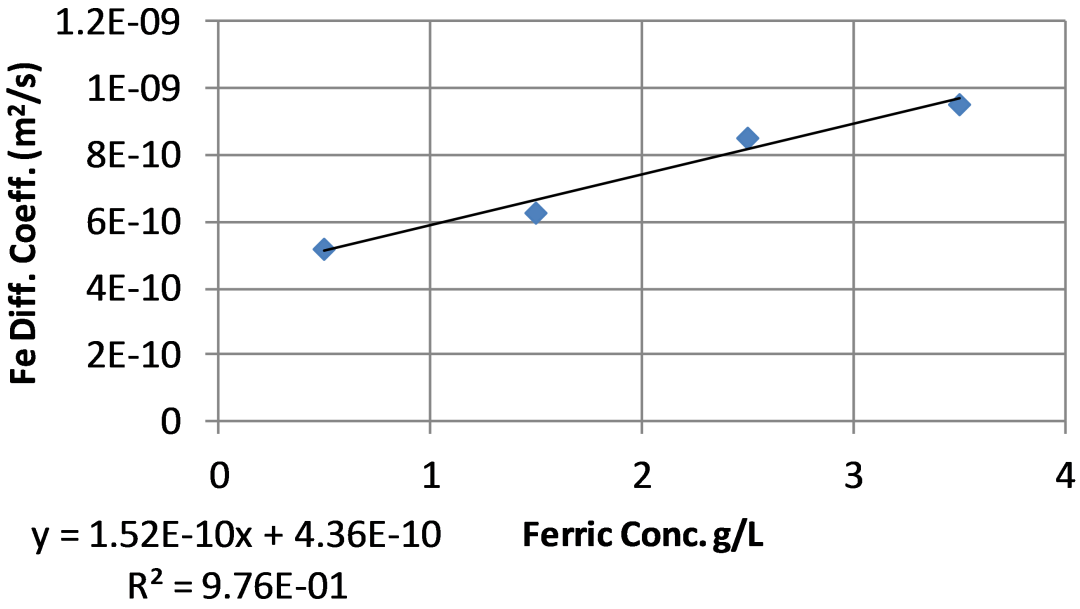

Figure 4.2: Ferric ion effect on diffusion coefficient. 40 g/l Cu^{2+}, 180 g/l H_2SO_4, 40 °C produced from data from reference [52].

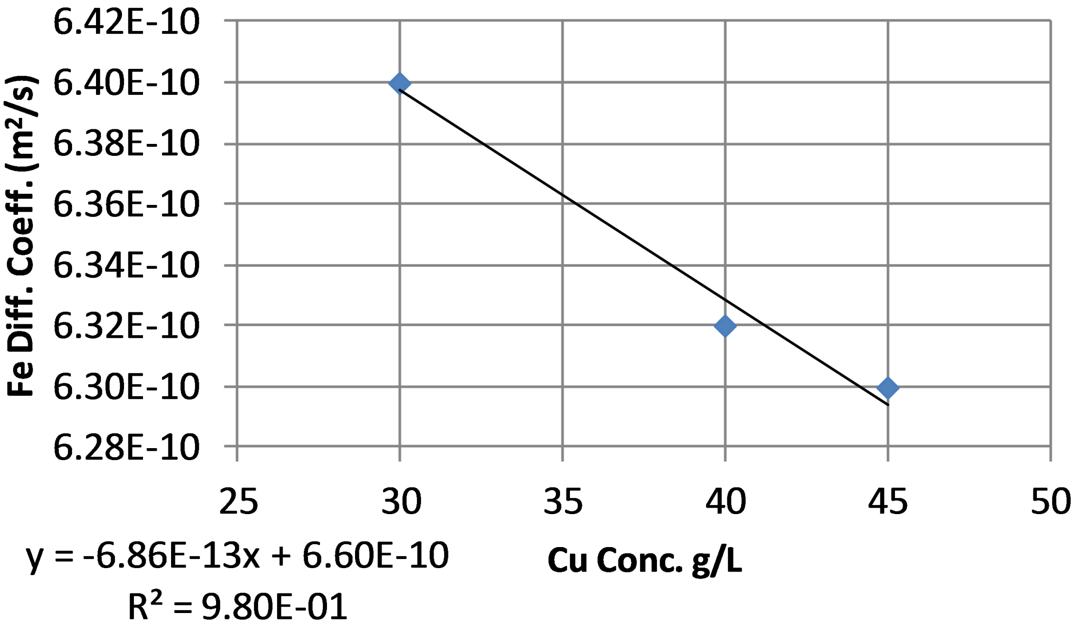

Figure 4.3: Copper concentration effect on diffusion coefficient. 1.5 g/l Fe^{3+}, 180 g/l H_2SO_4, 40 °C produced from data from reference [52].

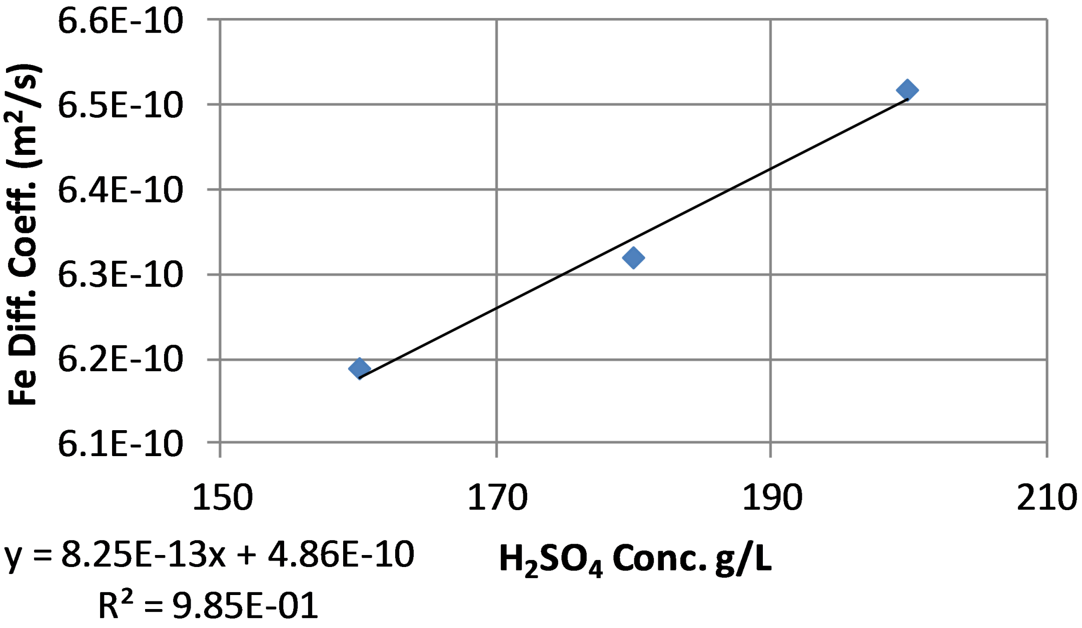

Figure 4.4: Sulfuric acid concentration effect on diffusion coefficient. 1.5 g/l Fe^{3+}, 40 g/l Cu^{2+}, 40 °C produced from data from reference [52].

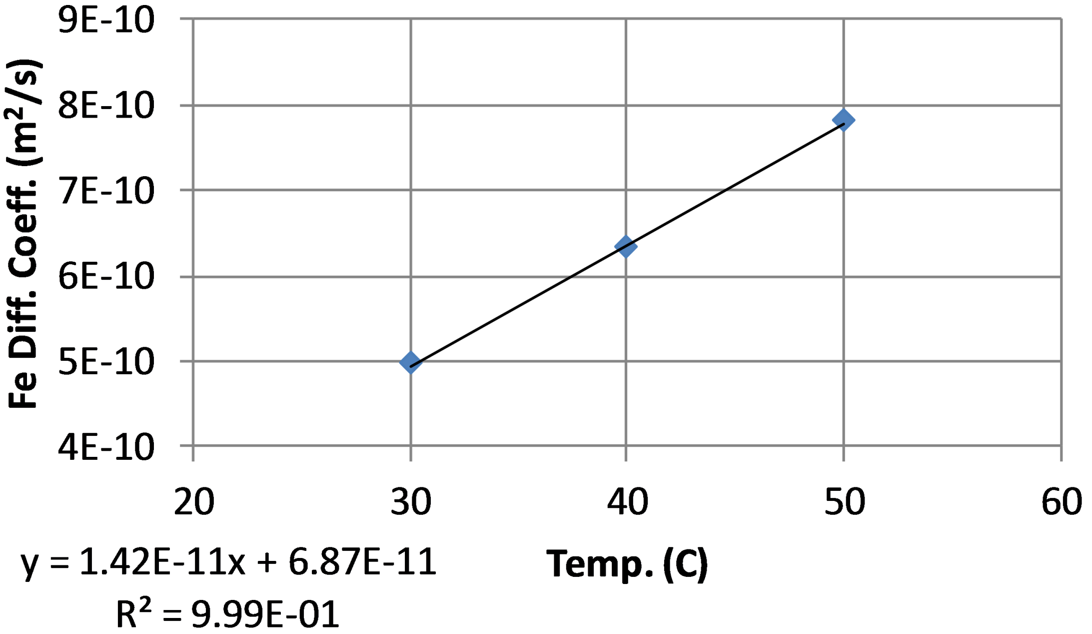

Figure 4.5: Temperature effect on diffusion coefficient. 1.5 g/l Fe^{3+}, 40 g/l Cu^{2+}, 180 g/l H_2SO_4 produced from data from reference [52].

linear regression. The results of the statistical analysis are shown in Table 4.2.

The results of the regression can be slightly misleading. In the initial analysis, each of the four areas considered shows a good linear fit of the data. However, the magnitudes of the effects varied widely. That is the reason for the contrasting P-values in each of the coefficients. Ferric ion concentration and temperature show the largest influence. Acid and copper concentrations show a negligible impact. Figure 4.6 shows the comparison plot of predicted versus experimental data. Equation (4.24) is provided for the effective diffusion coefficient of Fe^{3+}.

$$\begin{aligned} D_{\mathrm{Fe}^{3+}} = 10^{-10} * (-3.0114 + 1.5788(C_{\mathrm{Fe}^{3+}\ g/l}) - 1.4599 * 10^{-3}(C_{\mathrm{Cu\ g/l}}) \\ +8.250 * 10^{-3}(C_{\mathrm{H_2SO_4\ g/l}}) + 0.142(T°C)) \end{aligned} \tag{4.24}$$

This equation has the following range: $C_{\mathrm{Cu}^{2+}}$=30-45 (g/L), $C_{\mathrm{Cu}^{2+}}$=0-4 (g/L), $C_{i,\mathrm{H_2SO_4}}$=160-200 (g/L), T=30-65 °C.

4.2.8 Current Efficiency Determination

To reduce the computational expense of calculating iron species transport and reaction kinetics a comparative expression of the diffusion of ferric to copper ions was developed. The work of Ettel et al. [6] provides an interesting starting point for the discussion of determining current efficiency without direct calculation of Fe^{3+} transport and consumption with Butler-Volmer kinetics. Ettel's work focused on determining the mass transfer coefficient of copper in an electrowinning cell. The premise of the experiment was to add Ag^+ which would deposit at its limiting current density. Thus by assaying the deposit for silver in the copper, the mass transfer coefficient could be determined. Ettel provided equation (4.25) for the relationship of limiting current density to concentration.

Table 4.2: Regression results for ferric diffusion coefficient as shown in Figure 4.6.

Parameter	Coefficient	P-value
Intercept	-3.011	0.2607
Ferric ions (g/L)	1.579	6.18E-05
Copper (g/L)	-1.46E-03	0.9595
H2SO4 (g/L)	8.25E-03	0.4752
Temperature °C	0.142	1.17E-03

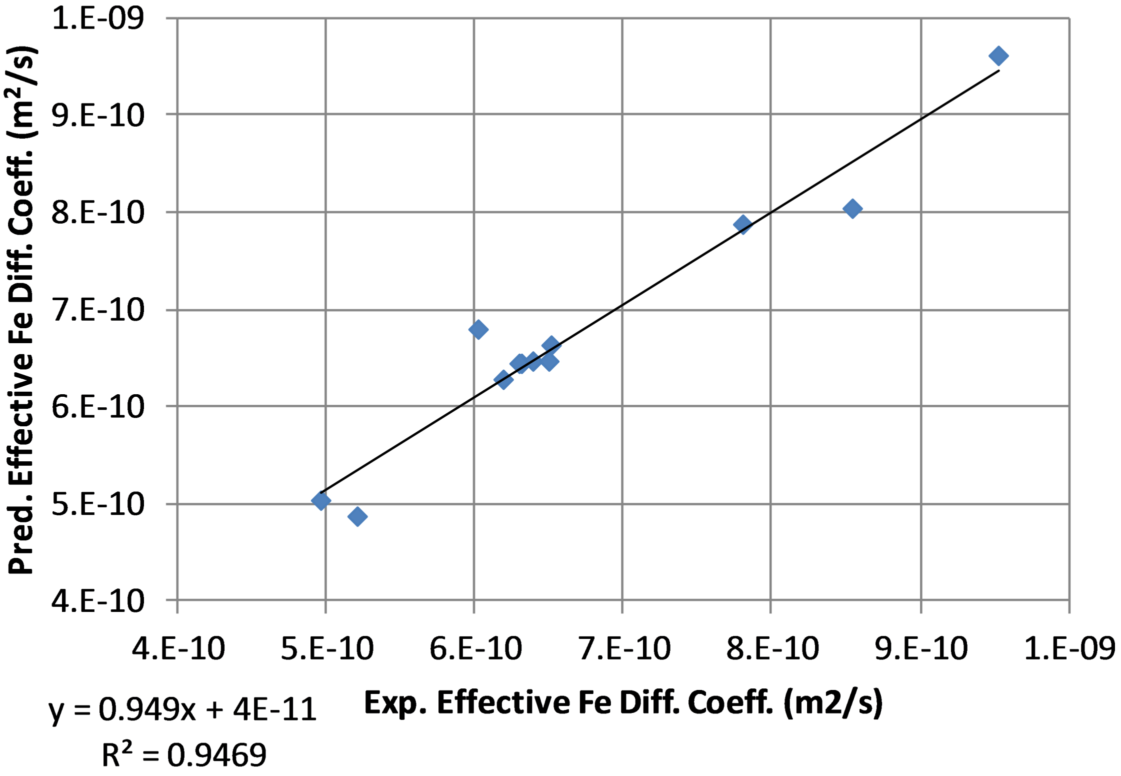

Figure 4.6: A comparison of experimental and predicted diffusion coefficient from data in reference [52].

$$i_{L,\mathrm{Ag}^+} = \frac{FC_{\mathrm{Ag}^+}}{k_{\mathrm{Ag}^+}} \tag{4.25}$$

Further Ettel provides a relationship between the mass transfer of copper to silver in naturally convected systems given in (4.26)

$$k_{\mathrm{Cu}^{2+}} = k_{\mathrm{Ag}^+} \left(\frac{D_{\mathrm{Cu}^{2+}}}{D_{\mathrm{Ag}^+}} \right)^{\frac{3}{4}} \tag{4.26}$$

Developing on the idea presented by Moats [52] of the Fe^{3+} ion being transported at its limiting current the following derivation is presented.

$$k_{\mathrm{Cu}^{2+}} = k_{\mathrm{Fe}^{3+}} \left(\frac{k_{\mathrm{Cu}^{2+}}}{D_{\mathrm{Fe}^{3+}}} \right)^{\frac{3}{4}} \tag{4.27}$$

Combining equations (4.25) and (4.27) for iron and substituting the definition of mass transfer coefficient yields the limiting current density.

$$I_{\mathrm{lim,Fe}^{3+}} = FC_{\mathrm{bulk,Fe}^{3+}} \left(\frac{N_{\mathrm{Cu}^{2+}}}{C_{\mathrm{bulk,Cu}^{2+}} - C_{\mathrm{electrode,Cu}^{2+}}} \right) \left(\frac{D_{\mathrm{Fe}^{3+}}}{D_{Cu^{2+}}} \right)^{\frac{3}{4}} \tag{4.28}$$

Further rearranging equation (4.1) and combining with (4.28) yields:

$$C.E. = 1 - \left(\frac{FC_{\text{bulk,Fe}^{3+}} \left(\frac{N_{\text{Cu}^{2+}}}{C_{\text{bulk,Cu}^{2+}} - C_{\text{electrode,Cu}^{2+}}} \right) \left(\frac{D_{\text{Fe}^{3+}}}{D_{\text{Cu}^{2+}}} \right)^{\frac{3}{4}}}{i_{\text{total}}} \right) \tag{4.29}$$

Thus current efficiency may be calculated without direct calculation of iron species in the electrochemical model. Elimination of Fe^{3+} species calculations and additional Butler-Volmer calculations for Fe^{3+} greatly reduces computational costs.

4.2.9 Echem and Fluid Models

The modeling aspects have been covered extensively in sections 3.2.2, 3.2.4, 3.2.5 for physical parameters and modeling methodologies for electrochemical and fluid dynamics except where expressly discussed in this chapter.

4.3 Results and Discussion

4.3.1 Speciation

As stated in section 4.1.2 the components of the acid-copper system dissociate via reactions presented in Table 4.3. These reactions were solved via a system of equations by minimizing the sum of squares error between equations (4.30) and (4.31) [2].

$$K = e^{\left(\frac{-\Delta G_r^\circ}{RT}\right)} \tag{4.30}$$

$$K = \frac{\prod_p \gamma_p^{\nu_j} m_p^{\nu_j}}{\prod_r \gamma_r^{\nu_a} m_r^{\nu_a}} \tag{4.31}$$

Activity calculations were performed as described in section 3.2.3.1.

Table 4.3: Speciation reactions.

Speciation Reaction	ΔG_r° j/mol
$\text{Cu}^{2+} + \text{SO}_4^{2-} \leftrightarrow \text{CuSO}^{\dagger}_{4(aq)}$	-13,070
$\text{H}^{+} + \text{CuSO}^{\dagger}_{4(\text{aq})} \leftrightarrow \text{CuHSO}^{+\ddagger}_{4(\text{aq})}$	-13,356
$\text{H}^{+} + \text{HSO}_4^{-} \leftrightarrow \text{H}_2\text{SO}_4$	11,380
$\text{H}^{+} + \text{SO}_4^{2-} \leftrightarrow \text{HSO}_4^{-}$	-11,280

Unless noted species energies are from reference [2]

†[104]

‡[105]

The results of these calculations are presented in Figures 4.7-4.9. As seen from Figure 4.9, $CuHSO^+_{4(aq)}$ is the dominant copper species. This result guided the selection of the $CuHSO^+_{4(aq)}$ as the electro-active species for copper deposition. Although all the major species of sulfuric acid are represented in the model, more than half of the sulfate exists as bisulfate. Ranges provided were selected as representative of typical industrial conditions and they are provided for comparative purposes.

4.3.2 Ferric/Ferrous Ratio

Figure 4.10 shows the ferric to ferrous ratio was calculated as described in section 4.2.2 and according to data in Tables 3.5, 3.6 and 4.4. The bulk concentration is strongly influenced by the inlet concentration.

Due to the nature of the experiments, there is some ambiguity in relation to the exact concentration of ferric concentration at the inlet. This is due to the copper leaching per-

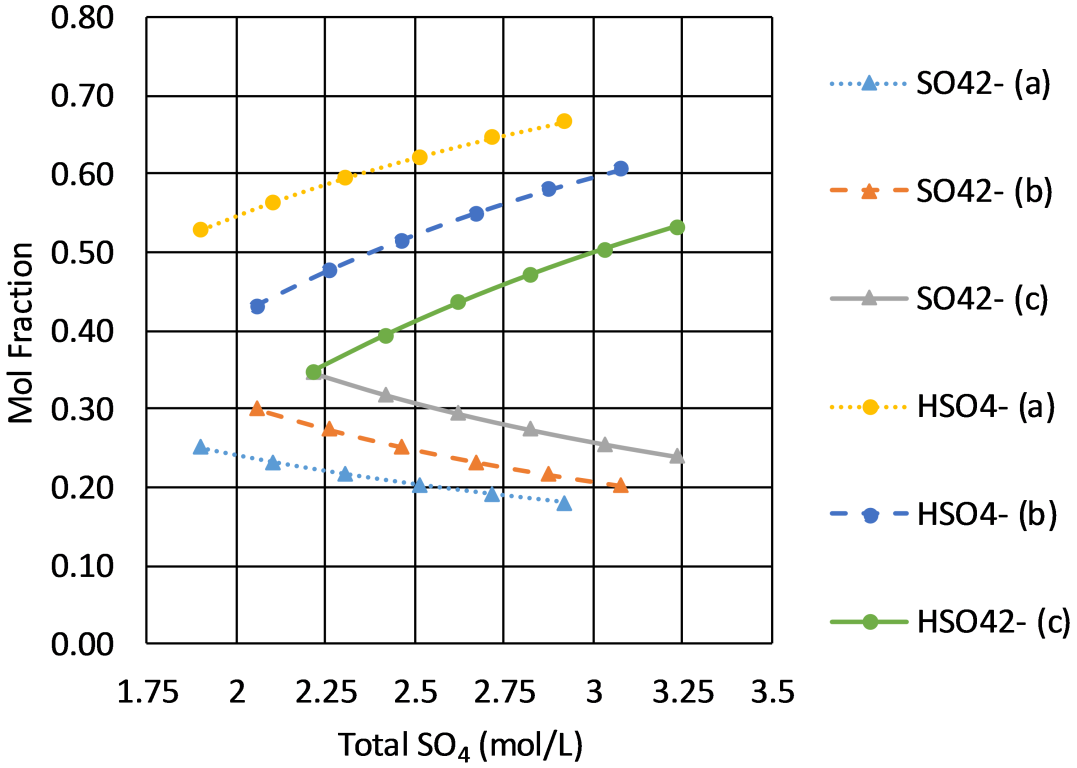

Figure 4.7: Sulfate mol fraction as a function of total sulfate, (a) 0.472 (mol/L) - 30 (g/L) Cu^{2+}, (b) 0.629 (mol/L) - 40 (g/L) Cu^{2+}, (c) 0.787 (mol/L) - 50 (g/L) Cu^{2+}. Note that mol fraction is cumulative with Figure 4.8.

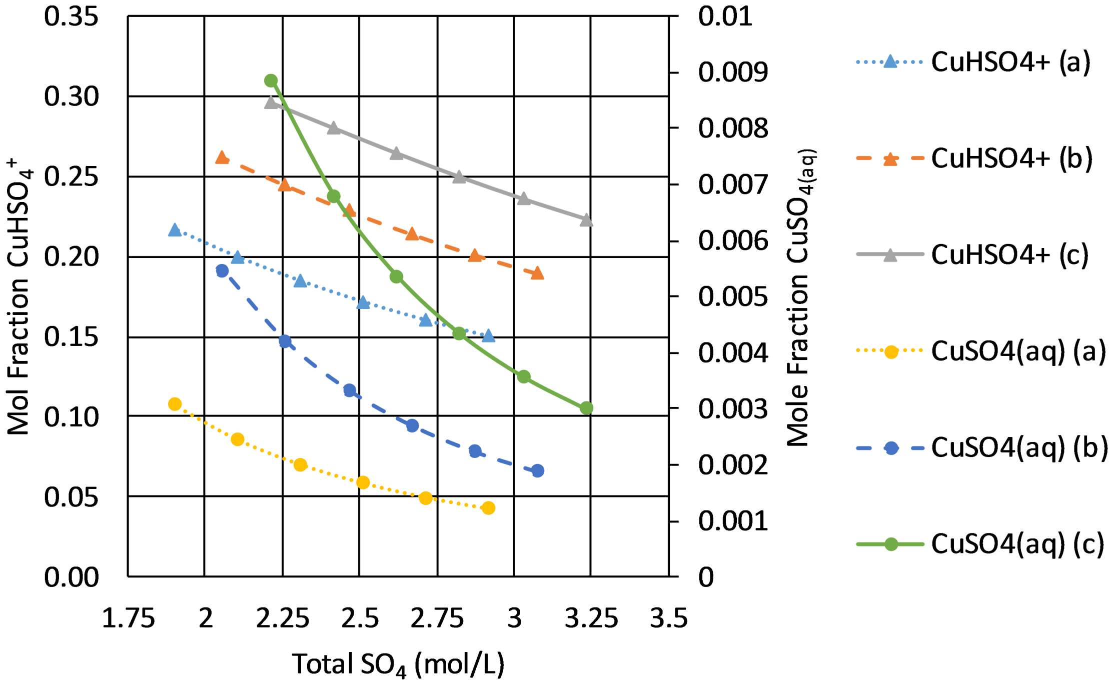

Figure 4.8: Copper species mol fraction of $CuHSO_4^+$ as a function of total sulfate, secondary axis is $CuSO_{4(aq)}$ (a) 0.472 (mol/L) - 30 (g/L) Cu^{2+}, (b) 0.629 (mol/L) - 40 (g/L) Cu^{2+}, (c) 0.787 (mol/L) - 50 (g/L) Cu^{2+}. Note that mol fraction is cumulative with Figure 4.7.

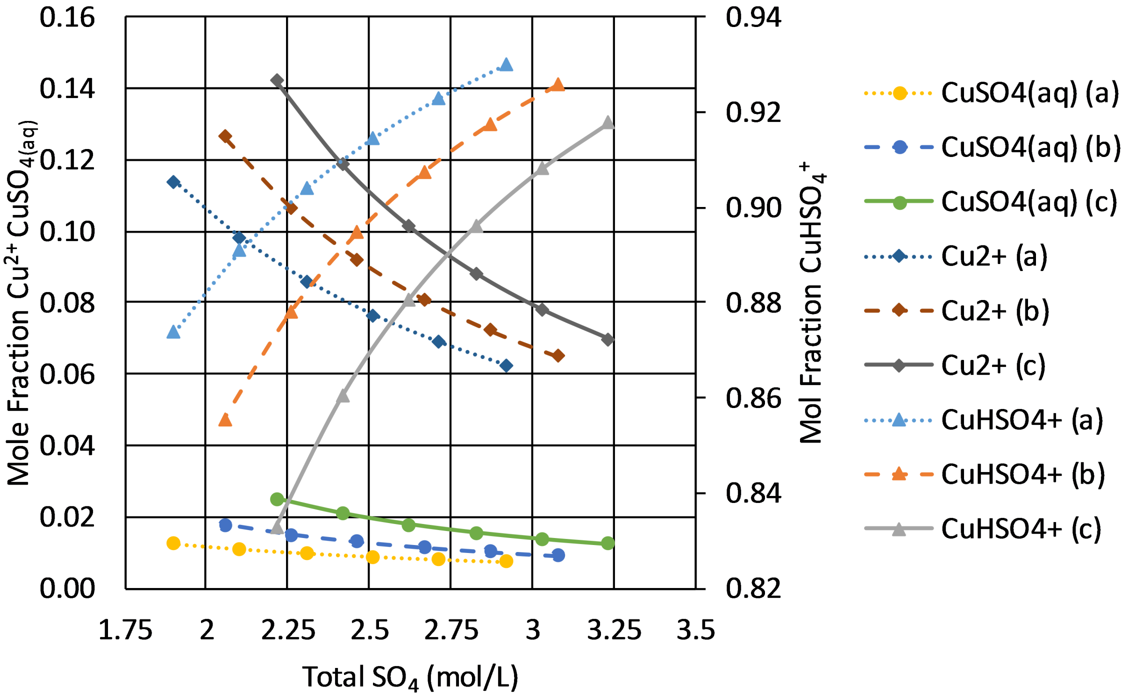

Figure 4.9: Copper species mol fraction as a function of total copper, secondary axis is $CuHSO^{+}_{4(aq)}$, (a) 0.472 (mol/L) - 30 (g/L) Cu^{2+}, (b) 0.629 (mol/L) - 40 (g/L) Cu^{2+}, (c) 0.787 (mol/L) - 50 (g/L) Cu^{2+}.

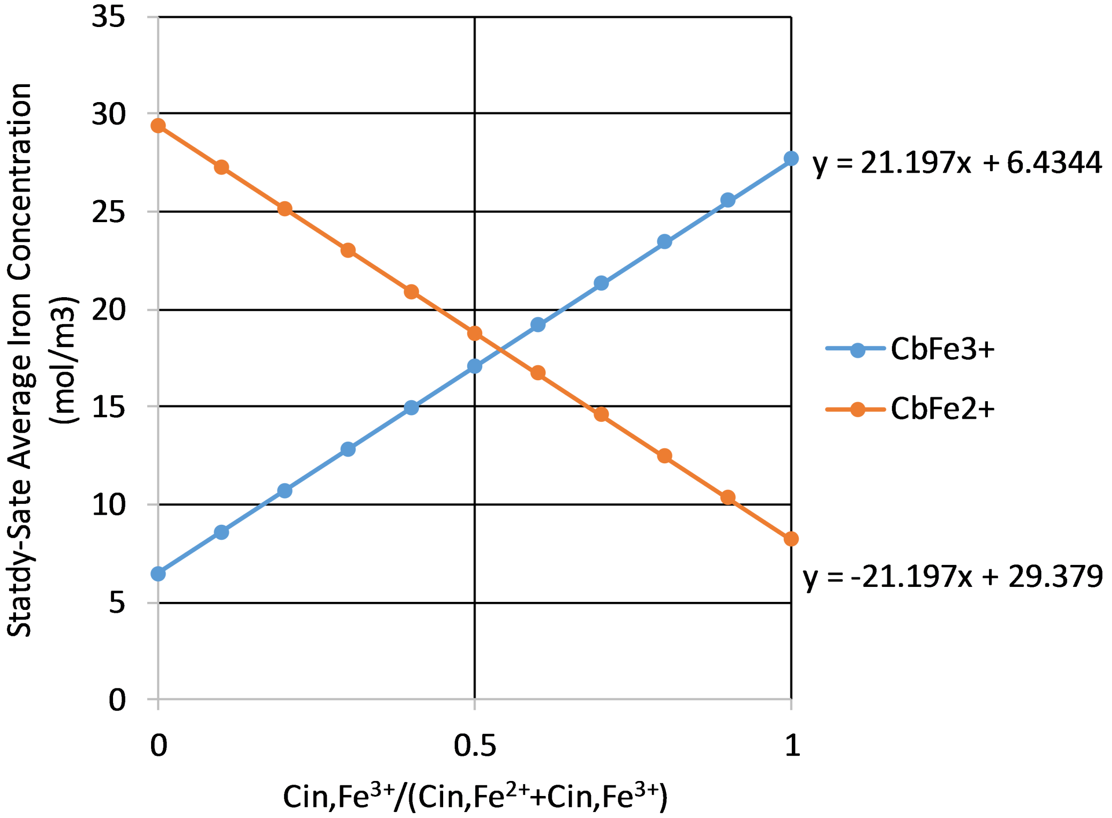

Figure 4.10: Comparison of steady-state average ferric ion fraction and inlet iron concentrations for 36 mol/m^3 total iron assuming Fe^{3+} and Fe^{2+} transport to the cathode is at its limiting current density. Calculated according to data in Tables 3.5, 3.6 and 4.4, 277 A/m^2.

Table 4.4: Conditions of Figure 4.10.

Parameter	Value
$D_{\mathrm{Fe}^{3+}}$	$7.26x10^{-10}$ (m^2/s)
$D_{\mathrm{Fe}^{2+}}$	$8.57x10^{-10}$ (m^2/s)
$\dot{V}$	$4.92x10^{-07}$ (m^3/s)
A_{cathode}	0.02376 (m^2)
A_{anode}	0.01583 (m^2)
δ*	$9.09X10^{-05}$ (m)

*Indicates typical diffusion layer thickness from model. For simplicity the cathode and anode diffusion layers were assumed to be the same thickness.

formed and the fact that cell electrolyte was never directly assayed for ferric ions. This will influence the oxidation state of the iron returning to the system. As such the specific ferric concentration used in the model is based on the overall current efficiency determined experimentally.

4.3.3 Current Efficiency via Comparative Diffusion

Although the experiments were conducted according to Tables 3.5 and 3.6, due to the cathode to anode size difference in 3D the effective current density for 2D representation was different and needed to be determined. This was done by taking a 3D scan and measuring the thickness of the center plane intersection. The equivalent current density determined is presented in Table 3.7. Note that the conversion from thickness to effective current density assumes 100% efficiency because the deposit is measured.

There are two apparent methods to calculate the current efficiency in modeling. One method is to run the electrochemical model assuming 100% current efficiency for copper. This is the same way utilized to determine the effective current density in Table 3.7. The current efficiency is then calculated according to equation (4.29). The local or total current is determined according to equation (4.32).

$$I_{\mathrm{actual}} = I_{\mathrm{loc}}(1 + (1 - C.E.)) \tag{4.32}$$

Another method is to assume that Fe^{3+} transport is included as a portion of overall

Cu^{2+} transport. Thus, the total transport is a summation of Fe^{3+} and Cu^{2+} with only Cu^{2+} included in the model. In this approach, the mass transfer coefficient of the copper is artificially high because the effects of Fe^{3+} are included with Cu^{2+} during the overall current determination. Correspondingly, the copper concentration is lower than expected. For these reasons the first method is utilized in this work.

4.3.4 Experimental Results

The primary result of experimentation was to produce deposits on stainless steel cathodes to calculate the local depositing current density. The methods to convert deposit thickness into depositing current density were discussed previously in section 3.3.1.1 equation 3.33. The experimentally determined current densities for each of the various cathode geometries may be found in Figures 4.11, 4.12, 4.13. Unless otherwise noted all results presented are determined from the model results.

4.3.4.1 Straight Cathode

For brevity the straight cathode is provided as the demonstration case from the three cathode geometries and as such received additional analysis. The simulation was run transiently in two main parts. The first ran to steady state conditions and the second ran immediately following to allow steady state time averaging. It was determined that it took approximately 60s to reach steady state as shown in Figure 4.14. The averaging occurred over a period of 30s. This figure also shows a lowering of the concentration at the cathode when compared to Figure 3.15. This begins to show the effects of speciation on various model outputs. Figure 4.14 also shows that 60s is still valid to reach steady state. Unless otherwise noted plots showing variables associated with the cathode are taken from the modeled cathode surface, or 0 distance. This applies to variables such as copper concentration, current density, mass transfer coefficient, etc. for this section as well as other geometric conditions.

Figure 4.15 shows the resolution of the boundary layer at the cathode. The results are very similar to those discussed in Figure 3.16 except lower due to the inclusion of additional electrolyte species in the model.

Figure 4.11 shows the current density as a function of position comparing the model

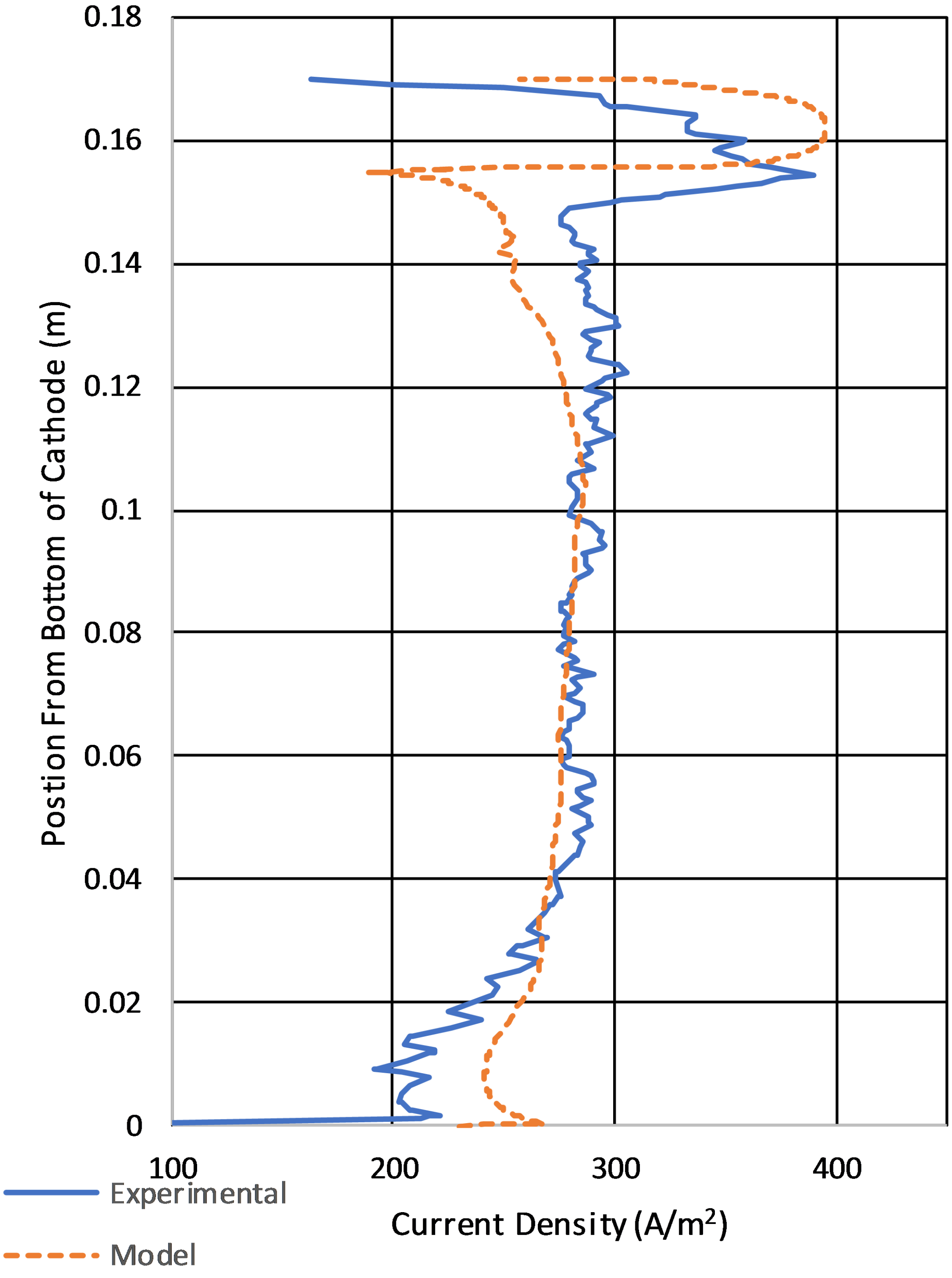

Figure 4.11: Average cathodic current density (60-90s) comparison model to experiment for straight cathode. 277.7 A/m^2, 40 g/L Cu^{2+}, 180 g/L H_2SO_4, 40 °C.

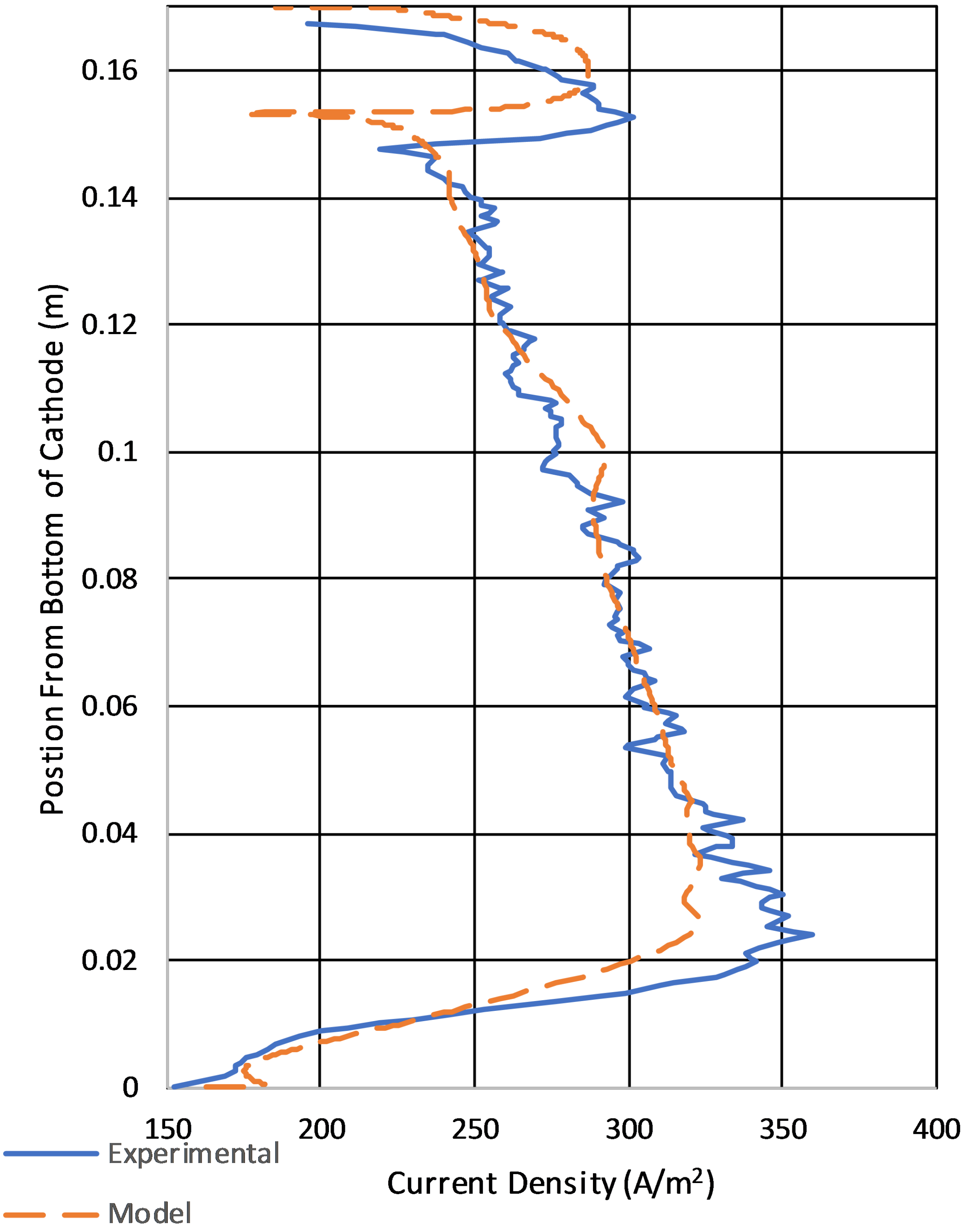

Figure 4.12: Average cathodic current density comparison (60-90s) model to experiment for tilted cathode. 277.7 A/m^2, 40 g/L Cu^{2+}, 180 g/L H$_2$SO$_4$, 40 °C.

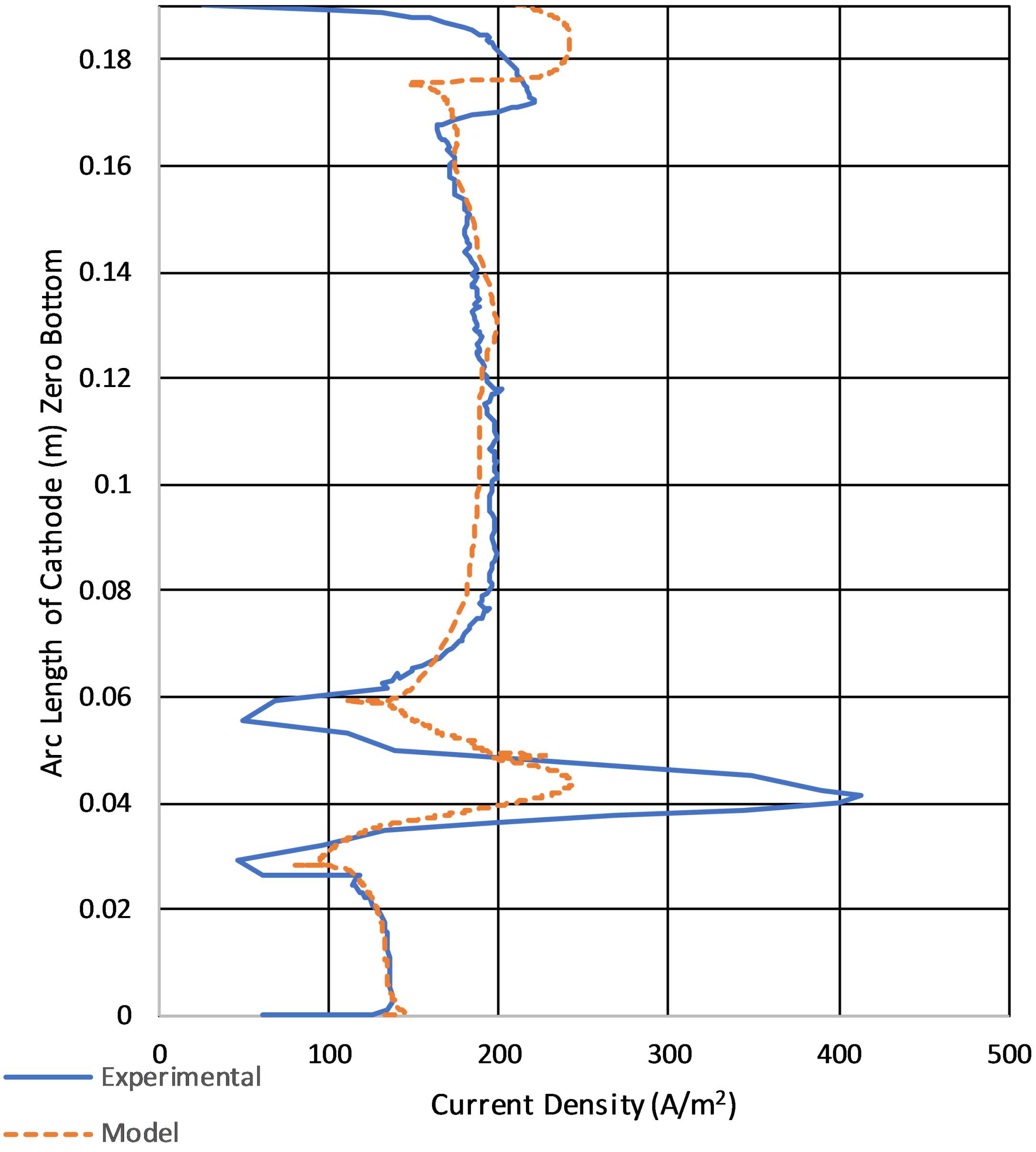

Figure 4.13: Cathodic current density comparison model to experiment for nodule cathode. 176.2 A/m^2, 40 g/L Cu^{2+}, 180 g/L H_2SO_4, 40 °C.

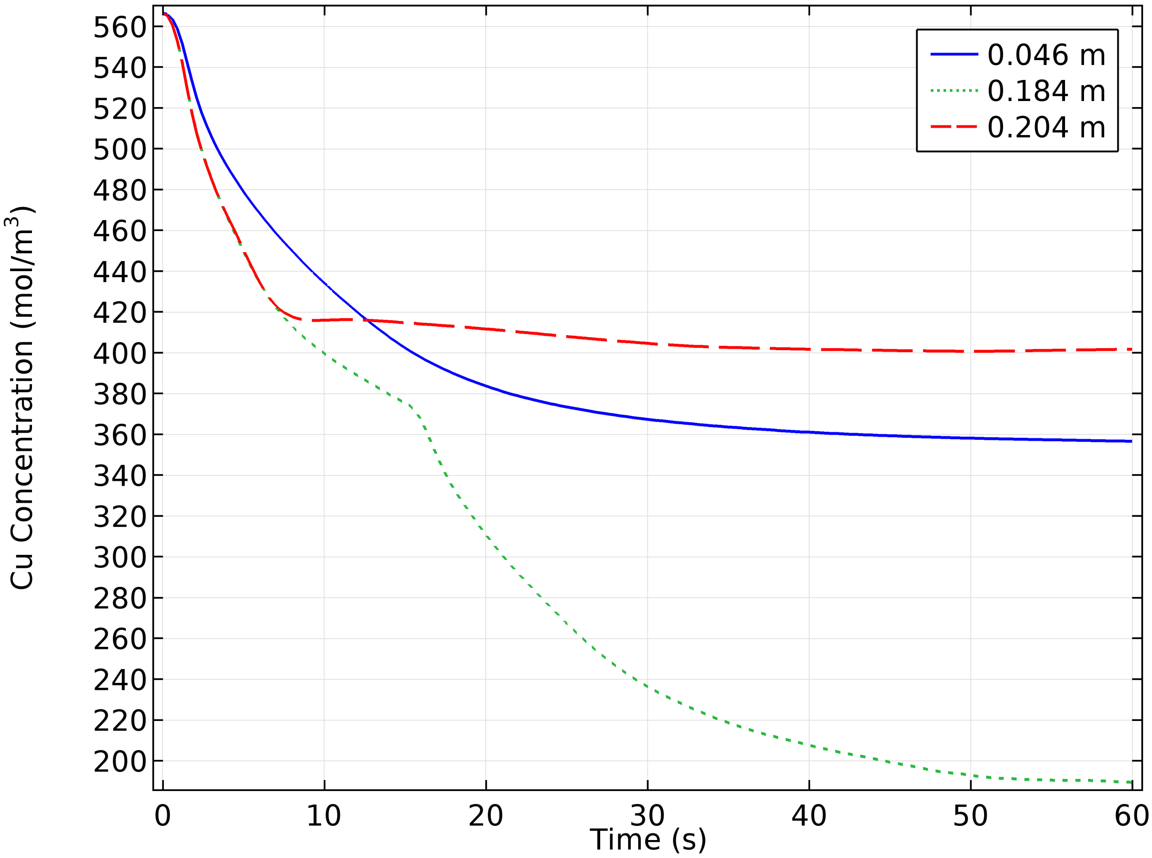

Figure 4.14: Cathode copper concentration (0-60s) at various points along the cathode. Dimensions given in the legend correspond to y axis positions along the cathode as shown in Figure 3.3 . Settings: 289.4 A/m^2, 40 g/L Cu^{2+}, 22.55 Fe^{3+} (mol/m^3), 180 g/L H_2SO_4, 40 °C.

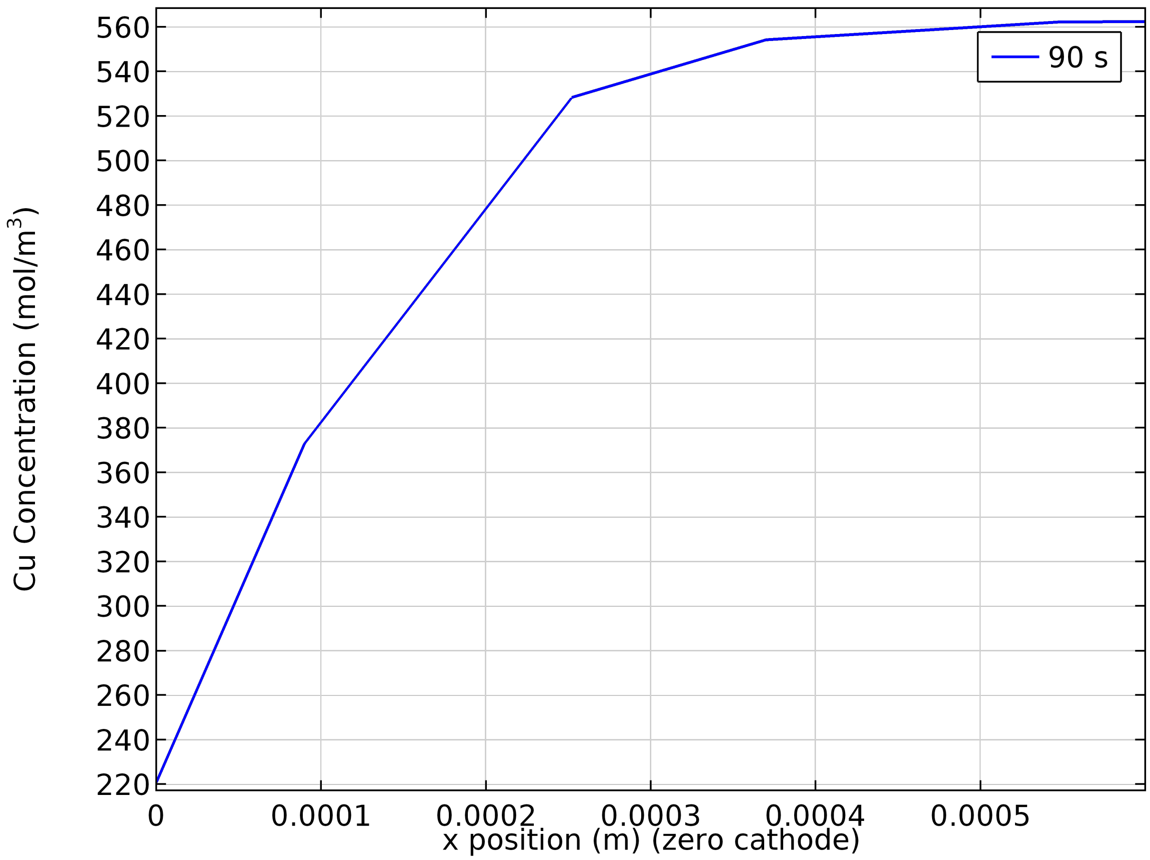

Figure 4.15: Modeled cathodic boundary layer at y position 0.15 m (see Figure 3.3 for reference). 277.7 A/m^2, 40 g/L Cu^{2+}, 180 g/L H_2SO_4, 40 °C.

results to those of the experiment. The magnitude, but not the position, of the ridge is predicted. This result is significant in that including speciation increased the magnitude of the of the current density along the ridge.

Figure 4.16 also provides interesting insights into the interaction of the mast transport conditions along the cathode. The current efficiency is the lowest on the top of the ridge where the Fe^{3+} is available at the highest concentrations due to the interaction of the top of cell vortex. This has implications to deposit rates and leveling where the highest current density areas exhibit the highest current efficiencies. The significance of Figure 4.16 shows the variation of the current efficiency across the cathode. Local current efficiency is dependent upon mass of Fe^{3+} due to the reaction occurring at the iron limiting current density. Because of this Figure 4.16 is almost the inverse in shape to Figure 4.22 which is of the copper mass transfer coefficient.

Figure 4.17 shows the copper concentration along the cathode. Figure 4.17 highlights the variation of the copper concentration along the cathode. As discussed above, the electrolyte flow plays a significant role in the transport to the cathode and development of the boundary layer. This figure also presents some counterintuitive results. The areas of lowest concentration also correspond to the areas of lowest current density. This will be a continuing topic of conversation as roughness and the resulting effect of the ratio of I/I_{limit} will be discussed. It is sufficient to note that visually this region below the ridge also corresponded to the roughest portion of the deposit.

Figure 4.18 shows the relative transport mechanism at the cathode surface split between diffusion and migration. It shows the importance of diffusion and how much migration drops in the presence of supporting electrolyte. This is significant in that the potential drop in the electrolyte decreases with the addition of supporting electrolyte. The effect of supporting electrolyte on the electroactive species is to lower the concentration at the cathode due to loss of migration flux. Hence, adding supporting electrolyte may not be the best course of action to reduce deposit roughness.

Figures 4.19 - 4.21 show the copper concentration, fluid velocity and gas fraction, respectively. Each shows the evidence of vortex at the top of the cell responsible for the ridge formation. These were discussed in section 3.4 and in outcome varied little.

Figure 4.19 shows the copper concentration in the cell and concentration transport

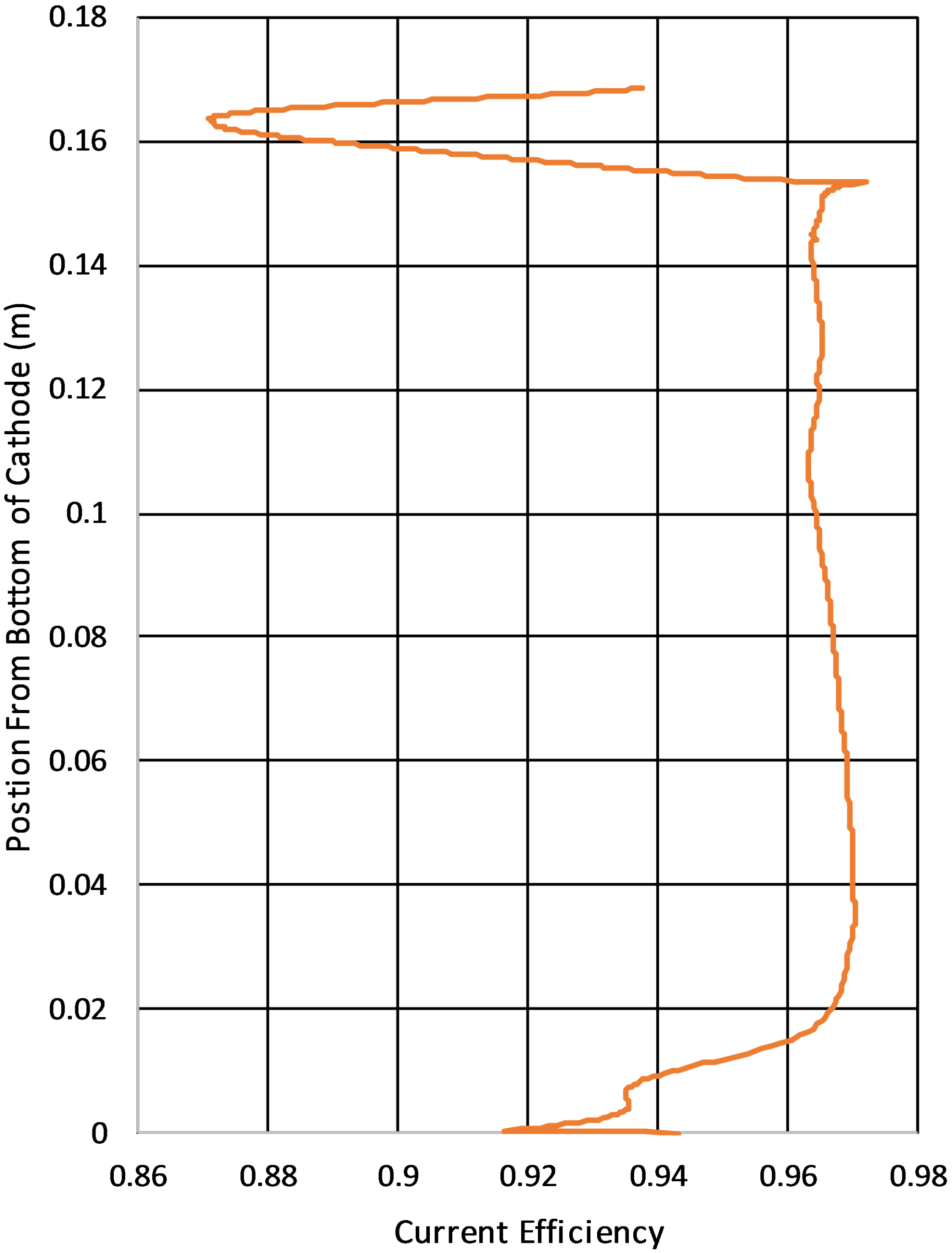

Figure 4.16: Modeled local cathodic average current efficiency (60-90s) 22.55 (mol/m^3) Fe^{3+}. 277.7 A/m^2, 40 g/L Cu^{2+}, 180 g/L H_2SO_4, 40 °C.

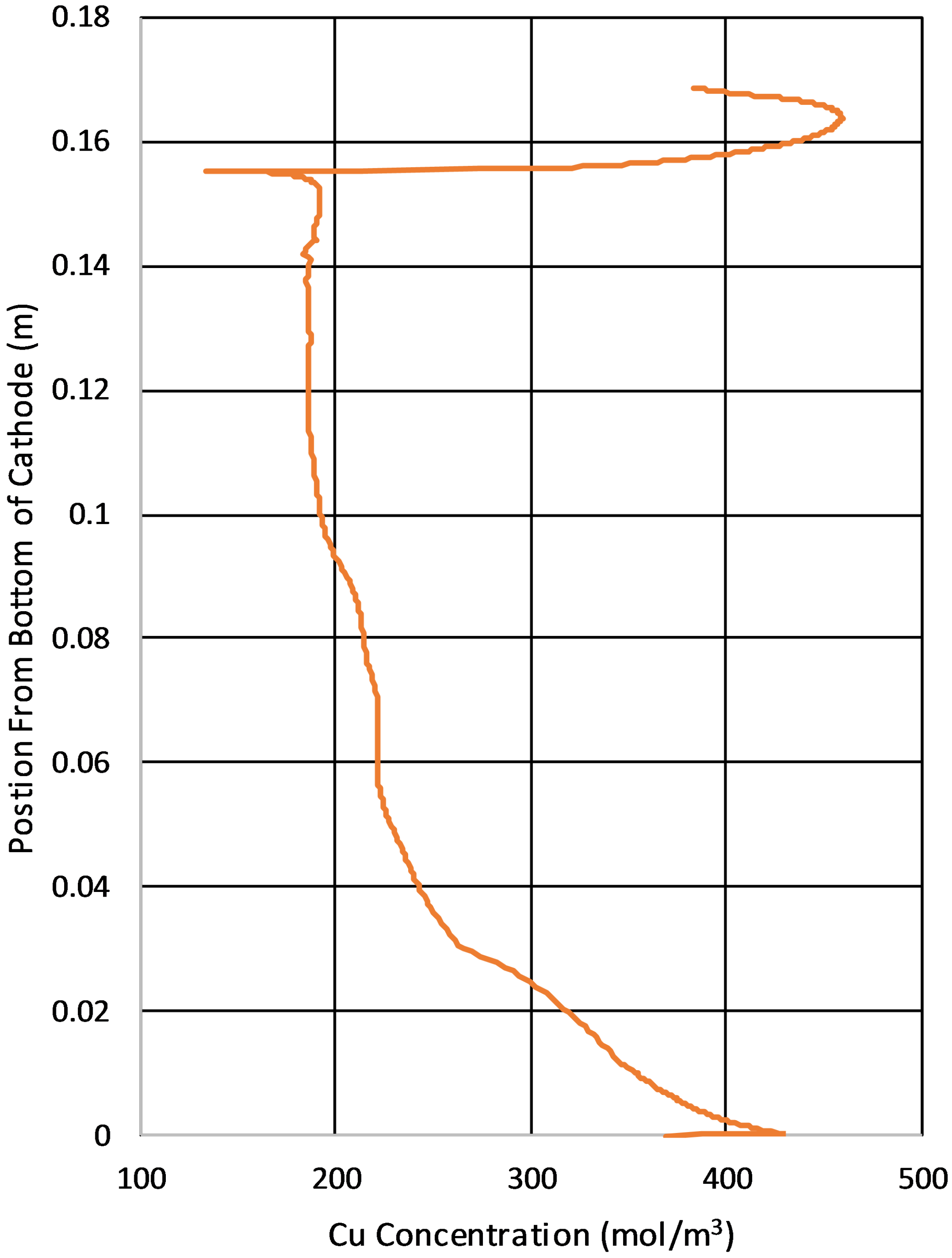

Figure 4.17: Modeled straight cathode copper concentration along the cathode (90s). 277.7 A/m^2, 40 g/L Cu^{2+}, 180 g/L H_2SO_4, 40 °C.

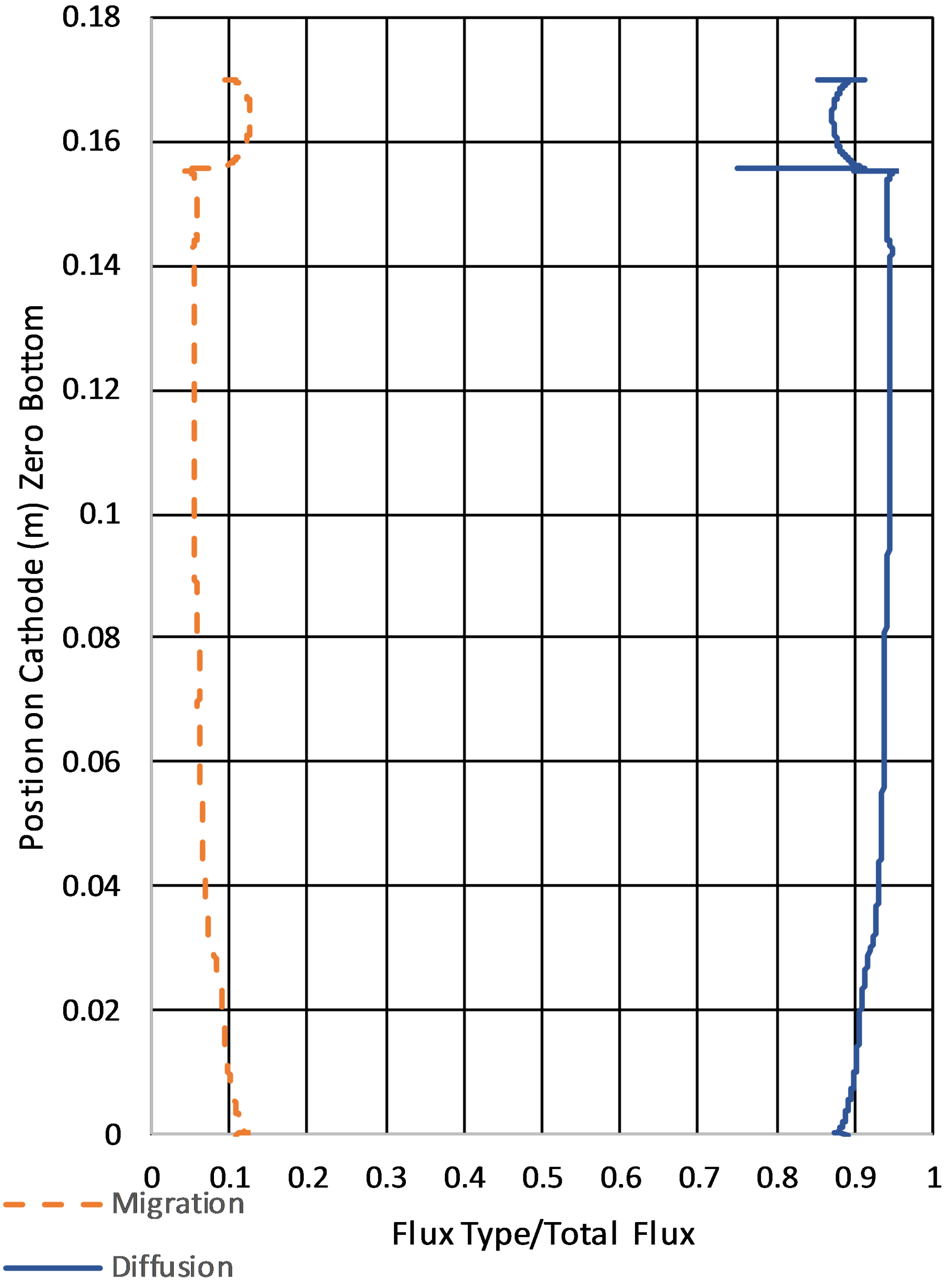

Figure 4.18: Modeled straight cathode on cathode flux type ratio ($CuHSO_4^+$) along the cathode at 90s of simulation. 277.7 A/m^2, 40 g/L Cu^{2+}, 180 g/L H_2SO_4, 40 °C.

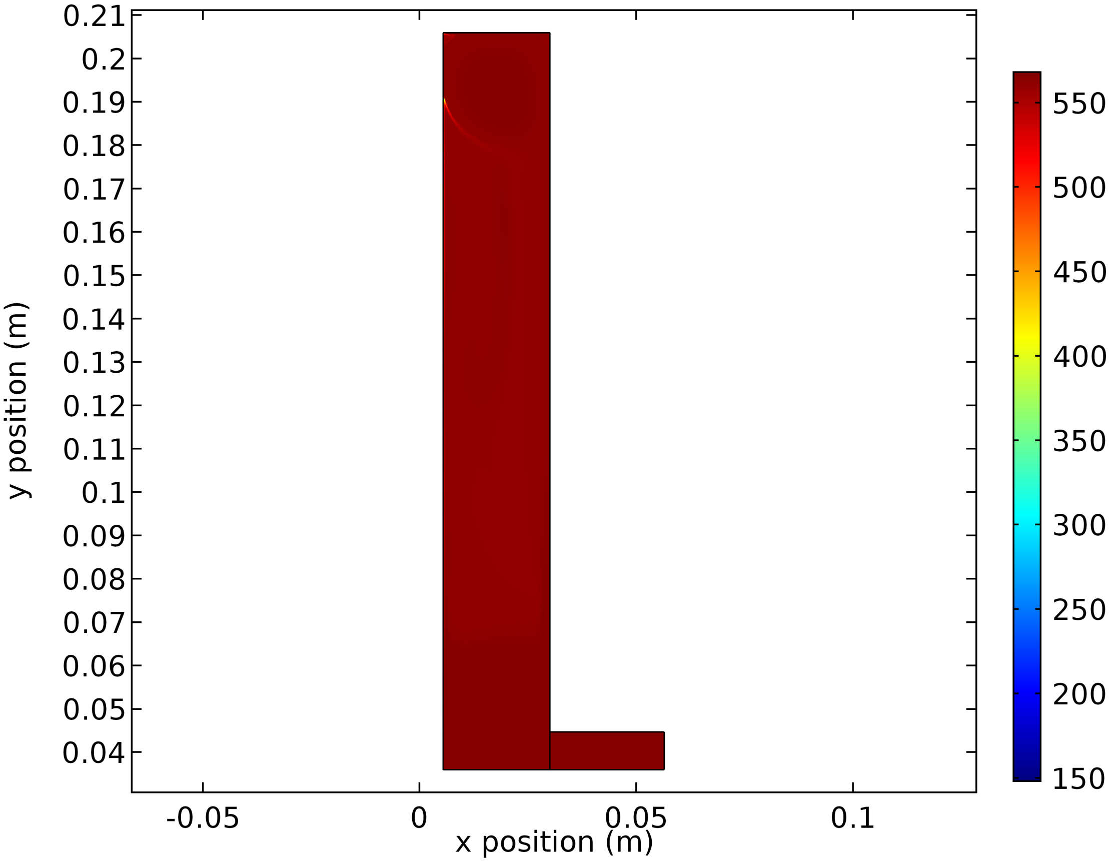

Figure 4.19: Modeled straight cathode cell copper concentration (mol/m^3) with arrows as velocity vectors. 277.7 A/m^2, 40 g/L Cu^{2+}, 180 g/L H_2SO_4, 40 °C.

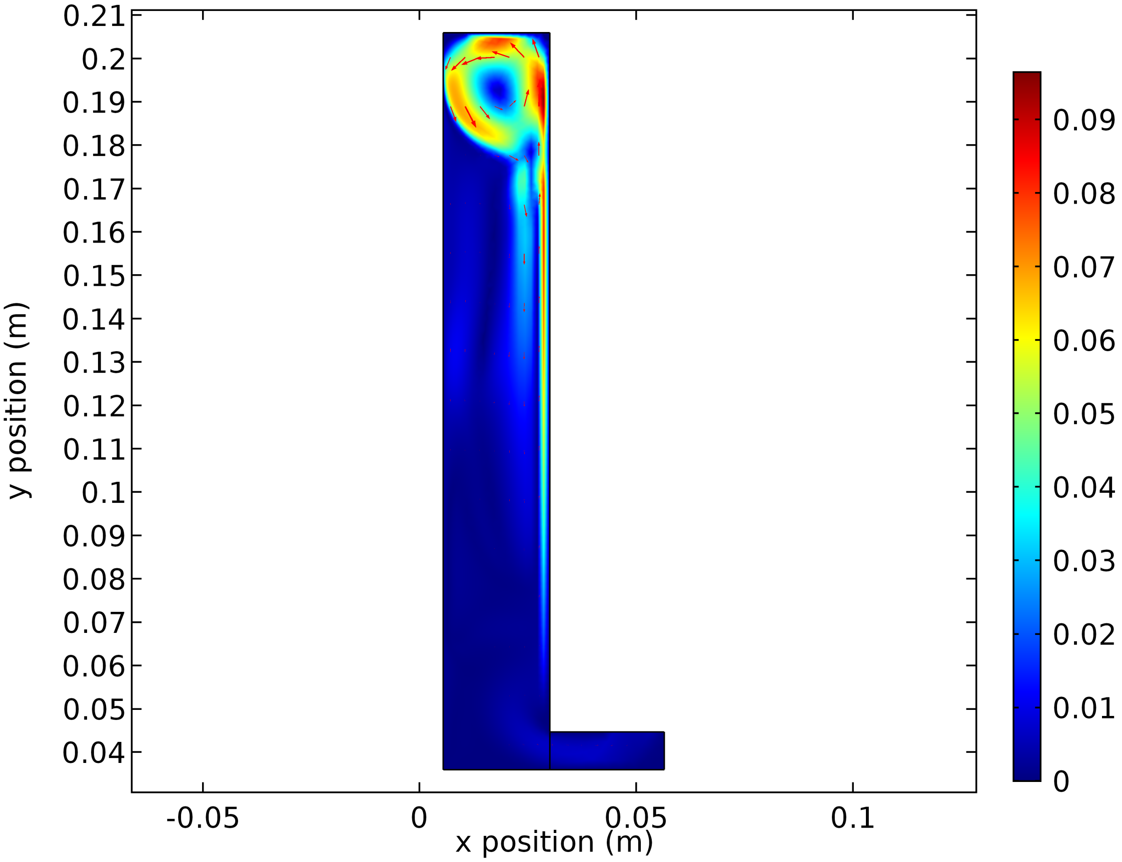

Figure 4.20: Modeled straight cathode cell electrolyte velocity (m/s) with arrows as velocity vectors. 277.7 A/m^2, 40 g/L Cu^{2+}, 180 g/L H_2SO_4, 40 °C.

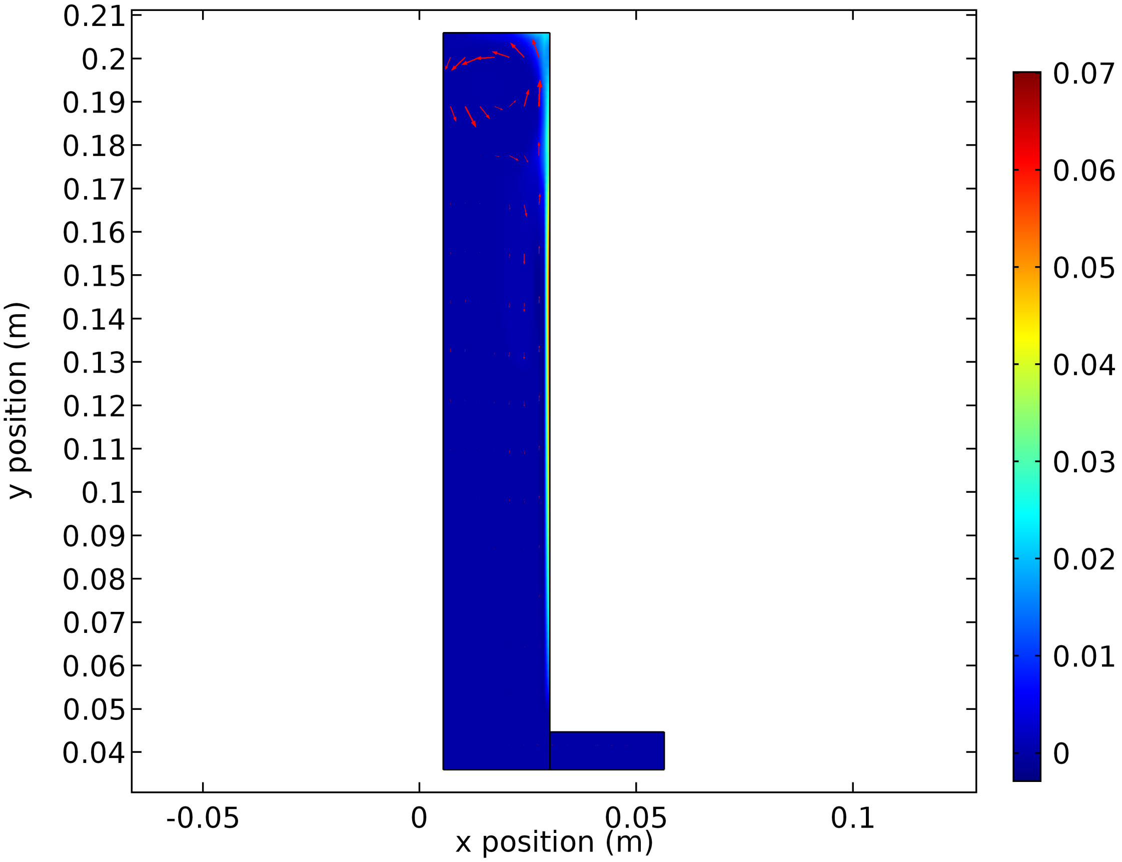

Figure 4.21: Modeled straight cathode cell gas fraction with arrows as velocity vectors. 277.7 A/m^2, 40 g/L Cu^{2+}, 180 g/L H_2SO_4, 40 °C.

of depleted electrolyte away from the cathode. Of note is the trailing low concentration flowing away from the cathode near the top of the cell. This shows specifically why the ridge and notch form at this specific location. The bubble induced flow at the top of the cell produces a vortex pushing the electrolyte down the cathode. Conversely, the depletion of copper from the electrolyte reduces the density and causes the electrolyte to rise along the cathode. These two opposing flows meet in this region causing a point of low copper concentration at the cathode.

Figure 4.20 shows the electrolyte velocity in the cell with the pronounced vortex at the top of the cathode. This vortex produces the mass transport condition which leads to the formation of a copper ridge. Figure 4.20 also indirectly shows a relatively smooth flow pattern which is a result of stock COMSOL fluid simulation aids to improve simulation robustness.

Figure 4.21 shows the gas fraction in the cell with the majority exiting the electrolyte at the top of the cell. This figure shows that there exists only a small region where the gas concentration exists in any appreciable concentration. That region is next to the anode. As such it is felt that the low gas concentration assumption remains valid for this model.

The mass transport coefficient provided in Figure 4.22 was calculated according to equation:

$$k = \frac{\mathrm{Flux}_{\mathrm{Cu}^{2+}}}{C_{\mathrm{Cu}^{2+},bulk} - C_{\mathrm{Cu}^{2+},\mathrm{electrode}}} \tag{4.33}$$

As discussed previously the mass transfer coefficient plot appears to be the inverse shape of the current density. Due to iron reactions at the cathode at the limiting current density the mass transport is highly correlated to the iron reaction rate. Figure 4.22 also shows a significant reason for the formation of the cathodic ridge due to transport properties in the electrolyte.

4.3.4.2 Tilted Cathode

The results of this section are similar to those discussed in the previous sections. For the sake of brevity only results unique to the tilted cathode will be discussed in greater detail. The tilted cathode model was run using the settings in Table 3.7. The averaged current efficiency of 60-90s was 95.849%. Figure 4.12 shows the experimental to model current density profile. The "ridge" at the top of the cathode appears similar, although positionally

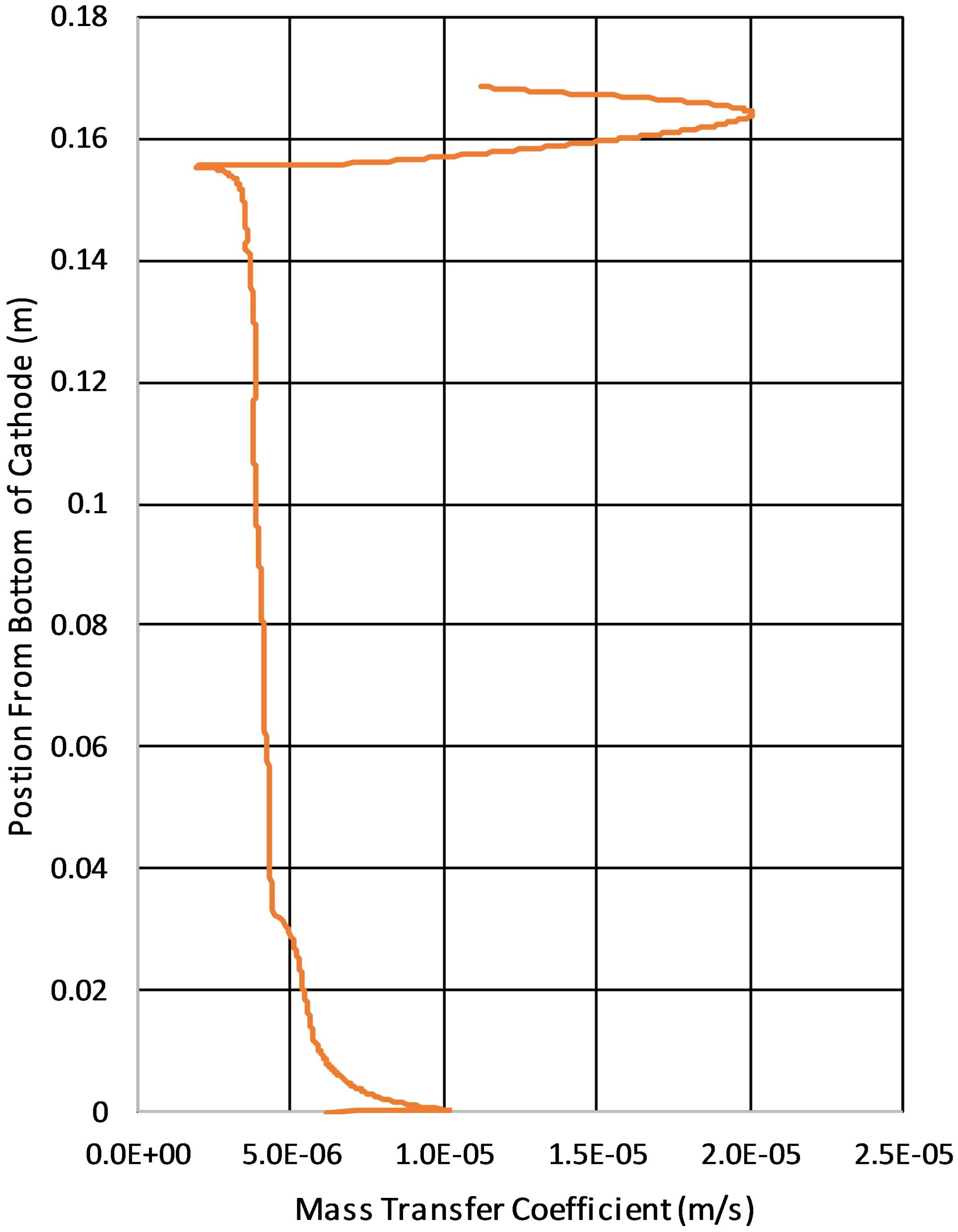

Figure 4.22: Modeled straight cathode average mass transfer coefficient (60-90s) along the cathode. (see Figure 3.3 for reference). 277.7 A/m^2, 40 g/L Cu2+, 180 g/L H_2SO_4, 40 °C.

displaced. The maximum current is also slightly lower then expected. The tilted cathode model was run using the settings in Table 3.7. The averaged current efficiency of 60-90s was 95.85%. Again, unless otherwise noted plots showing variables associated with the cathode are taken from the modeled cathode surface, or 0 distance.

Figure 4.12 shows the current density along the cathode. The current density along the ridge is decreased due to the increase in current density where the cathode is closest to the anode.

Figure 4.23 shows the copper concentration along the cathode. It is interesting to note the lower concentration of copper where the cathode is closest to the anode. From this plot it can be seen that the decrease of the current density at the ridge is due to the increased current density at the narrow point of the cathode gap rather than from mass transport effects. This is further shown in Figure 4.24.

Figures 4.24, 4.25 and 4.26 show the copper electrolyte concentration, the electrolyte velocity and the gas fraction, respectively. These are include to provide cell conditions. The gas fraction shows that most oxygen remains close to the anode before exiting at the top of the cell. These parameters serve to explain the results of the current density distribution.

4.3.4.3 Nodule Cathode

Out of all the current density profiles to obtain, the nodule was the most difficult. Extra care during the surface scan was needed to capture the surfaces around the nodule. Additional postprocessing was needed to convert the scan into current density. To do this a profile was obtained by using a mid plane intersection of the scan. This profile was then superimposed over the original profile. Marker lines were then inserted and measured normal to the original profile. In this way the deposit thickness was determined around the nodule. Figure 4.27 shows the measurement of the deposit thickness around the nodule. For convenience in reporting current density the data were transformed from X, Y to arc length (perimeter), Y. This was necessary as the original data had multiple Y's for some X's.

Another important distinction is that Figure 4.27 shows a point of zero current at the nodule base. This is due to the assumption of deposit growth normal to the electrode. However, in the reported data this point will not reach zero due to numerical integration

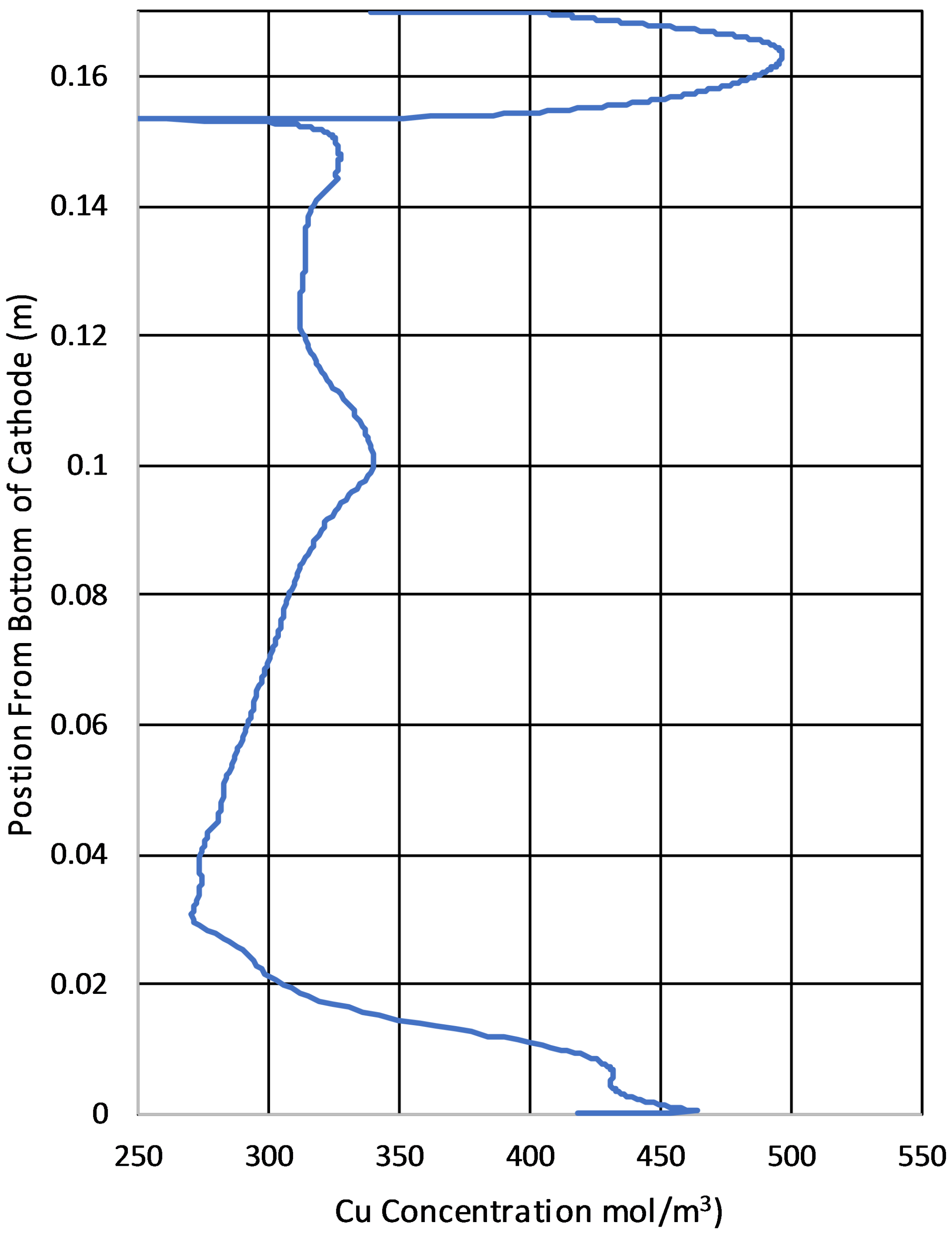

Figure 4.23: Modeled tilted cathode cathodic copper concentration along the cathode. 277.7 A/m^2, 40 g/L Cu^{2+}, 180 g/L H_2SO_4, 40 °C.

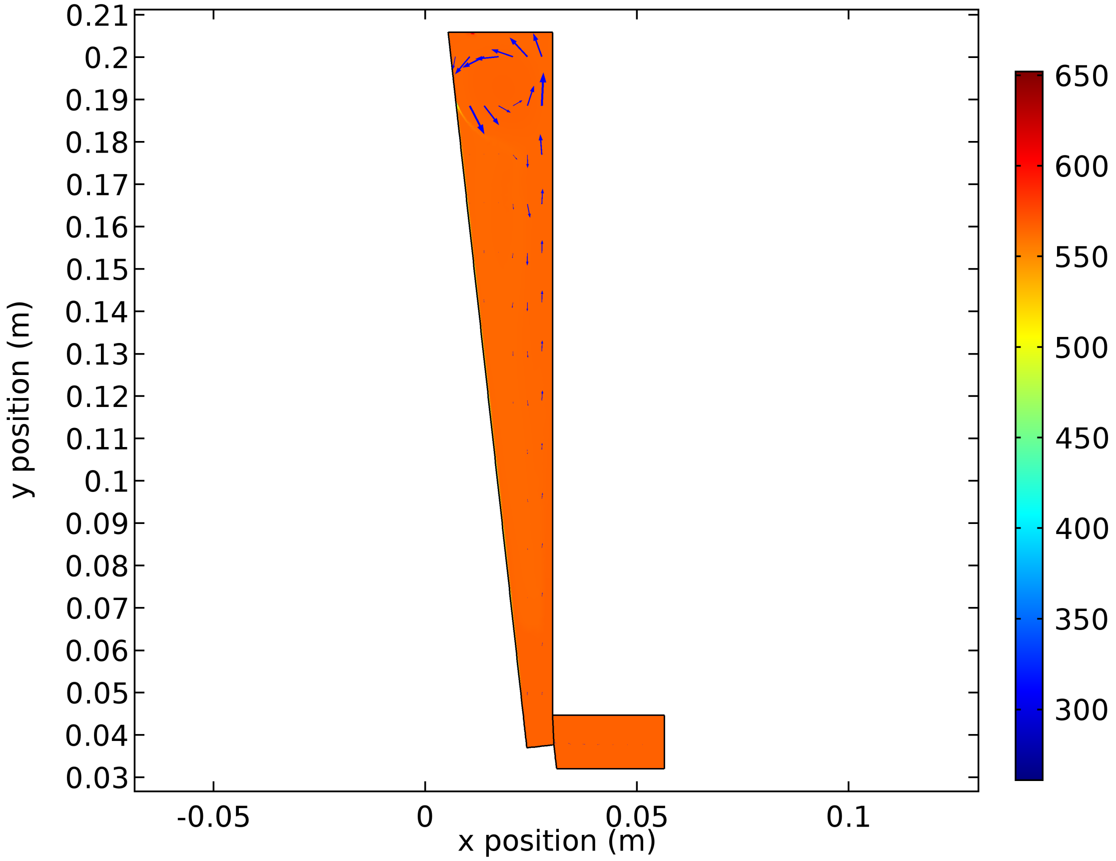

Figure 4.24: Modeled tilted cathode cell copper concentration (mol/m^3) with arrows as velocity vectors. 277.7 A/m^2, 40 g/L Cu^{2+}, 180 g/L H_2SO_4, 40 °C.

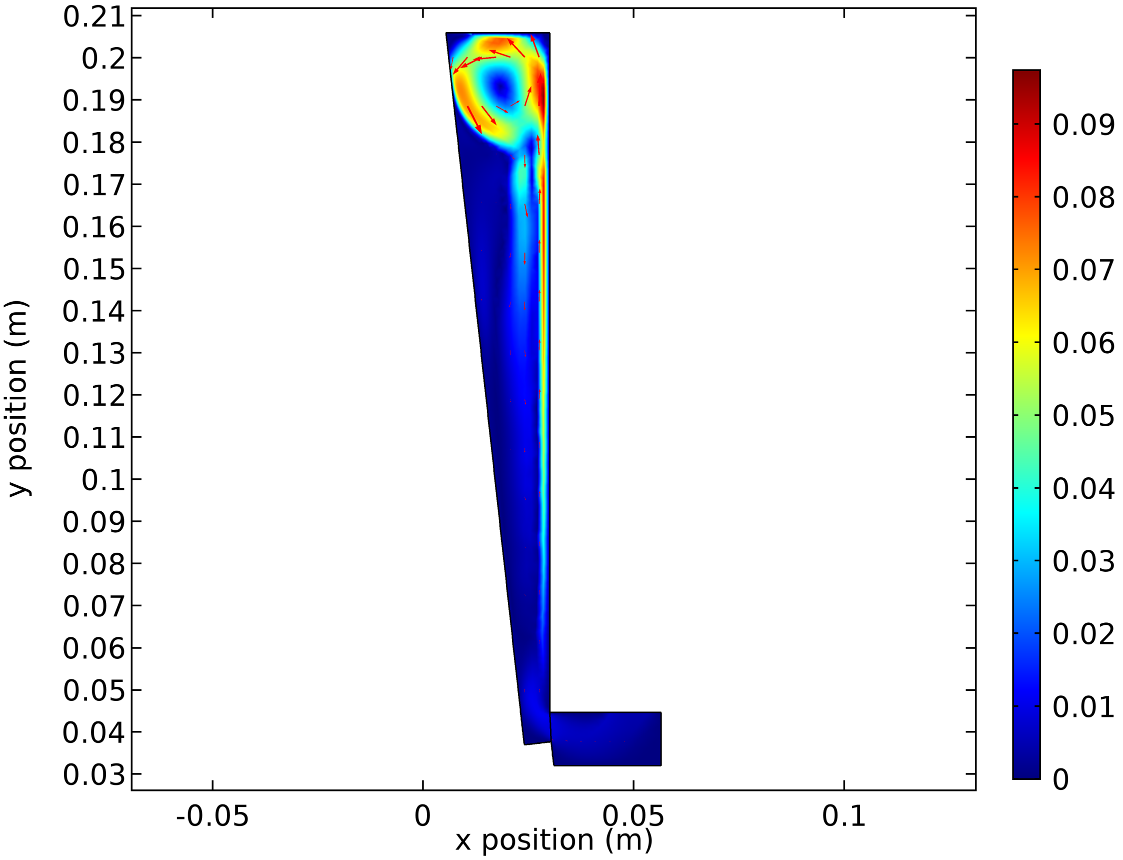

Figure 4.25: Modeled tilted cathode cell electrolyte velocity with arrows as velocity vectors. 277.7 A/m^2, 40 g/L Cu^{2+}, 180 g/L H_2SO_4, 40 °C.

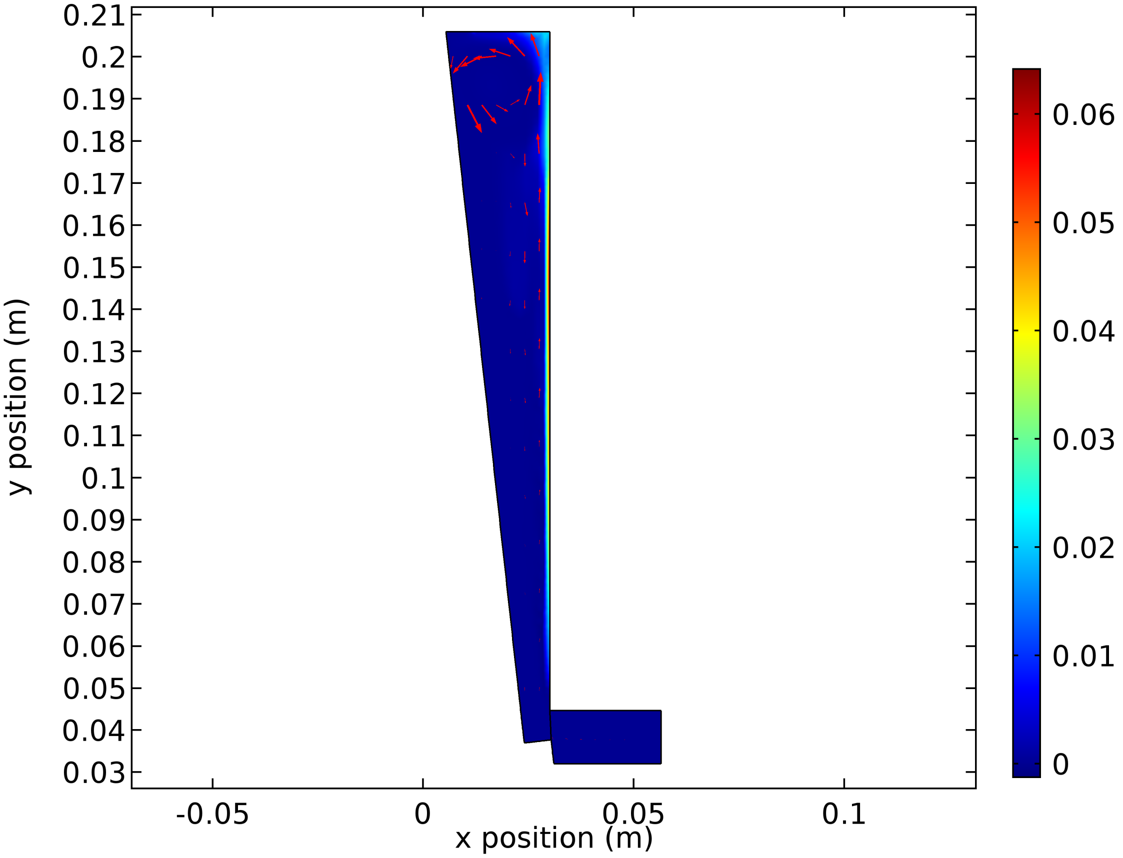

Figure 4.26: Modeled tilted cathode cell gas fraction with arrows as velocity vectors. 277.7 A/m^2, 40 g/L Cu^{2+}, 180 g/L H_2SO_4, 40 °C.

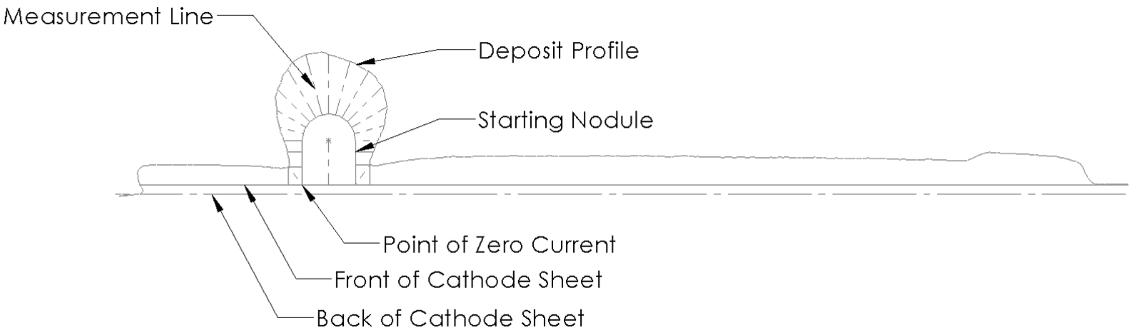

Figure 4.27: Nodule thickness conversion method.

averaging nearest points. Unless otherwise noted plots showing variables associated with the cathode are taken from the modeled cathode surface, or 0 distance.

The tilted cathode model was run using the settings in Table 3.7. The averaged current efficiency of 60-90s was 95.81%.

Figure 4.13 shows the cathodic current density as a function of position on the cathode. The results suggest that the cathode current density is underestimated by 1/2. The position of the current density appears to be a general match in the model with a slight shift of the ridge up the cathode from where it is located experimentally.

Figure 4.28 shows the current efficiency along the cathode as a function of position. This plot is effective at showing the variation of current efficiency along the cathode. It can be seen that the local mass transport conditions are influential due to iron being deposited at the limiting current density. Thus iron can have a smoothing effect on the copper deposit where high current density areas are shown to have lower current efficiencies.

Figure 4.29 shows the copper concentration along the cathode. Areas of high current density along the nodule are shown to have lower copper concentrations. This is important to note as this will increase local roughness, particularly at the nodule tip.

Figures 4.30, 4.31, and 4.32 show the copper electrolyte concentration, the electrolyte velocity and the gas fraction, respectively. These are included to show the particular cell conditions of interest around the nodule.

4.4 Summary

Overall the models show general agreement with the experimental data. The results show the the iron concentration greatly impacts the current efficiency and that local mass transport is a key contributer to localized variations. As shown by Figures 4.11, 4.12 and 4.13 the current density along the cathode is not uniform and varies greatly depending on the local mass transport. This model shows that the highest current density regions due to higher mass transport also have the lowest current efficiency. Thus, the iron has a type of smoothing effect on the deposit. Another effect of the supporting electrolyte is that the increased species improve conductivity lowering potential drop in the bulk electrolyte. However this improved conductivity comes at a cost. The addition of supporting electrolyte greatly diminishes the impact of migration as seen in Figure 4.18. This may

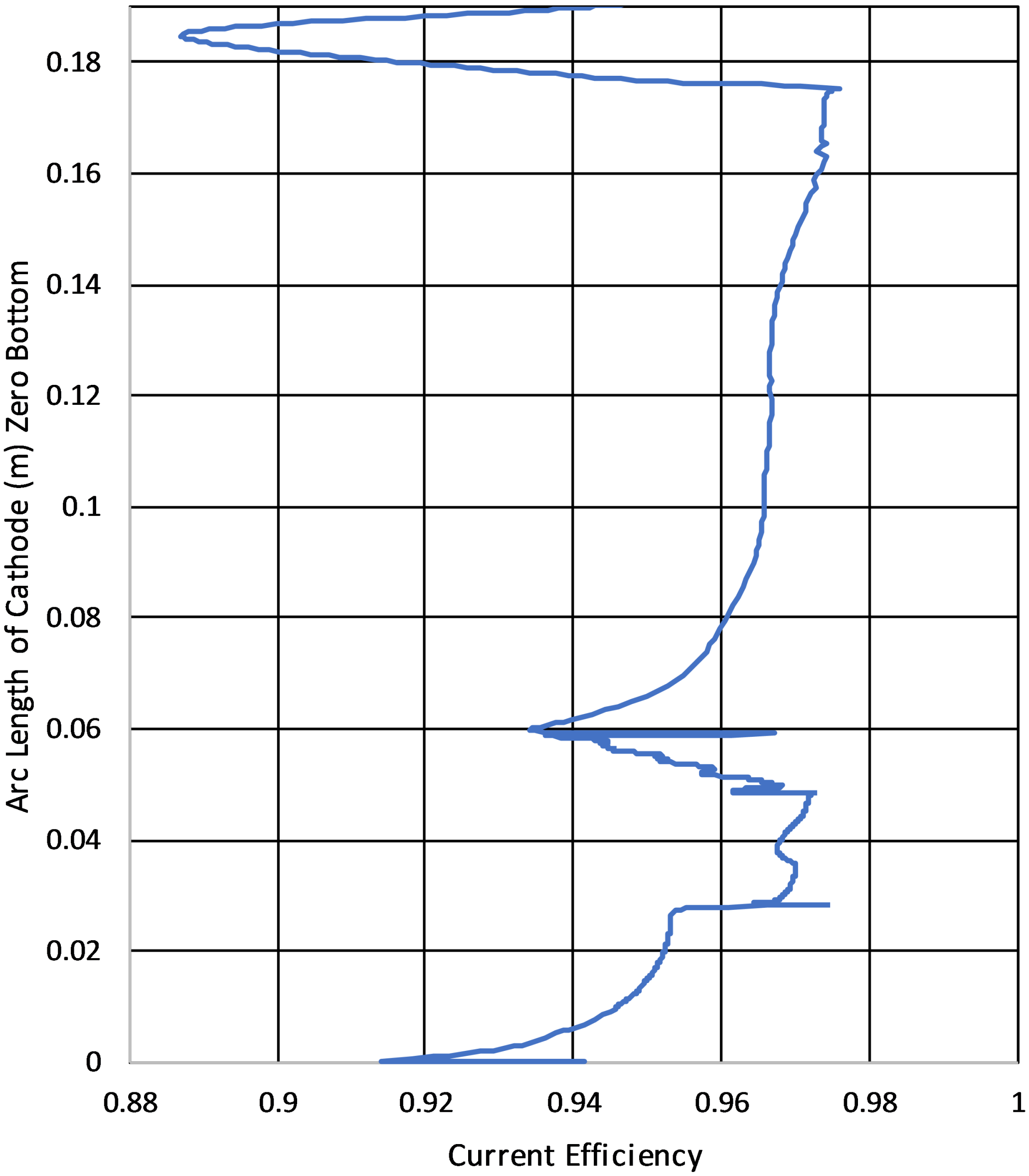

Figure 4.28: Modeled cathodic local average current efficiency (60-90s) 13.2 (mol/m^3) Fe^{3+}. 176.2 A/m^2, 40 g/L Cu^{2+}, 180 g/L H_2SO_4, 40 °C.

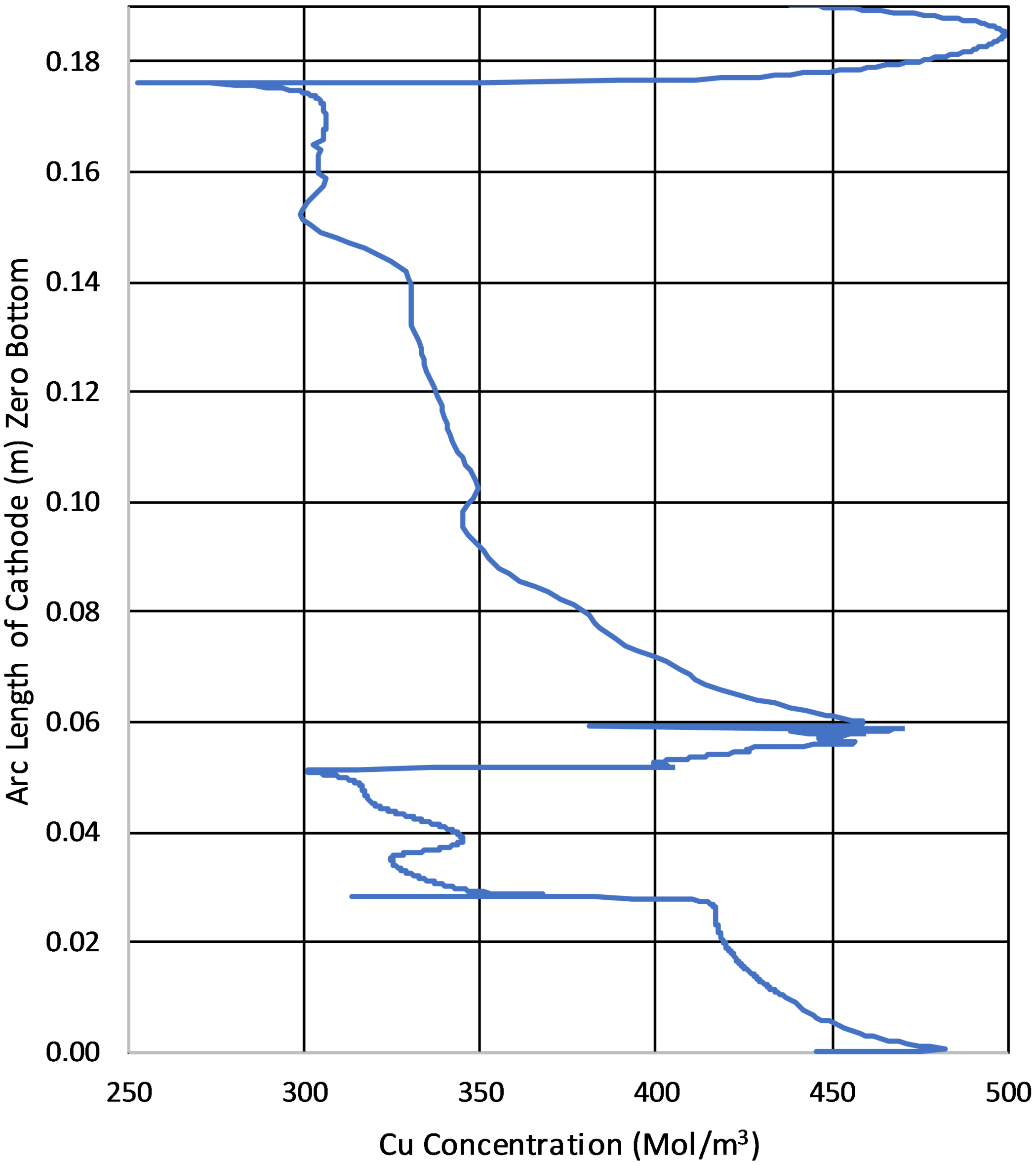

Figure 4.29: Modeled nodule cathode cathodic copper concentration along the cathode. 176.2 A/m^2, 40 g/L Cu^{2+}, 180 g/L H_2SO_4, 40 °C.

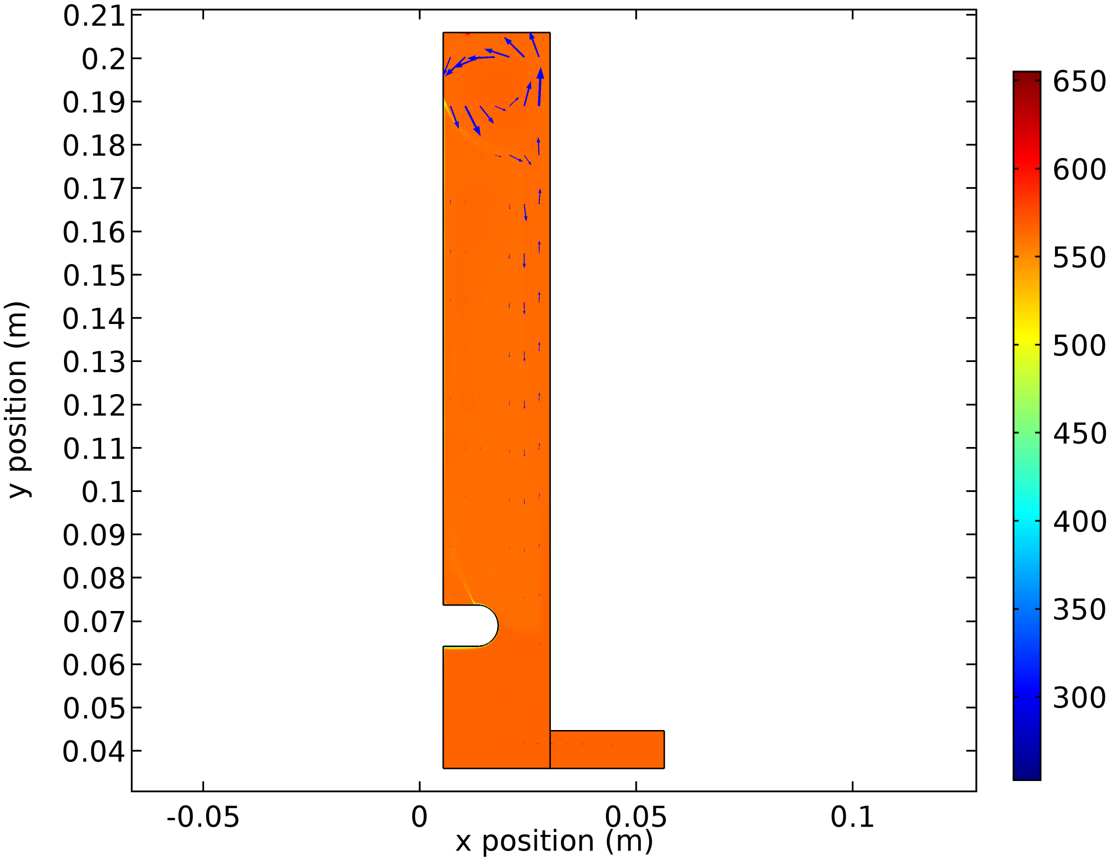

Figure 4.30: Modeled nodule cathode cell copper concentration (mol/m^3) with arrows as velocity vectors. 176.2 A/m^2, 40 g/L Cu^{2+}, 180 g/L H_2SO_4, 40 °C.

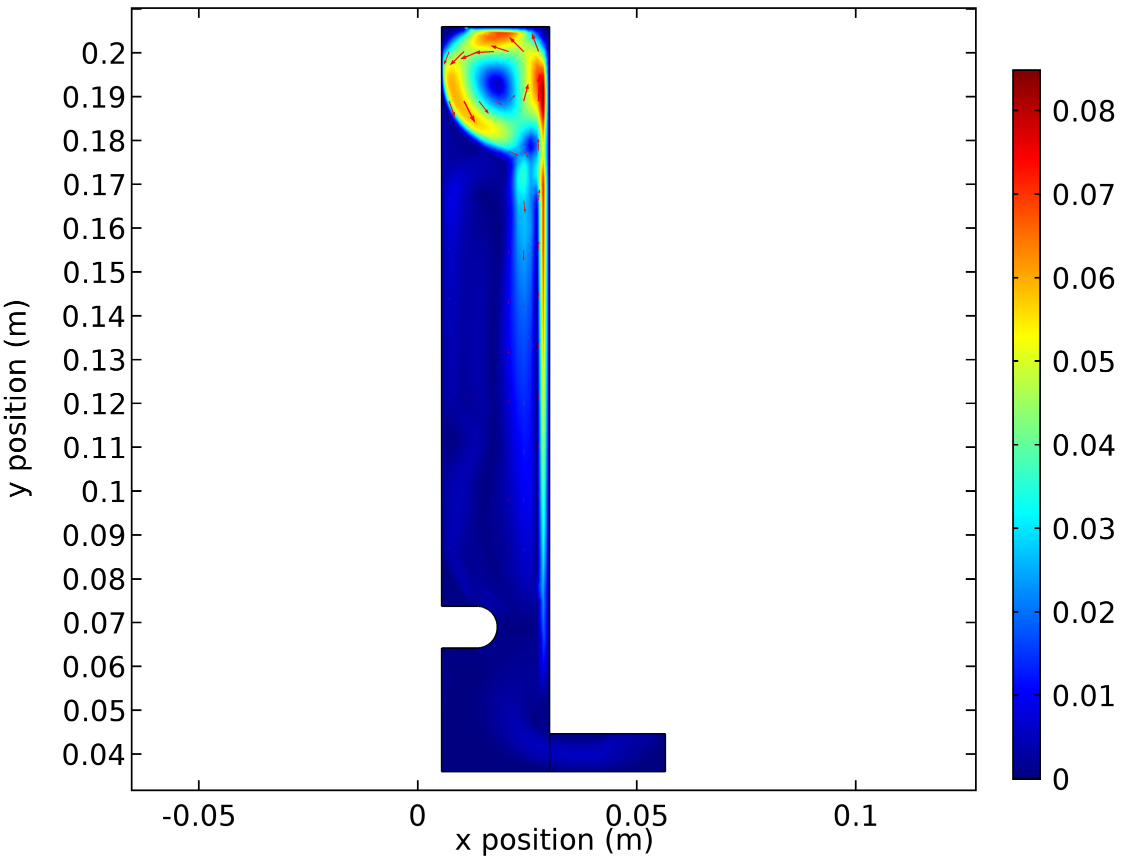

Figure 4.31: Modeled nodule cathode cell electrolyte velocity with arrows as velocity vectors. 176.2 A/m^2, 40 g/L Cu^{2+}, 180 g/L H_2SO_4, 40 °C.

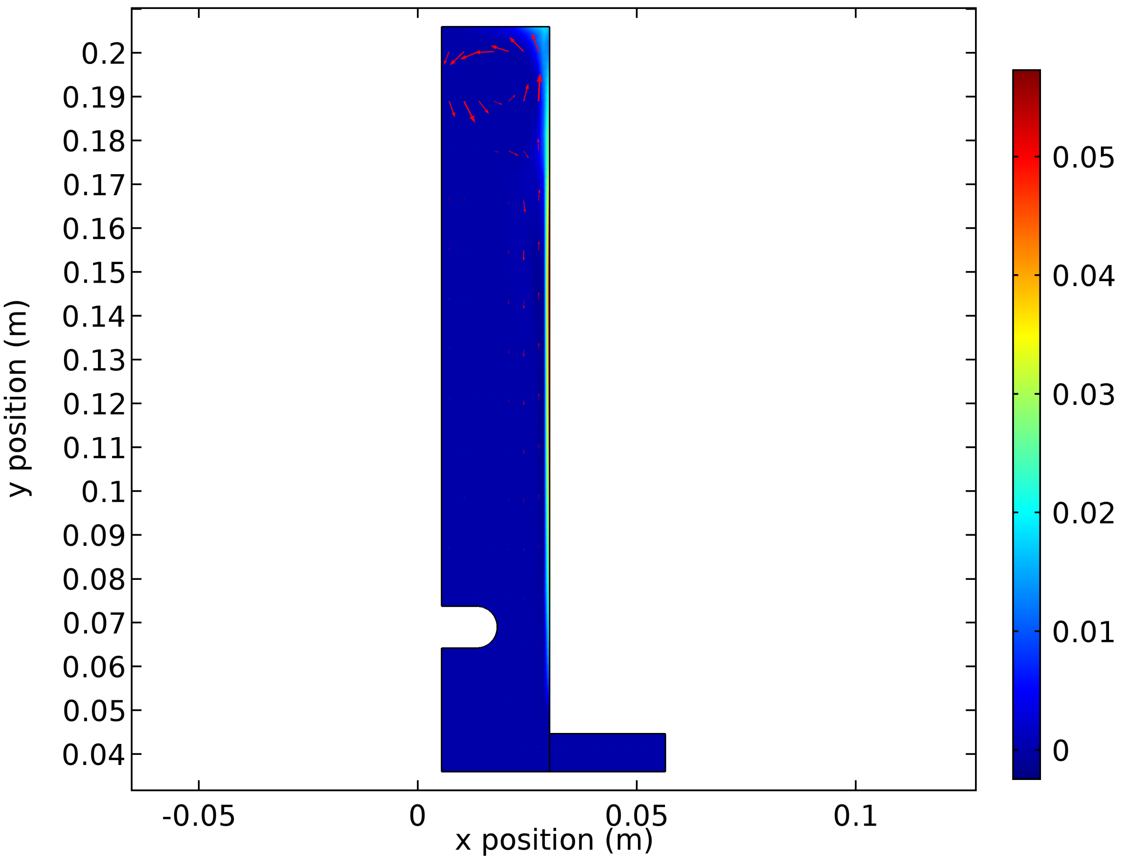

Figure 4.32: Modeled nodule cathode cell gas fraction with arrows as velocity vectors. 176.2 A/m^2, 40 g/L Cu^{2+}, 180 g/L H_2SO_4, 40 °C.

be compared to the 3 species straight cathode model in Figure 3.18. Thus, the supporting electrolyte lowers the migration of copper ions.These findings are in agreement with those of Newman [21]. This has an interesting impact on copper concentration at the cathode.

Figure 4.33 compares the results between the 3 species and the 5 species models. In Figure 4.33 (a) the 5 species model shows the correct amplitude of the current density on the ridge. However, in (b) and (c) the current density on the tilted cathode and the nodule show a slightly lower current density than the 3 species model. In each of these instances the ridge current density matches more closely with the 5 species model. It appears that the 5 species model is more sensitive to flow conditions. This is seen in Figure 4.33 (a) where the flow causes the boundary layer to thin at the top of the cathode (and match the experimental results more closely) and less accurate in the larger boundary of the slower flow toward the bottom.

Figure 4.34 shows the comparison of copper concentration along the cathode between the 3 different geometries studied. The shape of the plots appears to be consistent between the 5 species and 3 species models with the most significant difference being the drop-in concentration. This will have profound effect on the subsequent development of the model to predict tank house performance and roughness. As such, the 5 species model will be used for the remainder of this work.

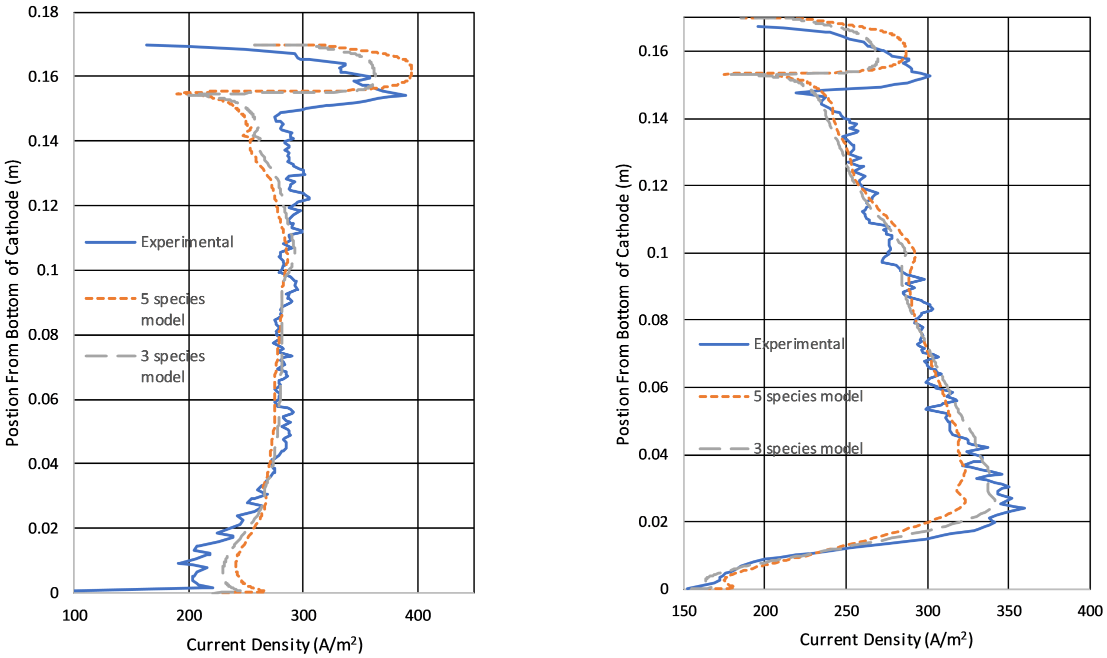

(a) Straight cathode

(b) Tilted cathode

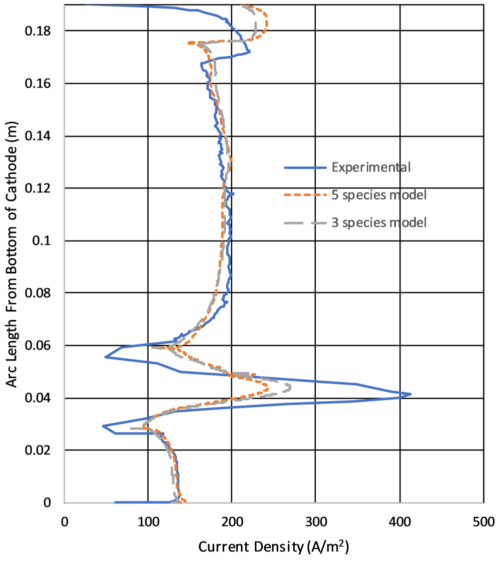

(c) Nodule cathode

Figure 4.33: Showing current density along the cathode with 5 species versus 3 species models.

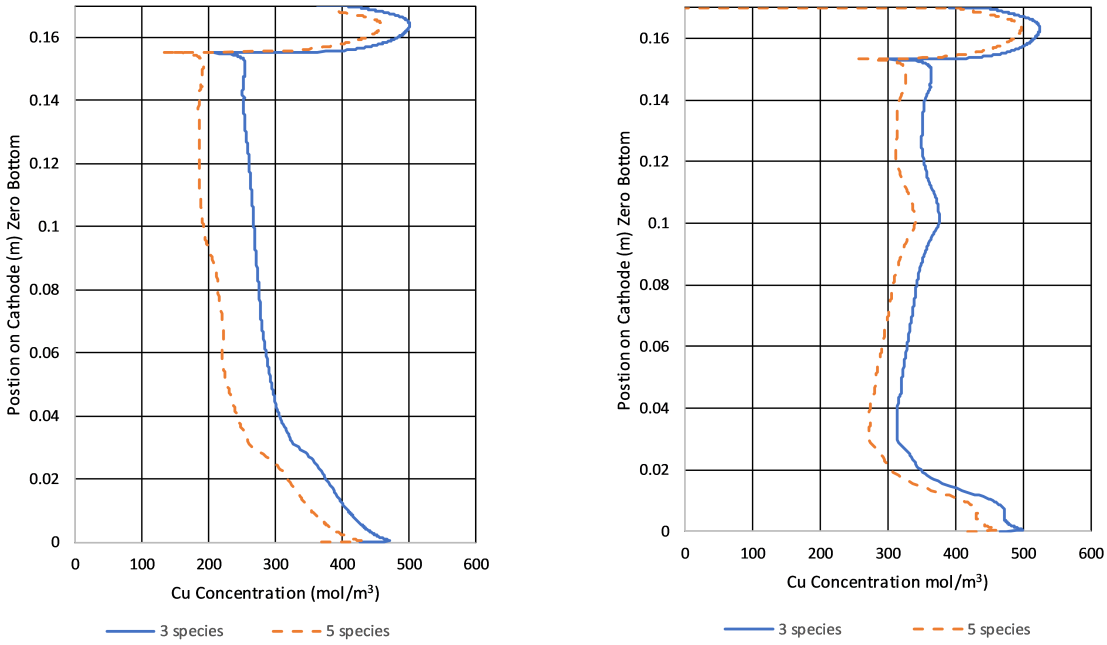

(a) Straight cathode

(b) Tilted cathode

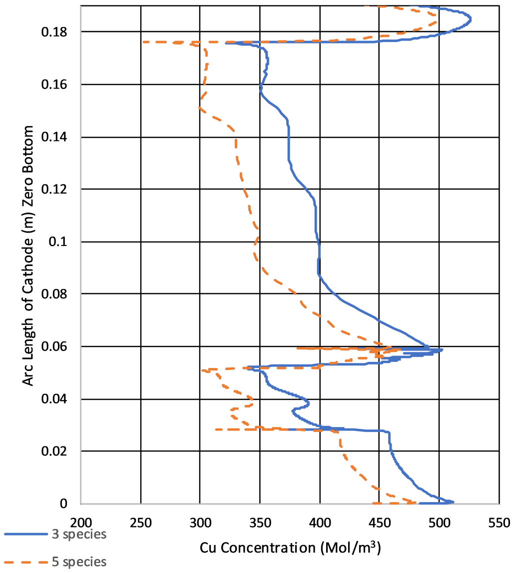

(c) Nodule cathode

Figure 4.34: Showing copper concentration along the cathode with 5 species versus 3 species models.

CHAPTER 5

INVESTIGATION OF FLUID DEPOSIT INTERACTION VIA TIME STEPPING

5.1 Introduction

To understand the developments of time stepping a brief review of Finite Element Methods is needed. Finite element methods are techniques to solve differential equations that describe physical phenomena. The equations used are based on the physics to be modeled. For example, the Navier–Stokes Equations are used to describe fluid flow, the Nernst–Planck Equations are utilized to determine ion transport and electrochemical outcomes and Butler–Volmer equations to describe electrode kinetics to name a few covered previously. These equations can be used to describe the effects of variables in the appropriate applications. To produce meaningful results the geometric areas that these equations are applied to are discretized in a mesh. This mesh has connecting points referred to as nodes. It is at these nodes that the equations are solved to produce results. Using discretization and solving these equations at the nodes is done by linear algebra techniques for solving systems of equations. Therefore, the finer the mesh, the more nodes and the larger the matrix requiring solving. The mesh resolution is directly related to the accuracy of the results, but it comes with computational costs.

This matrix is solved using numerical methods to determine the solutions to the specific boundary conditions applied to the model. Models most often fall under two categories: steady state conditions or dynamic conditions.

For dynamic models the solutions can become more complex. As mentioned, numerical methods are used to determine solutions. In transient models, solutions must be provided at every time of interest. Because of the nature of modeling the solution is not continuous, but a series of solutions at each time. Because of the extra computational expense of providing solutions at times of interest, economic means are used to reduce required solutions to a minimum. The first of these is the user input of the duration and the requested time resolution. This form the basis of how often the user needs a solution. These factors determine the minimum time step used by the model.

Using various algorithms and techniques an initial time step solution is determined, followed by successive solutions at subsequent points in time. What happens next is best described using Figure 5.1. The blue represents the perfect solution to the model being studied. The red line represents the approximation obtained by numerical methods. The red dots represent each time a solution is calculated. If the desired function doesn't change much with time the solver is able to extrapolate and take longer steps between needed solutions, thereby reducing the number of computations needed. In the areas where there is a larger change, the solutions cannot be extrapolated well and shorter steps between the solutions are needed.

The flows in our system have a small amount of turbulence due to bubble generation

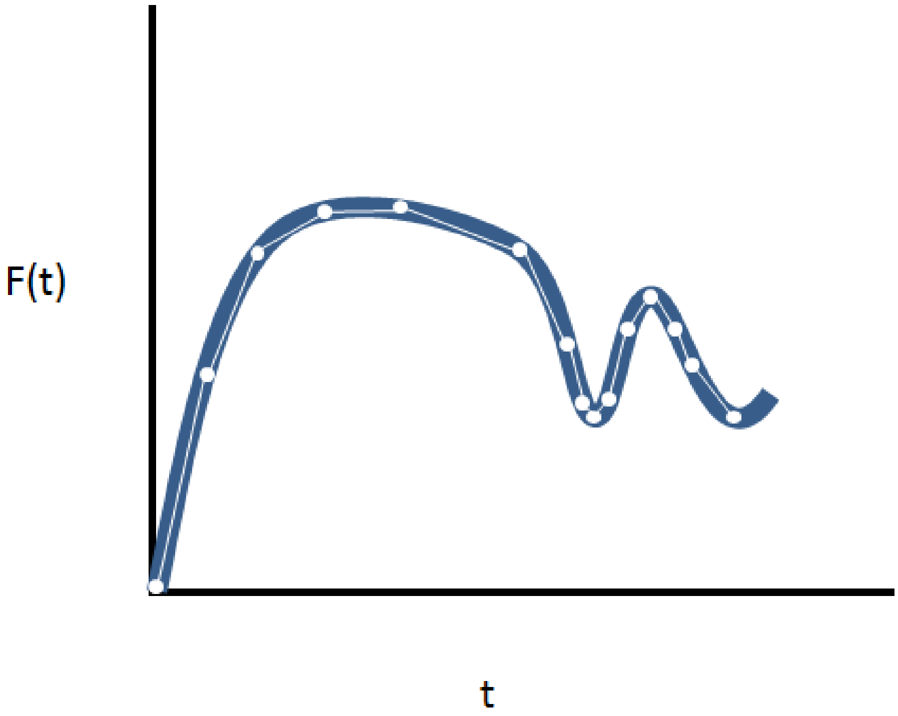

Figure 5.1: Representation of solution approximation through time. The white dots and connecting lines represent model calculation points. The blue line represents the experimental data.

near the anode. This means that the model requires small time steps to be able to compute accurate solutions. Consequently, in our previous model version and older computer equipment 6 days of plating required 300 days of computer time for our system.

In order to improve computation times, scientists and engineers have developed a number of approximations to reduce computational time in fluids - namely RANS (Reynolds-averaged Navier–Stokes equations) and LES methods (Large eddy simulation). Both methods use filtering to effectively average flows and reduce computational expense. However, LES and DNS require 3D modeling to resolve correctly. The region in which we are operating is transitional flow. It is low velocity and slightly turbulent. The above approximations work well for high Reynolds number systems where the amount of turbulence is high. Because of the transitional nature of the flows we decided to preclude using a turbulence model. Also, the turbulence experienced will not resolve correctly in 2D. However, results in the previous section demonstrate the validity of the approach.

The electrowinning system is interesting in this regard. Some aspects of the flow are turbulent, but the deposit growth is much more linear with time. Thus, in order to reduce the computation time, short-term current density calculations were used and extrapolated to calculate the deposit thickness. Fluid flow patterns were determined using much shorter-term fluid flow calculations. Thus, there are two different time scales of importance, a short one for the fluid and a longer one for the deposit.

Because of this time damped effect of the deposit on a transitory input this work attempts to study the fluid deposit interaction by running the fluid and electrochemical steps in a series of discrete simulations and extrapolating the deposit growth between them. There are two issues to this method which should be addressed. The first is that the data collection period for time averaging must be sufficiently long to capture a true average. This is represented in Figure 5.2.

The second is to not make the deposit interpolations between models too long. If the interpolation becomes too large the results will not be accurate as the intermediate interactions which influence the deposit are not captured. This work will seek to explore this concept.

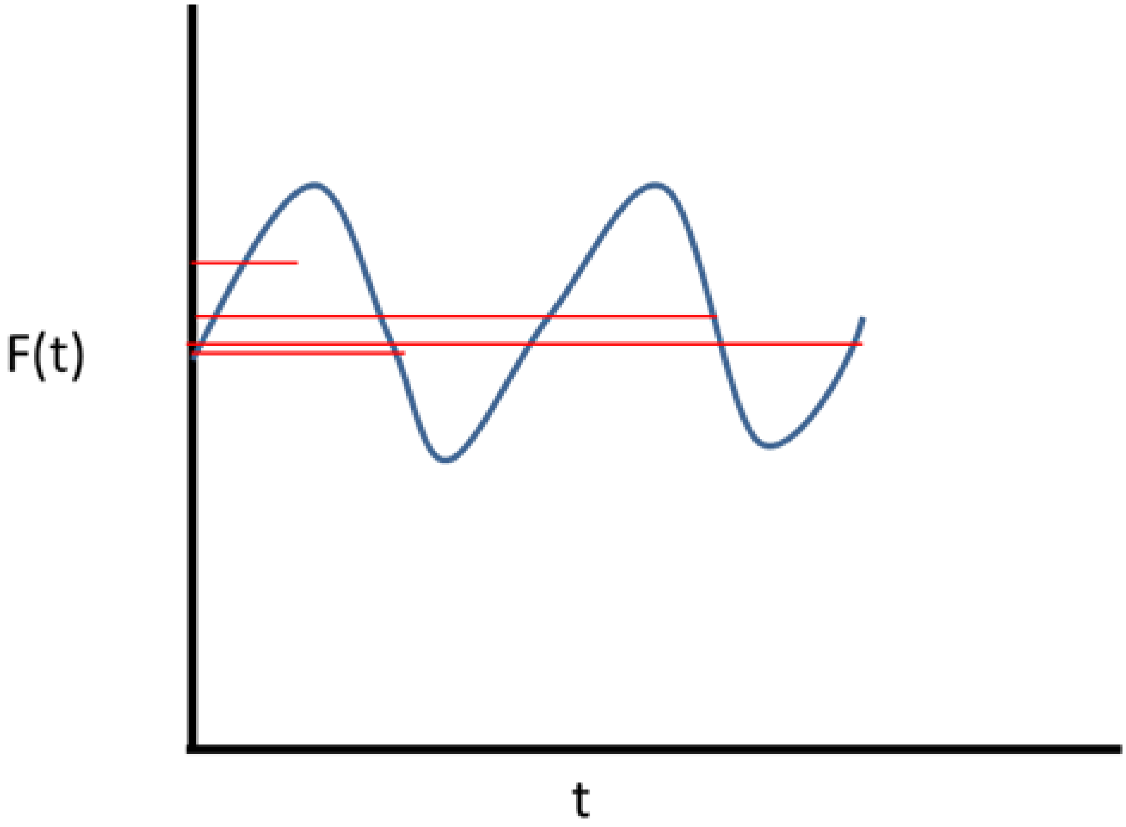

Figure 5.2: Time averaging of perturbations with different time lengths. The red lines represent the average value of the function over the time period associated with it.

5.2 Needs and Objectives

Due to the nature and high degree of nonlinearity of this model creating a viable method to solve for the equations and physics required a novel approach. First and foremost, the flow is slightly turbulent with a Reynolds number of approximately 10,000, which means for the fluid solver the step size will decrease and the overall solution time becomes prohibitive. There has been a significant body of work that has been developed to address turbulent flows in fluid flow models. All these ($k-\epsilon$, $k-\omega$, SST, LES (Large Eddy Simulation, etc.)) have been developed to reduce the computational cost of simulation while maintaining reasonable accuracy in the system studied. However, because of the nature of the mass transport and the variable nature of the various fluxes and the resulting effects on the deposit morphology the decision was made to forgo these methods, particularly because the system is in the transition range. A modified DNS (direct numerical simulation) method was used for the following reasons.

1. No loss of phenomenological resolution. Examples would include instantaneous current density, the ratio of current density to limiting current density, fluctuation in boundary concentrations etc. These are important because the effects of parameters such as these do not scale linearly and the original data may be examined on their own merit without time scale filtering.

2. The effects of the deposit will dampen the effects of the fluid velocity oscillations. Early modeling showed that the deposit averaged out the perturbations of the mass transport-current density interaction, effectively allowing averaging to be transferred from the fluid simulation to the deposit model. This would allow retention of full fidelity for the fluid simulation without the expense of full time scale simulation.

3. Deposit phenomena such as nucleation and roughness development are linked to mass transport-current density interaction. Losing the variation of these could result in loss of important variation.

4. Navier-Stokes equations describing laminar and turbulent flows provided the mesh resolution and time resolution needed.

However, DNS is still computationally expensive or prohibitive. It requires that the mesh resolution be sufficiently small to resolve all turbulent length scales. In this model, true DNS is not utilized because the mesh resolution is not sufficiently resolved to capture all bulk turbulence scales.

5.3 Methods

5.3.1 General Modeling Approach

To meet the needs and objectives outlined previously, we present a method of utilizing discrete simulations as part of an overall morphological simulation. To discuss the theory of simulation time stepping the following variables will be defined.

$$\xi_i = \text{Simulation Period} \tag{5.1}$$

In the simulation transient model ξ_i is the time duration of the ith simulation period. This represents the time period of fluid-electrochemical simulation in the fluid-electrochemical time scale.

$$\tau_i = \text{Time Step Period} \tag{5.2}$$

In the model τ_i is the deposit or real time duration of the ith simulation period. This is the real or deposit time that the simulation period is applied to. The model is run as shown in Figure 5.3. The first stage is that the model inputs are entered in by the user and run. This includes all the typical fluid and electrochemical parameters. It also includes the parameters needed for time looping. These include time to steady-state, number of desired time loops i, the length of real time of the first loop τ_1 and the length that the simulation will be time averaged ξ_1.

Due to the nature of the plating the deposit topography provides feedback to the fluid and electrochemical physics in subsequent steps. For this reason, the second step in Figure 5.3 shows the utilization of a geometric series. The use of a geometric series allows the nonlinear progression of real time. This allows for greater simulation accuracy in the initial loops of the model where it is most needed and lower resolution at the end. Thus, each time leap was calculated according to the expression [106]:

$$\text{Time Leap} = ar^n \tag{5.3}$$

where a is the first-time leap (τ_1), r is the exponent base, and n is the simulation number (which starts from 0).

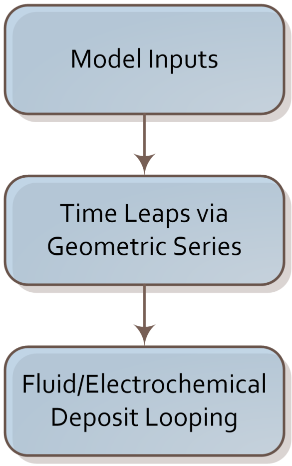

Figure 5.3: Solution method for electrochemical and deposit solutions.

The discrete time leap terms are summed and solved for final time [106]:

$$\text{Total Time} = \sum_i ar^{n-1} = \frac{a}{1-r} \tag{5.4}$$

Figure 5.4 shows the geometric series utilized for a first time leap (τ_1) of 1 hour and 15 steps:

Solving for r is the second step in Figure 5.3. This is only needed once at the beginning of the model. The last step is the calculation of the fluid-electrochemical loop shown as the last step. The details of this step are shown further in Figure 5.5.

The first step in Figure 5.5 shows the electrochemical initialization of the model. This is done with only the potential field in the electrochemical module being solved. This greatly reduces the convergence time of the first electrochemical transient step. Step 2 is a time dependent fluid-electrochemical step run to the point of steady state. Step 2 begins from

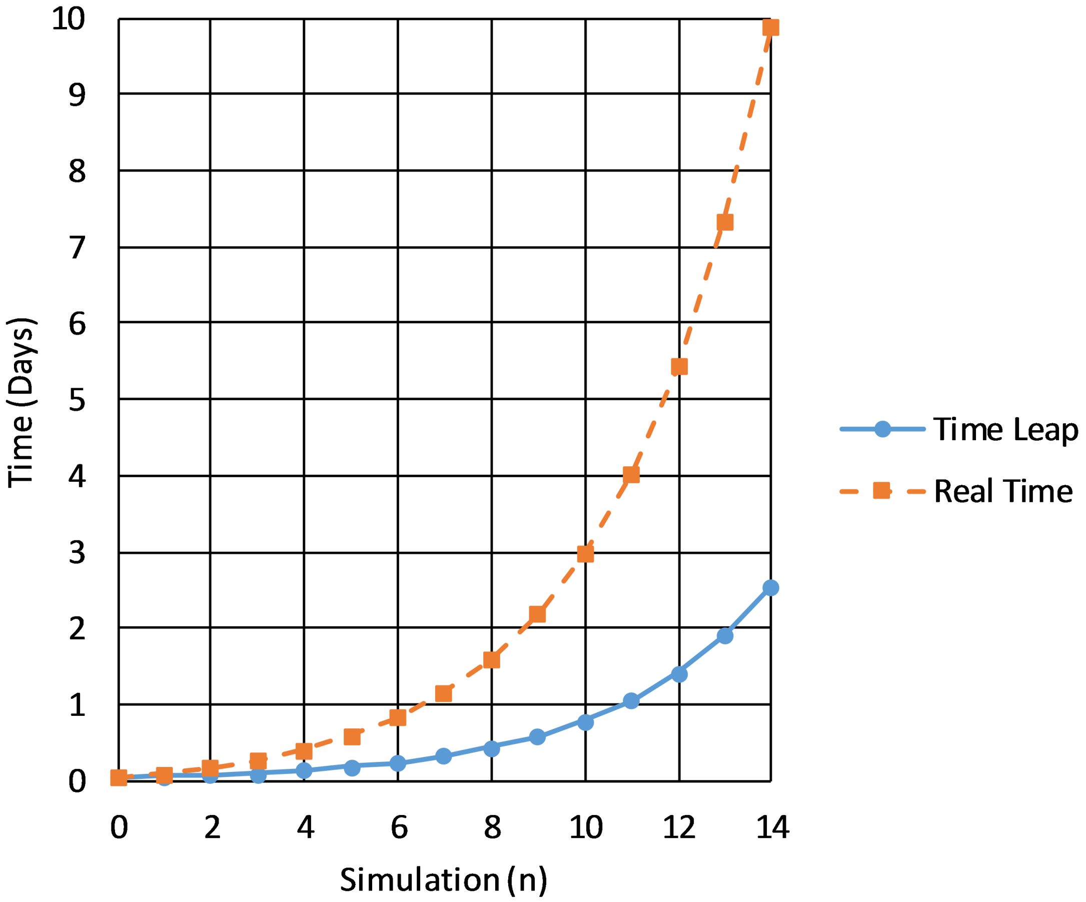

Figure 5.4: Simulation times as a function of simulation number and time (days).

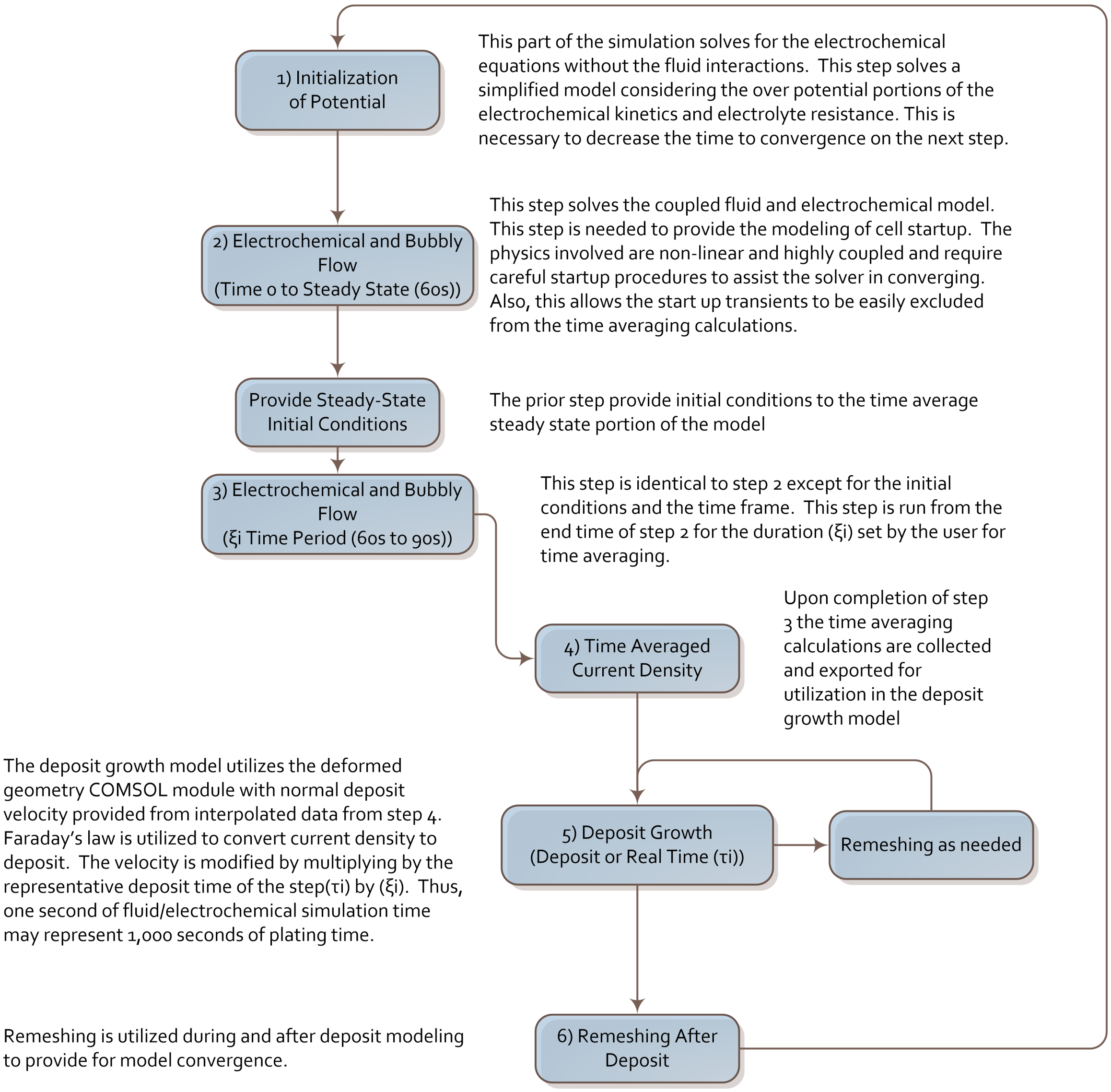

This part of the simulation solves for the electrochemical equations without the fluid interactions. This step solves a simplified model considering the over potential portions of the electrochemical kinetics and electrolyte resistance. This is necessary to decrease the time to convergence on the next step.

This step solves the coupled fluid and electrochemical model. This step is needed to provide the modeling of cell startup. The physics involved are non-linear and highly coupled and require careful startup procedures to assist the solver in converging. Also, this allows the start up transients to be easily excluded from the time averaging calculations.

The prior step provide initial conditions to the time average steady state portion of the model

This step is identical to step 2 except for the initial conditions and the time frame. This step is run from the end time of step 2 for the duration (ξi) set by the user for time averaging.

Upon completion of step 3 the time averaging calculations are collected and exported for utilization in the deposit growth model

The deposit growth model utilizes the deformed geometry COMSOL module with normal deposit velocity provided from interpolated data from step 4. Faraday's law is utilized to convert current density to deposit. The velocity is modified by multiplying by the representative deposit time of the step(τi) by (ξi). Thus, one second of fluid/electrochemical simulation time may represent 1,000 seconds of plating time.

Remeshing is utilized during and after deposit modeling to provide for model convergence.

Figure 5.5: Solution method for electrochemical and deposit solutions.

a point of zero current and ramps to the defined steady state current. The purpose of this step is to provide steady state initial conditions to step 3. Upon reaching the time defined by the user as steady state step 2 ends and transfers all fluid and electrochemical variables to step 3 as initial conditions. Step 3 runs for a period of time defined by the user (ξ_i). The simulation in step 3 is utilized as the source of the time averaging of current density. It is separate from step 2 so that the time averaging is not confounded by startup transients. Also, due to the nature of some of the calculations involved it was removed from step 2 to prevent divisions by zero at time 0. Upon completion of step 3 the time averaged current density is exported via step 4 to step 5 where the deposit growth is modeled. This is covered further in section 5.3.2. Remeshing is utilized as needed and at the end of the simulation with step 6. The loop is then repeated a number of times as specified by the user.

It is important to understand that upon the start of each loop the fluid and electrochemical model is started without any variables save the geometry being passed from the last loop. This ensures that the fluid-electrochemical model is influenced only by the geometry and not by any looping artifacts.

5.3.2 Deformation

The deposit growth velocity is expressed as:

$$V_{loc-ave} = \frac{i_{local-ave}\left(\frac{MW_{cu}}{\rho_{Cu}}\right)}{nF} \tag{5.5}$$

where $i_{local-ave}$ is a vector (see equation (5.6)) which is given by the equation:

$$i_{local-ave} = \frac{\int_0^{\xi_i} i_{loc}\mathrm{d}\xi}{\xi_i} \tag{5.6}$$

Position is given by the expression:

$$X_{loc_i} = \left(\frac{\tau_i}{\xi_i}\right) V_{loc-ave_i} \tag{5.7}$$

And the total deposit thickness as:

$$X_{loc} = \sum_j X_{loc_i} \tag{5.8}$$

This thickness is then used as the starting condition for the next simulation. The model is completed by looping in this manner. It is also important to note that these parameters ξ_i and τ_i need not be the same at each iteration.

5.3.3 Time Scales

Because of this methodology two time domains are possible and the total times represented below:

$$\text{Total Simulation Time} = \sum_i \xi_i \tag{5.9}$$

$$\text{Total Deposit Time} = \sum_i \tau_i \tag{5.10}$$

Therefore, to transform the simulation time denoted by ξ to display deposit or real time scale denoted by τ, the following transformation is utilized (whereξ_i and τ_i are constants defined above).

$$\text{Deposit Time} = \int_0^{\xi} \left(\frac{\tau_i}{\xi_i}\right) \mathrm{d}\xi \tag{5.11}$$

Further because of the loop described in Figure 5.5 the real or deposit time after any number of loops (j) becomes:

$$\text{Total Deposit Time} = \sum_j \left[\int_0^{\xi_i} \left(\frac{\tau_i}{\xi_i}\right) \mathrm{d}\xi\right] \tag{5.12}$$

Thus, the simulation result may be represented in either time domain. This is particularly useful when looking at fluid scale phenomena or overall deposit characteristics. Additionally, the computational time can be greatly reduced. Figure 5.4 shows the difference between time leaps and total deposit (real time) as described by equation (5.12).

5.3.4 Methodological Validation

Because this method involves significant extrapolation, the accuracy of this method depends on appropriate validation and careful selection of parameters. The simulation time is directly related to both the computational expense and the accuracy of the results. Two main concerns are expressed as:

1. Is τ_i of sufficient duration to capture a true representation of the average fluid velocity and electrochemical effects?
2. How much larger can ξ_i be than τ_i before significant solution degradation occurs?

Item 1, can be expressed in the following manner by Rewriting equations (5.5) and (5.6) we have:

$$\text{Vel}_{\text{local}-\text{ave}} = \frac{\int_0^{\xi_i} Vel_{loc}(t)\mathrm{d}t}{\xi_i} \tag{5.13}$$

Which if expressed as a a limit gives the true average:

$$\text{True } V_{loc-ave} = \lim_{\xi_i \to \text{Total Deposit Time}} \frac{\int_0^{\xi_i} Vel_{loc}(t)\mathrm{d}t}{\xi_i} \tag{5.14}$$

However, a more practical expression can be used to determine if ξ_i captures perturbations sufficient to be useful and this is defined as:

$$\frac{\int_0^{\xi_1} Vel_{loc}(t)\mathrm{d}t}{\xi_1} \approx \frac{\int_0^{\xi_2} Vel_{loc}(t)\mathrm{d}t}{\xi_2} \tag{5.15}$$

where $\xi_2 > \xi_1$. When $\Delta\xi_i$ fails to illicit sufficient differences to be satisfactory, then the DNS time is sufficiently long to provide a time average. With DNS simulations performed between geometric changes it is likely that if τ_i is too large the simulation will not be accurate. Stated in the inverse and mathematically as an error of deposit thickness:

$$\lim_{\tau_i \to \xi_i} \left(\frac{X_{loc}(\tau_1) - X_{loc}(\tau_2)}{X_{loc}(\tau_2)} \right) = 0 \tag{5.16}$$

However, it is often impractical or impossible to perform a full-time scale DNS simulation to determine the error so the following are provided as one means of quality determination. The first is supplied as a boundary error expression:

$$\frac{\int_0^L \frac{X_{loc}(\tau_1) - X_{loc}(\tau_2)}{X_{loc}(\tau_2)} \mathrm{d}L}{L} < \text{minimum quality} \tag{5.17}$$

where L is length of deposit. These are provided as illustrations of possible means of evaluating the changes in error based on ξ_i. Lastly, it is always helpful to evaluate the results of any model against physical experimentation and as such should be utilized as a final test to determine the suitability of the selected parameters of ξ_i and τ_i.

The issue then becomes how far can ξ_i diverge from τ_i and still produce viable results. This work will systematically explore the relationship between these variables and the effect they have on the simulation results.

5.3.5 Fluid and Echem Model

The model used is in basic functionality the same as described in Chapter 4. There are however notable additions in the need to add a deformation model.

5.3.6 Deformation and Solver

As discussed in section 5.3.2 equation (5.5) gives the local velocity. Figure 5.5 shows the general solution method and a more detailed discussion of the solution is warranted as this portion of the research was the most time consuming and costly of the project.

The deformed geometry physics module is used to create the deformation. Because of the nature of the fluid flow it became impractical to solve for deformation directly coupled to the echem and fluid solutions. As Figure 5.5 shows a time stepping methodology was utilized where the fluid and echem models are run for a short time and the results applied to the deformation model. The exact implementation of this methodology was complex.

The overall objective was to keep all development work within standard COMSOL functionality. This allows seamless adoption of end users utilizing COMSOL applications.

After the fluid-echem model is run the resulting current density versus position data is exported. These data are then reimported utilizing an interpolation function. This is critical for the deformation in terms of being able to remesh. Figure 5.6 shows conceptually remeshing. It is needed because the solution is determined via solution of simultaneous equations at nodes. As the nodes shift position they can become less ideally positioned increasing the solution errors. Also, the solution can become unstable as shown in Figure 5.7. This can be overcome by remeshing when certain threshold criteria are met.

This looping required custom programming which is made possible through the COMSOL application builder methods. These operate in a similar fashion to Excel VBA macros and include a recorder function. Each of the loops is saved internally as its own discrete result.

In addition to the average current density which is passed between model steps, every variable which requires an initial condition (real time, current efficiency, etc.) is passed

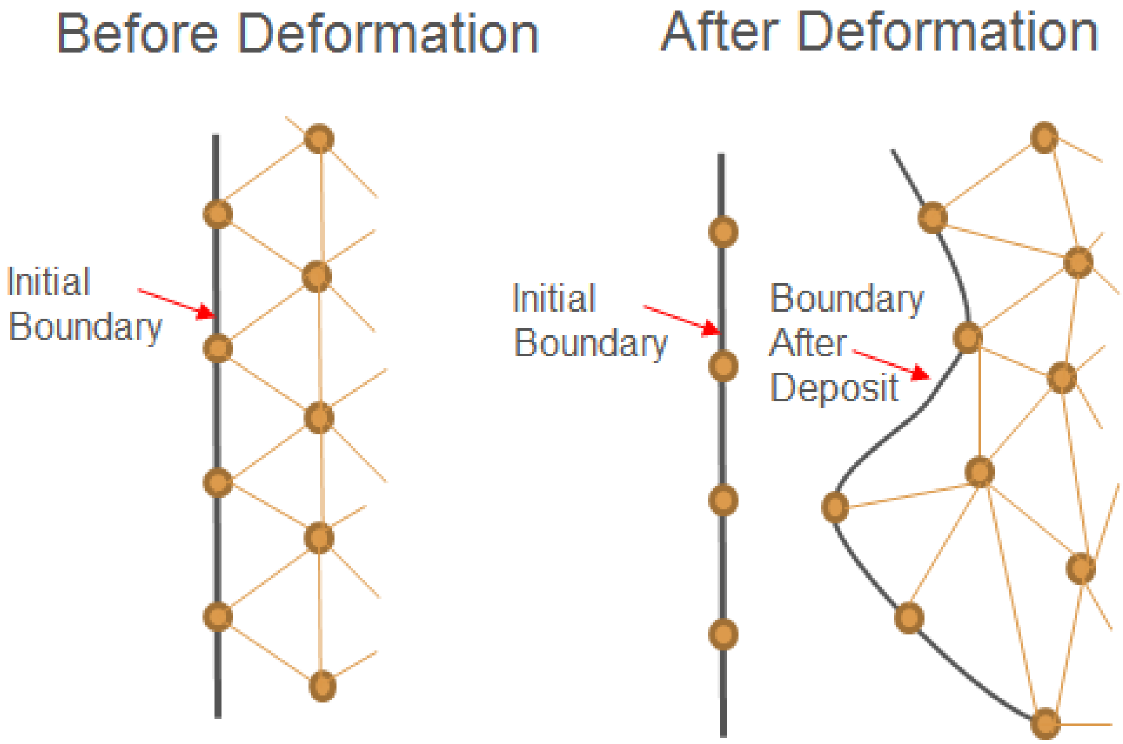

Figure 5.6: Schematic diagram showing remeshing.

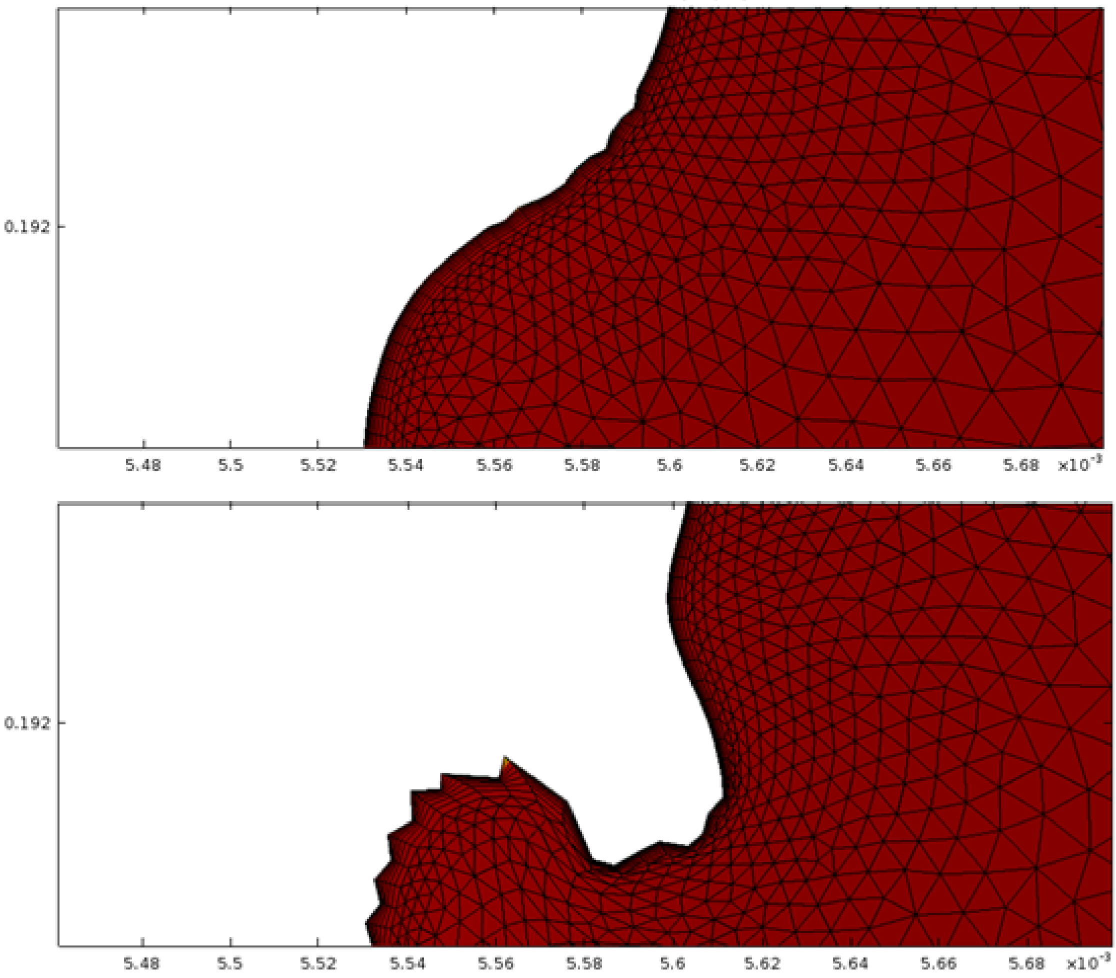

Figure 5.7: Meshing showing instabilities.

as well. The deformed geometry is saved and imported again to the model for use as the geometry for the following time step.

5.3.7 Assistance Methods for Numerical Methods

Due to the nature of this model and the discovery of negative feedback loops encountered in the model a number of numerical assistance methods were utilized to make convergence possible and allow running the simulated deposition to full time.

5.3.7.1 Fluid Helps

COMSOL is a commercially available finite element package that includes a number of standard features which assist general users achieve results. In the fluid model the standard configuration includes stream line diffusion and crosswind diffusion which reduce the apparent turbulence calculated by the model. This is discussed in COMSOL CFD documentation [102]. Referenced sources include [107], [108], [109] and [110]. All of these cover stabilization techniques applicable to fluid modeling.

5.3.7.2 Deposit Smoothing Helps

The majority of the difficulty of obtaining a solution with deformation came from numerically induced roughness interacting with mass transport and deforming meshes as shown in Figure 5.7. This section covers the different methods available to address this issue.

5.3.7.2.1 Savitzky Golay filter. Savitzky and Golay [111] propose a method of low pass filtering using polynomials fitted over a range of data. The proposed algorithm utilizes a polynomial of user defined order and fits the data in a range by regression. The data range recursively moves along the total data range. The original data point is replaced with the polynomial data point. Thus as the algorithm moves along the data set it is subsequently smoothed. This filter type is used in an array of fields. It is utilized to reduce computational expense.

5.3.7.2.2 Deposit smoothing parameter. COMSOL has a deposit smoothing parameter for use in the deformed geometry normal velocity boundary condition. This parameter was essential for any of the deformation studies performed and was set to 0.7 from the 0.5 default for the models performed in this section.

5.3.7.2.3 Artificial diffusion. For the electrochemical model portion the standard crosswind and stream line diffusions were utilized as the default. These were discussed above in section 5.3.7.1. The inconsistent stabilization methods were evaluated and not used. The node to node concentration differences were found to be troublesome in model development. This after several loops would induce artificial roughness.

5.3.7.2.4 Mesh size. Resolving the domain can also be an effective means of eliminating numerical instabilities particularly in mass transport system with high Peclet numbers meaning that diffusion/migration is of a much smaller magnitude than the convection.

5.4 Results and Discussion

The results of the deposition study were unexpected. Due to the complexity of the programming and the intensive time required to develop one of the time looping models only the straight cathode geometry was evaluated with looping. Figure 5.8 shows the results of the deposit models. For time stepping 7, 9, 11 and 15 loops were all modeled with results shown in Figure 5.8. Each of these started with a 1 hour real time step τ_i. The remesh settings had be modified between each of the models, most significantly between the 11 loop and 15 loop models. With the lower loop counts the deformation per step increased and the mesh deformation for remesh was adjusted appropriately. Fewer than 7 loops were not possible or not attempted owing to the difficulties experienced with remeshing large scale deformations in COMSOL. For reference the current density of a single simulation without deformation was used to extrapolate thickness as a test case. Extrapolation of single simulation was done with Faraday's law. This appeared to be the most accurate method of modeling deposit thickness as shown in Figure 5.8.

Due to the difficulty in determining the difference between the 7, 9, 11 and 15 loop deposit models, the deposit thickness of model 7 was subtracted from the other models. The resulting values are plotted in Figure 5.9. In light of the derivations and proofs in section 5.3.4 the results are often less than 0.25 mm showing little difference between the number of loops.

Figure 5.10 shows much the same as Figure 5.9, except that the data are presented as a % of the data from the 7 loop deposit model.

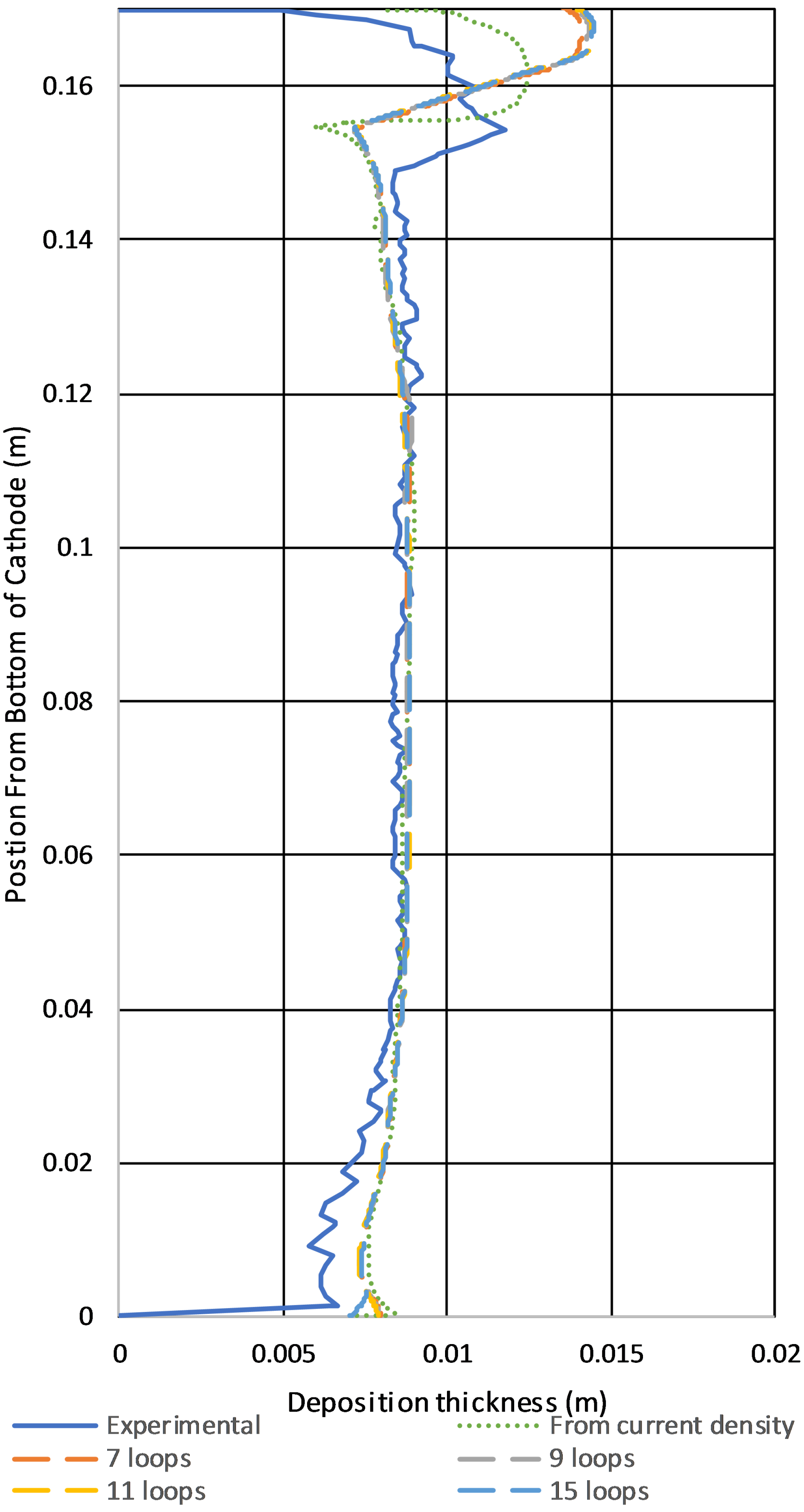

Figure 5.8: Comparison of various deposition models to straight cathode experimental data.

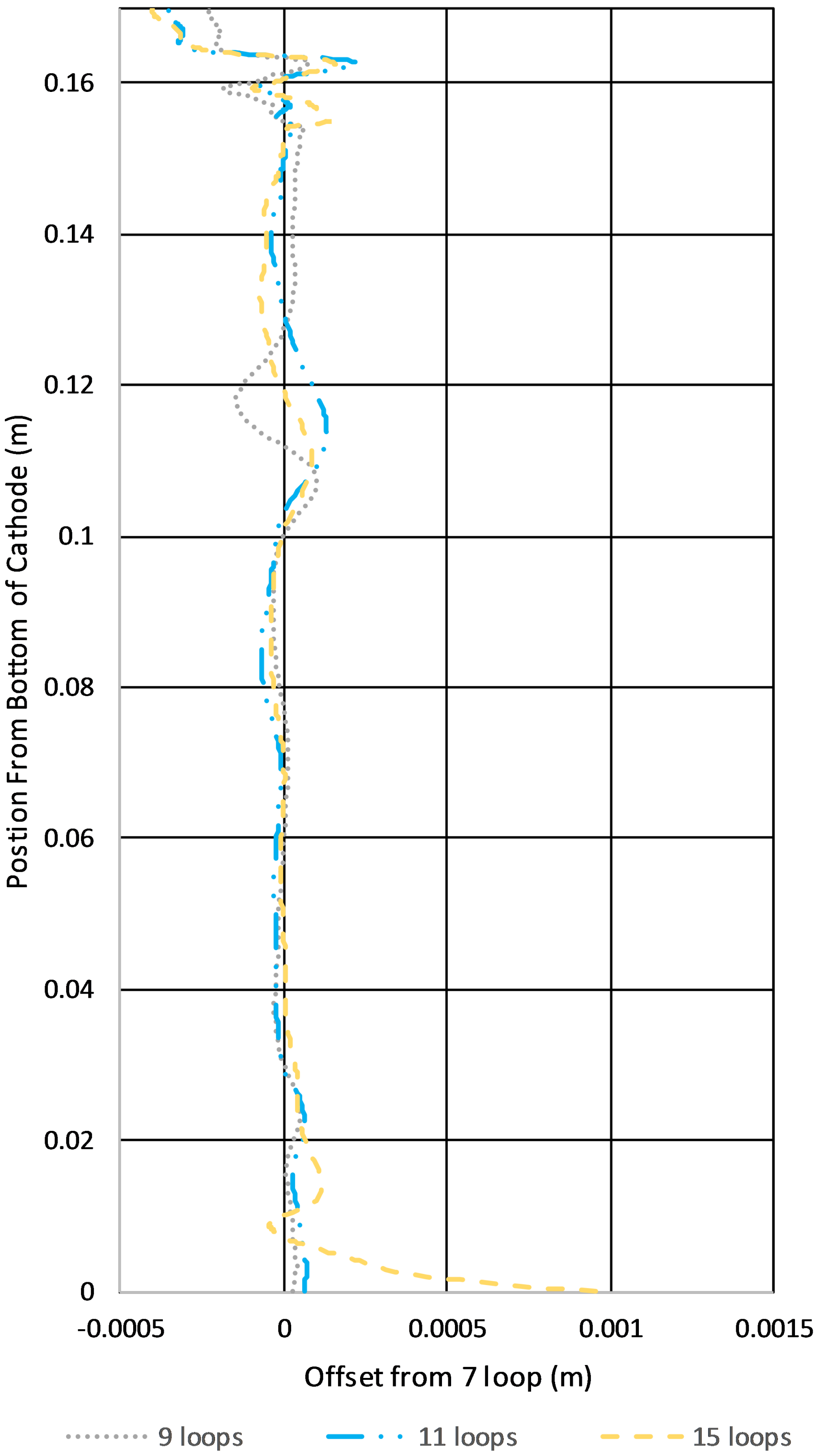

Figure 5.9: Comparison of models run with different number of loops. The difference is calculated by subtracting the 7 loop models from the others to provide for comparison.

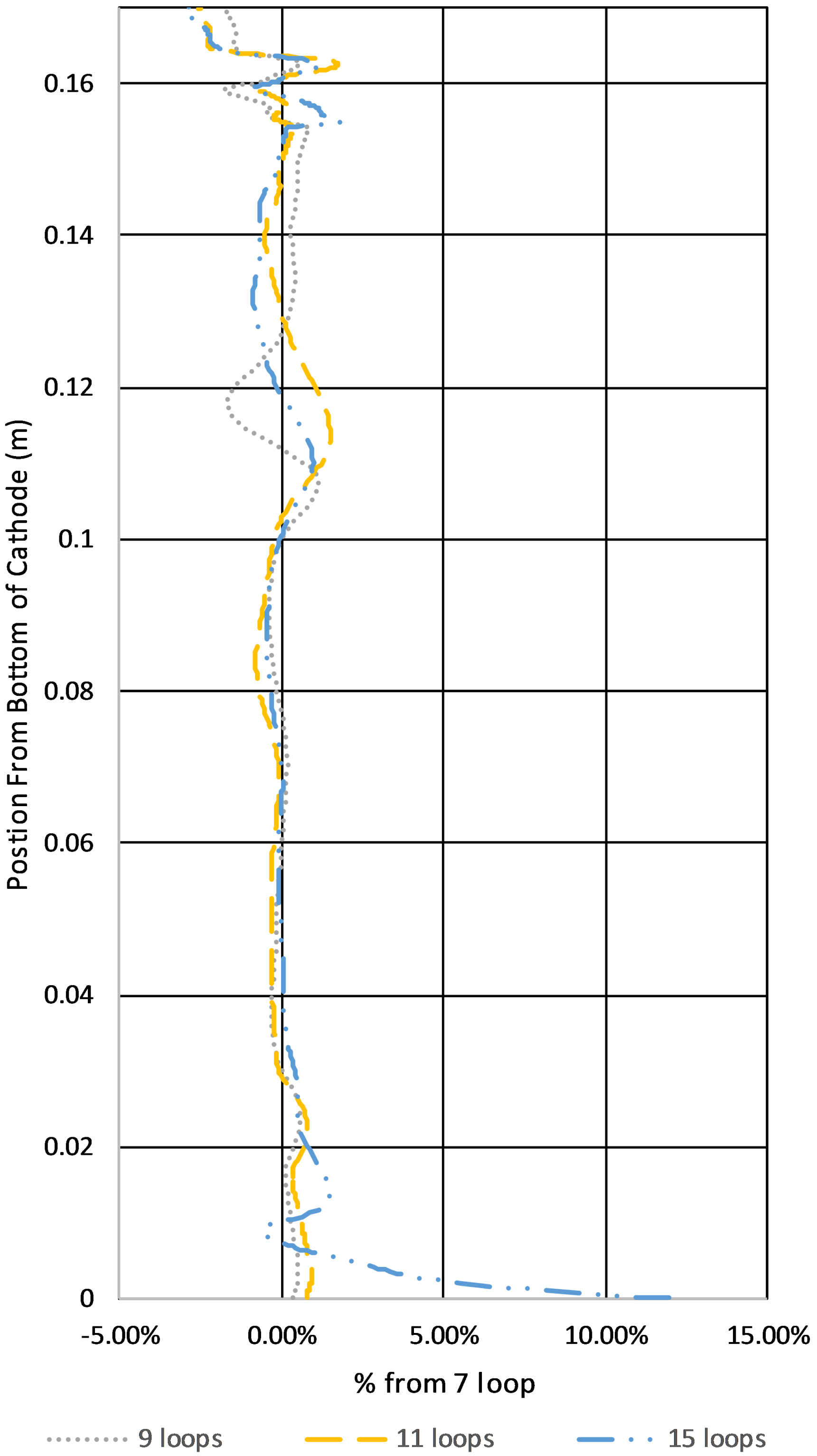

Figure 5.10: Comparison of models run with different number of loops. The difference is calculated by subtracting the 7 loop models from the others and dividing by the local thickness to provide as a % deviation for comparison.

Figure 5.8 shows that the looping deformation models overestimate the ridge thickness and position significantly. This may be due to a number of reasons.

- Inaccurate fluid simulation.
- Over interaction with the electric field causing increased deposition on the notch.
- Failure to account for changes of current density as perimeter increases.
- Nonconservative current density from the interpolation function versus surface area.
- Interpolation method utilized.
- Savitzky Golay Filter interactions.

The interpolation method utilized requires further clarification. Figure 5.11 shows the method utilized in part a. The interpolation function is called by the deformation module from the normal velocity as a function of position on the cathode. The small arrows represent the normal vectors with the large arrows the magnitude of the velocity at that point. While the deformation remains small between loops the error should remain low. However, part b shows the normal vector paths as the deposition occurs. Thus, for larger deformations tracking the function while considering the deposition path may be more beneficial. Also of note is that the current density will need to lower as the perimeter increases. While this may improve accuracy development and implementation time are prohibitive at this time.

However, this may be a moot point as the best accuracy was achieved without the use of looping of the deformed geometry module. Other methods listed in section 5.3.7 were tested, but only the deposit smoothing parameter and the Savitzky Golay filter were utilized.

5.4.1 Savitzky Golay Filter

As part of the development of the looping methodology a filter was needed to reduce the artificial roughness in the deposit. The filter was modified from excel VBA code associated with reference [112]. A valid criticism of utilizing filtering is that you may inadvertently filter out the very features that are of interest. To address these concerns the

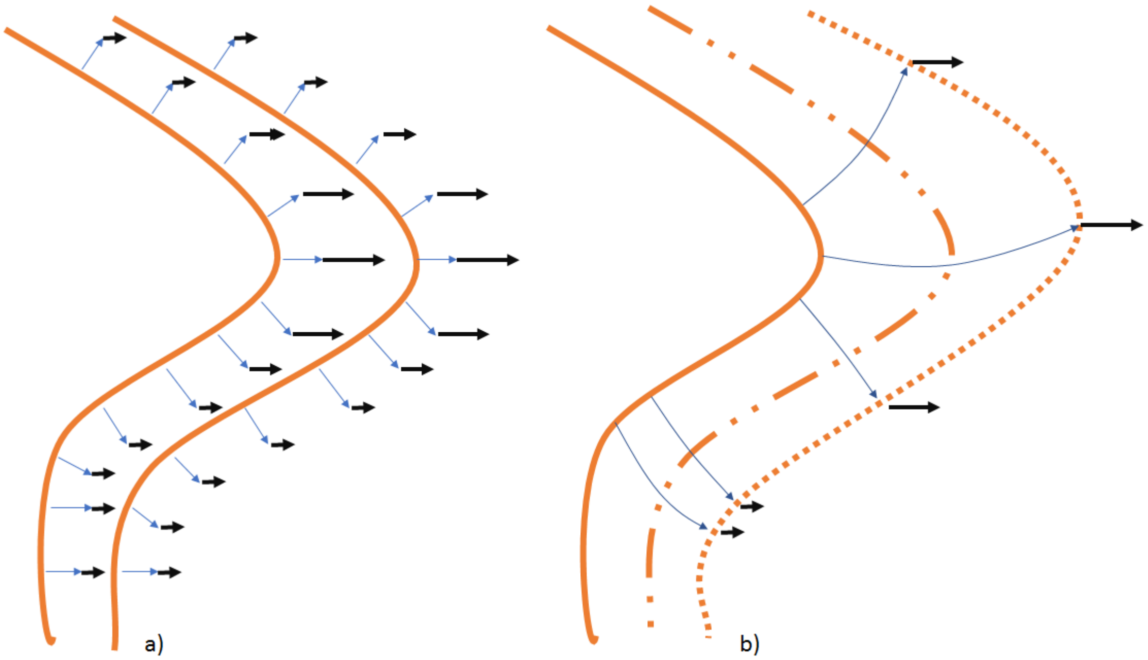

Figure 5.11: Deformation interpolation representation. a) showing current method as a function of height. b) showing normal path proposal where the interpolated magnitude is tracked via streamline.

following figures are provided. The intent of data smoothing and filtering in this work was to perform the minimum filtering to allow numerical stability. Figure 5.12 shows the numerical instabilities that were beginning to cause model failure. This figure is from the filter development on current density data prior to a deformed geometry failure. The parameters used are 2nd order polynomial and a smoothing window of 25 points. If left uncorrected these instabilities result in uneven deposits as shown in Figure 5.13.

When implemented as part of filtering every loop the noise levels in the results were much less severe as shown in Figure 5.14.

5.4.2 Deposit Rate Linearity

To further substantiate the proposal that a single simulation can be used to linearly represent deposit thickness with time, additional experimental data are presented which included tests run under constant voltage conditions. Table 5.1 includes the time to short parameters with the constant voltage experiments. These were run under the same general conditions as described in Tables 3.5 and 3.6. The data presented in Figures 5.15 and 5.16 show that in both instances the maximum projection of the deposit advanced linearly

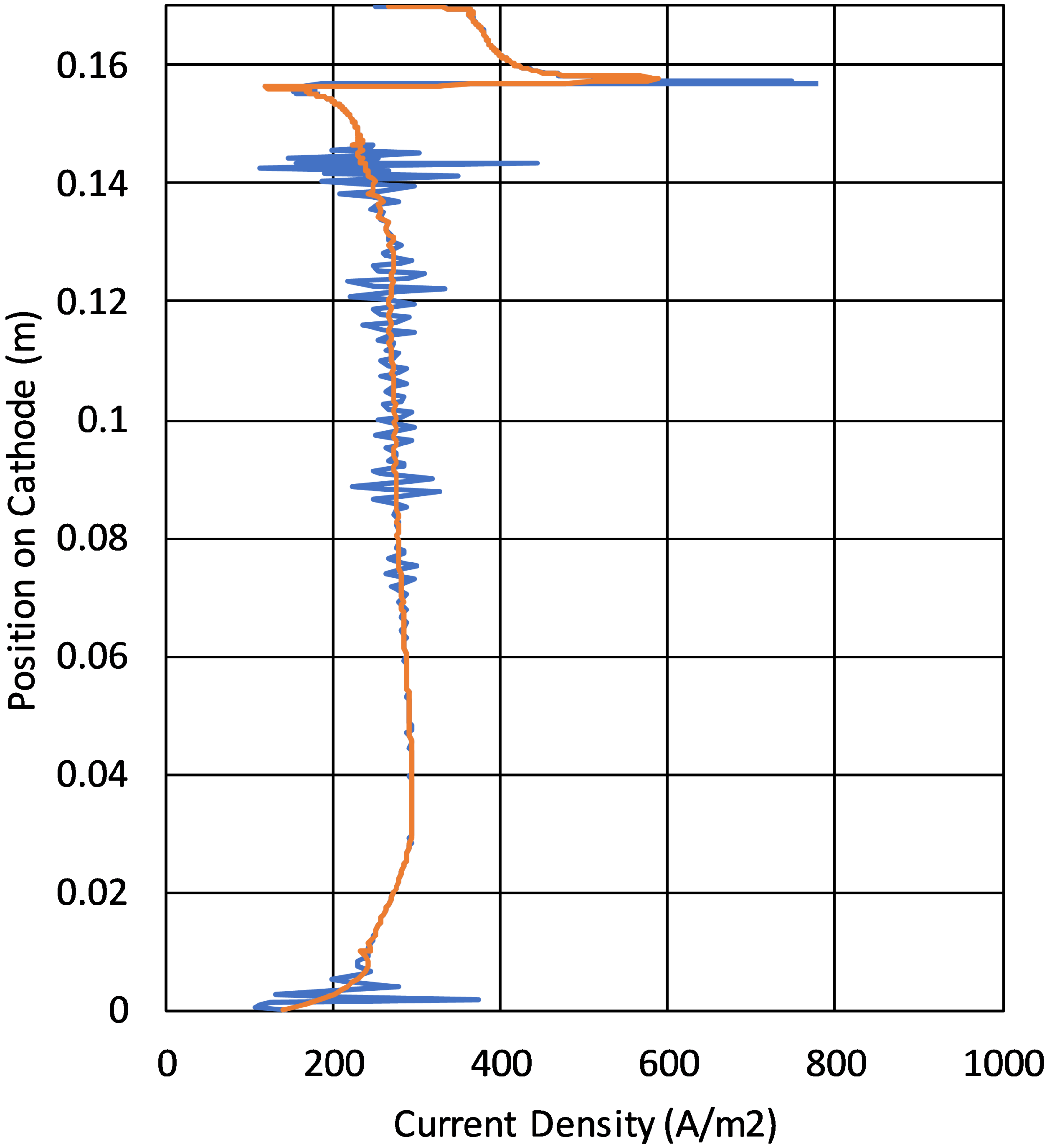

Figure 5.12: Smoothing current density prior to use in deformed geometry of worst case scenario proceeding model failure.

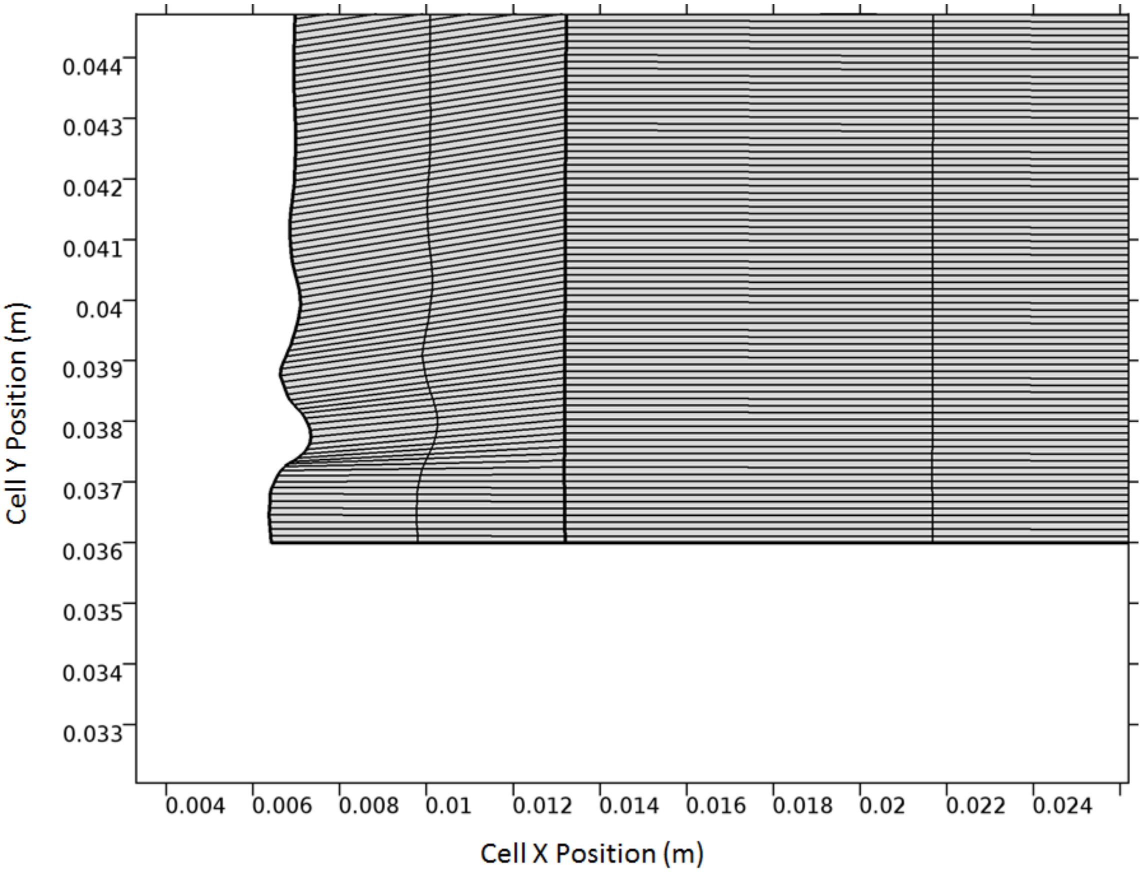

Figure 5.13: Example of numerical instabilities in the deposit surface caused by numerical instabilities. Shown is the deposit domain model which will provide deformed geometry to the electrochemical model. The failure occurred in the electrochemical model flowing this step. Axes are in m. The area shown is the lower left corner of the cell showing the cathode on the left. Reference Figure 3.3 for cell geometry. The additional lines show a mapped mesh which attempted to assist the deformation to prevent mesh element inversion.

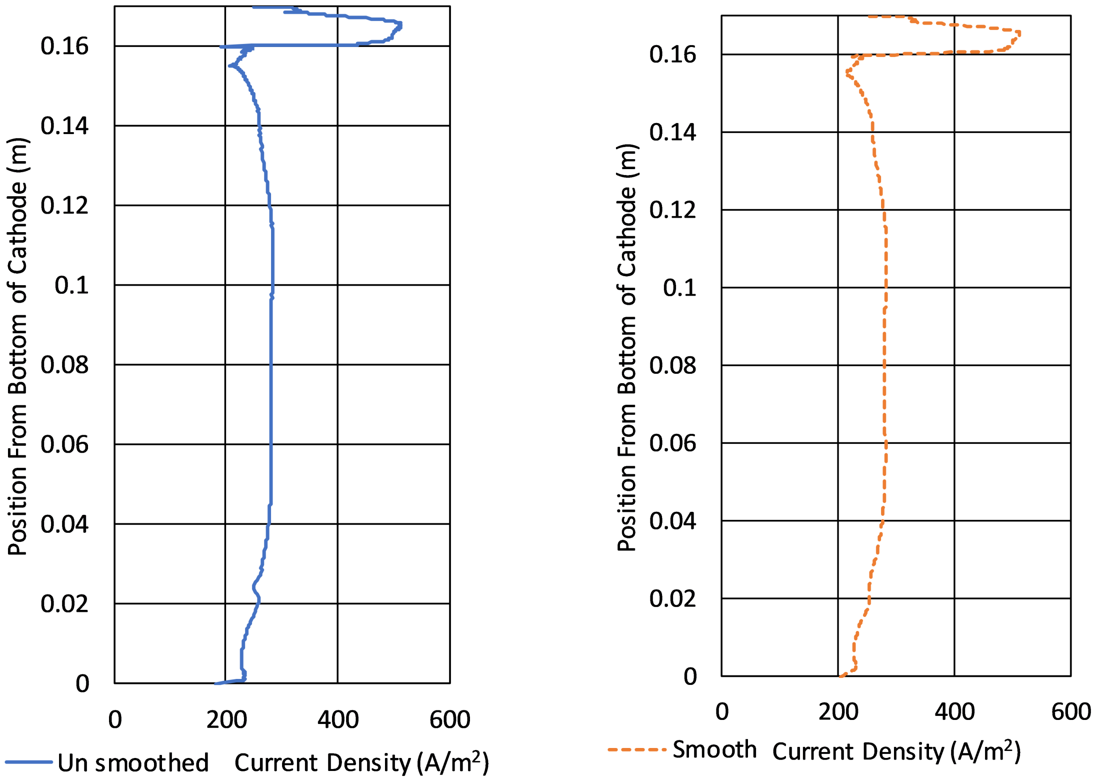

(a) Un-smoothed data from 15th loop

(b) Smoothed data from 15th loop

Figure 5.14: Before smoothing versus after smoothing comparison from data from the 15th loop from model shown in Figure 5.8

Table 5.1: Run time including constant voltage experiments.

Experiment	Run Time Constant Current (Days)	Run Time Constant Voltage (Days)
Straight	9.9	5.33
Tilted	8.6*	6.89*
Nodule	5.96**	5.33*

*Ran until shorting

**Ran until shorting. However, 3 nodules were on cathode and the largest shorted. See Figure 3.33.

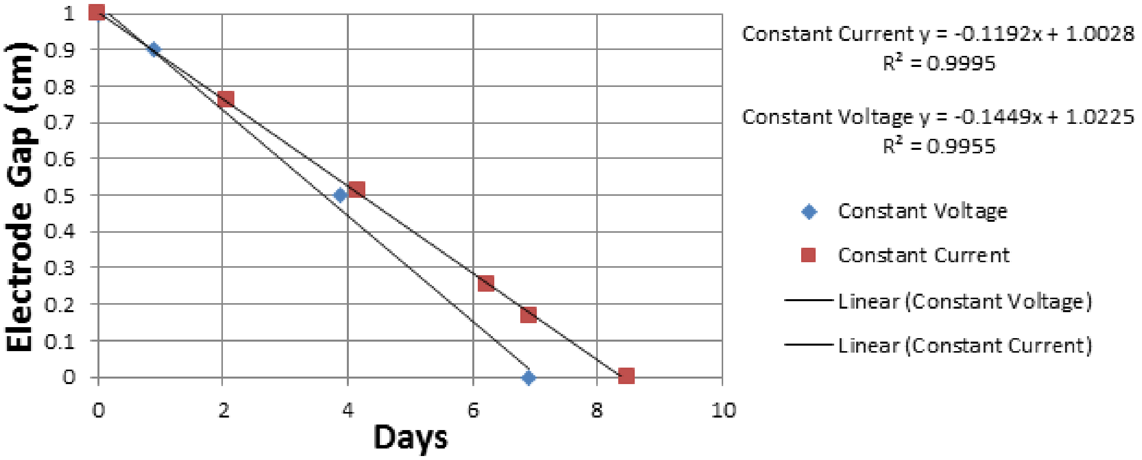

Figure 5.15: Tilted cathode comparison of constant current versus constant voltage conditions. See Tables 3.5 and 3.6 and 5.1 for operating conditions.

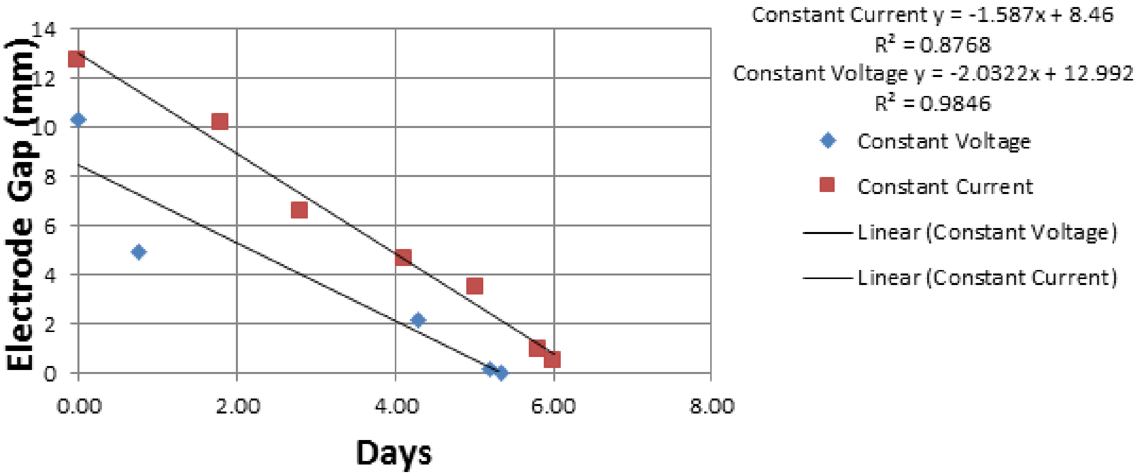

Figure 5.16: Nodule cathode comparison of constant current versus constant voltage conditions. See Tables 3.5 and 3.6 and 5.1 for operating conditions.

with time for both constant current and constant voltage conditions. These findings are important because it shows that the nodules and roughness from the tilted deposit show a linear growth rate rather than a time varying relationship. This validates the assumption of linear deposit growth rates in section 5.4 for a single loop deposit simulation.

5.5 Summary

The results of considering the fluid deposit interaction by time stepping were surprising. It was found that the best method for determining the deposit thickness was to take the time averaged current density and through Faraday's law determine thickness. The time looped examples were difficult to develop and did not in their current implementation improve accuracy. A number of possible reasons for the lack of accuracy was discussed previously. The Savitzky Golay filter was successfully utilized to eliminate numerical instabilities from negative feedback in the model with a minimum of topological interference. It is interesting to observe that electrowinning deposits exhibited similar tendencies to form deposit roughness. Although it is not believed that the model is predicting these in any way, it is subject to the same instabilities caused by high advection to comparatively slow diffusion found in the real system. These results allow confidence moving forward with a simple Faraday deposition model without the further need for sequential, incremental additive simulations to grow the deposits in repeated small steps. Further the results shown in section 5.4.2 validate the assumption of linear deposit growth rates.

CHAPTER 6

MODELING ROUGHNESS FOR DETERMINING SHORT CIRCUITING AND COSTS

6.1 Introduction

The purpose of this section is to perform failure and time to failure analysis. Failure in electrowinning is defined as short circuiting. This occurs when the deposit (typically an abnormal growth or nodule) bridges the gap between the cathode and anode. In this study, abnormal growth is presented as the roughness of a deposit, or as a statistical representation of nodule size/distribution. Nodules are considered statistical outliers of extreme roughness. As such statistical time to failure methods will be utilized to attempt to predict short circuiting through roughness.

Roughness of electrowon copper was investigated in the work of Shukla [32]. Part of his research focused on parameter effects on deposit roughness. In order to determine the roughness of deposited copper a design of experiments was performed by Shukla. The deposit was then sectioned and measured for feature height. This was provided both as a 2D section (length and feature height) as well as small 3D sections (length, width, feature height). The comparison between the line and the area data was used to extrapolate to a full-size cathode area. Further, the deposit roughness change with time was evaluated. Figures 6.1 and 6.2 provide maximum and average feature height as a function of I (current density) to I_{limit} (limiting current density). The I to I_{limit} ratio presented was determined by COMSOL modeling. The settings represented in Figure 6.1 correspond to the roughest parameters studied. Figure 6.2 shows the same type of data under the smoothest studied parameters.

These two Figures 6.1, 6.2 show the data over the range studied by Shukla [32]. It is clear that the upper and lower bounds of feature heights were not well explored by the

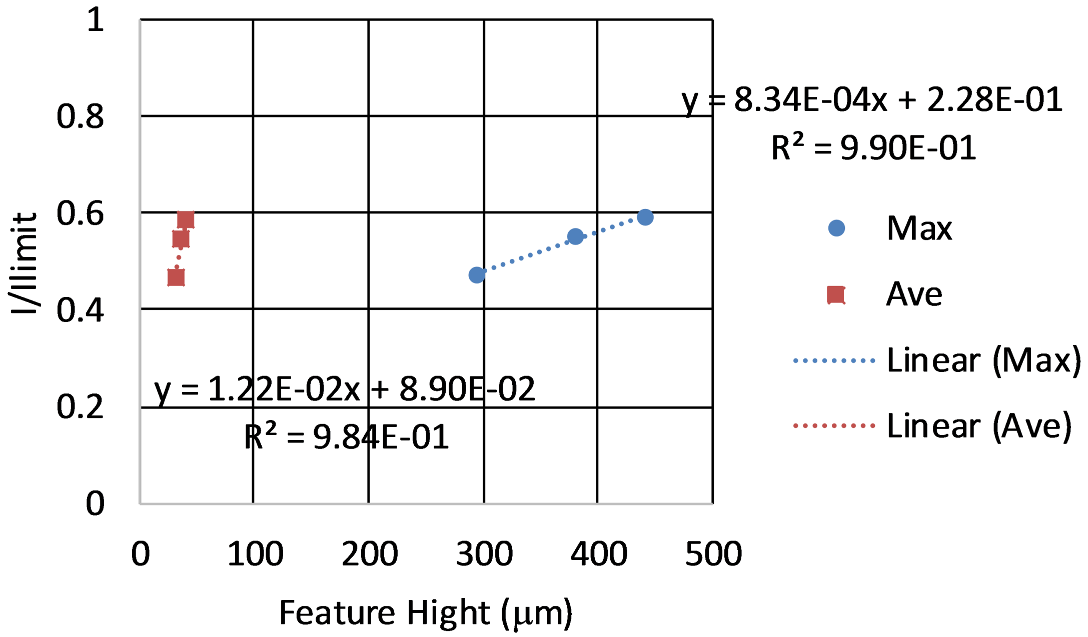

Figure 6.1: Maximum and average feature height as a function of i/i_{limit} for 20 hours of plating, rough conditions. From reference [32] 35 g/l Cu, 55 ^{oC}, 475 A/m^2 and 175 g/ton Guar equivalent.

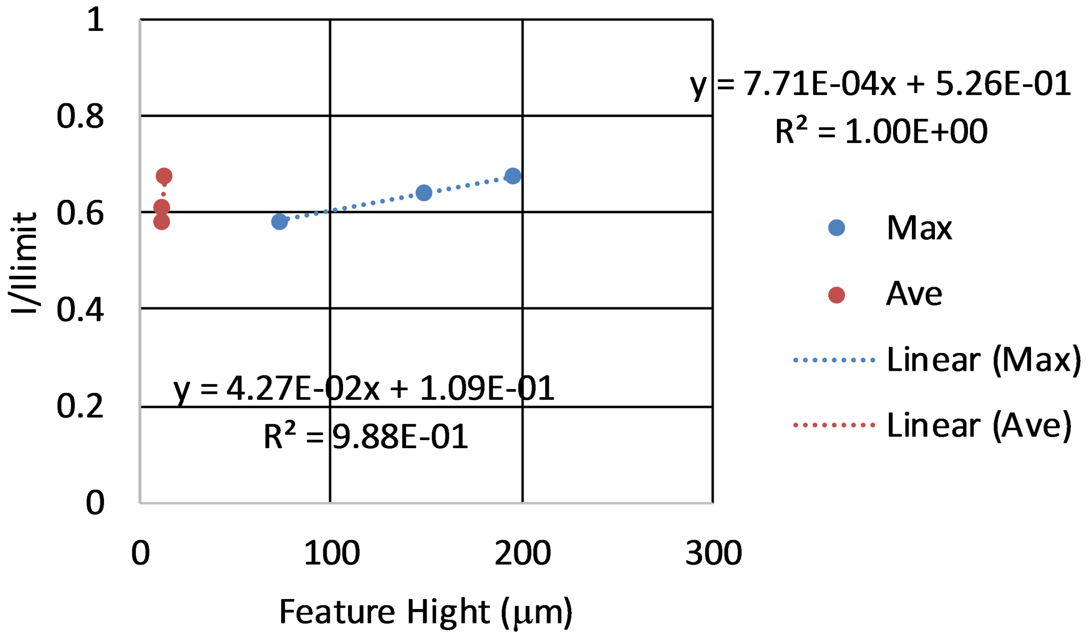

Figure 6.2: Maximum and average feature height as a function of $i/i/limit$ for 20 hours of plating, smooth conditions. From reference [32] 45 g/l Cu, 55 °C, 325 A/m^2 and 325 g/ton Guar equivalent.

experiment settings. As such extrapolation will be necessary for utilization in the current work.

6.2 Methods

6.2.1 Fluid and Electrochemical Model

The modeling aspects used for this section have been adequately covered previously in sections 4.2.3 − 4.2.7 and 4.2.9. The substance of this model utilizes the previous developments as outlined with further enhancements which are subsequently covered.

6.2.2 Statistical Roughness

Careful examination of the work of Shukla [32] reveals that the feature heights were measured from the apparent base of the feature to the highest projected point. From evaluation of the figures provided in that work it appears that the average deposit thickness lies in the arithmetic middle of the measured feature heights. These adjustments of Figures 6.1 and 6.2 are reflected in Table 6.1.

A word of caution is warranted in the use of these data. They represent very specific parameters and flow patterns induced by the geometry which the experiment was performed in. These coefficients should be measured again in the system of study for accurate representation of the desired system. They are included here for demonstration purposes.

As covered in section 6.1 roughness is a function of plating parameters and I (current density) to I_{limit}. Utilizing this relationship provided by Shukla [32] for a 20-hour maximum feature height the following relationship was derived:

$$\text{Maximum Feature Height} = 1/20\text{hrs} \int_0^t \frac{\left(\frac{I}{I_{limit}} - b\right)}{m} \mathrm{d}t \tag{6.1}$$

Equation (6.1) assumes that the maximum feature height begins at time and height 0 and

Table 6.1: Maximum and average feature height parameters. See Figures 6.1 and 6.2.

Parameter Set	Slope (m)	Intercept (b)
Rough maximum feature height	8.34x10^{-4}	2.28x10^{-1}
Rough average feature height	1.22x10^{-2}	8.90x10^{-2}
Smooth maximum feature height	7.71x10^{-4}	5.26x10^{-1}
Smooth average feature height	4.27x10^{-2}	1.09x10^{-1}

increases linearly to the 20th hour. Hence the 1/20hrs. Terms b and m are from the equation of a line $y = mx + b$ shown in Figure 6.1 and 6.2. The equation of the line is rearranged to its current form and integrated. This integration provides for maximum feature height as a function of time and is valid for both maximum and average feature heights. This assumption is drawn for the nodule experimentation showing a linear growth rate (for assumption basis see section 5.4.2). It was necessary to provide this expression in integral form because the i/i_{limit} term varies with time in the model. The integral form allows the variation of i/i_{limit} with time to be captured and accurately summed as an instantaneous function.

However, in the current model the expression for maximum and average feature height is needed outside of the range originally investigated. For average feature height the intercept is sufficient to use (noting utilization outside of data range) with the current linear interpolation as shown in Table 6.1. For maximum feature height is is apparent that intercept for maximum feature height leads to negative values at lower I to I_{limit} ratios. Because of this an interpolation function was used in COMSOL to represent the area not covered in Shukla's [32] work. This is shown in Figure 6.3. The three data points drawn from the data set can be seen between the I to I_{limit} ratio of 0.58 and 0.7. It is assumed the the line is linear out to 1 and becomes zero at an I to I_{limit} ratio of zero. To utilize this interpolation function equation (6.1) is modified in the following manner.

$$\text{Maximum Feature Height} = 1/20\text{hrs} \int_0^t \text{int}\left(\frac{I}{I_{limit}}\right) \mathrm{d}t \tag{6.2}$$

where int is the interpolated function returning maximum feature height.

The limiting current density is calculated via expressions derived from Ettel (see equation (2.2)). This was modified as shown below to establish the limiting current density for copper.

$$i_{limit,Cu^{2+}} = \frac{N_{Cu^{2+}} z F C_{bulk,Cu^{2+}}}{C_{bulk,Cu^{2+}} - C_{electrode,Cu^{2+}}} \tag{6.3}$$

6.2.3 Short Circuiting

The results in section 5.4 show that considering the fluid interaction and its effect on the current density distribution via time did not improve accuracy. Because of this current density will be utilized to directly determine the deposition thickness without additional

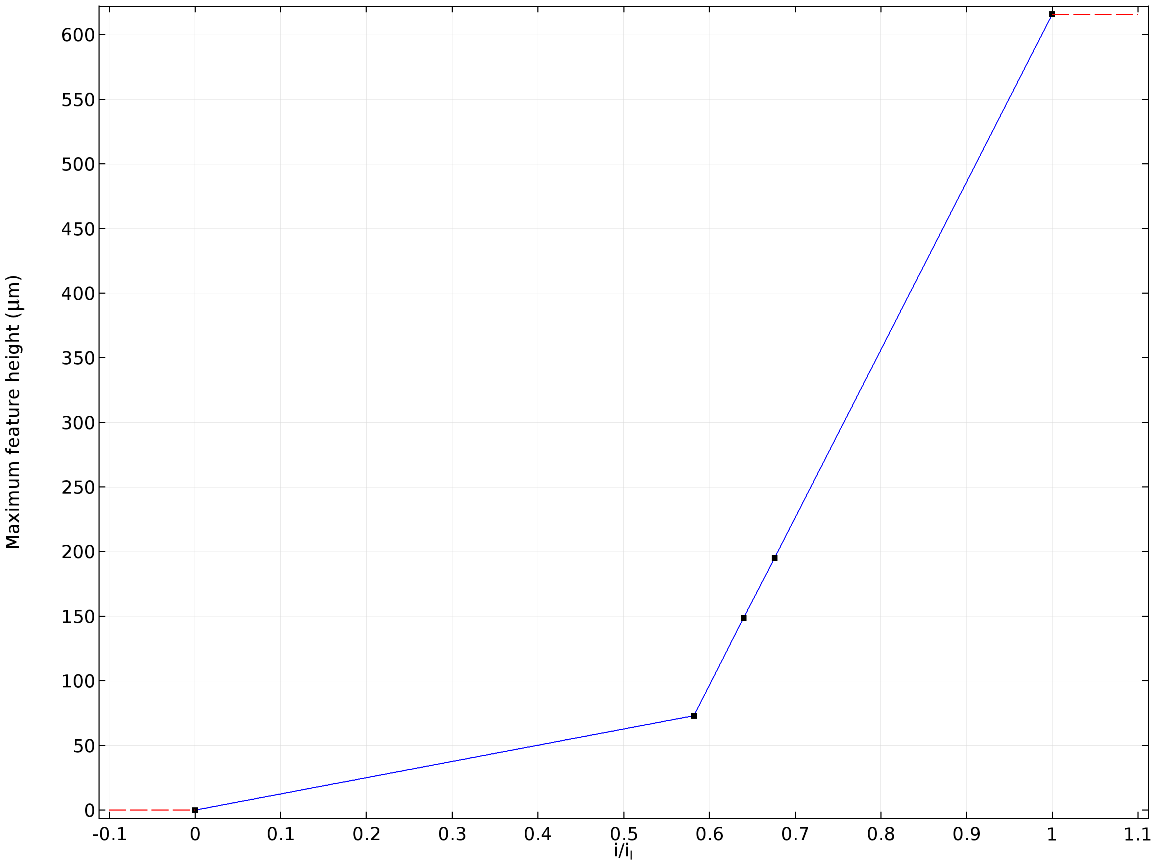

Figure 6.3: Maximum feature height as a function of I to I_{limit} for the smooth conditions discussed in Figure 6.2. Reproduced from modified data from reference [32] 45 g/l Cu, 55 °C, 325 A/m^2 and 325 g/ton Guar equivalent.

intermediate modeling. Further from section 5.4.2 the growth rate appears to be linear on the extremities as shown by Figure 5.16 which showed the linear growth rate of a synthetic nodule under constant current and voltage conditions.

To utilize these principles the following method is proposed. As demonstrated in previous sections, particularly Chapter 4 and Figure 5.8 the COMSOL models are able to reasonably predict the average current and deposit thicknesses. Shorting occurs when the deposit bridges the gap and makes electrical contact with the anode. Most often this is an abnormal growth (nodule). For this work it is assumed that statistically the maximum feature height discussed by Shukla [32] constitutes the extremity of the copper deposit. Combining average deposit thickness and maximum feature height gives the electrical thickness of the deposit which may short. This is expressed in equation (6.4):

$$\text{Electrical Thickness} = \text{Average Deposit Thickness} + \text{Maximum Feature Height} \tag{6.4}$$

Shorting occurs when total thickness in equation (6.4) becomes as large as the electrode gap. To implement in the model a stop condition is added to the solver so that the simulation is discontinued when the deposit thickness equals the electrode gap. The time to short is then determined from the stop time.

6.2.4 Statistical Interpolation

The work by Shukla [32] demonstrated that the Weibull distribution represented the data well in terms of describing the distribution of roughness. For discussion some of those findings are shown in Figure 6.4. These data points were determined from sample cross-sectioning along the length of a finite line. The cumulative distribution of each feature was determined according to equation (6.5).

$$\mathrm{F(x)} = N_{\text{sample}} * \frac{1}{N_{\text{Total samples}} + 1} \tag{6.5}$$

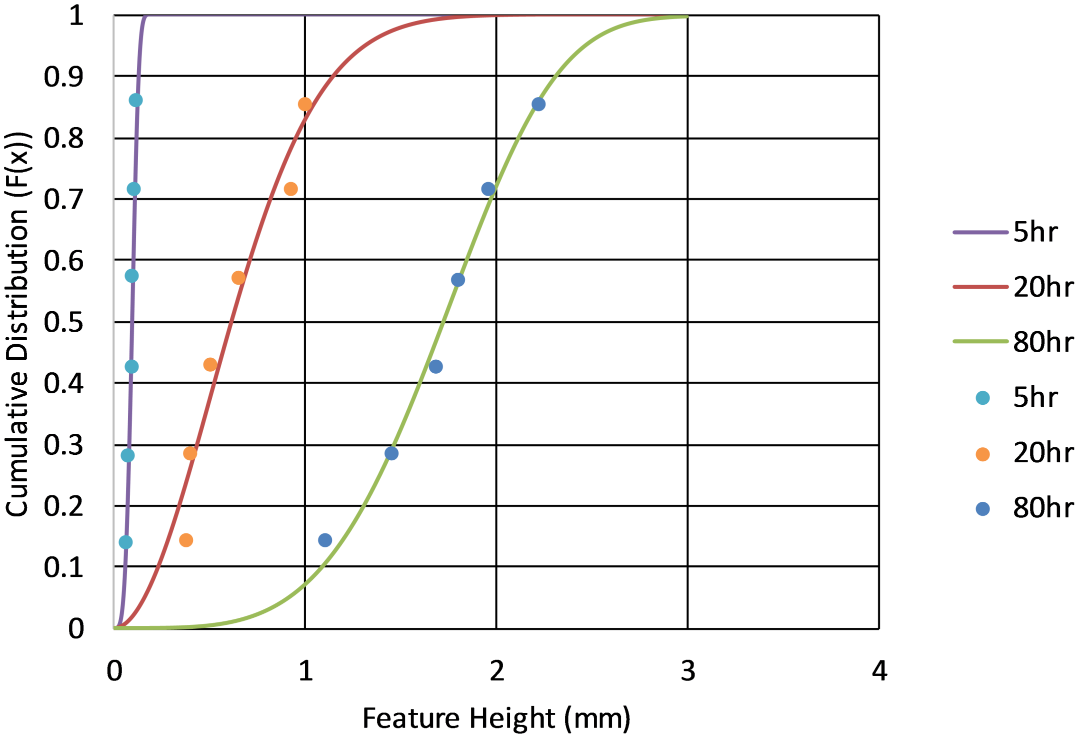

Figure 6.4: Cumulative feature height distribution for rough conditions showing distribution changes with time. Reproduced from reference [32] 35 g/l Cu, 55 $^{\circ C}$, 475 A/m^2 and 175 g/ton Guar equivalent.

where N_{sample} is the number of the sample sorted from smallest to largest and $N_{\text{Total samples}}$ is the total number of features.

Fit is shown by simple regression analysis. It is assumed that the data follow the form shown for the cumulative distribution function of a Weibull type as shown in equation (6.6) or linearized in equation (6.7).

$$\mathrm{F(x)} = 1 - e^{-(\beta^{-\alpha} x^{\alpha})} \tag{6.6}$$

$$\ln\left[\ln\left(\frac{1}{1-\mathrm{F(x)}}\right)\right] = \alpha \ln(x) - \alpha \ln(\beta) \tag{6.7}$$

where $\ln\left[\ln\left(\frac{1}{1-\mathrm{F(x)}}\right)\right] = y$, $\alpha = m$, $\ln(x) = x$ and $\alpha \ln(\beta) = b$. As such the parameters and fits of the data in Figure 6.1 are shown in Table 6.2.

The cumulative distribution function (CDF) represents the probability of a feature of any given size occurring. This is fundamental to the proposed statistical interpolation. From section 6.2.2 functions for both maximum and average feature height have been defined. Utilization of these two variables allows the solution of a Weibull distribution with parameters α and β by solving simultaneous equations. In order solve these equations two data points are needed for alpha and beta. Let these be defined as x_1 and $\mathrm{F}(x_1)$ and x_2 and $\mathrm{F}(x_2)$. These correspond to different feature height CDF probabilities. Further for simplicity an intermediate variable is defined for ease of use:

$$ff_i = \ln\left[\ln\left(\frac{1}{1-\mathrm{F(x_i)}}\right)\right] \tag{6.8}$$

where the subscript i denotes set 1 or 2. Solving equation (6.7) for α in light of equation (6.8) for data point 1 yields:

$$\alpha = \frac{ff_1}{\ln(x_1) - \ln(\beta)} \tag{6.9}$$

Substituting equation (6.9) into equation (6.7) for data point 2 yields:

$$ff_2 = \frac{ff_1}{\alpha \ln(x_1) - \alpha \ln(\beta)} \ln(x) - \frac{ff_1}{\alpha \ln(x_1) - \alpha \ln(\beta)} \ln(\beta) \tag{6.10}$$

Table 6.2: Weibull parameters and fits from Figure 6.1.

Test (hr)	α	Intercept (b)	β	R^2
5	3.843	8.681	0.102	0.9382
20	1.917	0.617	0.743	0.9967
80	4.102	2.352	1.885	0.9837

which when solved for β becomes:

$$\beta = e^{\left[\frac{\left(\frac{ff_2}{ff_1}\ln x_1\right)-\ln x_2}{\frac{ff_2}{ff_1}-1}\right]} \tag{6.11}$$

From the above derivation values of x_1 and x_2 need to be provided. From section 6.2.2 it is apparent that the average feature height sets F(x)=0.5 by definition of average. This shouldn't present error because the average will not change with extrapolated sample size. Therefore, equation (6.7) in terms of average feature height becomes F(x_1) = 0.5 and x_1 = average feature height.

The difficulty lies in determining F(x) for the maximum feature size. To begin to determine this relationship we must consider that the model is a 2D representation of a 3D cathode. Firstly, the 2D data are representative of the average and maximum feature height as a slice. Is it valid to compare slice data to an area? Secondly, how can a small modeled cathode be made to represent a large? Section 6.2.5.2 will discuss methods for addressing the first concern. The second is addressed from a method utilized in Shukla's work [32] shown in equation (6.12) comparing the area of the roughness sample to that of the model test scale.

$$T_{\text{test scale}} = \frac{A_{\text{cathode test scale}}}{A_{\text{sample coupon}}} \tag{6.12}$$

In this study, because of the use of Shukla's [32] data the area of the coupon is assumed to be 0.5 cm x 2.66 cm. The area of the test cathode is 0.170 m x 0.140m. It is assumed that the model gives the maximum feature height of the number of coupons needed to fill the area of the the test cathode. Again borrowing form Shukla's work [32], the F($x_{\text{full}_\text{size}}$) is:

$$F_{x,\text{test scale}} = 1 - \frac{1}{T_{\text{test scale}}} \tag{6.13}$$

This gives the maximum feature height calculated by the 2D model at 0.994412. This corresponds to $F_{x,\text{full scale}}$=0.994412. Or practically the maximum feature height found in one small cathode will have 99.44% of features of test cathode smaller than that size. Hence, by association equation (6.7) corresponds to F(x_2) = 0.9944 and x_2 = maximum feature height. Thus, α and β can be solved for solved for by equations (6.9) and (6.11) and the Weibull distribution may be solved for in this manner. Further extrapolations may be conducted for the tank house by further modifying equation (6.13):

$$T_{\text{full scale}} = \frac{A_{\text{cathode full scale}}}{A_{\text{cathode test scale}}} \tag{6.14}$$

In this study, it is assumed that a full-size cathode is 1 m^2 cathode. Compared to the area of the straight test cathode utilized in this study the value of equation (6.12) is 7519. Or in other words 7519 small cathode samples represent 1 side of a full-size cathode. Further, these assumptions can be extended to include the tank house by modifying equation (6.15) in the following way:

$$F_{x,\text{full scale}} = 1 - \frac{\text{Shorts per Harvest}}{T_{\text{full scale}} * 2 * \text{Cathodes per Tank} * \text{Tanks in Tank House}} \tag{6.15}$$

Thus, the time to short may be solved with a number of different considerations. The shorts per harvest are included so that the operator may include how many shorts in a given harvest cycle are acceptable. Or, for data validation the operator may provide the number of shorts typically seen developed in a harvest cycle. Thus, the operator can evaluate how close the model predicts the harvest time. Allowances are also made for number of cathodes and number of tanks. The 2 in the denominator represents that there are two sides to a cathode.

6.2.5 Electrowinning Costs

The modelling provides important process data that can be used to determine some of the costs associated with changes in process parameters such as current density. A simple way to assess basic costs (per mass of metal produced) associated with short-circuiting and current efficiency is presented as the sum of three 3 categories. These categories are:

- Electricity Costs per unit mass
- Operations Costs per unit mass
- Cost related to the harvest cycle per unit mass

Electrical energy in its simplest terms is cell voltage multiplied by the current and the time. This divided by the mass deposited in the given time and multiplied by the cost per kWh for electricity will give the Electrical Energy Cost per unit mass. This is shown in equation (6.16).

$$\text{Cu Electrical Costs (\$/kg)} = \frac{Energy}{Mass} * \frac{\$}{Energy} \tag{6.16}$$

Careful examination will reveal that they change both with position on the electrode and through time. In order to capture the effect of this variation the integral form calculation must be used. Energy is determined by the basic expression of V*I*time. For each time the average applied current and the average boundary current density is determined. Potential and current are then integrated with respect to time to capture the changes occurring over time (mainly in cell voltage). The integral below is applied to a single cathode anode couple.

$$\text{Energy} = \text{Cathode Area} \int_0^t (\text{Average Applied E} * \text{Average Boundary Current Desnsity})\, \mathrm{d}t \tag{6.17}$$

The same method is utilized with respect to mass. The volume is calculated via an area integral multiplied by the width of a single cathode and density. When the mass equation is applied to the final deposit the mass can be obtained as shown in equation (6.18).

$$\text{Mass} = \text{Density} \int_0^L (\text{Deposit Thickness})\, \mathrm{d}t * \text{Unit Width} \tag{6.18}$$

It is important to note that current efficiency is not included explicitly in equation (6.18) because the modeled current efficiency has already been accounted for in the calculation of deposit thickness.

The next item to consider are the costs associated with the harvesting cycle. These can be summed, at least initially, by the following expression:

$$\text{Harvest Costs (\$/kg)} = \frac{\text{Labor Cost Harvest} + (\text{Labor Cost Per Short} * \text{Shorts Per Harvest})}{\text{Deposited Mass}} \tag{6.19}$$

The initial cost model is comprised by combining labor costs per harvest and associated costs to clear one short then multiplying the result by the typical number of shorts cleared during that harvest. The resulting sum is then divided by the total deposited mass (number of cathodes*number of tanks*mass per cathode). This method will give the additional harvest cycle costs associated with copper production.

Lastly, additional costs associated with electrowinning need to be considered. These ancillary costs include items such as electrode replacements, heating, reagents, supplies, pumping etc. These are provided as a daily average for the tank house and divided by the total deposited mass as in equation (6.19). The expression below gives ancillary costs:

$$\text{Ancillary Costs}(\$/\text{kg}) = \frac{\sum(\text{Ancilary Costs Per day} * \text{DaysperHarvest})}{\text{DaysperHarvest}} \tag{6.20}$$

Combining the above equations will give you predicted copper production costs. This is represented in equation (6.21).

$$\begin{aligned} \text{Cu}(\$/\text{kg}) &= \frac{\text{Energy}}{\text{Mass}} * \frac{\$}{\text{Energy}} \\ &+ [(\text{LaborCostHarvest} + \text{LaborCostPerShort} * \text{ShortsPerHarvest}) \\ &+ \sum(\text{Ancilary Costs Per day} * \text{Days per Harvest})]/\text{TotalMass} \end{aligned} \tag{6.21}$$

6.2.5.1 Concerns and Limitations

This method raises a number of concerns, the first being that 2D slice roughness data are being utilized to represent an area. This assumption needs to be validated. Shukla [32] addresses this by comparing the slice data to what the average and maximum feature heights become as the measured cross section is polished to produce an area measurement. In this work the validation methodology is discussed in section 6.2.5.2.

The second item is that the fluid flow is different in the small tank than the production scale. Evidence of this is the ridge found on the top of test cell deposited cathodes. The fluid conditions of the large cell are different and need to be considered for greater accuracy. Also, the concerns of the linear representation to roughness are applicable owing to differing flow conditions.

6.2.5.2 Digital Image Processing

In light of the difficulty of translating line roughness data to area data an additional method was sought to allow the determination of feature height without large expenditures of effort. This will allow the comparison of slice roughness data to area roughness. The purpose of this section is to take a digital picture of a copper plated cathode and process it in such a manner that the equivalent radius of the resulting nodules and local distribution may be determined, the primary assumption being that the feature radius is the same projection height above the average deposit thickness.

The process utilized is shown in Figure 6.5 using the software FIJI and described as follows:

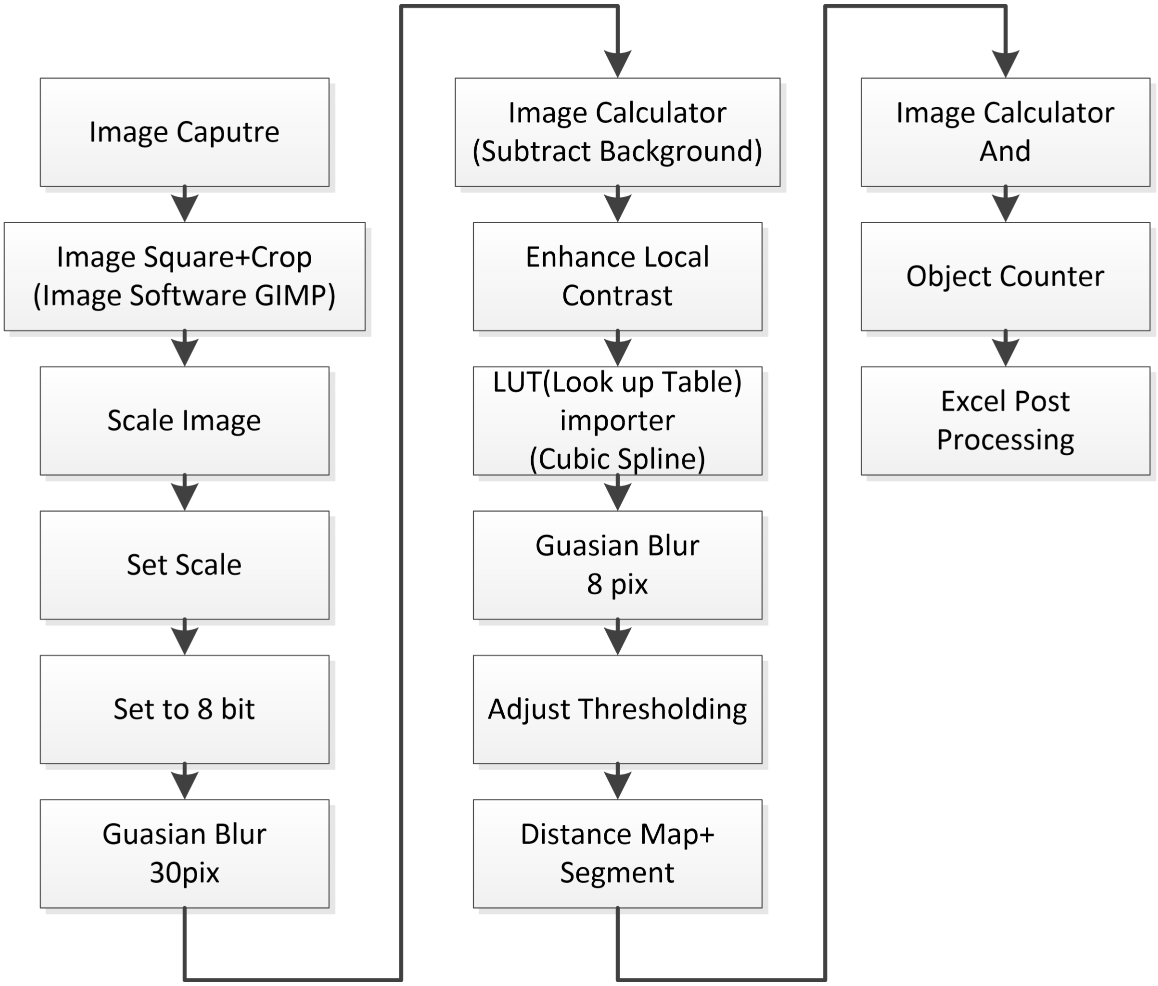

Figure 6.5: Flowchart showing digital image processing steps showing needed manipulations.

1. Image Capture

   The first stage of the project is capturing an image as seen in figure to the right.

2. Image Square and Crop

   The next step required the cropping of the image with the image editing software GIMP. This was done for the ease of use that this software provides.

3. Scale and Set Scale

   After cropping, the image was opened in Fiji and only one scale (x) was adjusted. This was done by finding the pixel ratio of width to number of x pixels and the same for the y. The smaller ratioed axis was scaled so that the pixels had the same spatial relationship. The length scale was then set 20 pixels to 1mm.

4. Set to 8 Bit

   This was done to allow the subsequent processing.

5. Gaussian Blur

   The image was then duplicated and blurred with a radius of 30 pixels to provide a base for removing the different tones of the background. This is a type of filter which takes a radius of pixels and applies averaging to the centerpoint. It is used to provide a background intensity that may be subtracted.

6. Image Calculator

   The 8-bit scaled image was then subtracted from the background giving a more uniform grayscale distribution.

7. Enhance Local Contrast

   The objective for this step was to improve the amplitude of the gradient at the nodule boundaries to make subsequent processing better able to pick out the edges.

8. LUT (look up table) Importer (Cubic Spline)

   In testing, the image still remained too noisy, so a cubic spline was applied to further reduce the texturing.

9. Gaussian Blur

   Gaussian blur was again applied at a radius of 8 pixels to reduce the sharpness of the image and assist in edge detection.

10. Adjust Thresholding

    This allowed the nodules to be clearly differentiated from the background. The specific setting allows a range of amplitudes from 60 to 255 on a 256 scale.

11. Distance Map

    The distance mapping allows the finding of the locations of the maximum distance away from edges. This allows the determination of segmentation.

12. Segmentation

    Segmentation is an output of the distance map. This shows the boundary divisions between the determined nodules.

13. Image Calculator (see Figure 6.6)

    Using the image calculator with the and function allows the merging of the binary nodule image and the segmentation lines. This allows the subsequent counters to see the separated nodules.

14. 3D Object Counter (see Figure 6.7)

    The object counter allows for fast and easy identification of all the nodules. The output was a txt file with locations and areas of the identified nodules.

15. Excel Postprocessing (see Figure 6.8)

    The output file of the object counter contained an index listing to the number of the nodule along with the area and position. The area was available because of the scale which was defined. In order to determine the equivalent hemispherical radius, the area of a circle was solved for the effective given area of each nodule. The results were then tabulated in a histogram to show the distribution of nodule sizes.

6.3 Results and Discussion

6.3.1 Feature Height From Model Results

As addressed previously additional work and calibration are needed to provide for accurate parameters for maximum and average feature height demonstration. It appears that the overall method is sound and in general agreement with correct principles. The issue is one of developing methodologies for meaningful roughness data. The methods discussed in the last section were utilized running the model under conditions specified for the straight cathode conditions in Tables 3.5, 3.6 and 3.7. Figure 6.9 shows the comparison of average deposit thickness, maximum and average feature height. The maximum feature

Figure 6.6: Processed image showing subdivided segments counted as features.

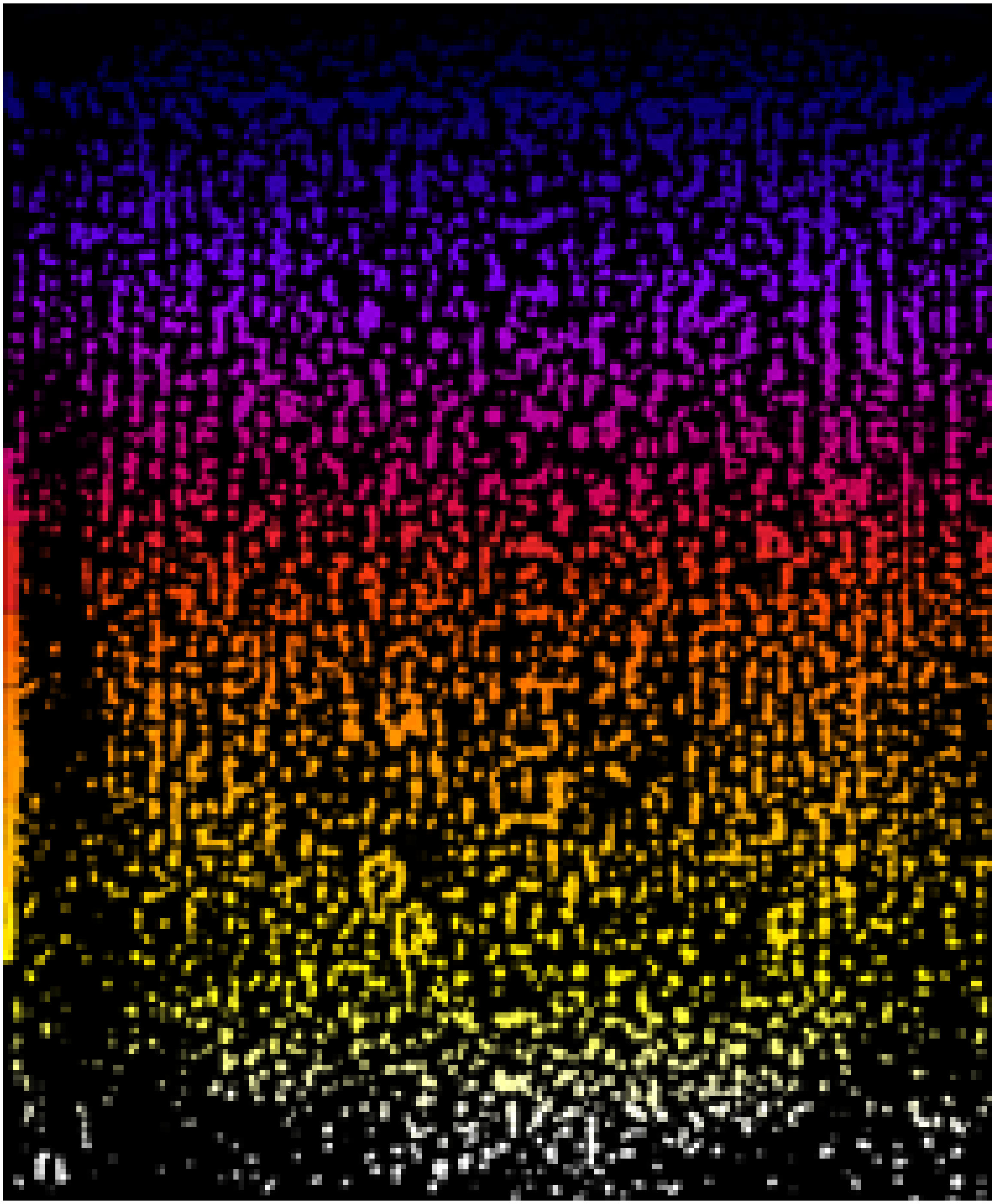

Figure 6.7: Showing identified features on cathode. Note that individual features are differentiated by a unique RGB (red, green, blue) color. Hence the rainbow appearance.

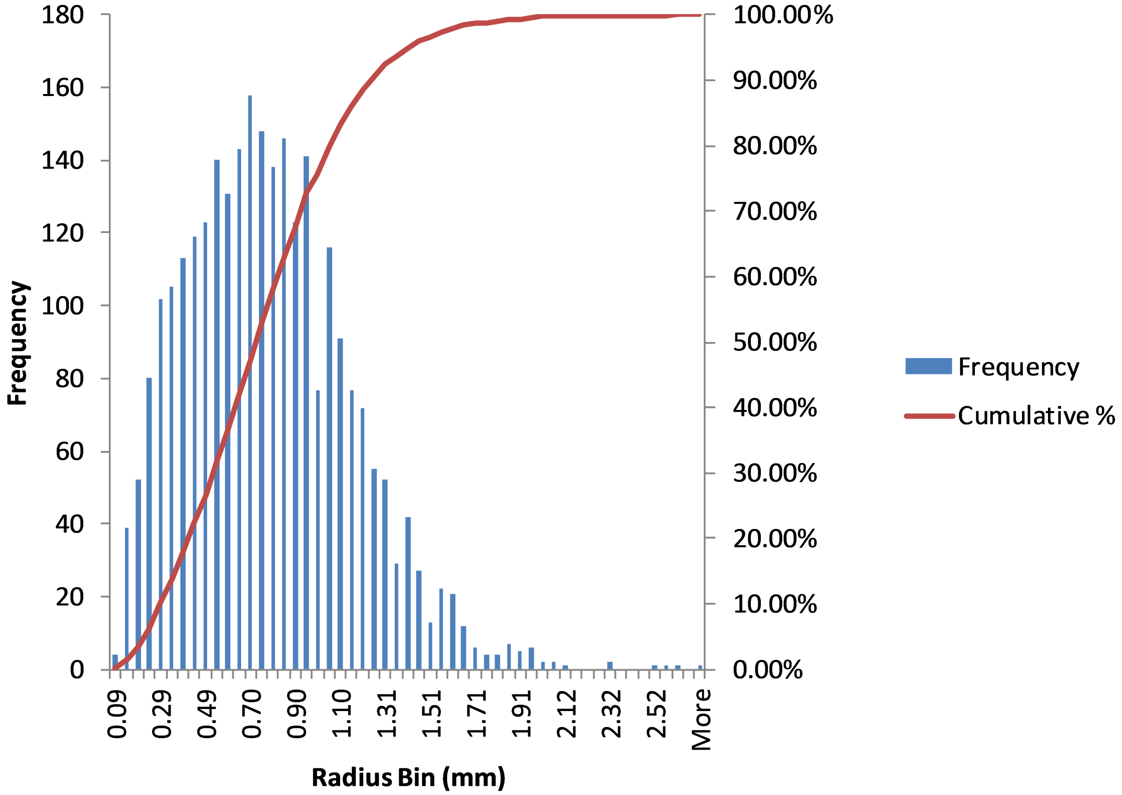

Figure 6.8: Feature size distribution as of the straight cathode run under conditions described in Tables 3.5, 3.6 and 3.7

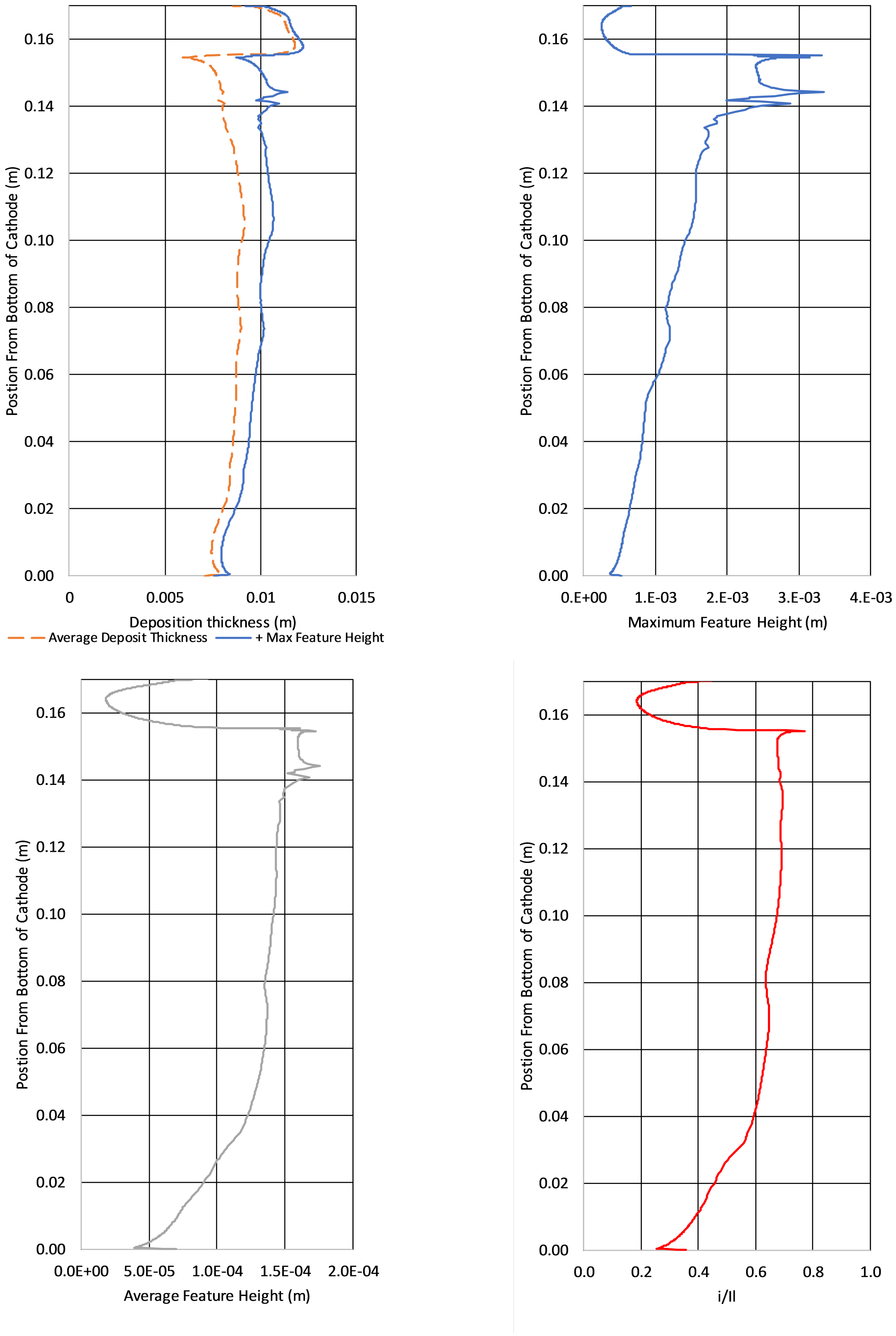

Figure 6.9: Plots showing deposition thickness, maximum feature height and average feature height as a function of cathode position.

height is strongly influenced by the local fluid conditions. Comparison to Figure 6.10 also shows visually general agreement where the area on the ridge is smoother than the area in the notch below the ridge. The average feature height appears reasonable with regard to the relationship to i/i_{limit}. In light of what the model seems to predict well is the row of nodules on the bottom side of the ridge. The model predicts the most significant features at this location. This result is what Figure 6.10 shows. The largest feature predicted by the model in Figure 6.9 is 3.338 mm.

6.3.2 Feature From Digital Image Processing

In view of the findings of section 6.3.1 it is beneficial to seek an alternate means of roughness validation. As discussed in section 6.2.5.2 digital image processing was utilized as an alternate method to determine feature sizes.

The results of the straight plate constant current cathode are shown in Table 6.3 and Figure 6.8.

To provide for a measure of validation of this technique 3 of the largest features on the flat portion of the cathode were found and measured with calipers. The closest and best fit point from the digital image processing was compared to the measured nodule. The results of this work can be seen in Table 6.4 and Figure 6.10.

The overall results of the digital image processing show promise, but are not as accurate as anticipated. It is clear that this method will need further refinement to be utilized for roughness measurements, particularly with regard to correlating the observed radius to feature height. It is interesting to note the comparison in the 3 methods as shown in Table 6.5.

6.3.3 Costs and Time to Short

As discussed previously the roughness data presented herein are of small test cell which exhibits much rougher deposits than their industrial counterparts. As such for demonstration a hypothetical test cell of the same size cathodes and a gap of 25.4 mm run under the conditions outlined in Tables 3.5, 3.6 and 3.7 for the straight cathode condition was performed. It was assumed that Fe^{3+} concentration was 22.55 mol/m^3 of Fe^{3+}, 14.29 mol/m^3 of Fe^{2+} for a total of 2 g/l of iron with current efficiency being calculated and considered in the model. Further, it was assumed that there were 50 cathodes per cell and

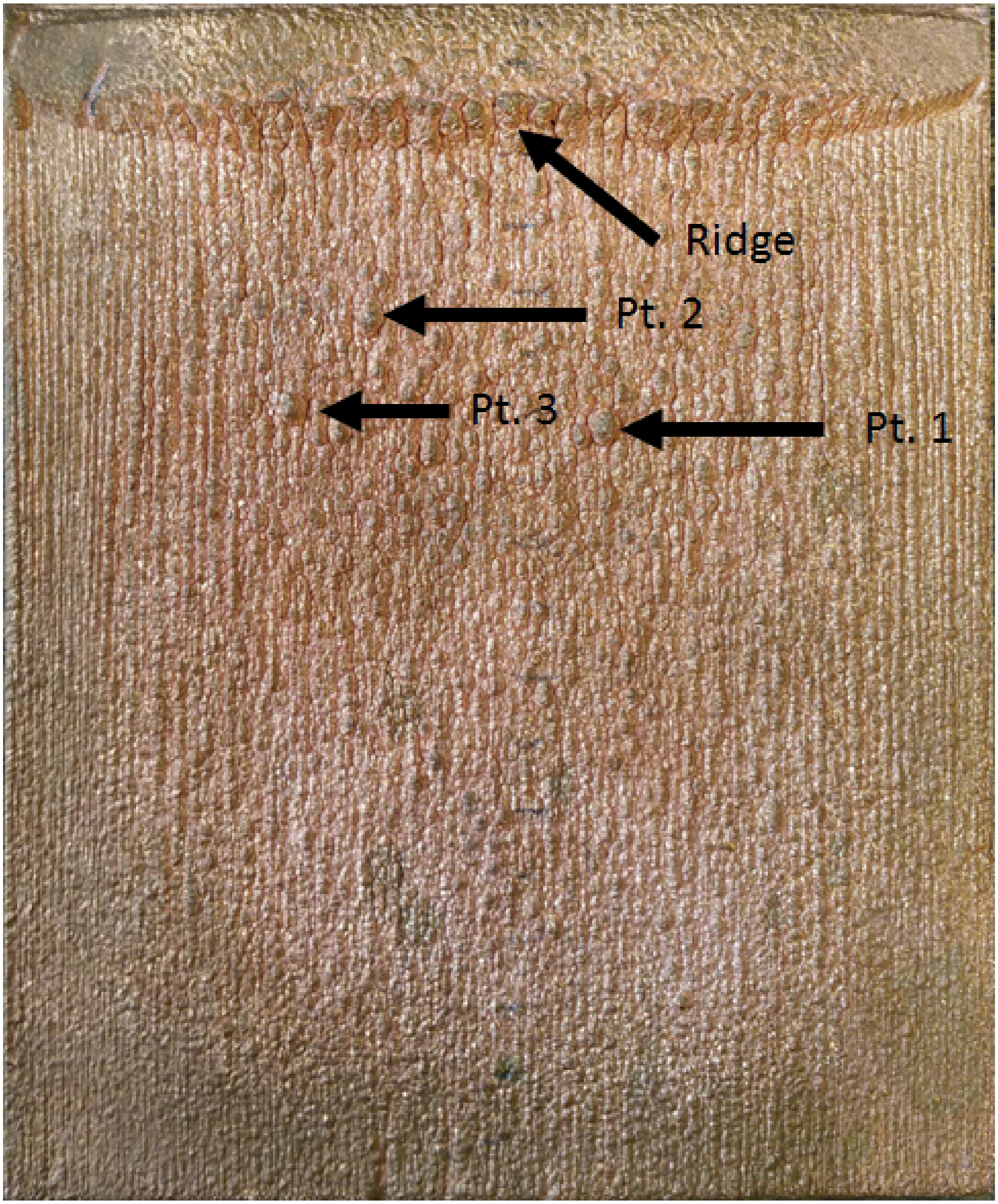

Figure 6.10: Largest 3 features as found on straight cathode run under conditions found in Tables 3.5, 3.6 and 3.7.

Table 6.3: Statistics of roughness analysis with digital image processing.

Variable	Feature Size (mm)
Maximum Feature Height	2.726
Averaged Feature Height	0.7547
Standard Deviation	0.374

Table 6.4: Largest 3 features as found on straight cathode run under conditions found in Tables 3.5, 3.6 and 3.7.

Feature	Major Dimension (mm)	Minor Dimension (mm)	X position (mm)	Y position (mm)
1 measured	5.67	4.43	84.49	109.44
1 image	2.79	NA	86.03	108.67
2 measured	5.60	3.89	51.95	127.5
2 image	3.00	NA	55.11	124.77
3 measured	4.94	4.14	40.40	112.33
3 measured	2.61	NA	33.11	111.13

Captured via caliper measurements

For image measurements the nearest match was found and converted to dia.

Table 6.5: Largest feature comparison between 3 methods.

Feature	Largest Feature (mm)
Model	3.344
Digital Image Processing	2.79
Measured	2.835*

* Pt. 1 Table 6.4 major dimension converted to radius.

20 tanks in the simulation. The results were as follows. The energy required (without shorting) is 1.79 (kWh/kg) and the cost (assuming no additional ancillary costs) of copper \$0.176 per kg with a power price of \$0.0984 per kWh. The simulation concluded with an equivalent time of 10.4 days when the first short was predicted to occur.

6.4 Summary

This section presented a methodology following the method described by Shukla [32] with insights from associated image processing to determine the average and maximum feature size. These parameters are then utilized to solve for necessary Weibull parameters which are used to calculate the time to short. The calculation may be run under one or multiple shorts, the latter being used to check the data against plant operating conditions. Overall the specific results under the conditions and methods presented appear to under represent shorting as typical tank houses corp between 6 and 10 days. Also, the apparent lack of accuracy of the digital image processing methods was not subsequently able to overcome these difficulties. As discussed in section 6.2.2 the range utilized in the model is outside of the range studied in Shukla's [32] work and a interpolation was utilized in out of bound ranges. Fortunately, the region of interest where the maximum feature height occurs is in the upper regions where I to I_{limit} is for which data from Shukla's [32] is available.

An interesting consideration in light of the findings of this section are how little the results of this section matter for actual tank hose optimization. The statement is bold considering the time and care developing the techniques of this section. To justify this remark, consider the following:

- Each tank house utilized different conditions and additives. This will influence maximum and average feature height greatly. The factors controlling roughness are numerous and best determined experimentally. Thus, a study at the tank house will be needed to calibrate to its roughness.

- Building on the last point the model assumes a linear feature data to represent an area. These are likely to not scale linearly. As data on full size cathode roughness have not been provided this remains an unanswered question. Methods to understand full size cathode feature will need to be better understood. Likely the utilization of digital image processing techniques could provide, if further developed, a cost-effective means of gathering such data.

- With the methods presented the Weibull parameters may be regressively tuned from operational data to determine the fits. This would allow methods accuracy to determine plant optimums.

From these points, it can be seen that the models may be easily modified when provided adequate plant data to ensure model accuracy and model functionality.

CHAPTER 7

FULLSIZE MODEL AND COMPARISON TO HISTORIC DATA

7.1 Introduction

After the progress shown in the proceeding sections developing and validating the model the next logical step is to simulate a full-size geometry. Chapter 4 demonstrates that speciated modeling generates reasonable deposit accuracy. This model will be utilized as the basis for a full size 2D model. In terms of validating this model several references prove useful as was covered in the literature search (see section 2.2). In light of these works the electrowinning settings shown in Figure 2.1 will be utilized to validate the copper mass transfer coefficient to the model results. In this manner, the model can be extended and compared to full size.

7.2 Methods

7.2.1 Historic Validation Data

The work of Ettel [6] and Gendron [7] will be compared to the results of the model via the calculation of the Cu mass transfer coefficient. This will allow the model to be tested against another cell height and as a second experimental reference point. Care will be taken to evaluate the periodic nature of the eddy flow and its effect on the mass transport coefficient. Table 7.1 contains the modeling parameters used for validation.

7.2.2 Fluid and Electrochemical Model

The modeling aspects used for this section have been adequately covered previously in sections 4.2.3 − 4.2.7 and 4.2.9. In substance, the models are the same except the omission of the inlet and outlet ports (due to short run times), modification of the geometry and increasing the mesh size. It is also important to note the material previously covered in section 5.3.7.1 as the true turbulence will be modified by these aids.

Table 7.1: Electrolyte parameters.

Reference	Parameter	Value
[6]	Copper	25 (g/l)
	Sulfuric acid	100 (g/l)
	Temp	25 °C
	Current Density	180 (A/m^2)
	Cathode Height	1 m
	Electrode Gap	26 mm
[7]	Copper	60 (g/l)
	Sulfuric acid	150 (g/l)
	Temp	40 °C
	Current Density	250 (A/m^2)
	Cathode Height	1 m
	Electrode Gap	26 mm*

*Not explicitly given for natural convection in reference [7]

7.2.3 Geometric and Mesh Considerations

The models presented in this section are modifications of previously developed models run with the settings found in Table 7.1. Boundary layers were utilized on the cathode to enhance accuracy. In the bulk electrolyte domain, the mesh was made as coarse as practical to reduce model run times. This is done at the sacrifice of some fluid flow accuracy, but with the validation presented this may be justified.

7.2.4 Mass Transport Coefficient

The models presented in this section are modifications of previously developed models run with the settings found in Table 7.1. To compare the data to the mass transfer coefficient presented in the literature the following expression was used:

$$k_{\mathrm{Cu}^{2+}} = \frac{N_{\mathrm{Cu}^{2+}}}{C_{\mathrm{bulk,Cu}^{2+}} - C_{\mathrm{electrode,Cu}^{2+}}} \tag{7.1}$$

where $k_{\mathrm{Cu}^{2+}}$ is the mass transfer coefficient of copper, $N_{\mathrm{Cu}^{2+}}$ is the molar flux and $C_{\mathrm{bulk,Cu}^{2+}}$ and $C_{\mathrm{electrode,Cu}^{2+}}$ are the bulk and electrode surface concentration of copper, respectively.

7.3 Results and Discussion

The following results are presented as discussed in the previous section.

7.3.1 Comparison to Ettel et al. [6]

The model was run under the conditions outlined in [6] (180 A/m^2, 25 g/l Cu, 100 g/l, H_2SO_4 and 25 °C). Figure 7.1 shows the comparison of the mass transport coefficient of the model versus the data presented by Ettel et al. [6]. It appears that 30s is not a sufficient averaging time to produce a smooth response. This is due to the transient eddies form and roll up the electrodes. This can be seen more clearly in Figure 7.2 which shows the fluid velocity. Figure 7.3 is also included showing the gas fraction. Figure 7.4 shows the copper

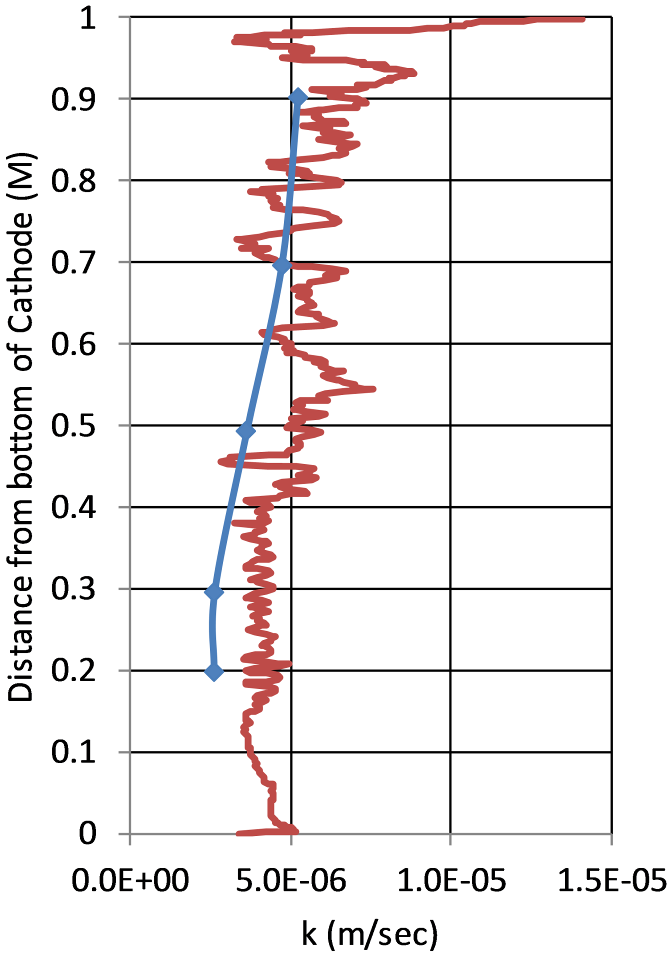

Figure 7.1: Plot showing the mass transport coefficient of the model averaged (60-90s) versus the experimental data presented in reference [6] Table 7.1.

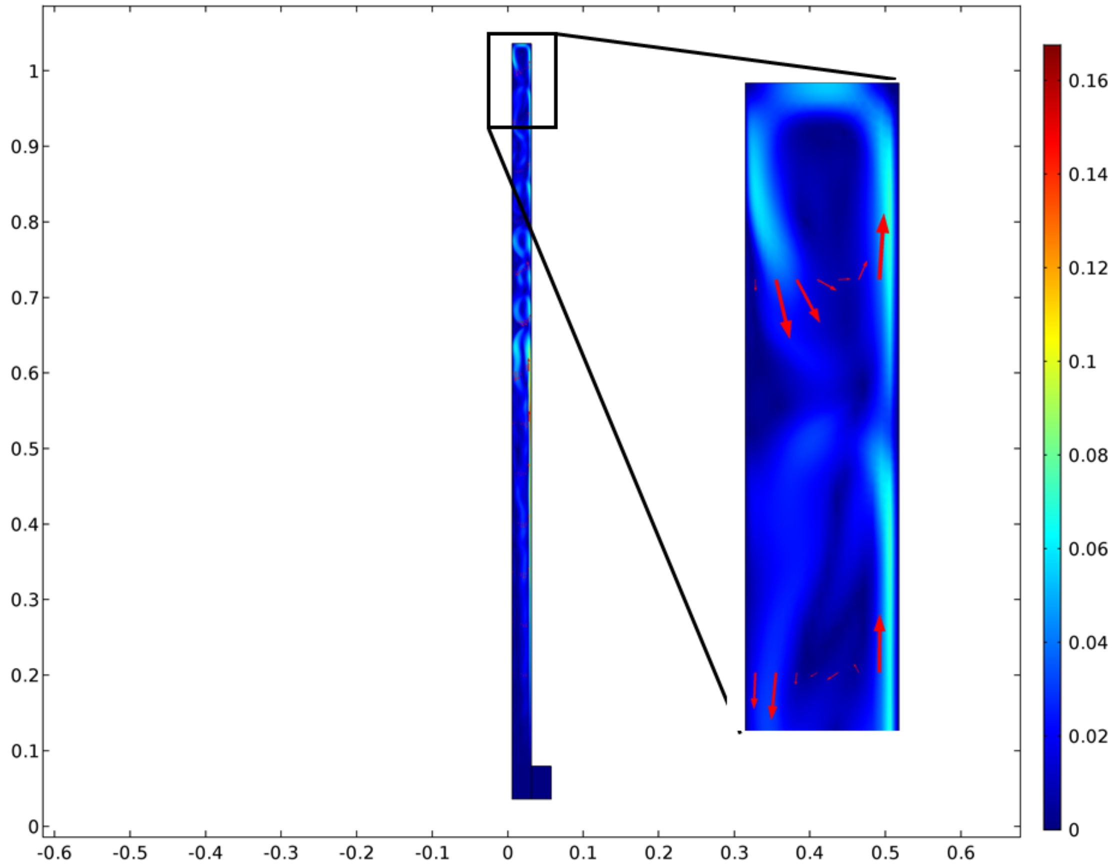

Figure 7.2: Velocity profile of the cell showing transient eddy formation (90s). Units (m/s) conditions found in reference [6] Table 7.1

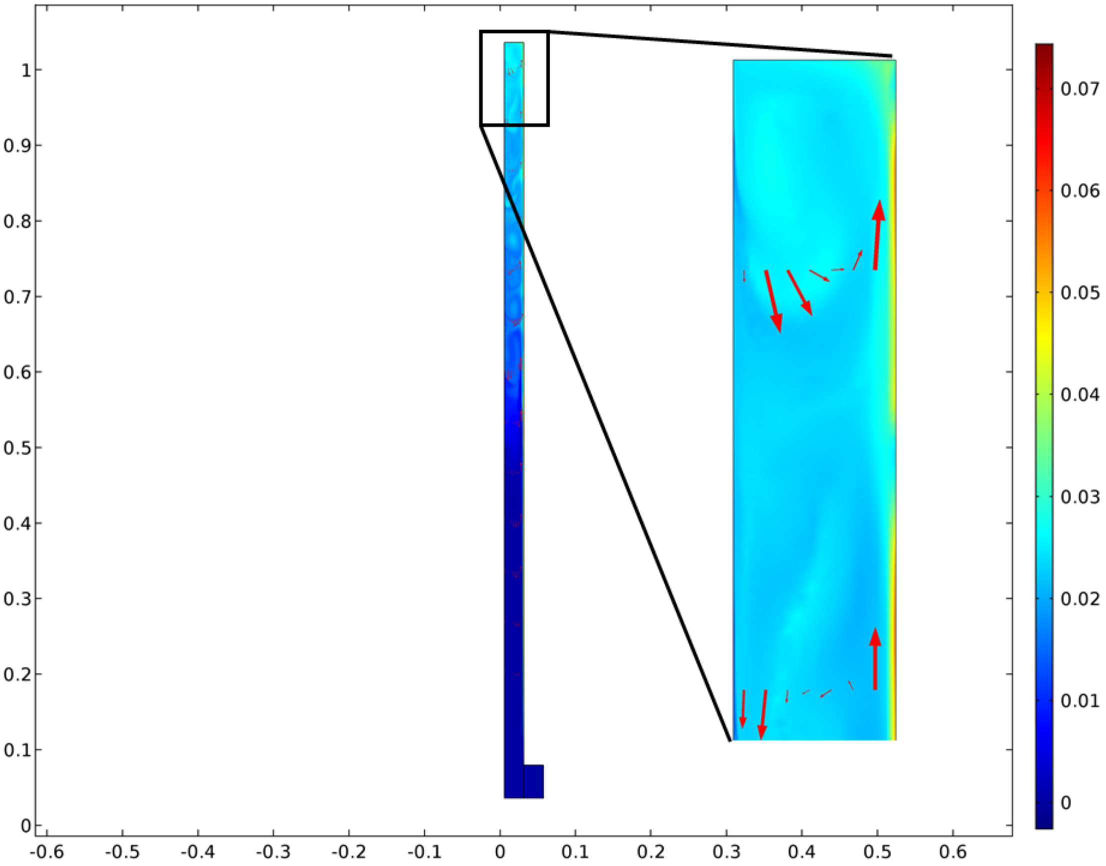

Figure 7.3: Gas fraction of the cell showing transient eddy formation (90s). Arrows velocity vectors, conditions found in reference [6] Table 7.1.

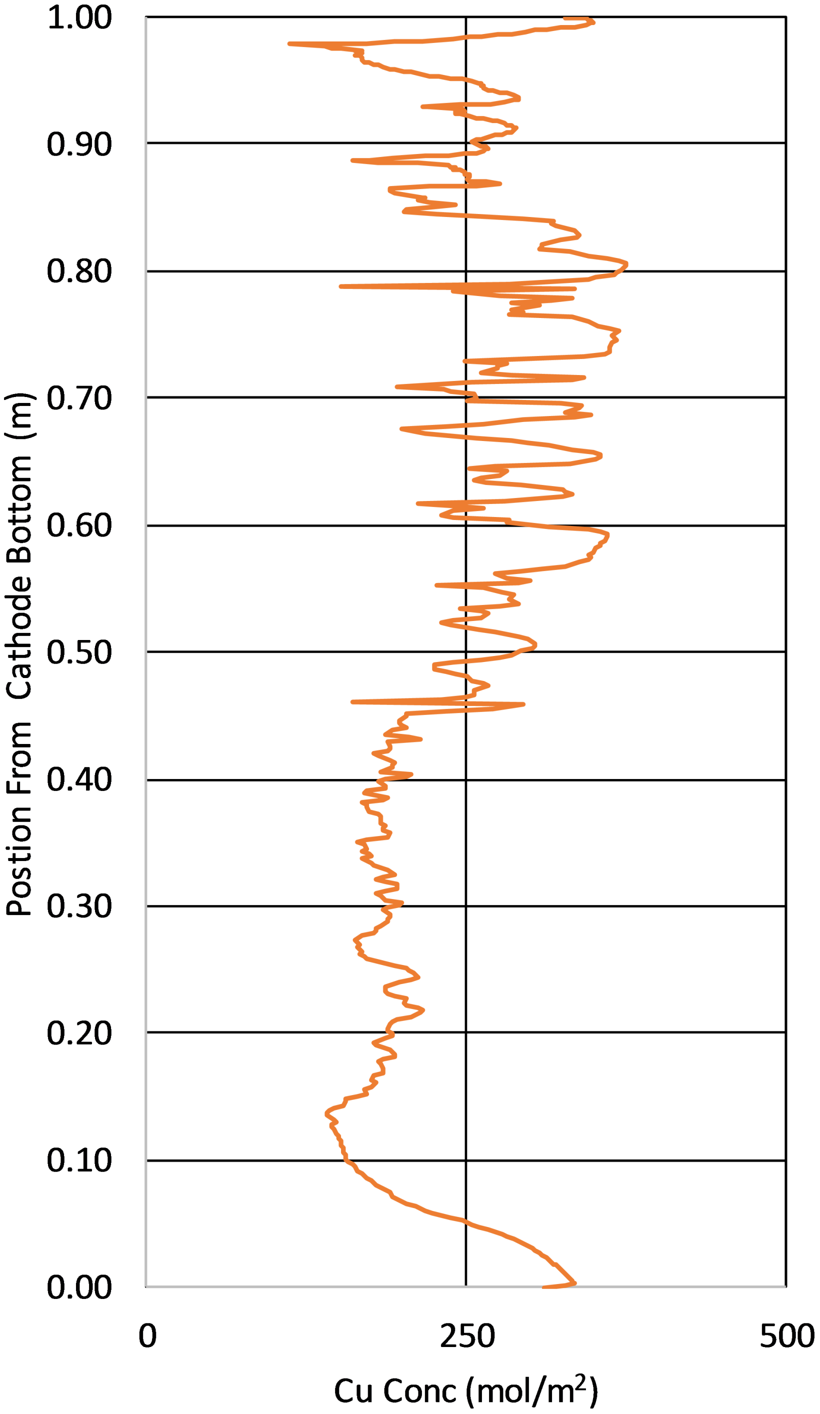

Figure 7.4: Copper concentration along the cathode averaged (90s). Conditions found in reference [6] Table 7.1.

concentration at the modeled cathode surface in the cell.

The mass transport coefficient appears to match well the results of Ettel. This suggests that the implemented model is successful in replicating the results of the experiment.

7.3.2 Comparison to Gendron et al. [7]

The model was run under the conditions outlined in [7] (250 A/m^2, 60 g/l Cu, 150 g/l, H_2SO_4 and 40 °C). Figure 7.5 shows the comparison of the mass transport of the model versus the data presented by Gendron et al. [7]. The modeled results seem to deviate significantly from Gendron at the upper limits of the cell. The turbulent mixing appears to be of a greater magnitude as compared to the conditions of Ettel [6]. This is expected with

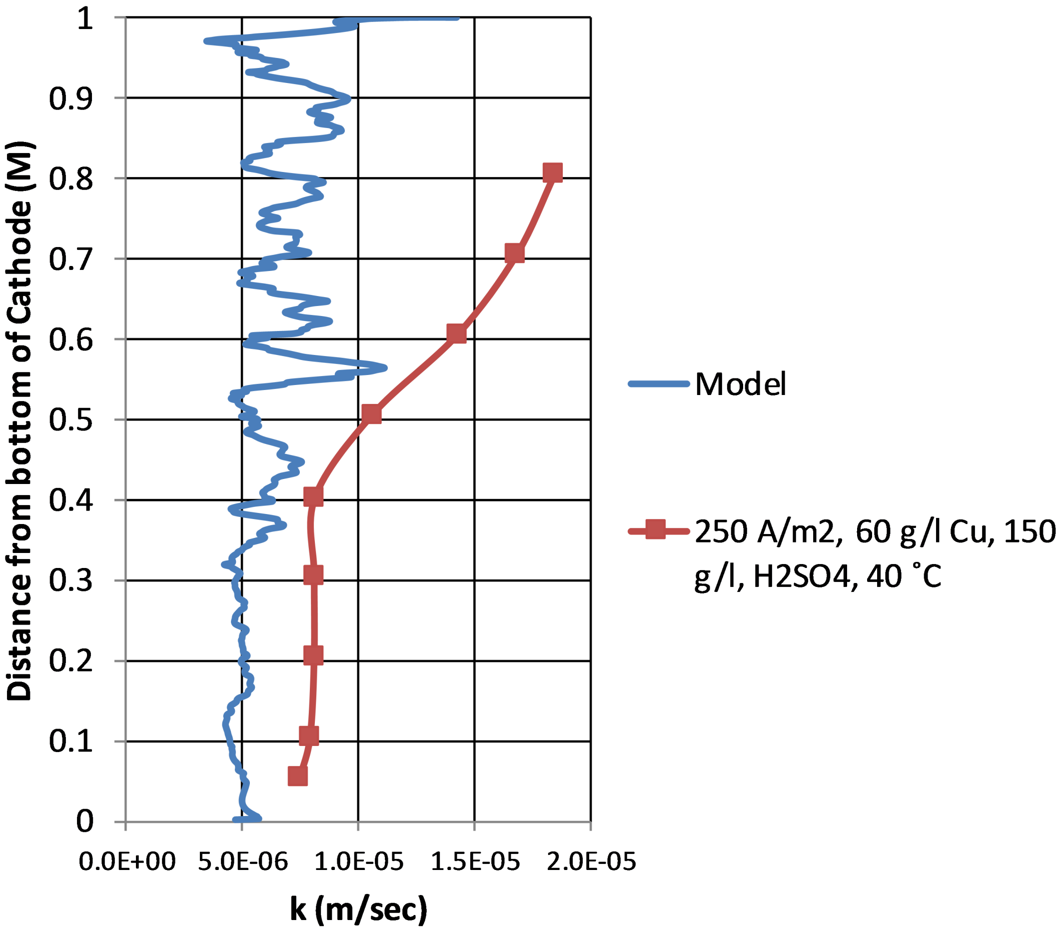

Figure 7.5: Plot showing the mass transport coefficient of the model averaged (60-90s) versus the experimental data presented in reference [7] Table 7.1.

the additional gas being generated at the anode. However, the model doesn't show the magnitude of mass transfer increase from the experimental data. It also appears that 30s is not a sufficient averaging time to produce a smooth response. This is due to the transient eddies that form and roll up the electrodes. This can be seen more clearly in Figure 7.6 which shows the fluid velocity. Figure 7.7 is also included showing the gas fraction, and Figure 7.8 shows the copper concentration at the modeled cathode surface in the cell.

The results are are mixed. The magnitude of the mass transport coefficient is similar, but not exact. The results show the same fluid structure, namely an apparent increase in turbulence at about 0.4 m from the cathode bottom. This is manifest in the increase in mass transport. The discrepancy between the model simulation and the measurements of Ettel may be related to silver ion depletion in Gendron's tests. Overall the results are quite similar. It is also important to note that the disturbance in the middle of Figure 7.6 is where

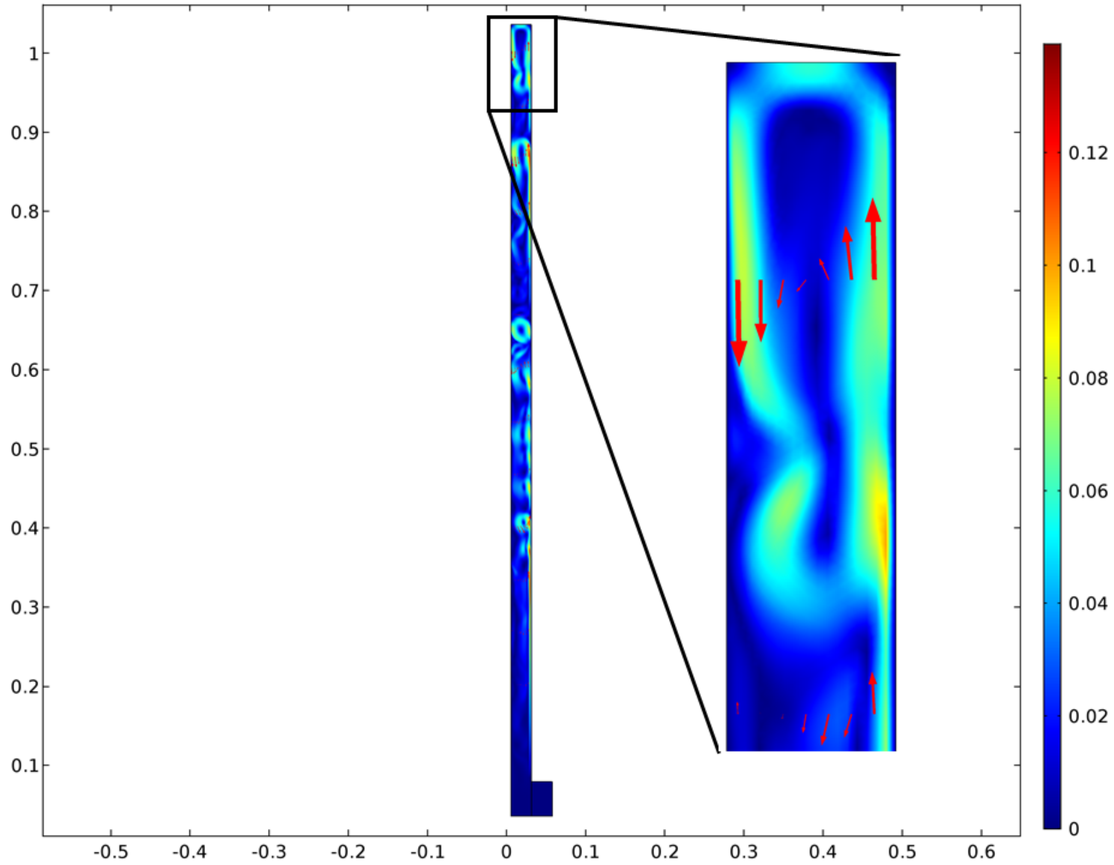

Figure 7.6: Velocity profile of the cell showing transient eddy formation (90s). Units (m/s) conditions found in reference [7] Table 7.1

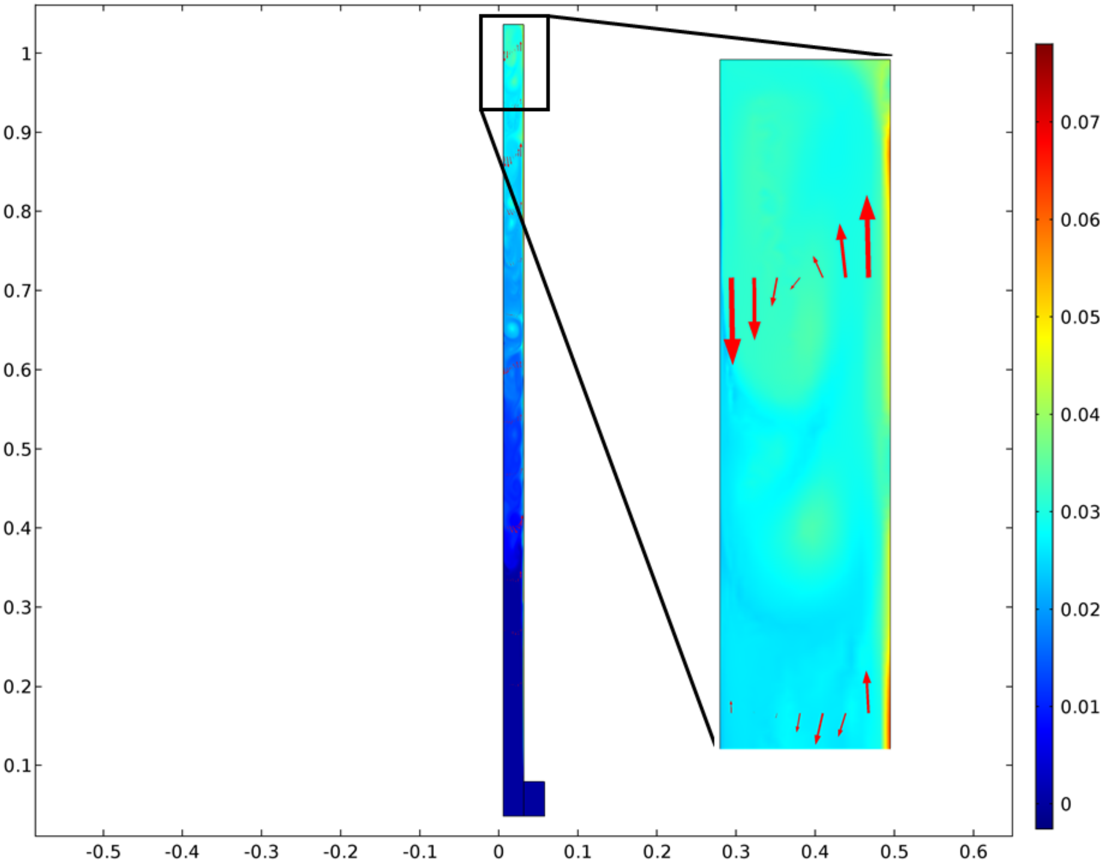

Figure 7.7: Gas fraction of the cell showing transient eddy formation (60s). Arrows velocity vectors, conditions found in reference [7] Table 7.1.

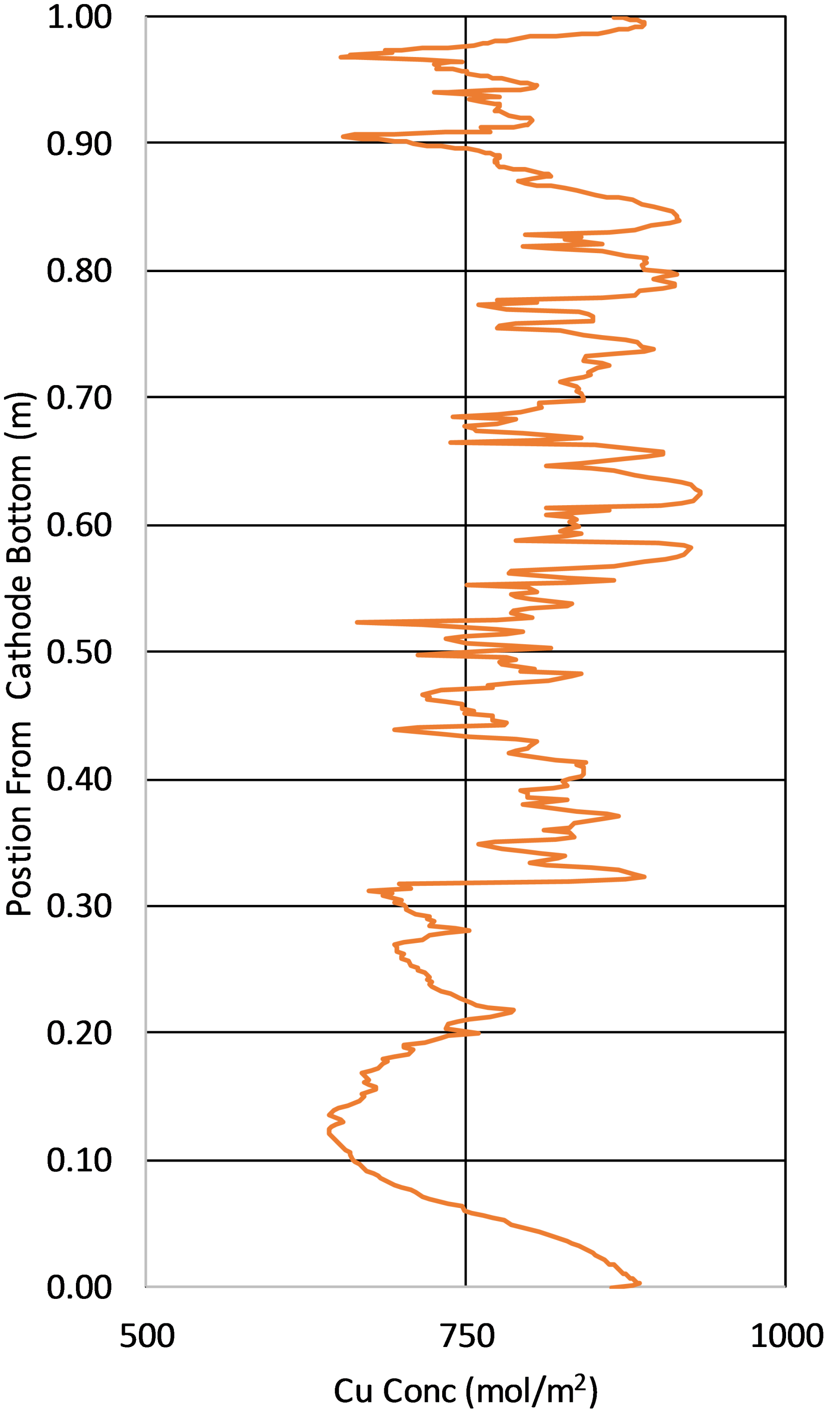

Figure 7.8: Copper concentration along the cathode averaged (60s). Conditions found in reference [7] Table 7.1.

there is a laminar stream separation for the cathode. This can be clearly seen in Figure 7.5.

7.4 Summary

In this chapter the mass transport of silver was utilized from data presented by Ettel et al. [6] and Gendron et al. [7] to determine the local copper mass transfer coefficient at the cathode. The experimental conditions were modeled as similarly as possible given the information presented in these [6], [7] works. The results varied. For the 25 g/l Ettel experiment the model seemed to show general agreement with the experimental data. For Gendron's work, the mass transport in the upper portions of the cathode were underestimated. It is difficult to make a firm conclusion from these comparisons without additional data or means of validation. Overall the model may predict well the conditions in full size tanks, but an additional data point would be well warranted.

CHAPTER 8

MODELING CONCLUSIONS

In the introduction the scope of work 1.3 was put forward as the objectives of this study. Nine different items were discussed and the associated conclusions are discussed as follows:

- **Develop a combined electrochemical multiphase fluid model which predicts local current density.**

  Chapters 3 and 4 cover the development of the base electrowinning models. The primary difference between the two approaches (5 species versus 3 species) was the consideration of speciation with the supporting electrolyte. It was found that the consideration of the supporting electrolyte with speciation lowered the copper concentration at the cathode due to lower migration of copper ions. Overall both the 5 species and the 3 species models gave reasonable predictions of the experimental current density. However, due to the additional insights provided by the 5 species model it was selected as the model of choice for further development.

- **Enhance model depth to consider species found in the electrolyte and local current efficiency.**

  Chapter 4 also covered the development of methods to calculate current efficiency via an expression to compare copper to iron diffusion coefficients. This expression proved very beneficial to reducing computational expense associated with the model. Although true Butler-Volmer electrode kinetics were attempted the additional computational time to use it to solve for the ferric ion reaction proved prohibitive. As such, the comparative diffusion method was used as a suitable alternative.

- **Perform a numeric study into the heterogeneous equilibrium speciation reactions and iron electrode kinetics.**

  Chapter 4 meets the objectives of providing speciation data for the copper - sulfate - acid system. This work presents previously unknown (to the author) results with regard to including $CuHSO_4^+$ as a constituent in the system. These results are covered extensively in sections 4.2.4 and 4.3.1. These sections show the importance of considering speciation as the concentrations of various constituents vary widely. As mentioned the Butler-Volmer electrode kinetics were tested, but not utilized owing to the additional computational time required.

- **Develop a model to evaluate fluid structure interactions with the deposit.**

  Chapter 5 presents the results of evaluating the fluid structure interaction of the deposit with current density. The findings were surprising in that a single representation of deposit thickness using Faraday's law was found to be the most accurate for describing the deposit topography. For the other models a looping method was employed utilizing a geometric series to perform nonlinear time leaps until the plating time was achieved. Seven to 15 loops were utilized with models showing little variation between the number of loops utilized. The results of this work show that single, linear deposit thickness computation is a viable alternative to more complex modeling. Potential explanations of results and future work are identified in section 5.4, but with the adequacy of a simple deposit model it will not be pursued at this time.

- **Develop a roughness model to use with the deposit model to predict short circuiting.**

  Chapter 6 presented the work associated with translating the model inputs into suitable roughness. Additional work in the form of digital image processing was undertaken to provide context for the presented results. The conclusion of this section was that although a model is provided, the nuances of tank house electrowinning make it necessary for real roughness data to be determined and utilized in the model. The current model will provide average and maximum feature height as a function of a ratio of I to I_{limit}. This serves as a base for predicting tank house shorting via area and opportunity comparison to determine the probability of shorting. This probability is incorporated into the model via a stop condition to determine the time to short. In this way the time to short may be predicted.

- **Translate learnings from small scale to full size configurations and compare to literature.**

  Chapter 7 covers the testing and validation of full size models to data found in literature. The results were mixed in that the model showed good agreement with one of the experiments but not the other. In terms of the higher temperature, higher current density experiment the model underestimated the mass transfer coefficients at the upper portion of the cathode. With these results it is felt that additional data points for validation or comparison to tank house conditions would be justified for further validation.

- **Develop a model for short circuit effects on current efficiency.**

  This portion of the project is under development at this time. The other sections provide sufficient depth and breadth to provide for the derivation of this section which will be accomplished for the project sponsors at a later date.

- **Cost parameters model to allow prediction of operating costs.**

  Chapter 5 presented the development of a cost model to be incorporated with the roughness and short circuiting model. This was not covered in great depth as these are parameters unique to each tank house and will be provided and utilized by the project sponsors. For this work it was sufficient to define the electrochemical current efficiencies and power consumptions with derivations for additional operational cost to be added as required.

- **Perform Experimentation and develop instrumentation to validate the modeling.**

  Integral to the modeling efforts was the parallel work of validation with experimentation. These results can be found in each of the appropriate chapters. Overall the model results were in agreement with the experimental results except where noted.

- **Conclusion.**

  The fundamental objective of this work was to enable improved predictions of electrowinning tank house performance through more advanced modeling. In this purpose this work presents methods and models to achieve those ends. It is hoped that the work will provide a useful and meaningful method to improve tank house performance and profitability for years to come.

REFERENCES

[1] Aphichart Rodchanarowan, Prashant K Sarswat, Ravindra Bhide, and Michael L Free, "Production of copper from minerals through controlled and sustainable electrochemistry," *Electrochimica Acta* **140**, pp. 447–456 (2014).

[2] Michael L Free, *Hydrometallurgy: fundamentals and applications*, John Wiley & Sons (2013).

[3] D Ziegler and JW Evans, "Mathematical modeling of electrolyte circulation in cells with planar vertical electrodes i. electrorefining cells," *Journal of The Electrochemical Society* **133**(3), pp. 559–566 (1986).

[4] D Ziegler and JW Evans, "Mathematical modeling of electrolyte circulation in cells with planar vertical electrodes ii. electrowinning cells," *Journal of the Electrochemical Society* **133**(3), pp. 567–576 (1986).

[5] Donald Paul Ziegler, "A study of electrowinning and electrorefining cell hydrodynamics," PhD thesis University of California, Berkeley (1984).

[6] VA Ettel, BV Tilak, and AS Gendron, "Measurement of cathode mass transfer coefficients in electrowinning cells," *Journal of the Electrochemical Society* **121**(7), pp. 867–872 (1974).

[7] AS Gendron and VA Ettel, "Hydrodynamic studies in natural and forced convection electrowinning cells," *The Canadian Journal of Chemical Engineering* **53**(1), pp. 36–40 (1975).

[8] S Kisdnasamy and PS Neelakantaswamy, "A quantitative assessment of bubble-curtain effects upon interelectrode resistance of a conductimetric cell," *Journal of Applied Electrochemistry* **14**(6), pp. 749–754 (1984).

[9] TV Nguyen, CW Walton, Ralph E White, and J Van Zee, "Parallel-plate electrochemical reactor model a method for determining the time-dependent behavior and the effects of axial diffusion and axial migration," *Journal of the Electrochemical Society* **133**(1), pp. 81–87 (1986).

[10] William H Smyrl and John Newman, "Current distribution at electrode edges at high current densities," *Journal of The Electrochemical Society* **136**(1), pp. 132–139 (1989).

[11] Fritz H Bark and Farid Alavyoon, "Free convection in an electrochemical system with nonlinear reaction kinetics," *Journal of Fluid Mechanics* **290**, pp. 1–28 (1995).

[12] Guillermo Marshall and Pablo Mocskos, "Growth model for ramified electrochemical deposition in the presenceof diffusion, migration, and electroconvection," *Physical Review E* **55**(1), pp. 549 (1997).

[13] Anders A Dahlkild, "Modelling the two-phase flow and current distribution along a vertical gas-evolving electrode," *Journal of Fluid Mechanics* **428**, pp. 249–272 (2001).

[14] Fumio Hine and Koichi Murakami, "Bubble effects on the solution ir drop in a vertical electrolyzer under free and forced convection," *Journal of the Electrochemical Society* **127**(2), pp. 292–297 (1980).

[15] A Sokolichin, G Eigenberger, and A Lapin, "Simulation of buoyancy driven bubbly flow: established simplifications and open questions," *AIChE Journal* **50**(1), pp. 24–45 (2004).

[16] Mandin Philippe, Hamburger Jérôme, Bessou Sebastien, and Picard Gérard, "Modelling and calculation of the current density distribution evolution at vertical gas-evolving electrodes," *Electrochimica Acta* **51**(6), pp. 1140–1156 (2005).

[17] Rolf Wüthrich, Ch Comninellis, and Hannes Bleuler, "Bubble evolution on vertical electrodes under extreme current densities," *Electrochimica Acta* **50**(25), pp. 5242–5246 (2005).

[18] ML Free, R Bhide, A Rodchanarowan, and N Phadke, "Electrochemical modeling of electrowinning performance.," In *Sohn International Symposium; Advanced Processing of Metals and Materials Volume 6: New, Improved and Existing Technologies: Aqueous and Electrochemical Processing* volume 6 , pp. 479–491 (2006).

[19] L Cifuentes, JM Castro, G Crisóstomo, JM Casas, and J Simpson, "Modelling a copper electrowinning cell based on reactive electrodialysis," *Applied Mathematical Modelling* **31**(7), pp. 1308–1320 (2007).

[20] VM Volgin and AD Davydov, "The limiting current density of copper electrodeposition on vertical electrode under the conditions of electrolyte natural convection," *Russian Journal of Electrochemistry* **44**(4), pp. 459–469 (2008).

[21] John Newman and Karen E Thomas-Alyea, *Electrochemical systems*, John Wiley & Sons (2012).

[22] Kemal Aldas, Nur Pehlivanoglu, and Mahmut D Mat, "Numerical and experimental investigation of two-phase flow in an electrochemical cell," *International Journal of Hydrogen Energy* **33**(14), pp. 3668–3675 (2008).

[23] MC Ribeiro, LGC Rego, and PCT DAjello, "Diffusion, reaction and forced convection in electrochemical cells," *Journal of Electroanalytical Chemistry* **628**(1), pp. 21–26 (2009).

[24] A Pohjoranta, A Mendelson, and R Tenno, "A copper electrolysis cell model including effects of the ohmic potential loss in the cell," *Electrochimica Acta* **55**(3), pp. 1001–1012 (2010).

[25] VM Volgin and AD Davydov, "Numerical simulation of natural convection of electrolyte solution with three types of ions in the electrochemical cell with vertical electrodes," *Russian Journal of Electrochemistry* **46**(12), pp. 1360–1372 (2010).

[26] S Kawai, Y Fukunaka, and S Kida, "Numerical calculation of transient current density distribution along vertical plane electrode in cuso4–h2so4 electrolyte solution," *Journal of the Electrochemical Society* **157**(3), pp. F40–F48 (2010).

[27] Martin J Leahy and M Philip Schwarz, "Experimental validation of a computational fluid dynamics model of copper electrowinning," *Metallurgical and Materials Transactions B* **41**(6), pp. 1247–1260 (2010).

[28] Michael L Free, "Improved modeling of metal extraction and electrowinning," *1st International Metallurgical Meeting (Metal Extraction, Lima, Peru, October 2012)* **2**, pp. 1–13 (2012).

[29] KR Kim, SY Choi, S Paek, JY Park, IS Hwang, and Y Jung, "Electrochemical hydrodynamics modeling approach for a copper electrowinning cell," *Int. J. Electrochem. Sci* **8**, pp. 12333–12347 (2013).

[30] Helen Hemmati, Ali Mohebbi, Ataallah Soltani, and Shahram Daneshpajouh, "Cfd modeling of the electrolyte flow in the copper electrorefining cell of Sarcheshmeh copper complex," *Hydrometallurgy* **139**, pp. 54–63 (2013).

[31] Martin J Leahy and M Philip Schwarz, "Flow and mass transfer modelling for copper electrowinning: development of instabilities along electrodes," *Hydrometallurgy* **147**, pp. 41–53 (2014).

[32] Abhijeet Shukla, "Modeling and measuring electrodeposition parameters near electrode surfaces to facilitate cell performance optimization," PhD thesis The University of Utah (2013).

[33] Abhijeet Shukla and Michael Free, "Modeling and measuring electrodeposition parameters near electrode surfaces to facilitate cell performance optimization," In *Proc. 7th International Symposium on Hydrometallurgy (MetSoc, Westmont, Canada, September 2014)* volume 2 , pp. 67–68 (2014).

[34] Mark Robison and Michael L Free, "Modeling and experimental validation of electroplating deposit distributions from copper sulfate solutions," *ECS Transactions* **61**(21), pp. 27–36 (2014).

[35] Mark Robert Robison, "Modeling and experimental validation of electroplating deposit distributions in copper sulfate solutions," Master's thesis The University of Utah (2014).

[36] Weizhi Zeng, Joshua Werner, and Michael L Free, "Experimental studies on impurity particle behavior in electrolyte and the associated distribution on the cathode in the process of copper electrorefining," *Hydrometallurgy* **156**, pp. 232–238 (2015).

[37] Weizhi Zeng, Michael L Free, Joshua Werner, and Shijie Wang, "Simulation and validation studies of impurity particle behavior in copper electrorefining," *Journal of The Electrochemical Society* **162**(14), pp. E338–E352 (2015).

[38] Mahjabin Najminoori, Ali Mohebbi, Babak Ghadami Arabi, and Shahram Daneshpajouh, "CFD simulation of an industrial copper electrowinning cell," *Hydrometallurgy* **153**, pp. 88–97 (2015).

[39] Rainier Hreiz, Lokmane Abdelouahed, Denis Fünfschilling, and François Lapicque, "Electrogenerated bubbles induced convection in narrow vertical cells: A review," *Chemical Engineering Research and Design* **100**, pp. 268–281 (2015).

[40] Rainier Hreiz, Lokmane Abdelouahed, Denis Füenfschilling, and François Lapicque, "Electrogenerated bubbles induced convection in narrow vertical cells: PIV measurements and Euler–Lagrange CFD simulation," *Chemical Engineering Science* **134**, pp. 138–152 (2015).

[41] Giuliana Litrico, Camila B Vieira, Ehsan Askari, and Pierre Proulx, "Strongly coupled model for the prediction of the performances of an electrochemical reactor," *Chemical Engineering Science* (2016).

[42] Thomas J O'Keefe, SF Chen, JS Cuzmar, and V Ettel, "Application of electrochemical tracer techniques for determining mass transfer conditions during metal deposition," *Hydrometallurgical Reactor Design and Kinetics* , pp. 359–371 (1986).

[43] Thomas J O'Keefe, JS Cuzmar, and SF Chen, "Calculation of mass transfer coefficients in metal deposition using electrochemical tracer techniques," *Journal of The Electrochemical Society* **134**(3), pp. 547–551 (1987).

[44] Derek C Price and William G Davenport, "Densities, electrical conductivities and viscosities of $CuSO_4/H_2SO_4$ solutions in the range of modern electrorefining and electrowinning electrolytes," *Metallurgical Transactions B* **11**(1), pp. 159–163 (1980).

[45] Marc Laliberte and W Edward Cooper, "Model for calculating the density of aqueous electrolyte solutions," *Journal of Chemical & Engineering Data* **49**(5), pp. 1141–1151 (2004).

[46] Marc Laliberté, "Model for calculating the viscosity of aqueous solutions," *Journal of Chemical & Engineering Data* **52**(2), pp. 321–335 (2007).

[47] Mohammed Taghi Zafarani-Moattar and Roghayeh Majdan-Cegincara, "Viscosity modeling and prediction of aqueous mixed electrolyte solutions," *Industrial & Engineering Chemistry Research* **48**(12), pp. 5833–5844 (2009).

[48] Stephen F Agnew, "Rescaled specific volume model for electrolyte solution density," *Journal of Chemical & Engineering Data* **57**(1), pp. 60–65 (2011).

[49] MK Tham and KE Gubbins, "Effect of salts on the diffusion of dissolved non-electrolytes," *Journal of the Chemical Society, Faraday Transactions 1: Physical Chemistry in Condensed Phases* **68**, pp. 1339–1346 (1972).

[50] Donald G Miller, Joseph A Rard, Lee B Eppstein, and RA Robinson, "Mutual diffusion coefficients, electrical conductances, osmotic coefficients, and ionic transport coefficients ij for aqueous $CuSO_4$ at 25 ° C," *Journal of Solution Chemistry* **9**(7), pp. 467–496 (1980).

[51] Brent W Madsen, "Determination of ferric ion diffusion and activity coefficients from chronopotentiometric data," *U. S. Dept. of Interior, ,* p. 23 (1982).

[52] M Moats and Y Khouraibchia, "Effective diffusivity of ferric ions and current efficiency in stagnant synthetic copper electrowinning solutions," *Minerals and Metallurgical Processing* **26**(4), pp. 179–186 (2009).

[53] Olivier Bernard, Werner Kunz, Pierre Turq, and Lesser Blum, "Self-diffusion in electrolyte solutions using the mean spherical approximation," *Journal of Physical Chemistry* **96**(1), pp. 398–403 (1992).

[54] Michael S Moats, J Brent Hiskey, and Dale W Collins, "The effect of copper, acid, and temperature on the diffusion coefficient of cupric ions in simulated electrorefining electrolytes," *Hydrometallurgy* **56**(3), pp. 255–268 (2000).

[55] Olivier Bernard, Werner Kunz, Pierre Turq, and Lesser Blum, "Conductance in electrolyte solutions using the mean spherical approximation," *Journal of Physical Chemistry* **96**(9), pp. 3833–3840 (1992).

[56] Andrzej Anderko and Malgorzata M Lencka, "Modeling self-diffusion in multicomponent aqueous electrolyte systems in wide concentration ranges," *Industrial & Engineering Chemistry Research* **37**(7), pp. 2878–2888 (1998).

[57] Susan L Stipp, "Speciation in the Fe(II)-Fe(III)-SO_4-H_2O system at 25° C and low pH sensitivity of an equilibrium model to uncertainties," *Environmental Science & Technology* **24**(5), pp. 699–706 (1990).

[58] JM Casas, F Alvarez, and L Cifuentes, "Aqueous speciation of sulfuric acid–cupric sulfate solutions," *Chemical Engineering Science* **55**(24), pp. 6223–6234 (2000).

[59] Peiming Wang, Andrzej Anderko, and Robert D Young, "A speciation-based model for mixed-solvent electrolyte systems," *Fluid Phase Equilibria* **203**(1), pp. 141–176 (2002).

[60] P Wang, RD Springer, A Anderko, and RD Young, "Modeling phase equilibria and speciation in mixed-solvent electrolyte systems," *Fluid Phase Equilibria* **222**, pp. 11–17 (2004).

[61] Guikuan Yue, Liming Zhao, Oscar G Olvera, and Edouard Asselin, "Speciation of the H_2SO_4–$Fe_2(SO_4)_3$–$FeSO_4$–H_2O system and development of an expression to predict the redox potential of the Fe^{3+}/Fe^{2+} couple up to 150° C," *Hydrometallurgy* **147**, pp. 196–209 (2014).

[62] E Samson, J Marchand, and JJ Beaudoin, "Modeling the influence of chemical reactions on the mechanisms of ionic transport in porous materials: an overview," *Cement and Concrete Research* **30**(12), pp. 1895–1902 (2000).

[63] E Samson, G Lemaire, J Marchand, and JJ Beaudoin, "Modeling chemical activity effects in strong ionic solutions," *Computational Materials Science* **15**(3), pp. 285–294 (1999).

[64] Andrzej Anderko, Peiming Wang, and Marshall Rafal, "Electrolyte solutions: from thermodynamic and transport property models to the simulation of industrial processes," *Fluid Phase Equilibria* **194**, pp. 123–142 (2002).

[65] JB Hasted, DM Ritson, and CH Collie, “Dielectric properties of aqueous ionic solutions. parts i and ii,” *The Journal of Chemical Physics* **16**(1), pp. 1–21 (1948).

[66] PS Krishna Mohana Rao and D Premaswarup, “Dielectric properties of aqueous electrolytic solutions,” *Transactions of the Faraday Society* **66**, pp. 1974–1980 (1970).

[67] Peiming Wang and Andrzej Anderko, “Computation of dielectric constants of solvent mixtures and electrolyte solutions,” *Fluid Phase Equilibria* **186**(1), pp. 103–122 (2001).

[68] E Mattsson and JO’M Bockris, “Galvanostatic studies of the kinetics of deposition and dissolution in the copper+ copper sulphate system,” *Transactions of the Faraday Society* **55**, pp. 1586–1601 (1959).

[69] Mary-Elizabeth Wagner, Rodrigo Valenzuela, Tomás Vargas, Melanie Colet-Lagrille, and Antoine Allanore, “Copper electrodeposition kinetics measured by alternating current voltammetry and the role of ferrous species,” *Journal of The Electrochemical Society* **163**(2), pp. D17–D23 (2016).

[70] CSC Bose and NA Hampson, “Oxygen reduction on lead sulfuric acid solutions,” *Bulletin of Electrochemistry* **4**(5), pp. 437–442 (1988).

[71] Timo Laitinen and Jürgen P Pohl, “The kinetics of oxide growth and oxygen evolution during potentiostatic polarization of lead in h2so4 electrolytesinvestigations on the temperature dependence,” *Electrochimica acta* **34**(3), pp. 377–385 (1989).

[72] EN Codaro and JR Vilche, “A kinetic study of the electroformation of PbO_2 on Pb electrodes in sulphuric acid solutions,” *Electrochimica acta* **42**(4), pp. 549–555 (1997).

[73] D Pavlov and B Monahov, “Temperature dependence of the oxygen evolution reaction on the Pb/PbO_2 electrode,” *Journal of the Electrochemical Society* **145**(1), pp. 70–77 (1998).

[74] JV Petrocelli and AA Paolucci, “Overvoltage at oxidation-reduction electrodes,” *Journal of The Electrochemical Society* **98**(7), pp. 291–295 (1951).

[75] L Cifuentes and R Glasner, “Kinetics of the electrolytic Fe2+/Fe3+ oxidation on various anode materials,” *Revista de Metalurgia* **39**(4), pp. 260–267 (2003).

[76] L Cifuentes, R Glasner, and JM Casas, “Aspects of the development of a copper electrowinning cell based on reactive electrodialysis,” *Chemical Engineering Science* **59**(5), pp. 1087–1101 (2004).

[77] L Cifuentes and J Simpson, “Temperature dependence of the cathodic and anodic kinetics in a copper electrowinning cell based on reactive electrodialysis,” *Chemical Engineering Science* **60**(17), pp. 4915–4923 (2005).

[78] S Sandoval, P Cook, C Morales, and T Robinson, “Demonstration of the ferrous/ferric anode reaction for copper electrowinning,” *Copper 2010 Proceedings* **4**, pp. 1617–1634 (2010).

[79] V Tjandrawan and MJ Nicol, “Electrochemical oxidation of iron (ii) ions on lead alloy anodes,” *Hydrometallurgy* **131**, pp. 81–88 (2013).

[80] Youness Khouraibchia and Michael S Moats, "Evaluation of the effect of copper electrowinning parameters on current efficiency and energy consumption using surface response methodology," *ECS Transactions* **28**(6), pp. 295–306 (2010).

[81] Mingming Zhang and Ramana Reddy, "Electrical field and current density distribution modeling of aluminum electrodeposition in ionic liquid electrolytes," *ECS Transactions* **1**(16), pp. 47–60 (2006).

[82] Gert Nelissen and Robrecht Belis, "Advanced simulations of copper layer thickness distribution on printed circuit boards," *Metal Finishing* **107**(3), pp. 27–29 (2009).

[83] Ioanna Giannopoulou, Dimitrios Panias, and Ioannis Paspaliaris, "Electrochemical modeling and study of copper deposition from concentrated ammoniacal sulfate solutions," *Hydrometallurgy* **99**(1), pp. 58–66 (2009).

[84] Wu Heng, Tang Zhen'an, Wang Zhu, Cheng Wan, and Yu Daquan, "Simulation of through via bottomup copper plating with accelerator for the filling of TSVs," *Journal of Semiconductors* **34**(9), pp. 096001 (2013).

[85] Leandro Pinto, Paola Quaino, Elizabeth Santos, and Wolfgang Schmickler, "On the electrochemical deposition and dissolution of divalent metal ions," *ChemPhysChem* **15**(1), pp. 132–138 (2014).

[86] DV Patil, KN Premnath, D Desai, and Sanjoy Banerjee, "Electrodeposition modeling using coupled phase-field and lattice boltzmann approach," *International Journal of Modern Physics C* **25**(01), pp. 1340018 (2014).

[87] MT Johnson, CHC Keck, and KT Faber, "Experimental model validation of high aspect ratio through-hole filling by additive-assisted copper electrodeposition," *Journal of The Electrochemical Society* **164**(2), pp. D48–D52 (2017).

[88] JR Rawling and LD Costello, "Mixing characteristics of a copper refinery tankhouse cell," *JOM* **21**(5), pp. 49–52 (1969).

[89] FM Kimmerle, RL LeRoy, and O Vittori, "Concentration profiles in electrowinning circuits i. current efficiency," *Journal of The Electrochemical Society* **128**(9), pp. 1864–1869 (1981).

[90] RL LeRoy, FM Kimmerle, F Routhier, and O Vittori, "Concentration profiles in electrowinning circuits ii. time and position dependence of metal ion concentration," *Journal of The Electrochemical Society* **128**(9), pp. 1869–1873 (1981).

[91] AC Scott, RM Pitblado, and GW Barton, "A mathematical model of a zinc electrowinning cell," In *Proceedings of the Twentieth International Symposium on the Application of Computers and Mathematics in the Mineral Industries, Metallurgy* volume 2 , pp. 51–62 (1987).

[92] Hossein Aminian, Claude Bazin, and Daniel Hodouin, "Residence time distributions in SX–EW equipment," *International Journal of Mineral Processing* **54**(3), pp. 235–242 (1998).

[93] Ilkka S Laitinen and Juha T Tanttu, "Modelling and simulation of a copper electrolysis cell group," *Simulation Modelling Practice and Theory* **16**(8), pp. 900–909 (2008).

[94] Ilkka Laitinen, "Modelling, simulation and optimization of a copper electrolysis cell group," *Tampereen teknillinen yliopisto. Julkaisu-Tampere University of Technology. Publication; 828* (2009).

[95] A Blackett and M Nicol, "The simulation of current distribution in cells during the electrowinning of copper," In *Copper 2010, Proceedings, Hamburg, Germany, June 6-10, 2010* volume 4 , pp. 1281–1292 (2010).

[96] AM Lafront, B Veilleux, and E Ghali, "Electrochemical polarization studies of nodulation phenomenon during copper electrolysis," In *Electrometallurgy 2001: Proceedings of 31st Annual Hydrometallurgy Meeting, August 26-29, 2001, Toronto, Ontario, Canada* volume 20 , pp. 389–400 (2001).

[97] Michael Free, Aphichart Rodchanarowan, Nikit Phadke, and Ravindra Bhide, "Evaluation of the effects of additives, pulsing, and temperature on morphologies of copper electrodeposited from halide media," *ECS Transactions* **2**(3), pp. 335–343 (2006).

[98] Aphichart Rodchanarowan and Michael L Free, "The influence of organic additives on surface microroughness of copper deposits from cuprous solution under potentiostatic conditions," *Materials Transactions* **53**(9), pp. 1695–1698 (2012).

[99] *Comsol 5.2 CFD Users Reference*, Comsol.

[100] COMSOL Multiphysics, "Comsol multiphysics user guide (version 4.3 a)," *COMSOL, AB* , pp. 39–40 (2012).

[101] M Hammoudi, C Henao, K Agbossou, Y Dubé, and ML Doumbia, "New multi-physics approach for modelling and design of alkaline electrolyzers," *International Journal of Hydrogen Energy* **37**(19), pp. 13895–13913 (2012).

[102] *CFD Module Users Guide, version 5.2*, Comsol (2015).

[103] "Comsol multiphysics ® v. 5.2a,", `www.comsol.com`.

[104] DD Waeman, William H Evans, VB Paskes, RH Schumm, SM Bailey, I Halow, et al., "The NBS tables of chemical thermodynamic properties," *J. Phys. Chem. Ref. Data* **11** (1982).

[105] JP Gustafsson, "Visual minteq ver. 3.0," *Department of Land and Water Resources Engineering, Royal Institute of Technology: Stockholm, Sweden* (2011).

[106] James Stewart, "Calculus, brooks," *Cole Publishing Company* **6**, pp. 378 (1999).

[107] Thomas JR Hughes and Michel Mallet, "A new finite element formulation for computational fluid dynamics: Iii. the generalized streamline operator for multidimensional advective-diffusive systems," *Computer Methods in Applied Mechanics and Engineering* **58**(3), pp. 305–328 (1986).

[108] Isaac Harari and Thomas JR Hughes, "What are C and h?: Inequalities for the analysis and design of finite element methods," *Computer Methods in Applied Mechanics and Engineering* **97**(2), pp. 157–192 (1992).

[109] G Hauke and TJR Hughes, "A unified approach to compressible and incompressible flows," *Computer Methods in Applied Mechanics and Engineering* **113**(3-4), pp. 389–395 (1994).

[110] Guillermo Hauke, "Simple stabilizing matrices for the computation of compressible flows in primitive variables," *Computer Methods in Applied Mechanics and Engineering* **190**(51), pp. 6881–6893 (2001).

[111] Abraham Savitzky and Marcel JE Golay, "Smoothing and differentiation of data by simplified least squares procedures," *Analytical Chemistry* **36**(8), pp. 1627–1639 (1964).

[112] Phillip Barak, "Smoothing and differentiation by an adaptive-degree polynomial filter," *Analytical Chemistry* **67**(17), pp. 2758–2762 (1995).